Hybrid Monte Carlo – Deterministic Neutron Transport Methods Using Nonlinear Functionals

by

Emily R. Wolters

A dissertation submitted in partial fulfillment
of the requirements for the degree of
Doctor of Philosophy
(Nuclear Engineering and Radiological Sciences)
in The University of Michigan
2011

Doctoral Committee:

Professor Edward W. Larsen, Co-Chair
Professor William R. Martin, Co-Chair
Professor James Paul Holloway
Associate Professor Divakar Viswanath

To Mom and Dad, who encouraged me to work hard, to think critically, and to be assertive. Also, to Brook Johnson and Julia Kesten, my unwavering cheerleaders.

Acknowledgements

I am exceptionally grateful to my research advisors, Professor Ed Larsen and Professor Bill Martin, for their enthusiasm, mentorship, and patience throughout my academic career. Working with them has been a grand privilege, and I have probably abused the luxury of being able to pick their brains on anything “transport”. I look forward to now becoming their colleague and (eventually) deserving the respect they gave me from “Day One”. Special thanks must also be given to Professor James Holloway and Professor Divakar Viswanath for the time and interest they invested in this work, and for serving on my doctoral committee.

Professor Ziya Akcasu and Professor Han Joo (Seoul National University) held valuable discussions with myself and my advisors that made this dissertation a more complete body of work. Professor Gary Was, Professor Ron Fleming, and Pam Derry piqued my interest in nuclear engineering many years ago, so I may have chosen another profession without them. Peggy Gramer was there at every turn, answering every little question for the last several years.

Finally, I would like to recognize a few classmates: Dr. Kaushik Banerjee, whose brilliance I hope rubbed off on me slightly; Jinan Yang, my motivating study partner for the doctoral candidacy exam; and Eva Sunny, whose encouragement and friendship made my final years of graduate school infinitely more enjoyable. My success has been greatly influenced by these friends and colleagues, and I cannot thank them enough.

This work was supported by a U.S. Department of Energy Nuclear Engineering and Health Physics Scholarship, a University of Michigan Rackham Predoctoral Fellowship, and a University of Michigan Rackham Presidential Fellowship.

Table of Contents

List of Figures

List of Tables

Abstract

Several new hybrid Monte Carlo-deterministic methods based on nonlinear functionals are developed in this dissertation. The nonlinear functional approach consists of two fundamental steps: (1) the Monte Carlo estimation of *nonlinear functionals,* which are ratios of integrals of the particle flux, and (2) the deterministic solution of low-order algebraic equations that contain these functionals as parameters.

The nonlinear functionals for each hybrid method are formulated by taking space-angle-energy moments of the transport equation and performing algebraic manipulations to obtain a finite system of “low-order” equations. The stochastic nonlinear functional estimates are used in the low-order equations to solve for the particle flux. If the structure of the low-order equations is favorable, and the functionals are defined appropriately, the solution of the low-order equations will have less variance than the direct Monte Carlo estimate of the solution. Theoretical justification is given that stochastic estimates of the nonlinear functionals should have less variance than direct estimates of standard linear quantities when the same Monte Carlo histories are used to evaluate the numerator and denominator of each functional.

The new H-MC-S_2 and H-MC-S_2X methods incorporate functionals resembling flux-weighted cross sections and quadrature. The low-order equations of these methods resemble the one-group S_2 equations, but have no energy, angular, or spatial truncation errors. Simulations show that the variance of the H-MC-S_2X final solution is less than the variance of the standard Monte Carlo solution, leading to a reduction in computational cost for several test problems.

The new HCMFD-II, HCMFD-III and HCMFD-IV methods improve the previously-published CMFD-Accelerated Monte Carlo method by utilizing angular moments of the transport equation to reduce statistical errors in the CMFD nonlinear functionals. These new methods more efficiently converge the fission source in criticality simulations. Consequently, they require fewer inactive and active cycles, and fewer particles per cycle, leading to a large reduction in computational cost.

The techniques in this dissertation are explored for a subset of neutron transport problems including continuous energy fixed source problems and monoenergetic criticality problems. Our numerical results indicate that these nonlinear functional techniques are promising and should be extended to more realistic problems.

Chapter 1

Introduction

1.1 Overview

This dissertation comprises the derivation and evaluation of several new "hybrid" stochastic – deterministic numerical methods for solving the Boltzmann equation for neutron transport. The specific "hybrid" approach in this work is the use of stochastically-computed *nonlinear functionals* (ratios of integrals of the particle flux) in low-order deterministic equations to efficiently increase the accuracy of neutron transport simulations.

The nonlinear functionals for a given hybrid method are defined by taking space-angle-energy moments of the transport equation and performing algebraic manipulations to achieve low-order equations with a desired structure. When this is done "correctly", Monte Carlo estimates of the nonlinear functionals have much less variance than direct estimates of the flux integrals. The nonlinear functional estimates are used in the low-order equations to solve for the particle flux. If the structure of the low-order equations is favorable, the solution of these low-order equations should have less variance than the direct Monte Carlo estimate of the solution.

The nonlinear functional approach is more complicated than conventional Monte Carlo, but it can offer major computational advantages, particularly for systems with high dominance ratios. In this work, we show that the errors in conventional deterministic and stochastic methods can be suppressed by using hybrid techniques with the nonlinear functional approach, leading to more accurate solutions at a lower computational cost.

In this chapter, we review the Boltzmann neutron transport equation and the conventional deterministic and stochastic techniques used to numerically solve it. We describe the strengths and weakness of the conventional methods, and we identify specific problems for which hybrid numerical methods have been used to improve numerical results. We review two previously-developed hybrid methods that use the nonlinear functional approach, and finally, we preview the new methods that are developed in the remainder of the dissertation.

1.2 The Boltzmann Equation for Neutron Transport

The steady-state Boltzmann neutron transport equation,

$$\begin{aligned}\hat{\Omega}\cdot\vec{\nabla}\psi(\vec{r},E,\hat{\Omega})+\Sigma_t(\vec{r},E)\psi(\vec{r},E,\hat{\Omega})\\ =\int_{4\pi}\int_0^{\infty}\Sigma_s(\vec{r},E'\to E,\hat{\Omega}\cdot\hat{\Omega}')\psi(\vec{r},E',\hat{\Omega}')dE'd\hat{\Omega}'+S(\vec{r},E,\hat{\Omega}),\end{aligned} \tag{1.1}$$

governs the neutron angular flux, $\psi(\vec{r},\hat{\Omega},E)$, a density-like quantity, in six-dimensional phase space: space $\vec{r}$, angle $\hat{\Omega}$, and energy E [1]. Each term in the Boltzmann equation corresponds to a physical process that changes a neutron's phase space: birth, collisions, and leakage. In this work, we use Cartesian coordinates for space, $\vec{r}=x\hat{i}+y\hat{j}+z\hat{k}$, and spherical coordinates for angle,

$$\hat{\Omega}=\hat{\Omega}(\mu,\gamma)=\sqrt{1-\mu^2}\cos(\gamma)\hat{i}+\sqrt{1-\mu^2}\sin(\gamma)\hat{j}+\mu\hat{k}, \tag{1.2}$$

where $\mu=\cos(\theta)$. The polar angle is $\theta\in[0,\pi]$, and the azimuthal angle is $\gamma\in[0,2\pi]$.

Neutron transport problems are typically classified as fixed source or fission source (criticality) problems. In fixed source problems, neutrons are released into the system with a known distribution: $S(\vec{r},E,\hat{\Omega})=\frac{1}{4\pi}Q(\vec{r},E)$. In fission source problems, fissile material releases neutrons during fission events with a distribution related to the unknown scalar flux:

$$S(\vec{r},E,\hat{\Omega})=\frac{\chi(E)}{4\pi k_{eff}}\int_0^{\infty}\nu\Sigma_f(\vec{r},E)\phi_0(\vec{r},E)dE, \tag{1.3}$$

where the scalar flux $\phi_0(\vec{r},E)$ is defined as the zero$^{\text{th}}$ angular moment of the angular flux:

$$\phi_0(\vec{r},E) = \int_{4\pi} \psi(\vec{r},E,\hat{\Omega})d\Omega. \tag{1.4}$$

Fission source problems are solved numerically by iterative techniques, and are also known as *criticality* or *eigenvalue* problems.

Once neutrons are "born" in a system, they undergo a series of physical processes referred to collectively as "neutron transport". While inside the system, neutrons stream between collisions with the nuclei in the system materials; neutrons also "leak" into or out of the system when they physically cross any system boundary. The probability per unit distance traveled of a collision, and the type of collision (i.e., scatter, absorption, fission), are driven by parameters called *cross sections*. Each material has a set of interaction cross sections $\left(\Sigma_s(E),\Sigma_\gamma(E),\ldots\right)$ that govern the different nuclei-neutron interaction probabilities. The total interaction cross section is the sum of the individual interaction cross sections [1]:

$$\Sigma_t(E) = \Sigma_s(E) + \Sigma_\gamma(E) + \Sigma_f(E) + \ldots \tag{1.5}$$

Cross sections have a unique and complex dependence on neutron energy. They can contain large peaks (*resonances*) over narrow energy ranges. Cross section behavior is therefore difficult to model because simple discretization of the energy range would require tens of thousands of grid points. Instead of a simple discretization, the multigroup approximation is conventionally used to discretize the energy variable. This approximation is discussed later.

Much attention has been devoted to developing algorithms for solving the transport equation, particularly in the application of nuclear fission reactors and radiation shielding problems. The desired quantities in most radiation transport problems are:

a) the scalar flux distribution or eigenfunction $\phi_0(x,E)$,

b) the eigenvalue k_{eff} ,

c) various response rates, i.e. $R_i(x) = \int_0^\infty \Sigma_i(x,E)\phi_0(x,E)dE.$

Numerous techniques have been developed to solve the Boltzmann equation for these quantities. In the following section, we describe the characteristics of the conventional classes of numerical methods: deterministic and stochastic (Monte Carlo) techniques.

1.3 Deterministic Methods

Deterministic methods are characterized by the discretization of the neutron transport equation to obtain an algebraic system of equations for the scalar flux [1]. An excellent review of deterministic methods is given in [2]. The primary limitation in deterministic methods is the number of unknowns that can be stored in memory. The errors in deterministic methods decrease as the various grids decrease in size (and the number of unknowns increases). Therefore, the size of available computer memory and computational performance can limit the accuracy of deterministic calculations.

1.3.1 Spatial Discretization

The spatial discretization of the transport equation consists of dividing the system domain into a structured or unstructured grid. “Homogenization” of materials within a cell is often performed in order to reduce the number of spatial unknowns, computational cost and memory requirements.

1.3.2 Angular Discretization

Discretization of the angular variable is generally performed in two different ways. For example, quantities in the transport equation can be expanded in spherical harmonic functions (the P_N method), or they may be evaluated at discrete angles (the S_N or discrete ordinates method). The diffusion approximation can also be used by integrating the transport equation to yield the balance equation:

$$\vec{\nabla}\cdot\vec{\phi}_1(\vec{r},E)+\Sigma_a(\vec{r},E)\phi_0(\vec{r},E)=S(\vec{r},E), \tag{1.6}$$

and applying the approximation $\vec{\phi}_1(\vec{r},E)=-D(\vec{r})\vec{\nabla}\phi_0(\vec{r},E)$, where the *neutron current* has been defined: $\vec{\phi}_1(\vec{r},E)=\int_{4\pi}\hat{\Omega}\psi(\vec{r},E,\hat{\Omega})d\Omega$. Use of the diffusion approximation is limited to problems in which leakage, absorption rates, and flux gradients are small. When these circumstances do not apply, diffusion theory is not accurate.

1.3.3 Energy Discretization

Energy discretization is the most complex and difficult step of a deterministic calculation. As previously alluded, the multigroup (MG) approximation is typically required. This approximation consists of partitioning the energy range into "groups" and condensing the continuous energy cross sections over each group with a weighting function. The subscript g is used to denote a quantity that has been condensed over the g^{th} energy group: $E_g \le E \le E_{g-1}$. In order to rigorously preserve reaction rates, the exact angular flux must be applied as the weighting function. This technique eliminates the energy dependence of the cross section but introduces angular dependence of the resulting multigroup cross section:

$$\Sigma_{t,g}(\vec{r},\hat{\Omega}) \equiv \frac{\int_{E_g}^{E_{g-1}} \Sigma_t(\vec{r},E)\psi(\vec{r},\hat{\Omega},E)dE}{\int_{E_g}^{E_{g-1}} \psi(\vec{r},\hat{\Omega},E)dE}. \tag{1.7}$$

The true angular dependence of the rigorously-collapsed multigroup cross section cannot be incorporated into conventional deterministic code frameworks [2]. In addition, the exact angular flux is unknown; it is precisely the quantity we are trying to compute. In practice, the angular flux weighting function is replaced by an approximate "spectrum" function, $W(E)$, determined from a simplified "spectrum calculation".

$$\Sigma_{t,g}^{i} = \frac{\int_{E_g}^{E_{g-1}} \Sigma_t^i(E)W(E)dE}{\int_{E_g}^{E_{g-1}} W(E)dE}. \tag{1.8}$$

The rationale for using Eq. (1.8) is that when the true flux is separable in angle and energy, the angular dependence cancels, leaving only energy dependence. In addition, the spatial dependence is considered separable from energy or calculated with a simple 1-D calculation. While Eq. (1.8) has become the standard for energy discretization in deterministic methods, it can incur unacceptable errors when the true flux is *not* separable in angle and energy, or when the spectrum is inadequately computed. Refining the group structure mitigates these errors, but computational expense and memory limitations prevent the use of an arbitrarily fine group structure. The consistent P_N and extended transport approximations [2] are alternatives to using an isotropic weighting function, but these techniques require angularly-dependent spectrum calculations.

The major difficulty in deterministic methods therefore lies in the generation of the multigroup cross sections. The determination of the appropriate weighting functions and optimum group structure is time-consuming, and significant errors may occur when these steps are not adequately performed.

1.3.4 Challenges in Deterministic Methods

In addition to the difficulties presented by the multigroup approximation, the spatial and angular discretization schemes introduce truncation errors. These errors are reduced as the grids are refined, but the grid size is often limited by computational resources. The number of unknowns for a typical fission reactor problem can quickly become intractable even on supercomputers. In addition, it is difficult to optimize the grid parameters *a priori*.

1.3.5 Advantages of Deterministic Methods

Despite the difficulties in discretization and multigroup cross section generation, most commercial neutron transport codes are based on deterministic methodologies. After preparation of the multigroup cross sections, the transport equation can be discretized in angle and space, and the resulting algebraic system of equations can be solved on a computer. For fixed source problems, the transport equation reduces to a matrix system, $\mathbf{H}\boldsymbol{\psi} = \mathbf{q}$. For fission source problems, the transport equation is formulated as an eigenvalue problem, $\mathbf{Af} = k\mathbf{f}$, where $\mathbf{f}$ is the fission source [2].

Deterministic methods have certain computational advantages. For example, the discretized diffusion equations are elliptic and spread information throughout the system infinitely fast. This feature is particularly helpful for analyzing large, loosely-coupled systems like thermal fission reactors. Also, deterministic methods excel at calculating both global (i.e. eigenvalue) and local (i.e. eigenfunction) quantities.

1.4 Monte Carlo Methods

Monte Carlo methods are a fundamentally different approach to simulating solutions of the Boltzmann transport equation. In contrast with deterministic methods, Monte Carlo methods model the exact geometry and physics (i.e. continuous energy, angle, space) of a system by simulating neutron "histories": the random sequence of physical processes a neutron undergoes from birth to death. Monte Carlo solutions have no truncation errors, but they do have stochastic uncertainties.

1.4.1 Random Sampling

To begin a Monte Carlo simulation, the starting location, direction and energy of a neutron are randomly sampled from specified probability distributions. The neutron travels in a straight path until it collides with an nucleus at a location randomly sampled from the interaction probability density function. The type of collision and collision properties (e.g. emergent direction and energy from a scatter) are sampled in accordance with the cross sections. The process of transporting the particle according to probability distributions repeats until the particle exits the system or is absorbed. The next history then begins and is completely independent of the previous history.

During each history, information is collected about the neutron's path and interactions throughout the system. Suppose that x is a random variable representing some property of a neutron history (for example, the flux within a particular spatial cell) with *pdf mean* $\bar{x} = E\left[x\right]$ and *pdf variance* $\sigma^2(x) = E\left[\left(x - E\left[x\right]\right)^2\right]$. The "pdf" acronym describes inherent properties of the probability density function. The *pdf variance* describes how far values of x are expected to be "distributed" from the mean in the probability density function.

The Monte Carlo simulation generates the samples $(x_1, \ldots, x_N)$ of x over N neutron histories. The *sample mean*

$$\hat{x}_N = \frac{1}{N}\sum_{n=1}^{N} x_n, \tag{1.9}$$

is an unbiased estimator of the pdf mean, i.e. $E\left[\hat{x}_N\right]=E\left[x\right]=\bar{x}$. The *variance of the sample mean* [2] is

$$\sigma^2(\hat{x}_N)=\frac{\sigma^2(x)}{N}. \tag{1.10}$$

We therefore have distinguished two types of variances. To understand the *variance of the sample mean*, say we perform several independent simulations with N histories each, and generate a sample mean from each simulation. This "collection" of sample means has its own distribution, and Eq. (1.10) states that the variance of this distribution is the pdf variance divided by the number of samples used to estimate the sample mean. This interpretation makes sense: as the number of samples N becomes larger, each sample mean becomes more accurate, and the collection of sample means becomes more closely distributed to the pdf mean.

In Monte Carlo simulations, a finite number of samples are generated, and the true mean is unknown. To estimate the pdf variance, $\sigma^2(x)$, of a finite set of samples, an unbiased estimator called the *sample pdf variance* [2] is used:

$$S^2=\frac{N}{N-1}\left[\left(\widehat{x^2}\right)_N-(\hat{x}_N)^2\right], \tag{1.11}$$

where $\left(\widehat{x^2}\right)_N \equiv \frac{1}{N}\sum_{n=1}^{N} x_n^2$ and $E\left[S^2\right]=\sigma^2(x)$. To estimate the variance of the sample mean with a finite number of samples, the *sample variance of the sample mean* is used:

$$S_N^2=\frac{1}{N-1}\left[\left(\widehat{x^2}\right)_N-(\hat{x}_N)^2\right]. \tag{1.12}$$

Monte Carlo simulations are generally used to compute *sample means* [Eq. (1.9)] and *sample variances of the sample mean* [Eq. (1.12)]. In this work, when we refer to a "mean" and "variance", we are referring to the *sample mean* and *sample variance of the sample mean* unless otherwise specified. We now briefly describe how Monte Carlo generates means and variances of random variables for *fixed source* and *criticality* problems.

Fixed source calculations simulate a fixed number of neutron histories; each neutron is born with a specified distribution in energy, angle and space. The desired quantities (i.e. flux, reaction rates) are averaged over these histories, and the variance of these estimates are estimated from Eq. (1.12).

Criticality calculations consist of several sequential fixed source calculations, called *cycles* (or *generations*). The first cycle utilizes an arbitrary fission source distribution. The fission source distribution for subsequent cycles is defined from the previous cycle fission sites. The initial “inactive” cycles are used solely to “converge” the fission source to the true distribution. Subsequent “active” cycles are performed to tally information about the desired quantities. Therefore, averaging is done twice: the samples generated by each history are averaged with a cycle to produce a cycle mean, and then the cycle means are averaged over all cycles to produce the final reported mean. The final reported variance is the sample variance of the sample (cycle) means.

1.4.2 Challenges in Monte Carlo

Monte Carlo excels at computing global quantities such as the eigenvalue or system-integrated power, but the computation of detailed local quantities, such as the flux within a spatial cell, can be difficult to estimate accurately. In Monte Carlo, data can only be collected in regions of phase space where random neutrons “travel”. In areas of low neutron population (such as at the edge of a shielding material), variance may be unacceptably large due to undersampling. Variance reduction (VR) techniques have been successfully developed to bias particle travel through undersampled regions. However, VR techniques require user expertise to provide the optimum biasing parameters: this procedure can be time-consuming and difficult, although progress has been made in recent years to develop automatic variance reduction techniques. Lastly, for large, loosely coupled problems such as fission reactors, Monte Carlo can be extremely slow to converge the fission source because different areas of the problem cannot “see” each other. In other words, standard Monte Carlo information does not spread easily throughout the system. While one area of the problem may be converging, another area might not. Acceleration of the convergence of the fission source in Monte Carlo is the subject of much research.

1.4.3 Advantages of Monte Carlo

While Monte Carlo can be computationally expensive, it is favored for certain applications because of its ability to model the exact geometry and energy-dependent physics. There are no concerns regarding homogenization, multigroup condensation, grid size, truncation errors, etc. In addition, the statistical variance in a Monte Carlo calculation can be quantified by Eq. (1.10) where $\sigma^2(x)$ is estimated by the sample variance in Eq. (1.11). Most importantly, the Central Limit Theorem (CLT) can be used to interpret the *standard deviation of the sample mean*, or simply, the "standard deviation", $\sigma(\hat{x}_N) = \frac{\sigma(x)}{\sqrt{N}}$, as a 68.3% confidence level, meaning that it is 68.3% likely that the estimated mean $\hat{x}_N$ lies within one standard deviation of the pdf mean $\overline{x}$. The CLT states [2] that as N approaches infinity, then the independent estimates of $\hat{x}_N$ are *normally distributed* with the following probability density function:

$$f_N(\hat{x}_N) = \sqrt{\frac{N}{2\pi}} \frac{1}{\sigma(x)} e^{-\left[\frac{N(\hat{x}_N - \overline{x})^2}{2\sigma^2(x)}\right]}. \tag{1.13}$$

It can be shown that the probability that $\hat{x}_N$ lies within M standard deviations of the pdf mean is $erf\left[\frac{M}{\sqrt{2}}\right]$, where erf is the error function. Therefore, while a particular random variable may not be normally distributed, *independent estimates of the mean are normally distributed when the number of histories is large*. In practical terms, increasing the number of histories in a Monte Carlo calculation makes it more likely that an individual estimate of the mean is closer to the true mean. [Note: The Central Limit Theorem does not apply when the mean is obtained using dependent histories, as is the case in correlated cycle criticality calculations.]

1.5 The Need for Hybrid Methods

We have discussed the main strengths and weaknesses of conventional deterministic and Monte Carlo methods. Next, we identify some specific neutron transport problems that cause difficulty for conventional numerical techniques and discuss how hybrid methods have been implemented to mitigate these problems.

1.5.1 Automated Variance Reduction in Monte Carlo

To date, most "hybrid" techniques have been designed to automate the generation of variance reduction parameters (such as weight windows) in Monte Carlo. These techniques begin with a deterministic calculation to generate biasing parameters, and then the Monte Carlo simulation is performed using the parameters. For example, deterministic adjoint calculations have been used to automatically generate weight windows for Monte Carlo simulations [3][4][5]. These techniques are useful in Monte Carlo simulations for which the flux is desired in a local region, or at all physical locations in the system. Classic weight window methods are applied to source-detector problems and used to steer particles toward a particular region of low particle density (in shielding models, for example). We do not discuss these methods in further detail because they are fundamentally different from the "hybrid" approach used in this work, and because issues of low particle density are not frequent in reactor physics criticality calculations (the focus of this work). However, these "hybrid" methods could be used *with* the new hybrid methods presented in this dissertation to analyze shielding applications.

1.5.2 Transport Effects

Deterministic methods utilize numerous approximations to discretize the exact transport equation into a set of linear equations solvable on a computer. Sometimes the resulting numerical solution differs from the true solution because the true physics cannot be accurately modeled. The physics that cannot be accurately modeled without an ultra-fine space-angle-energy grid are referred to as *transport effects*. For example, at some material interfaces, the angular flux exhibits a strong correlation between energy and angle. These "transport effects" are difficult to capture using conventional deterministic methods due to the limitations of the multigroup approximation. Transport effects are only associated with deterministic methods, since Monte Carlo methods model the exact physics and geometry. These effects can be described by refining the spatial, energy, and angular grids, but several calculations may be necessary to determine the required level of refinement.

It is important to address the issue of transport effects in computational modeling because candidate future nuclear reactors, such as the Very High Temperature Reactor (VHTR) and the Advanced Burner Reactor (ABR), have new geometries and materials (i.e. voids, streaming regions, steel reflectors) that cause transport effects not well modeled by existing numerical techniques.

The existence of transport effects is well-known. For example, Aliberti, et al. [6] and Lebrat, et al. [7], considered the specific example of a model fast reactor consisting of a cylindrical core surrounded by a reflector. Near the core-reflector interface, the direction of a neutron is strongly correlated to its energy, causing a significant spectral effect near the interface. Aliberti and Lebrat attempted to calculate local reaction rates near the core-reflector interface and the global eigenvalue for this problem using a conventional 33-group discrete ordinates deterministic method, and they observed significant errors. They achieved satisfactory results after refining the group structure to 300 groups, but general use of such a fine grid was considered prohibitively expensive. They developed an improved 33-group methodology by using a spatially-dependent spectral weighting function (generated from a coupled core-reflector spectrum calculation).

The generation of spatially-dependent spectra for multigroup cross section generation near interfaces has also been recommended by other authors [8][9]. This approach is a costly but effective workaround for the multigroup approximation. Alternatively, Hanshaw [10][11] developed an adjoint weighting function which improves results for problems with strong spatial and angular variation. However, this method still approximates the rigorous multigroup cross section in Eq. (1.7).

The inherent complexity of neutron transport problems makes it difficult to know where transport effects will occur, and how to alter deterministic methods to best treat them. We suggest that it may be advantageous to avoid the multigroup approximation altogether, and this idea is the driving force behind the first two hybrid methods developed in this work, H-MC-S_2 and H-MC-S_2X.

1.5.3 Fission Source Convergence

Convergence of the fission source is a significant computational burden in Monte Carlo criticality calculations. For large systems, the dominance ratio $DR = \frac{k_2}{k_1}$ (the ratio of the second to first eigenvalue) is close to unity. In these cases, the higher-order eigenfunction modes decay slowly, and the true eigenfunction is poorly resolved for a long time. The Monte Carlo estimate of the fission source is unstable, and in some cases never fully converges. Slow fission source convergence is an inherent undesirable property of standard Monte Carlo calculations, and it can cause significant uncertainty in the true power distribution of a reactor.

1.5.4 Functional Monte Carlo

E. W. Larsen and J. Yang first proposed the use of nonlinear functionals to accelerate Monte Carlo convergence of the fission source in the "Functional Monte Carlo" (FMC) method [12][13][14]. In FMC, Monte Carlo is used to estimate nonlinear functionals, which are ratios of space-angle-energy moments of the angular flux, resembling Eddington factors. The functionals are used in quasi-diffusion-like equations with no truncation errors to estimate the eigenvalue and eigenfunction.

Larsen and Yang demonstrated that FMC estimates of the eigenvalue and eigenfunction are more accurate and stable than standard Monte Carlo estimates of these quantities. To date, FMC has been developed and tested in planar geometry with continuous energy-dependence. The caveat of the FMC method is the algebraic complexity of the low-order equations; algebraic manipulations are required to eliminate the particle current and keep only even-order angular moments of the flux in the functional definitions.

1.5.5 Coarse Mesh Finite Difference-Accelerated Monte Carlo

M.J. Lee, H.G. Joo, K. Smith, and D.J. Lee proposed "Coarse Mesh Finite Difference (CMFD)-Accelerated Monte Carlo" after Larsen and Yang introduced the FMC method. CMFD-Accelerated Monte Carlo also uses stochastically-computed nonlinear functionals to accelerate convergence of the fission source in Monte Carlo [15][16][17]. This method is based on the well-known deterministic CMFD method [18]. In CMFD, transport-corrected diffusion theory is performed on a coarse grid to accelerate source convergence in fine-grid transport calculations. The CMFD "diffusion" equations utilize nonlinear functionals that contain the ratio of the particle current to the scalar flux. In CMFD-Accelerated Monte Carlo, these nonlinear functionals are estimated during each Monte Carlo cycle, and then used in the CMFD equations to obtain a coarse grid estimate of the fission source. The CMFD fission source is then optionally used to modify the Monte Carlo fission source for the next cycle (known as "feedback").

CMFD-Accelerated Monte Carlo has been developed and tested in planar and x-y geometry with multigroup energy dependence. Lee, et al., showed that applying "CMFD feedback" accelerates convergence of the Monte Carlo fission source and makes the apparent variance of the resulting eigenfunction closer to the true variance.

The performances of CMFD-Accelerated Monte Carlo and FMC have been directly compared for a limited number of test problems by Lee, et al. [15] Preliminary results indicated that CMFD-Accelerated Monte Carlo is not efficient as Functional Monte Carlo for accelerating source convergence. In Chapter 5, we explain that this loss of efficiency is likely due to the current terms appearing the CMFD functionals. We then develop three improved hybrid Monte Carlo-CMFD techniques called HCMFD-II, HCMFD-III, and HCMFD-IV.

1.6 Dissertation Outline

In this work, we develop several hybrid methods using the nonlinear functional approach. These hybrid methods consist of two steps: (1) the stochastic estimation of nonlinear functionals, and (2) the deterministic solution of algebraic low-order equations that contain these functionals as parameters. Optionally, the solution of the low-order equations may be used to provide feedback to the Monte Carlo simulation in criticality problems. We explore methods with different low-order equation structures: the first two methods resemble discrete ordinates equations, and the last three methods resemble diffusion equations.

1.6.1 The H-MC-S_2 Method

In Chapter 2, we develop the first hybrid method, H-MC-S_2, from the planar geometry, continuous-energy Boltzmann equation in steady state. The transport equation is integrated over space (one spatial cell), energy (all energy), and angle ("negative" and "positive" directions) to obtain low-order equations resembling the one-group S_2 (discrete ordinates) equations. The nonlinear functionals are defined by performing algebraic manipulations to isolate ratios of space-angle-energy moments of the angular flux. The functionals resemble flux-weighted cross sections and flux-weighted quadrature but do *not* use the multigroup approximation in energy. A diamond-difference approximation is introduced in space to close the system of equations. Therefore, the method has no approximations in angle or energy, but it has statistical and spatial truncation errors.

We show by numerical simulations that the H-MC-S_2 method is more accurate than conventional stochastic and deterministic methods for a continuous-energy fixed source "core-reflector" problem with significant "transport effects". We also show the H-MC-S_2 solution has lower variance than the direct Monte Carlo estimate of the solution for the same number of histories, which translates to a 50% computational savings.

1.6.2 The H-MC-S_2X Method

The H-MC-S_2X method developed in Chapter 3 is based on the H-MC-S_2 method. A spatial tent function operator is applied to the transport equation before integration over space, energy, and angle. The operator eliminates the introduction of spatial approximations and spatial truncation error; consequently, the H-MC-S_2X method has only statistical errors. Again, we show that the H-MC-S_2X method is more accurate than standard Monte Carlo and discrete ordinates methods for a continuous-energy fixed source problem with "transport effects".

Chapter 4 presents theoretical justification and numerical results, showing that the nonlinear functionals in the H-MC-S_2X method can be computed more accurately, and with less variance, than standard Monte Carlo estimates of linear quantities. Both continuous-energy and mono-energetic problems fixed source are examined. We show that the H-MC-S_2X method performs well on mono-energetic problems, with a computational cost of about 20-25% that of standard Monte Carlo. For energy-dependent problems, some loss of efficiency is observed, and the computational cost rises to about 50% that of standard Monte Carlo. This degradation appears to be due to decreased statistical correlation in the functional numerators and denominators, and we suggest future work to improve the efficiency of the H-MC-S_2X in energy-dependent problems.

1.6.3 The HCMFD-II, HCMFD-III, and HCMFD-IV Methods

In Chapter 5, we examine the previously-published CMFD-Accelerated Monte Carlo Method (referred to as "HCMFD-I" in this work to emphasize similarity to our proposed methods). CMFD-Accelerated Monte Carlo utilizes diffusion-like low-order equations, but it is applicable to all transport problems. A stochastically-computed nonlinear "correction factor" accounts for deviations from transport theory, and the CMFD low-order equations have no truncation errors.

We provide theoretical justification that the particle current terms appearing in the CMFD functionals may cause the nonlinear functional to have large statistical errors. We suggest that these statistical errors cause a loss of efficiency when compared to the Functional Monte Carlo method (which does not have current terms). Using higher-order angular moments of the transport equation, we redefine the functional in three different ways without changing its expected value. The redefined functionals have less statistical error than the original functional, and are used in the proposed generalized CMFD methods: HCMFD-II, HCMFD -III, and HCMFD-IV. These methods are developed for the planar geometry, monoenergetic, steady state Boltzmann transport equation and tested primarily on eigenvalue problems. The low-order equations for the generalized methods are *identical* to CMFD-Accelerated Monte Carlo, and the redefined nonlinear functionals are slightly more complex than those in CMFD-Accelerated Monte Carlo, but not unduly so. In addition, the generalized HCMFD methods are much simpler to implement than Functional Monte Carlo.

For a monoenergetic fixed source problem, we show that the HCMFD-II, -III and –IV methods computational costs (24%, 21%, 18%) are comparable to the H-MC-S_2X method (18%), where the percentages are the fraction of standard Monte Carlo computing time required to achieve a given statistical error. These numbers are advantageous, but much more significant gains in computational efficiency are seen for criticality problems. Numerical results show that these new generalized HCMFD methods are more effective at converging the fission source than CMFD-Accelerated Monte Carlo and standard Monte Carlo. The computational savings over standard Monte Carlo is *substantial*: the new methods require *less than 1-5%* of the computing time to achieve equivalent real errors with standard Monte Carlo. The HCMFD-I method, in comparison, requires approximately 10-20% of the standard Monte Carlo computing time. This time savings refers only to the number of histories in active cycles; additionally, the number of inactive cycles in each hybrid method can be drastically reduced because of immediate source convergence.

1.6.4 Summary

Overall, the “functional” methods developed by Yang, et al., Lee, et al., and proposed by us in this work represent a new strategy for using Monte Carlo in particle transport simulations. In this thesis, we demonstrate that there are numerous different approaches that can be advantageous. We partially explore two classes of nonlinear functional methods (discrete ordinates-like and diffusion-like) by developing and testing these methods on subsets of neutron transport problems. The nonlinear functional methods developed in this thesis are shown to effectively reduce the standard Monte Carlo computing time for a variety of problems, although the efficiency is problem-dependent.

Our analysis and results are limited to 1-D (planar geometry), but there is no obvious reason why the aforementioned nonlinear functional methods should not work efficiently in 2-D. The H-MC-S_2 and H-MC-S_2X methods are developed for fixed source calculations but could certainly be extended to criticality calculations. In addition, the HCMFD-II, -III, and -IV methods are developed for monoenergetic problems, but extension to multigroup energy problems should be straightforward. Therefore, the work in this dissertation should help to lay the foundation for future work on more realistic problems.

1.7 References

[1] J.J. Duderstadt and L.J. Hamilton, *Nuclear Reactor Analysis*, John Wiley and Sons (1976).

[2] E.E. Lewis and W.F. Miller, Jr., *Computational Methods of Neutron Transport*, American Nuclear Society, Inc. (1993).

[3] T.L. Becker, A.B. Wollaber, and E.W. Larsen, “A Hybrid Monte Carlo–Deterministic Method for Global Particle Transport Calculations,” *Nucl. Sci. Eng.*, **155**, 155–167 (2007).

[4] T.L. Becker and E.W. Larsen, “The Application of Weight Windows to ‘Global’ Monte Carlo Problems,” *Proc. 2009 International Conference on Advances in Mathematics, Computational Methods, and Reactor Physics,* May 3-7, 2009, Saratoga Springs, New York, CD-ROM, American Nuclear Society (2009).

[5] J.C. Wagner, E.D. Blakeman, D.E. Peplow, “Forward-Weighted CADIS Method for Global Variance Reduction,” *Trans. Am. Nucl. Soc.*, **97**, 630–633 (2007).

[6] G. Aliberti, G. Palmiotti, M. Salvatores, J.F. Lebrat, J. Tommasi, and R. Jacqmin, “Methodologies for Treatment of Spectral Effects at Core-Reflector Interfaces in Fast Neutron Systems,” *Proc. 2004 International Conference on the Physics of Reactors*, April 25-29, 2004, Chicago, Illinois, CD-ROM, American Nuclear Society (2004).

[7] J.F. Lebrat, R. Jacqmin, F. Gabrielli, M. Carta, V. Peluso, G. Buzzi, G. Bianchini, A. D’Angelo, G. Aliberti, and G. Palmiotti, “Fast Reactor Core-Reflector Interface Effects Revisited,” *Proc. 2002 International Conference on the Physics of Reactors*, October 7-10, 2002, Seoul, Korea, CD-ROM, American Nuclear Society (2002).

[8] R. Corcuera and A. Khairallah, “Fine Neutron-Spectrum Effects on Spatial Calculations for Fast-Reactor Design,” *Nucl. Sci. and Eng.*, **53**, 420-435 (1974).

[9] D. Meneghetti and K.E. Phillips, “Fine-Spectral Interface Effects of Resonance Scattering Upon Multigroup Cross Section Averaging,” *J. Nucl. Eng.*, **24**, 509-524 (1970).

[10] H.L. Hanshaw, A. Haghighat, and J.C. Wagner, “Multigroup Cross-Section Generation with Spatial and Angular Adjoint Weighting”, Trans. Am. Nucl. Soc., 73, 175-177 (1995).

[11] H.L. Hanshaw, “Multigroup Cross Section Generation with Spatial and Angular Adjoint Weighting,” MS Thesis, Pennsylvania State University, (1995).

[12] E.W. Larsen and J. Yang, “A Functional Monte Carlo Method for k-Eigenvalue Problems,” *Nucl. Sci. Eng.*, **159**, 107-126 (2008).

[13] J. Yang and E.W. Larsen, “Application of the ‘Functional Monte Carlo’ Method to Estimate Continuous Energy Eigenvalues and Eigenfunctions,” *Proc. 2009 International Conference on Advances in Mathematics, Computational Methods,*

and Reactor Physics, May 3-7, 2009, Saratoga Springs, New York, CD-ROM, American Nuclear Society (2009).

[14] J. Yang and E.W. Larsen, “Calculation of k-Eigenvalues and Multigroup Eigenfunctions Using the Hybrid ‘Functional Monte Carlo’ Method,” *Proc. PHYSOR 2010 – Advances in Reactor Physics to Power the Nuclear Renaissance,* May 9-14, 2010, Pittsburgh, Pennsylvania, CD-ROM, American Nuclear Society (2010).

[15] M.J. Lee, H.G. Joo, D. Lee, and K. Smith, “Application of CMFD Acceleration to Monte Carlo Simulation for Eigenvalue Problems,” Personal Communication, Saratoga Springs, NY (2009).

[16] M.J. Lee, H.G. Joo, D. Lee, and K. Smith, “Investigation of CMFD Accelerated Monte Carlo Eigenvalue Calculation with Simplified Low Dimensional Multigroup Formulation,” *Proc. 2010 International Conference on the Physics of Reactors*, May 9-14, 2010, Pittsburgh, PA, CD-ROM, American Nuclear Society (2010).

[17] M.J. Lee, H.G. Joo, D. Lee, and K. Smith, “Multigroup Monte Carlo Reactor Calculation with Coarse Mesh Finite Difference Formulation for Real Variance Reduction,” *Proc. 2010 Joint International Conference on Supercomputing in Nuclear Applications and Monte Carlo,* October 17-21, 2010, Tokyo, Japan, CD-ROM, SNA+MC2010 (2010).

[18] K.S. Smith, “Nodal Method Storage Reduction by Nonlinear Iteration,” *Trans. Am. Nucl. Soc.,* **44**, 265-266 (1983).

Chapter 2

The Hybrid Monte Carlo – S_2 Method

2.1 Introduction

In this chapter, we develop the first of several hybrid methods discussed in this dissertation. The Hybrid Monte Carlo-S_2 method (abbreviated as H-MC-S_2) was motivated by the difficulty of using deterministic techniques to accurately solve problems with significant transport effects. As described in the previous chapter, deterministic methods use the multigroup approximation to discretize the continuous energy variable. However, the multigroup approximation can incur unacceptable errors for problems with transport effects unless very fine energy groups are used. Fine-group deterministic calculations are computationally expensive for realistic problems such as reactor physics calculations, so their usefulness is limited. We were therefore motivated to develop an alternative method with the following properties:

(1) The method should incorporate computationally inexpensive low-order equations similar to coarse-group deterministic methods.

(2) The method should minimize or eliminate discretization errors in energy and angle.

(3) When tested on problems with transport effects, the method should be more accurate and less expensive than conventional deterministic methods that use the multigroup approximation.

In the H-MC-S_2 method, the multigroup approximation and hence multigroup cross sections are not used. Instead, physically meaningful quantities called "nonlinear functionals" are introduced [1]. Each nonlinear functional is simply the ratio of two correlated physical quantities, similar to multigroup cross sections. The nonlinear functionals can be estimated with only small statistical error using Monte Carlo, and they preserve the exact physics of the problem in the low-order equations. We demonstrate in this chapter that the H-MC-S_2 method produces solutions with no energy or angular truncation errors; only spatial truncation errors and statistical errors will occur. These can be controlled by refining the grid size and increasing the number of neutron histories, respectively. Also, we show that the H-MC-S_2 method produces solutions with less statistical error than standard Monte Carlo solutions.

We now develop the H-MC-S_2 method and demonstrate its capabilities on 1-D, fixed source problems with isotropic scattering. We begin the derivation with the neutron transport equation.

2.2 Transport Equation

To begin, we consider the planar geometry neutron transport equation and boundary conditions:

$$\begin{gathered}\mu\frac{\partial}{\partial x}\psi(x,\mu,E)+\Sigma_t(x,E)\psi(x,\mu,E)\\ =\frac{1}{2}\int_0^\infty\Sigma_s(x,E')p(x,E'\to E)\phi(x,E')dE'+\frac{1}{2}Q(x,E), \qquad (2.1)\\ 0\le x\le X, \qquad -1\le\mu\le 1, \qquad 0<E<\infty\end{gathered}$$

$$\psi(0,\mu,E)=\psi(0,-\mu,E), \qquad 0<\mu\le 1, \qquad 0<E<\infty \qquad (2.2)$$

$$\psi(b,\mu,E)=0, \qquad -1\le\mu<0, \qquad 0<E<\infty. \qquad (2.3)$$

The following assumptions have been made: (a) no fission, (b) no inelastic scattering, (c) no upscattering, and (d) P_0 elastic scattering (isotropic). These assumptions have been made only for simplicity. Any changes in these assumptions can be incorporated with only slight modifications to the derivation of the method.

For completeness, we define the probability density function used in the elastic scattering kernel, valid when the temperature of nuclei is zero:

$$p(x, E' \to E) = \begin{cases} \dfrac{1}{\left(1-\alpha(x)\right)E'}, & \alpha(x)E' < E < E' \\ 0, & \textit{otherwise}, \end{cases} \tag{2.4}$$

$$\text{where } \alpha(x) = \left(\frac{A(x)-1}{A(x)+1}\right)^2 .$$

Here, $A(x)$ is the atomic mass of the material at location x. It is useful to recognize that because $p(x, E' \to E)$ is a probability density function, its integral over outgoing energy is unity: $\int_0^\infty p(x, E' \to E)dE = 1$.

2.3 Derivation of the H-MC-S$_2$ Method

The goal of this method, as in most numerical transport, is to compute one or more response rates (i.e. reaction rates, scalar flux) at locations throughout the system. These locations are determined by defining a mesh $\left\{x_{j+1/2},\ j = 0, \dots J\right\}$ that covers the entire range of the geometry and includes mesh points at material interfaces. The width of the j^{th} cell is $h_j = x_{j+1/2} - x_{j-1/2}$. The response rate averaged over cell j is

$$R_j = \frac{1}{h_j}\int_{x_{j-1/2}}^{x_{j+1/2}}\int_0^\infty\int_{-1}^1 r(x, E)\psi(x, \mu, E)d\mu dEdx, \tag{2.5}$$

where the response function $r(x, E)$ is known and given. For example, the response function $r(x, E) = \Sigma_a(x, E)$ yields the spatially-averaged absorption rate in cell j. The response function $r(x, E) = 1$ yields the energy-integrated, spatially-averaged scalar flux in cell j. The response functions must be chosen *a priori*, but an arbitrary number of them may be chosen simultaneously. In the following derivation, we have chosen a single response function $r(x, E)$.

2.3.1 Special Notation

The H-MC-S$_2$ method incorporates quantities that have been integrated over *subsets* of the full $\Omega \in 4\pi$ ($-1 \le \mu \le 1$ in 1-D) angular range. This contrasts with S_N

methods that evaluate quantities at discrete angles Ω_n (μ_n in 1-D) and P_N methods that require the computation of angular moments over the full angular range. Therefore, we introduce some new notation. In 1-D, the superscript $\left(^+\right)$ denotes angular integration over the sub-range $0 < \mu \leq 1,$ while the superscript $\left(^-\right)$ denotes angular integration over the sub-range $-1 \leq \mu < 0$. Therefore,

$$\psi^{\pm}(x,E) \equiv \pm\int_0^{\pm 1} d\mu \psi(x,\mu,E) . \tag{2.6}$$

Any quantity that is integrated over all angles $\left(-1 \leq \mu \leq 1\right)$ can thus be written as the sum of integrals over the two sub-ranges. For example, the scalar flux can be written $\phi(x,E) = \psi^+(x,E) + \psi^-(x,E)$. Also, the response rate can be written $R_j = R_j^+ + R_j^-$, where

$$R_j^{\pm} = \pm \frac{1}{h_j} \int_{x_{j-1/2}}^{x_{j+1/2}} \int_0^{\infty} \int_0^{\pm 1} r(x,E) \psi(x,\mu,E) d\mu dE dx. \tag{2.7}$$

2.3.2 Procedure

Before proceeding, we first clarify that the unknown quantities in this method are different than those in conventional deterministic methods. Conventional deterministic methods solve equations for the cell-averaged group-wise scalar fluxes, $\phi_{g,j}$. The desired response rates are then calculated by post-processing the group fluxes with the multigroup cross sections:

$$R_j = \sum_{g=1}^{G} \Sigma_{g,j} \phi_{g,j} . \tag{2.8}$$

In the H-MC-S$_2$ method, we formulate equations for $R_j^{\pm}$ directly by performing straightforward manipulations of the transport equation. In doing so, we introduce no approximations in energy or angle, and we avoid the generation of multigroup cross sections.

We begin the derivation of this method by applying the operators

$$\mathrm{H}_j^+\left(\cdot\right) = \int_0^X \int_0^\infty \int_0^1 \chi_j(x)\left(\cdot\right) d\mu\, dE\, dx \tag{2.9}$$

and

$$\mathrm{H}_j^-\left(\cdot\right) = \int_0^X \int_0^\infty \int_{-1}^0 \chi_j(x)\left(\cdot\right) d\mu\, dE\, dx \tag{2.10}$$

to the transport equation, where $\chi_j(x)$ is the histogram function

$$\chi_j(x) = \begin{cases} \dfrac{1}{h_j}, & x_{j-1/2} < x < x_{j+1/2} \\ 0, & otherwise \end{cases} \tag{2.11}$$

These operators simply average each term in the transport equation over spatial cell j, and then integrate over all energy and over a specified angular sub-range. Application of these operators to the transport equations yields two modified cell balance equations. Cell balance is now held over two angular sub-ranges rather than over all angles. The result of applying H_j^+ to the transport equation and using $\int_0^\infty p(x, E' \to E)dE = 1$ to simplify the scattering kernel is:

$$\begin{aligned} \frac{1}{h_j}\int_{x_{j-1/2}}^{x_{j+1/2}} \int_0^\infty \int_0^1 \mu \frac{\partial}{\partial x}\psi(x,\mu,E) d\mu\, dE\, dx + \frac{1}{h_j}\int_{x_{j-1/2}}^{x_{j+1/2}} \int_0^\infty \Sigma_t(x,E)\psi^+(x,E) dE\, dx \\ = \frac{1}{2h_j}\int_{x_{j-1/2}}^{x_{j+1/2}} \int_0^\infty \Sigma_s(x,E')\left[\psi^+(x,E') + \psi^-(x,E')\right] dE'\, dx \\ + \frac{1}{2h_j}\int_{x_{j-1/2}}^{x_{j+1/2}} \int_0^\infty Q(x,E) dE\, dx. \end{aligned} \tag{2.12}$$

We now proceed to manipulate this balance equation in order to formulate equations for $R_j^\pm$. First, we simplify the leakage term without approximation. The spatial partial derivative in the integrand allows the integrand to be evaluated at spatial integral endpoints only, yielding:

$$\begin{aligned}
&\frac{1}{h_j}\int_0^\infty\int_0^1 \mu\psi(x_{j+1/2},\mu,E)\,d\mu\,dE\,dx - \frac{1}{h_j}\int_0^\infty\int_0^1 \mu\psi(x_{j-1/2},\mu,E)\,d\mu\,dE\,dx \\
&+\frac{1}{h_j}\int_{x_{j-1/2}}^{x_{j+1/2}}\int_0^\infty \Sigma_t(x,E)\psi^+(x,E)\,dE\,dx \\
&\qquad = \frac{1}{2h_j}\int_{x_{j-1/2}}^{x_{j+1/2}}\int_0^\infty \Sigma_s(x,E')\left[\psi^+(x,E')+\psi^-(x,E')\right]dE'\,dx \\
&\qquad + \frac{1}{2h_j}\int_{x_{j-1/2}}^{x_{j+1/2}}\int_0^\infty Q(x,E)\,dE\,dx
\end{aligned} \tag{2.13}$$

Next, we introduce the unknown response rates into Eq. (2.13) by multiplying and dividing each flux-containing term by an “appropriate” unknown. The “appropriate” unknown for each term is the one whose integral over space, energy and angle match the limits of integration of the original term. Performing this procedure on Eq. (2.13), we obtain:

$$\begin{aligned}
&\frac{1}{h_j}\left[\frac{\int_0^\infty\int_0^1 \mu\psi(x_{j+1/2},\mu,E)\,d\mu dE}{\int_0^\infty r(x_{j+1/2},E)\psi^+(x_{j+1/2},E)\,dE}\right]R^+_{j+1/2} \\
&-\frac{1}{h_j}\left[\frac{\int_0^\infty\int_0^1 \mu\psi(x_{j-1/2},\mu,E)\,d\mu dE}{\int_0^\infty r(x_{j-1/2},E)\psi^+(x_{j-1/2},E)\,dE}\right]R^+_{j-1/2} \\
&+\frac{1}{h_j}\left[\frac{\int_{x_{j-1/2}}^{x_{j+1/2}}\int_0^\infty \Sigma_t(x,E)\psi^+(x,E)\,dEdx}{\frac{1}{h_j}\int_{x_{j-1/2}}^{x_{j+1/2}}\int_0^\infty r(x,E)\psi^+(x,E)\,dEdx}\right]R^+_j \\
&\qquad = \frac{1}{2h_j}\left[\frac{\int_{x_{j-1/2}}^{x_{j+1/2}}\int_0^\infty \Sigma_s(x,E')\psi^+(x,E')\,dE'dx}{\frac{1}{h_j}\int_{x_{j-1/2}}^{x_{j+1/2}}\int_0^\infty r(x,E)\psi^+(x,E)\,dEdx}\right]R^+_j \\
&\qquad + \frac{1}{2h_j}\left[\frac{\int_{x_{j-1/2}}^{x_{j+1/2}}\int_0^\infty \Sigma_s(x,E')\psi^-(x,E')\,dE'dx}{\frac{1}{h_j}\int_{x_{j-1/2}}^{x_{j+1/2}}\int_0^\infty r(x,E)\psi^-(x,E)\,dEdx}\right]R^-_j \\
&\qquad + \frac{1}{2h_j}\int_{x_{j-1/2}}^{x_{j+1/2}}\int_0^\infty Q(x,E)\,dE, \qquad 1\le j\le J
\end{aligned} \tag{2.14}$$

Here, we have introduced the new unknowns

$$R^{\pm}_{j+1/2} = \int_0^{\infty} r(x_{j+1/2}, E)\psi^{\pm}(x_{j+1/2}, E)dE \tag{2.15}$$

in order to keep the limits of integration consistent in the numerator and denominator of the leakage term. This increases the number of unknowns but not the number of equations. The eventual remedy for this will be the introduction of an approximation relating $R^{\pm}_{j}$ and $R^{\pm}_{j+1/2}$. However, for now, we return to Eq. (2.14).

The procedure used to obtain Eq. (2.14) from Eq. (2.13) does not introduce any error: it simply multiplies each term by unity. After some simple cancellation of cell widths, we obtain the following equation:

$$\begin{aligned}
&\frac{1}{h_j}\left[\frac{\int_0^{\infty}\int_0^{1}\mu\psi(x_{j+1/2},\mu,E)d\mu dE}{\int_0^{\infty} r(x_{j+1/2},E)\psi^{+}(x_{j+1/2},E)dE}\right]R^{+}_{j+1/2} \\
&-\frac{1}{h_j}\left[\frac{\int_0^{\infty}\int_0^{1}\mu\psi(x_{j-1/2},\mu,E)d\mu dE}{\int_0^{\infty} r(x_{j-1/2},E)\psi^{+}(x_{j-1/2},E)dE}\right]R^{+}_{j-1/2} \\
&+\left[\frac{\int_{x_{j-1/2}}^{x_{j+1/2}}\int_0^{\infty}\Sigma_t(x,E)\psi^{+}(x,E)dEdx}{\int_{x_{j-1/2}}^{x_{j+1/2}}\int_0^{\infty} r(x,E)\psi^{+}(x,E)dEdx}\right]R^{+}_{j} \\
&\qquad=\frac{1}{2}\left[\frac{\int_{x_{j-1/2}}^{x_{j+1/2}}\int_0^{\infty}\Sigma_s(x,E')\psi^{+}(x,E')dE'dx}{\int_{x_{j-1/2}}^{x_{j+1/2}}\int_0^{\infty} r(x,E)\psi^{+}(x,E)dEdx}\right]R^{+}_{j} \\
&\qquad+\frac{1}{2}\left[\frac{\int_{x_{j-1/2}}^{x_{j+1/2}}\int_0^{\infty}\Sigma_s(x,E')\psi^{-}(x,E')dE'dx}{\int_{x_{j-1/2}}^{x_{j+1/2}}\int_0^{\infty} r(x,E)\psi^{-}(x,E)dEdx}\right]R^{-}_{j} \\
&\qquad+\frac{1}{2h_j}\int_{x_{j-1/2}}^{x_{j+1/2}}\int_0^{\infty} Q(x,E)dE, \qquad 1\le j\le J.
\end{aligned} \tag{2.16}$$

A similar procedure is carried out for the H^{-}_{j} operator, and the following equation is obtained:

$$
\begin{aligned}
&\frac{1}{h_j}\left[\frac{\int_0^\infty\int_{-1}^0 \mu\psi(x_{j+1/2},\mu,E)d\mu dE}{\int_0^\infty r(x_{j+1/2},E)\psi^-(x_{j+1/2},E)dE}\right]R_{j+1/2}^-\\
&-\frac{1}{h_j}\left[\frac{\int_0^\infty\int_{-1}^0 \mu\psi(x_{j-1/2},\mu,E)d\mu dE}{\int_0^\infty r(x_{j-1/2},E)\psi^-(x_{j-1/2},E)dE}\right]R_{j-1/2}^-\\
&+\left[\frac{\int_{x_{j-1/2}}^{x_{j+1/2}}\int_0^\infty \Sigma_t(x,E)\psi^-(x,E)dEdx}{\int_{x_{j-1/2}}^{x_{j+1/2}}\int_0^\infty r(x,E)\psi^-(x,E)dEdx}\right]R_j^-\\
&\qquad=\frac{1}{2}\left[\frac{\int_{x_{j-1/2}}^{x_{j+1/2}}\int_0^\infty \Sigma_s(x,E')\psi^+(x,E')dE'dx}{\int_{x_{j-1/2}}^{x_{j+1/2}}\int_0^\infty r(x,E)\psi^+(x,E)dEdx}\right]R_j^+\\
&\qquad+\frac{1}{2}\left[\frac{\int_{x_{j-1/2}}^{x_{j+1/2}}\int_0^\infty \Sigma_s(x,E')\psi^-(x,E')dE'dx}{\int_{x_{j-1/2}}^{x_{j+1/2}}\int_0^\infty r(x,E)\psi^-(x,E)dEdx}\right]R_j^-\\
&\qquad+\frac{1}{2h_j}\int_{x_{j-1/2}}^{x_{j+1/2}}\int_0^\infty Q(x,E)dE, \qquad 1\le j\le J.
\end{aligned}
\tag{2.17}
$$

Certain ratios in Eqs. (2.16) and (2.17) have been bracketed for clarity. We now define these bracketed ratios as the special *nonlinear functionals*:

$$
\mu_{j+1/2}^{\pm}\equiv\frac{\int_0^\infty\int_0^{\pm1}\mu\psi(x_{j+1/2},\mu,E)d\mu dE}{\int_0^\infty\int_0^{\pm1} r(x_{j+1/2},E)\psi(x_{j+1/2},\mu,E)d\mu dE},
\qquad 0\le j\le J
\tag{2.18}
$$

$$
\Sigma_{i,j}^{\pm}\equiv\frac{\int_{x_{j-1/2}}^{x_{j+1/2}}\int_0^\infty\int_0^{\pm1}\Sigma_i(x,E)\psi(x,\mu,E)d\mu dEdx}{\int_{x_{j-1/2}}^{x_{j+1/2}}\int_0^\infty\int_0^{\pm1} r(x,E)\psi(x,\mu,E)d\mu dEdx}.
\qquad i=\{s,t\},\ 1\le j\le J
\tag{2.19}
$$

The nonlinear functionals in Eq. (2.19) are similar to multigroup cross sections. However, no approximation has been made in defining these functionals; they incorporate the true angular flux rather than an approximate energy spectrum. Also, it is easy to see an analogy between the functionals in Eq. (2.18) and the discrete angles μ_n used in discrete ordinates methods.

Replacing the notation in Eqs. (2.16) and (2.17) by the shorthand functional notation and the source notation

$$Q_j \equiv \frac{1}{h_j}\int_{x_{j-1/2}}^{x_{j+1/2}}\int_0^{\infty} Q(x,E)dEdx\,, \tag{2.20}$$

Eqs. (2.16) and (2.17) can be written:

$$\begin{gathered}\frac{1}{h_j}\left[\mu^+_{j+1/2}R^+_{j+1/2} - \mu^+_{j-1/2}R^+_{j-1/2}\right] + \Sigma^+_{t,j}R^+_j = \frac{1}{2}\Sigma^+_{s,j}R^+_j + \frac{1}{2}\Sigma^-_{s,j}R^-_j + \frac{1}{2}Q_j \\ 1 \le j \le J,\end{gathered} \tag{2.21}$$

$$\begin{gathered}\frac{1}{h_j}\left[\mu^-_{j+1/2}R^-_{j+1/2} - \mu^-_{j-1/2}R^-_{j-1/2}\right] + \Sigma^-_{t,j}R^-_j = \frac{1}{2}\Sigma^+_{s,j}R^+_j + \frac{1}{2}\Sigma^-_{s,j}R^-_j + \frac{1}{2}Q_j \\ 1 \le j \le J.\end{gathered} \tag{2.22}$$

We assume momentarily that the nonlinear functionals are known. The method for determining the functionals will be discussed shortly. Eqs. (2.21) and (2.22) are exact equations that relate the cell-boundary response rates, $R^{\pm}_{j+1/2}$, and the cell-averaged response rates, $R^{\pm}_j$. Due to the introduction of the $R^{\pm}_{j+1/2}$ unknowns, we have $4J+2$ unknowns but only $2J$ equations. Additional equations are needed to close the system. The $R^{\pm}_{j+1/2}$ unknowns can naturally be related to the $R^{\pm}_j$ unknowns using any spatial differencing approximation. The diamond difference approximation is used here for simplicity:

$$R^{\pm}_j = \frac{1}{2}\left(R^{\pm}_{j+1/2} + R^{\pm}_{j-1/2}\right), \quad 1 \le j \le J. \tag{2.23}$$

This spatial differencing approximation introduces spatial truncation error because it is not an exact relationship. However, this approximation becomes more accurate as the spatial grid is refined.

Finally, we derive two additional equations from the boundary conditions. We apply $\int_0^\infty \int_0^1 r(0,E)(\cdot)\,d\mu dE$ to the Eq. (2.2) and $\int_0^\infty \int_{-1}^0 r(X,E)(\cdot)\,d\mu dE$ to Eq. (2.3) to obtain

$$R_{1/2}^{+} = R_{1/2}^{-}, \tag{2.24}$$

$$R_{J+1/2}^{-} = 0. \tag{2.25}$$

Eqs. (2.18)-(2.25) constitute a completely specified low-order system of equations for $R_{j+1/2}^{\pm}$ and $R_j^{\pm}$, assuming that the nonlinear functionals $\mu_{j+1/2}^{\pm}$, $\Sigma_{t,j}^{\pm}$ and $\Sigma_{s,j}^{\pm}$ are known. This system of equations is *exact* in energy and angle; the only approximation made was the spatial diamond difference relation in (2.23). We note that the low-order equations in Eqs. (2.21)-(2.22) bear resemblance to work by Roberts and Anistratov [2], but their work was fundamentally different from our approach. Eqs. (2.21)-(2.23) also resemble the standard one-group S_2 equations. We note that if $\mu_{j+1/2}^{+} = -\mu_{j+1/2}^{-} = \frac{1}{\sqrt{3}}$, $\Sigma_{t,j}^{+} = \Sigma_{t,j}^{-} = \Sigma_{t,j}$, and $\Sigma_{s,j}^{+} = \Sigma_{s,j}^{-} = \Sigma_{s,j}$, Eqs. (2.21)-(2.23) become the one-group S_2 equations.

Therefore, Eqs. (2.21)-(2.22) are easily solved using a discrete ordinates-like transport sweep and source iteration, where the right hand side of these equations contains the source to be iterated upon numerically:

$$S_j^{\pm} = \frac{1}{2}\Sigma_{s,j}^{+} R_j^{+} + \frac{1}{2}\Sigma_{s,j}^{-} R_j^{-} + \frac{1}{2} Q_j, \quad 1 \le j \le J. \tag{2.26}$$

While these equations have almost identical structure to the discrete ordinates equations, they differ in one important way: they have no approximation in energy or angle, due to the nature of the nonlinear functionals. In the H-MC-S_2 equations, the S_2 discrete ordinates and multigroup cross sections are replaced by nonlinear functionals in the form of flux-weighted angles and cross sections. We have until now assumed that the nonlinear functionals are known. However, they are dependent on the unknown angular flux and must be estimated before Eqs. (2.21)-(2.25) can be solved. We choose to estimate these functionals using Monte Carlo to avoid the introduction of any truncation errors in the estimation of the functionals.

2.4 Monte Carlo Computation of the Functionals

The integrals in the nonlinear functional definitions are standard physical quantities (current, scalar flux, reaction rates) that can be computed with a Monte Carlo simulation. Monte Carlo easily estimates such integral quantities with "tallies", data structures that keep track of interesting quantities. During a simulation, each neutron history makes a contribution to a tally when its phase space matches the tally phase space. To estimate the nonlinear functionals in Eqs. (2.18) and (2.19), we simulate the exact physics and geometry of the problem in Monte Carlo and tally the appropriate integrals over many neutron histories. Each nonlinear functional is estimated at the end of the simulation by taking ratios of the appropriate tallies.

2.4.1 Cell-Averaged Functionals

Estimation of the nonlinear functionals $\Sigma_{s,j}^{\pm}$ and $\Sigma_{t,j}^{\pm}$ [defined in Eq.(2.19)] is straightforward. Modified path length estimator tallies are used to estimate the following integrals:

(1) $$\int_{x_{j-1/2}}^{x_{j+1/2}}\int_0^\infty\int_0^{\pm1}\Sigma_t(x,E)\psi(x,\mu,E)d\mu dEdx,$$

(2) $$\int_{x_{j-1/2}}^{x_{j+1/2}}\int_0^\infty\int_0^{\pm1}\Sigma_s(x,E)\psi(x,\mu,E)d\mu dEdx,$$

(3) $$\int_{x_{j-1/2}}^{x_{j+1/2}}\int_0^\infty\int_0^{\pm1}r(x,E)\psi(x,\mu,E)d\mu dEdx.$$

Path length estimators have bounded variance: as the number of histories increases, the variance decreases. Therefore, simulating more histories lowers the variance of the quantity.

Before discussing the estimation of the $\mu_{j+1/2}^{\pm}$ functionals, we note that the above integral labeled (3) is, in fact, the average desired response rate. Therefore, the very quantity we are trying to calculate is intermediately estimated in the Monte Carlo calculation. We will discuss this in more detail shortly.

2.4.2 Cell-Edge Functionals

Estimation of the nonlinear functionals $\mu^{\pm}_{j+1/2}$ [defined in Eq. (2.18)] require a surface crossing (current) estimator

$$(1) \qquad \int_0^{\infty}\int_0^{\pm 1} \mu\psi(x_{j+1/2},\mu,E)\,d\mu dE,$$

and a surface flux (secant) estimator:

$$(2) \qquad \int_0^{\infty}\int_0^{\pm 1} r(x_{j+1/2},E)\psi(x_{j+1/2},\mu,E)\,d\mu dE.$$

The current estimator has bounded variance. However, the surface flux estimator tally is undesirable because it has unbounded variance [3]. The physical interpretation of flux is “path length swept out per unit volume per unit time” by a neutron. We consider a particle passing through a thin foil detector of width Δx and surface area A at angle $\hat{\Omega}$ as depicted in Figure 2.1. The particle is assumed not to collide within the thin foil. The path length within the foil is $\Delta s = \frac{\Delta x}{|\cos\theta|} = \frac{\Delta x}{|\mu|}$, and the scalar flux (path length swept out per unit volume per unit time) is $\phi = \frac{\Delta s}{A\Delta x} = \frac{1}{A|\mu|}$. For particles with angles $\theta \to \pm\frac{\pi}{2}$, arbitrarily long track lengths can be tallied, causing the variance of this estimator to be unbounded although the mean is finite in general. The variance of the secant estimator can be controlled by using a cutoff: particles with $|\mu| \le \varepsilon$ are not tallied as $\frac{1}{|\mu|}$ but as $\frac{2}{|\varepsilon|}$ (the approximate expected value for particles with angles in this range). This method disallows arbitrarily long path lengths and therefore introduces a small bias in the result.

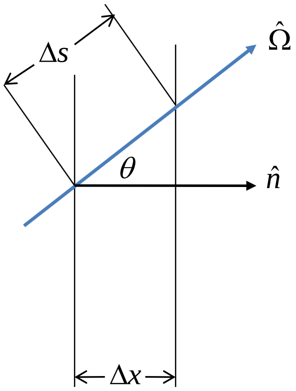

Figure 2.1 Particle passing through thin foil detector.

The unbounded variance of the surface flux estimator makes it unfavorable. When the H-MC-S$_2$ method was tested using this estimator to estimate the denominator integral of $\mu^{\pm}_{j+1/2}$, poor results were observed due to high variance propagating through the system via the $\mu^{\pm}_{j+1/2}$ nonlinear functionals. We did not test the method using a cutoff: this method would lessen the variance of the result but would also introduce a small unknown bias in the functionals. Instead, we redefined the $\mu^{\pm}_{j+1/2}$ functionals by approximating the denominator integral with path length estimators,

$$\tilde{\mu}^{\pm}_{j+1/2} \equiv \frac{\int_0^{\infty}\int_0^{\pm 1} \mu\psi(x_{j+1/2},\mu,E)\,d\mu dE}{G_{j+1/2}} \qquad (2.27)$$
$$0 \le j \le J$$

$$G^{\pm}_{j+1/2} = \begin{cases} \frac{1}{2}\left(R^{+}_{j+1} + R^{-}_{j+1}\right) & j = 0 \\ \frac{1}{h_j + h_{j+1}}\left(h_{j+1}R^{\pm}_{j} + h_j R^{\pm}_{j+1}\right) & j = 1,\dots J-1 \\ R^{\pm}_{j} & j = J. \end{cases} \qquad (2.28)$$

The definitions for $R^{\pm}_{j}$ in Eq. (2.7) hold. The definitions for $G^{\pm}_{1/2}$ and $G^{\pm}_{J+1/2}$ attempt to preserve the reflecting and vacuum boundary conditions, respectively.

The approximation in Eq. (2.27) introduces spatial truncation error into the H-MC-S_2 method, but this error is negligible compared to the statistical noise which is introduced by the surface flux estimator, and is comparable to the truncation error already introduced by Eq. (2.23). Therefore, this approximation does not degrade the method.

2.4.3 Why Not Standard Monte Carlo?

Standard Monte Carlo calculations compute scalar fluxes and response rates directly. We are proposing the computation of nonlinear functionals, *ratios* of these types of quantities. One may question the strategy of using Monte Carlo to estimate the functionals in Eqs. (2.19) and (2.27) instead of estimating the desired response rates directly. This strategy is based on the following fundamental hypothesis:

> Hypothesis: *Monte Carlo estimates of the nonlinear functionals in Eqs. (2.19) and (2.27) are more accurate and have less variance than direct Monte Carlo estimates of the desired response rates, provided the numerator and denominator in the functionals are evaluated using the same particle histories.*

This hypothesis is based on the observation that Monte Carlo estimates of the nonlinear functionals are *weakly*-dependent on the number of Monte Carlo particles in the simulation, while direct Monte Carlo estimates of the reaction rates depend *strongly* on these numbers. Analyses in Chapter 4 confirm the basic truth of this hypothesis using the concept of correlated random variables and numerical comparisons.

2.5 Computation of Multiple Reaction Rates

We have described how to use the H-MC-S_2 method to compute a single response rate. To do this, a single Monte Carlo calculation is performed with four tallies to compute a set of nonlinear functionals, which is then input to a modified discrete ordinates calculation. To compute *n* response rates, one Monte Carlo calculation is performed with $3+n$ tallies to compute *n* sets of functionals (one for each response rate). Each set of functionals is sent to a separate modified discrete ordinates calculation, the output of each being the different response rates.

The cost of a Monte Carlo calculation is usually dominated by geometry tracking, so a few additional tallies do not increase the computational cost significantly. These additional tallies would also be required if standard Monte Carlo were being used as sole computational method. The additional computer time required for the additional deterministic calculations is negligible compared to the time required for the Monte Carlo calculation, due to the simplicity of the low-order equations. Therefore, provided the response rates are decided *a priori* to the Monte Carlo simulation, computation of multiple response rates does not increase the computational expense significantly.

2.6 Computation of Group-Wise Response Rates

There are two methods to obtain group-wise response rates with the hybrid method. We use the term "group-wise" to mean "integrated over a particular energy group". The first and simpler method (used in this work) is to create an artificial response function

$$\tilde{r}(x,E) = \begin{cases} r(x,E), & E \in E_g \\ 0, & E \notin E_g . \end{cases} \tag{2.29}$$

The use of this response function yields the response rate integrated only over the energy range of interest:

$$R_g(x) = \int_{\Delta E_g} dE\, r(x,E)\phi(x,E) . \tag{2.30}$$

An alternative (not explored in this work) is to integrate the transport equation over energy groups instead of the entire energy space. This would result in low-order equations resembling multigroup equations but having no approximation in energy or angle.

2.7 Numerical Results

2.7.1 Core-Reflector Problem

We consider the Core-Reflector Problem depicted in Figure 2.2. This test problem is a simplified version of the fast reactor criticality test problem in [4] and [7]. The core region in this problem contains a uniformly distributed isotropic, monoenergetic (10 keV) source rather than a fission source. Despite simplifications in materials and sources, this problem exhibits severe transport effects at the core-reflector boundary, just as the original problem did.

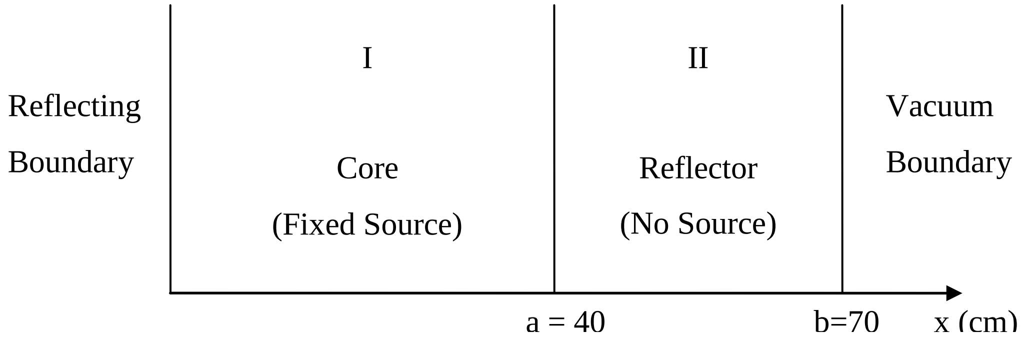

Figure 2.2 Geometry of Core-Reflector Problem.

Location [cm]	$\sigma_{s,el}$ **[barn]**	σ_{γ} **[barn]**
$0 < x < 40$	11	$\frac{0.316228}{\sqrt{E}} + \begin{cases} 10.238, & E \in [1139, 1159] \\ 0.0912, & E \in [2345, 2354] \end{cases}$
$40 < x < 70$	$\begin{matrix} 131, & E \in [1900, 3900] \\ 4, & \textit{otherwise} \end{matrix}$	$\frac{0.094868}{\sqrt{E}} + \begin{cases} 0.1022, & E \in [1900, 3900] \\ 0.1054, & E \in [7606, 7626] \end{cases}$

Table 2.1 Material specifications over the energy range [0, 10000] eV.

The continuous energy cross sections in the core and reflector are artificial cross sections developed from ENDF/B-VII.0 data [6] for Fe-56 and Na-23, respectively. The core and reflector material have atomic masses of 56 and 23, and number densities of 0.0848 and 0.0254 barn^{-1}cm^{-1}, respectively. The resonances in the true data were replaced by histogram approximations that approximately preserve the area under each resonance. (This made it easier to represent the cross sections in our research codes.) Figure 2.3 compares the ENDF-BVII.0 data with the artificial cross sections used here.

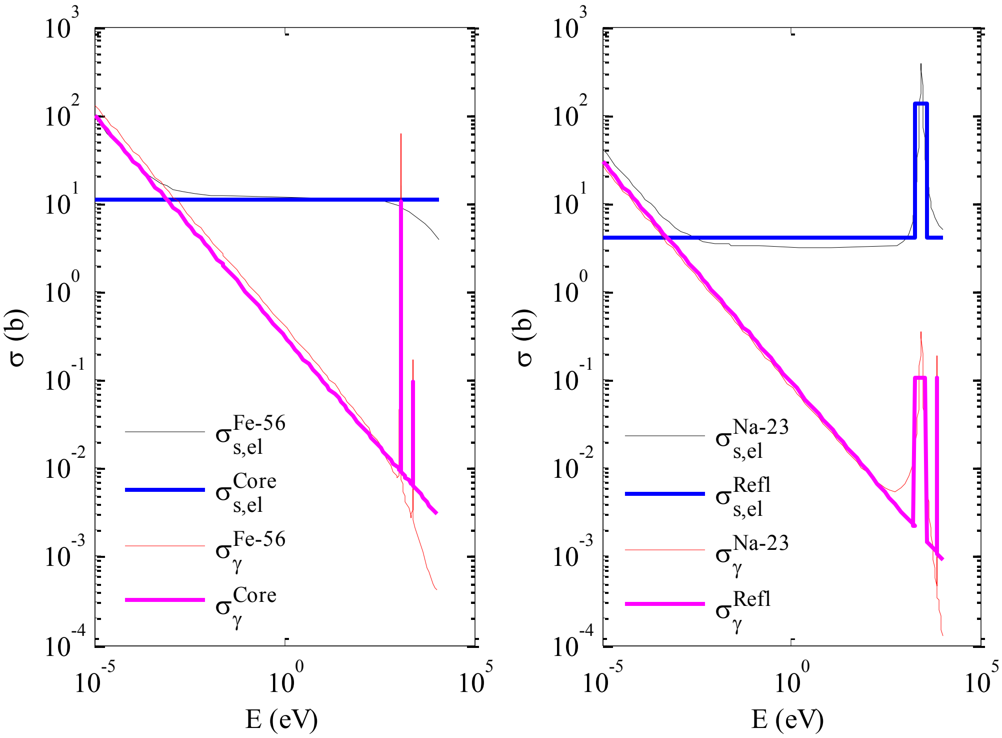

Figure 2.3 Core and reflector cross sections and ENDF/B-VII.0 data for Fe-56 and Na-23.

2.7.1.1 Description of transport effects

Before presenting numerical results, we describe the transport effects in the Core-Reflector Problem. All results here use the artificial cross sections. Figure 2.4 shows the energy-dependent partial current and net current crossing through the core-reflector interface obtained from a benchmark Monte Carlo simulation. This figure shows that the interface current is strongly dependent on energy. At most energies, the net flow of neutrons is from the core to the reflector, as signified by the positive net current in Figure 2.4(b). However, for energies near 1 to 2 keV, the net current reverses, and many more neutrons flow back towards the core.

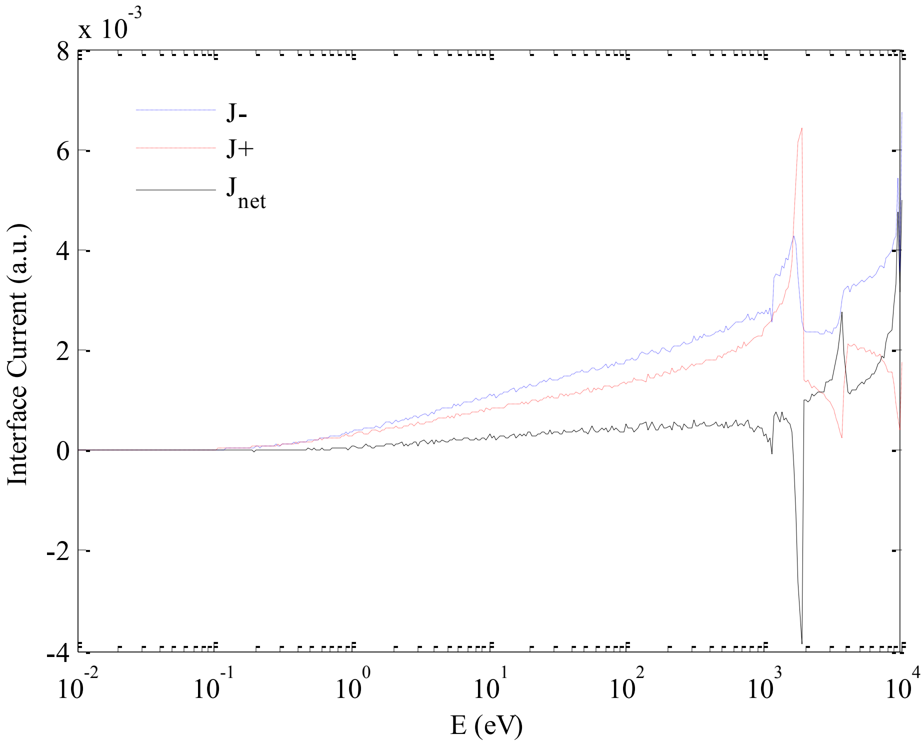

Figure 2.4 Spectra of the partial and net currents at the core-reflector interface.

This behavior is due to the large resonance in the core material. Neutrons in the core are likely to be absorbed between 1 and 2 keV due to the large resonance in that energy range. Therefore, there is an absence of neutrons exiting the core at that energy. We can infer from these graphs that the flux is highly anisotropic at energies such as the core resonance energy. This anisotropic character cannot be preserved when using the multigroup approximation, which assumes isotropic flux dependence within an energy group.

Next, we examine the energy dependence ("spectrum") of the core and reflector flux when averaged over all angle and space. Spectra are typically used as the weighting function in multigroup calculations. The angularly- and spatially-averaged core and reflector spectra for the test problem are plotted in Figure 2.5. We note from this figure that the two spectra have different shapes, caused by the cross section resonances and the geometry. However, these shapes are averaged over the entire spatial region and all angles, so they do not necessarily represent the true energy distribution of the flux at various points throughout the system. In fact, the flux spectrum near the interface region is a combination of these two spectra and is strongly dependent on angle. For example, the spectrum of neutrons located just inside the reflector and traveling with $\mu > 0$ is similar to the core spectrum. At the same spatial location, the spectrum of neutrons traveling with $\mu < 0$ is similar to the reflector spectrum.

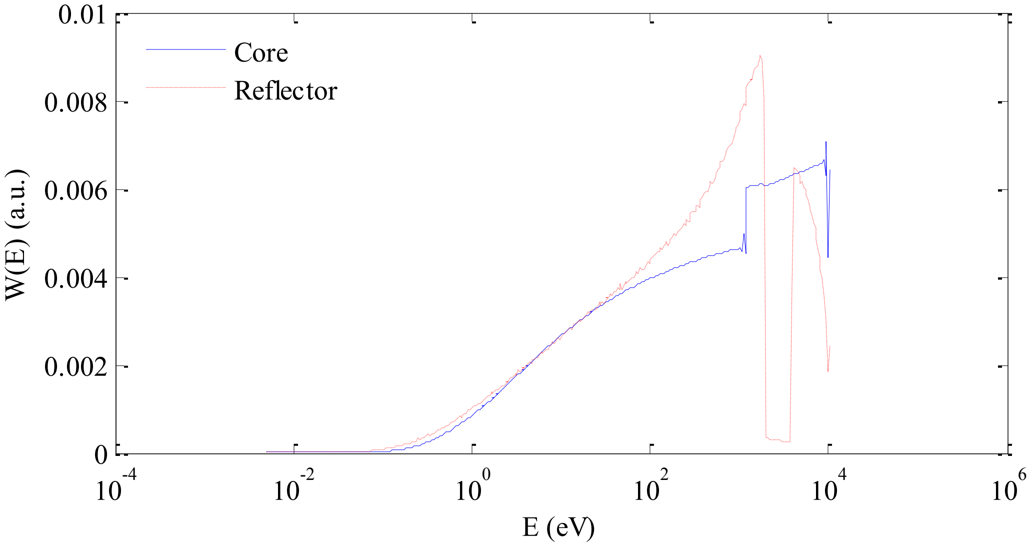

Figure 2.5 Core and reflector spectra for the test problem.

Again, these directional spectral differences are not captured with the multigroup approximation, which assumes the same spectrum for neutrons traveling in all directions. We show here that multigroup methods do not perform well near the interface unless many groups are used, as was observed by Aliberti and Lebrat [4][7].

In the following sections, we use the Core-Reflector Problem to compare the statistical properties of the H-MC-S_2 method to that of Monte Carlo, and the accuracy of H-MC-S_2 with that of conventional deterministic methods, namely multigroup discrete ordinates. We compute the energy-integrated scalar flux and the capture rate. In this H-MC-S_2 method, these quantities can be obtained by choosing $r_1(x,E) = 1$ and $r_2(x,E) = \Sigma_\gamma(x,E)$, respectively.

2.7.2 Comparison with Standard Monte Carlo

The variance *(sample variance of the mean)* of a standard Monte Carlo solution can be directly computed during a single simulation, but the variance of the H-MC-S_2 solution may only be estimated over many simulations, due to complexities in calculating the covariance of the functionals and then propagating the statistical error algebraically. To compare the statistical properties of standard Monte Carlo with that of H-MC-S_2, twenty five independent estimates of the scalar flux were obtained with each method (a different random number seed was used for each estimate). The numerical properties of the Monte Carlo simulations are presented in Table 2.2.

# of Independent Simulations (K)	Histories per Simulation (N)	Grid Size [cm]
25	50,000	0.5

Table 2.2 Monte Carlo numerical properties for variance estimation of test problem.

The pdf variances of the distributions of H-MC-S_2 and MC solutions over the 25 simulations were computed using:

$$S_j^{\,2} = \frac{K}{K-1}\left[\widehat{\phi_j^2} - \left(\hat{\phi}_j\right)^2\right], \tag{2.31}$$

where S_j^2 is the variance of the cell-averaged scalar flux ϕ_j , and $\hat{\phi}_j = \frac{1}{K}\sum_{k=1}^{K}\phi_j^{(k)}$ and $\widehat{\phi_j^2} = \frac{1}{K}\sum_{k=1}^{K}(\phi_j^{(k)})^2$. For each method, the sum of relative variances (SRV)

$$\mathrm{SRV} = \sum_{j=1}^{J}\frac{S_j^{\,2}}{\left(\hat{\phi}_j\right)^2}, \tag{2.32}$$

was calculated to give an approximation of the overall variance of the H-MC-S_2 and standard Monte Carlo solutions over many simulations. The figure of merit,

$$\text{FOM} = \frac{1}{\text{SRV} \cdot T}, \tag{2.33}$$

where T is the computational cost of the method, is often used to characterize the performance of stochastic methods because it is independent of the number of histories (SRV is inversely proportional to the number of histories, and T is directly proportional to the number of histories). We compare the performance of H-MC-S_2 and standard Monte Carlo in the following table.

Method	SRV	T	FOM
Monte Carlo	2.10e-02	262	0.182
H-MC-S_2	9.66e-03	305	0.339

Table 2.3 Figure of merit comparison for calculation of test problem scalar flux.

If a standard Monte Carlo simulation achieves a given error (standard deviation) in a given time, then the *fractional computing time*

$$f^{(m)} = \frac{FOM^{(MC)}}{FOM^{(m)}} \tag{2.34}$$

is the fraction of time required by method m to achieve the same error. For this problem, $f^{(\text{H-MC-S}_2)} = 0.53,$ meaning that the H-MC-S_2 method is *more efficient* than standard Monte Carlo because it only requires 53% of the standard Monte Carlo computing time to achieve a given error. This numerical result is our first confirmation that these nonlinear functional methods *more accurately* compute solutions than standard Monte Carlo.

We now make a note about the computational times required for each method. The 17% increase in computational time required for the H-MC-S_2 method over conventional Monte Carlo is due primarily to the additional tallies required for the H-MC-S_2 nonlinear functionals. [The deterministic calculation is less than 0.5% of the cost of each H-MC-S_2 calculation.] However, optimal implementation of these tallies could reduce this extra expense to a negligible amount, making the computational times almost equal. In this case, the fractional computing time reduces to:

$$f^{(m)} \approx \frac{\text{SRV}^{(m)}}{\text{SRV}^{(MC)}}. \tag{2.35}$$

If this problem were to be performed with optimal implementation of tallies, the fractional computing time would be approximately 0.46. The fractional computing times reported in later chapters assume optimal implementation of tallies and use Eq. (2.35).

We also emphasize that the H-MC-S_2 method introduces spatial truncation error [Eqs. (2.23) and (2.27)] that is not present in standard Monte Carlo. In problems with a smoothly varying solution, these errors are insignificant compared to statistical errors. However, when the solution is discontinuous or varies rapidly, care must be taken to discretize the problem appropriately. This concern is discussed in Section 2.7.6.

2.7.3 Comparison with Standard Deterministic Methods

We now compare the accuracies of H-MC-S_2 and multigroup discrete ordinates (MGS_N). We calculate the energy-integrated scalar flux and capture rate for the test problem. The numerical parameters of each method are summarized in Table 2.4.

Method	Grid Spacing [cm]	# of Histories	Energy Groups, Quadrature Order
Benchmark Monte Carlo	0.5 (scalar flux) 0.1-0.5 cm (capture rate)	$2x10^6$ (scalar flux) $4x10^6$ (capture rate)	Continuous energy, Continuous angle
H-MC-S_2	0.5 (scalar flux) 0.1-0.5 cm (capture rate)	$5x10^5$ (scalar flux) $1x10^6$ (capture rate)	Continuous energy, Continuous angle (“Exact” collapse to G=1, S_2)
MGS_N	0.5 (scalar flux) 0.1-0.5 cm (capture rate)	-	G=11, 21, 51, 101, 251, S_{16}

Table 2.4 Numerical properties for Core-Reflector Problem.

2.7.3.1 Multigroup cross section generation

Before presenting the discrete ordinates results, we describe how the multigroup cross sections were obtained and illustrate the complexity of this process.

For a 1-D problem, an infinite medium (0-D) spectrum calculation is presumed to be sufficient to generate cross section weighting functions. An infinite medium Monte Carlo calculation was performed for each material (core and reflector) to compute the fine group spectrum and fine group cross sections. These spectra are shown in Figure 2.6 and are similar to the spectra in Figure 2.5.

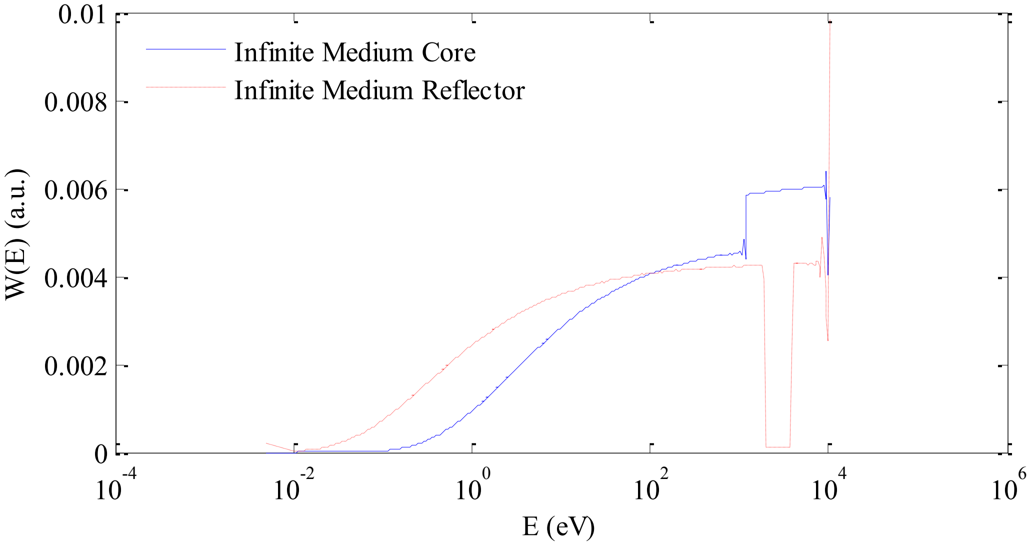

Figure 2.6 Infinite medium spectrum results for Core-Reflector Problem.

The fine-group cross sections and weighting functions for material i were generated in Monte Carlo by the following formula (conventional multigroup definition):

$$\Sigma_h^{(i)} = \frac{\int_{E_h}^{E_{h-1}} \Sigma^{(i)}(E) W^{(i)}(E)}{\int_{E_h}^{E_{h-1}} W^{(i)}(E)}, \tag{2.36}$$

$$W_h^{(i)} = \int_{E_h}^{E_{h-1}} W^{(i)}(E)dE, \tag{2.37}$$

with fine energy bins $\{E_h, h = 0, \ldots H+1\}$. The fine group structure for this calculation utilized $H = 500$ equal lethargy groups from $E_0 = 10$ keV to $E_H = 1$ eV and one additional group below 1 eV. Additional procedures were used to generate the multigroup transfer cross sections $\Sigma_{s,h'\to h}$, which represents the probability of a material scattering a neutron from energy group h' to energy group h.

The resulting 501-group cross sections were collapsed to $G = 11$, 21, 51, 101, and 251 groups:

$$\Sigma_g^{(i)} = \frac{\sum_{h\in g} \Sigma_h^{(i)} W_h^{(i)}}{\sum_{h\in g} W_h^{(i)}}. \tag{2.38}$$

The coarse group structures utilized $G = 11$, 21, 51, 101, and 251 equal lethargy groups from $E_0 = 10$ keV to $E_G = 1$ eV and one additional group below 1 eV.

Computing multigroup cross sections in this manner is consistent with conventional methods. However, using the infinite medium spectrum to collapse cross sections rather than the true spectrum causes error in the multigroup approximation. In practical reactor calculations, higher dimension spectrum calculations are performed, but for a 1-D slab problem, a 0-D spectrum calculation is appropriate. The most important point is that the spectrum calculation is almost always performed in a dimension lower than that of the actual problem, therefore always incurring spatial and angular approximations that are likely to be largest near material interfaces.

2.7.4 Computation of Scalar Flux

The scalar flux for the test problem was computed on a uniform 0.5 cm grid using MGS$_{16}$ ($G = 11$, 21, 51, 101, 251) and H-MC-S$_2$ (5x10^5 particles). The scalar flux results for both methods are compared to a benchmark Monte Carlo calculation (2x10^6 particles) in Figure 2.7.

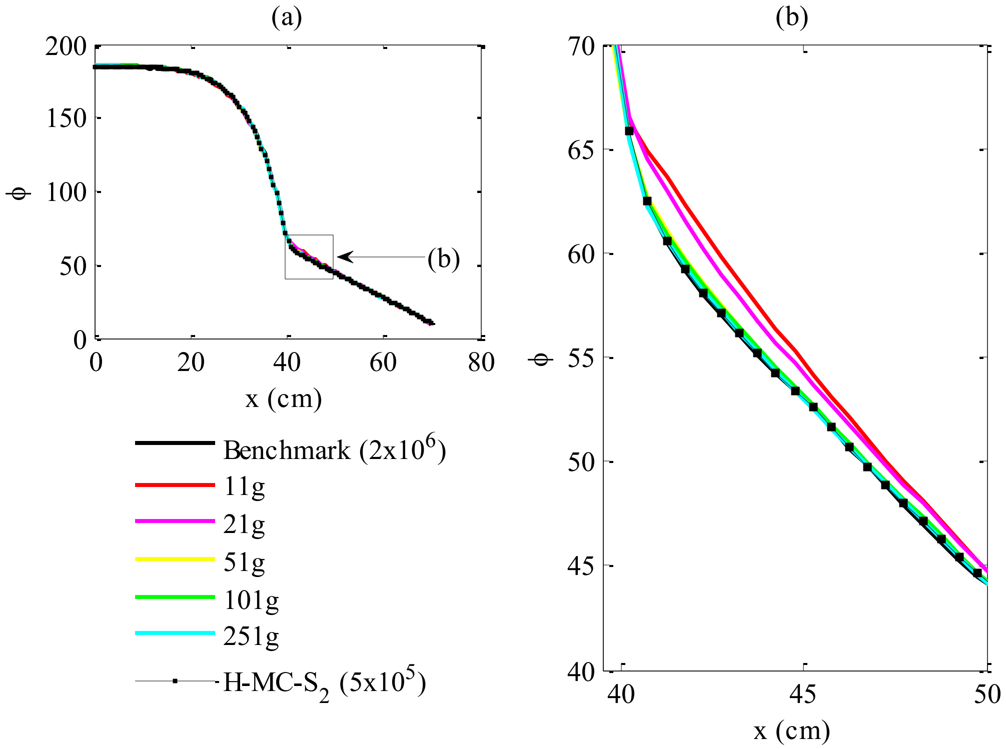

Figure 2.7 Scalar flux over (a) slab and (b) interface region.

Figure 2.7(a) depicts the solution over the full slab, and Figure 2.7(b) zooms in at the solution close to the interface ($x = 40$ cm). Major differences are observed between the multigroup ordinates solutions and the benchmark Monte Carlo solution for the region just inside the reflector ($40 \text{ cm} < x < 50 \text{ cm}$). In Figure 2.8, the magnitude of error in each calculations relative to the benchmark is plotted, along with the uncertainty in the benchmark calculation, 'Benchmark 1 σ'. Only errors greater than the benchmark uncertainty are considered significant.

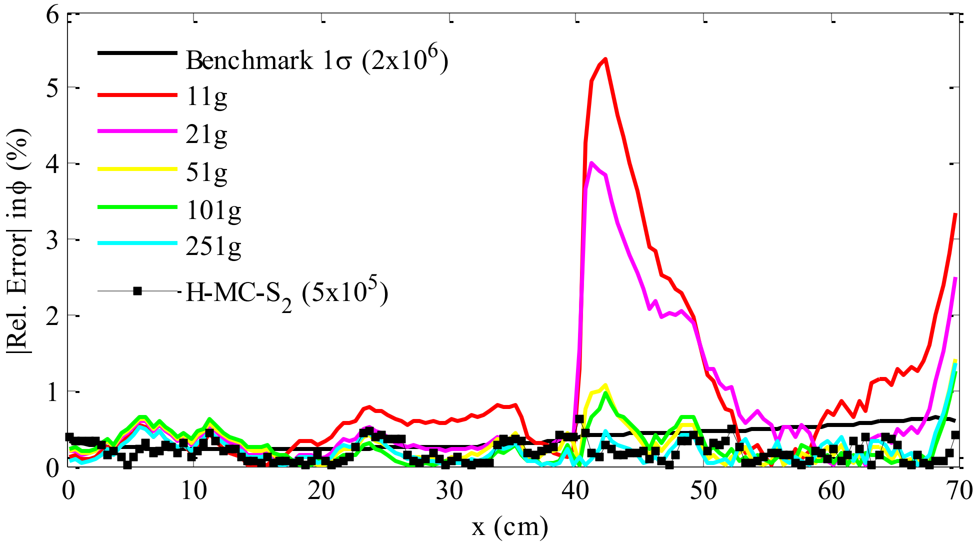

Figure 2.8 Relative error in scalar flux compared to benchmark solution.

Examining Figure 2.7 and Figure 2.8, we see that the H-MC-S_2 calculation performed well in all parts of the problem. The relative error for the H-MC-S_2 method is within benchmark uncertainty for almost every data point. This is remarkable, considering that H-MC-S_2 used only 25% as many histories as the benchmark Monte Carlo solution. Clearly, increasing the number of particles would further improve the hybrid result, but an excellent result is nonetheless obtained with less computational time than the benchmark solution. One important point, however, is that the H-MC-S_2 is not devoid of spatial error. Unlike standard Monte Carlo, care must be taken to appropriately discretize the problem in transition regions. We discuss an example of this in the calculation of the capture rate in the next section.

In contrast to H-MC-S_2, the MGS_{16} methods performed poorly near material interfaces. While the MGS_{16} results approached the benchmark solution as the group structure was refined, a minimum of 251 groups was needed to achieve the same accuracy as the one-group S_2–like hybrid method. This result confirms our understanding that the multigroup approximation is the origin of most of the error.

Since the spectral effects occur mostly in the *resonance group* (630.957 eV to 10 keV), a calculation was performed to compute the resonance group flux. As expected, the MGS_{16} errors were more severe for this calculation than for the total energy-integrated scalar flux. The error in the resonance component of the scalar flux is plotted in Figure 2.9.

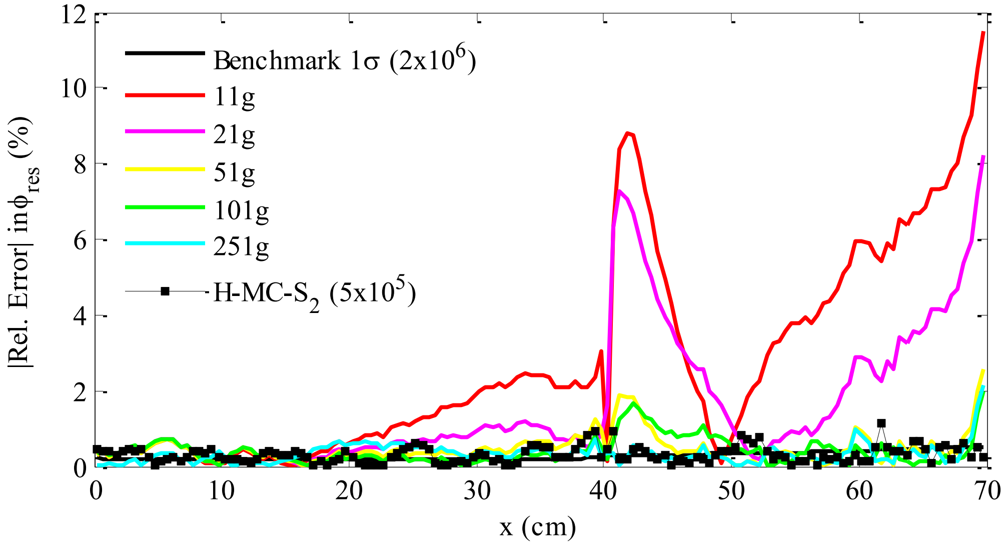

Figure 2.9 Error in resonance group scalar flux.

Figure 2.8 and Figure 2.9 indicate that even for a simple scalar flux calculation, a 251 group structure is required to reduce the MGS_{16} error near material interfaces to acceptable levels. This is an important result: the one-group H-MC-S_2 method performs at the same level as the 251 group structure by incorporating directional and spatial information. It should be noted that both 51g and 101g calculations perform reasonably well but still exhibit systematic errors at the interface and vacuum boundary, with errors up to 2%.

2.7.5 Computation of Resonance-Group Capture Rate

The neutron capture rate in the resonance group was computed on a non-uniform grid using MGS_{16} ($G = 11$, 21, 51, 101, 251) and H-MC-S_2 ($1\text{x}10^6$ particles). A fine spatial grid (0.1 cm) was used in the vicinity of the interface, $39 < x < 42$, and a coarse grid (0.5 cm) was used elsewhere. The fine grid was necessary to suppress spatial truncation error near the interface, where the solution has a large spatial gradient. We note that more histories were used for this problem because computation of resonance capture is more stochastically variable than computation of the scalar flux. The ratio of H-MC-S_2 particles to standard Monte Carlo particles was kept the same at 1:4.

The capture rate results are compared to a benchmark Monte Carlo calculation ($4\text{x}10^6$ particles) in Figure 2.10. In Figure 2.11, the magnitude of relative error in these calculations to the benchmark is plotted, along with the uncertainty in the benchmark calculation, 'Benchmark 1σ'.

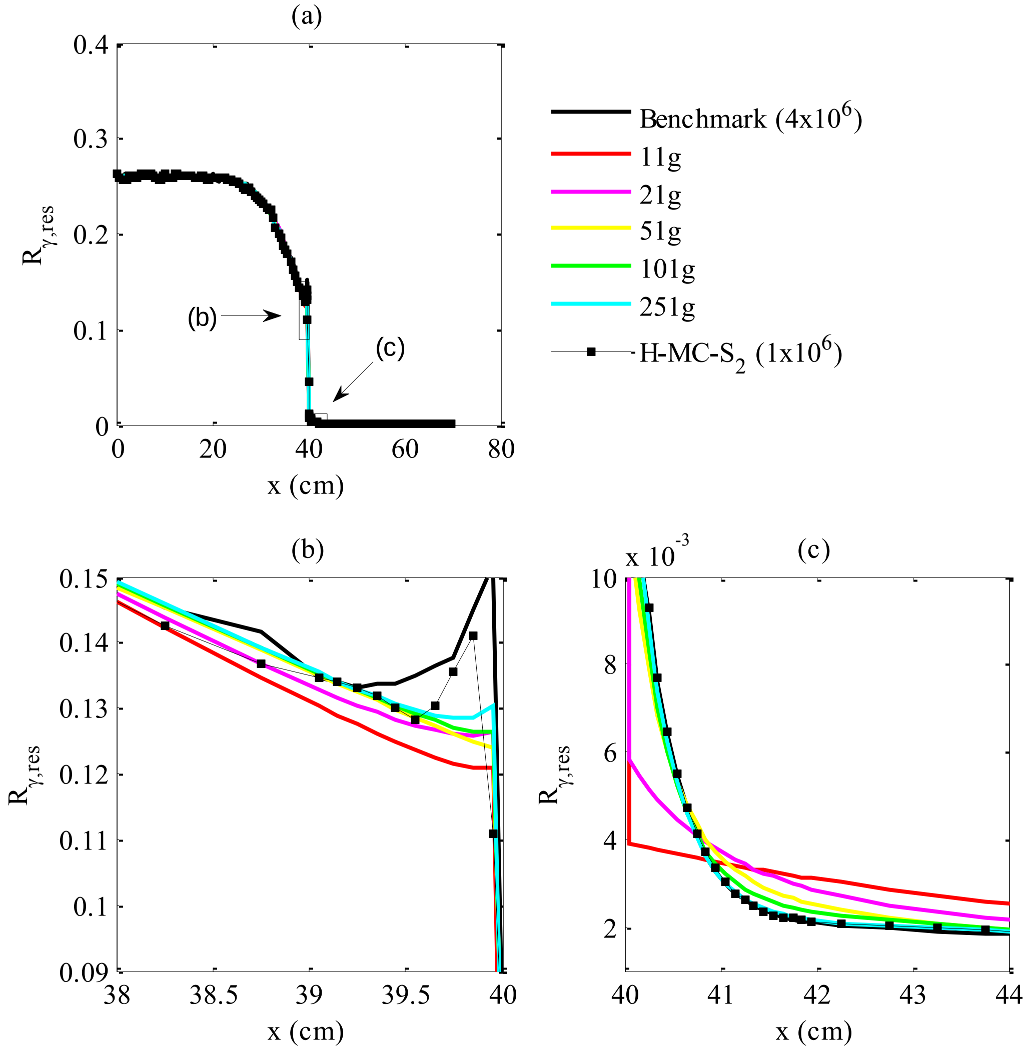

Figure 2.10 Resonance group capture rates for (a) slab, and (b)-(c) interface region.

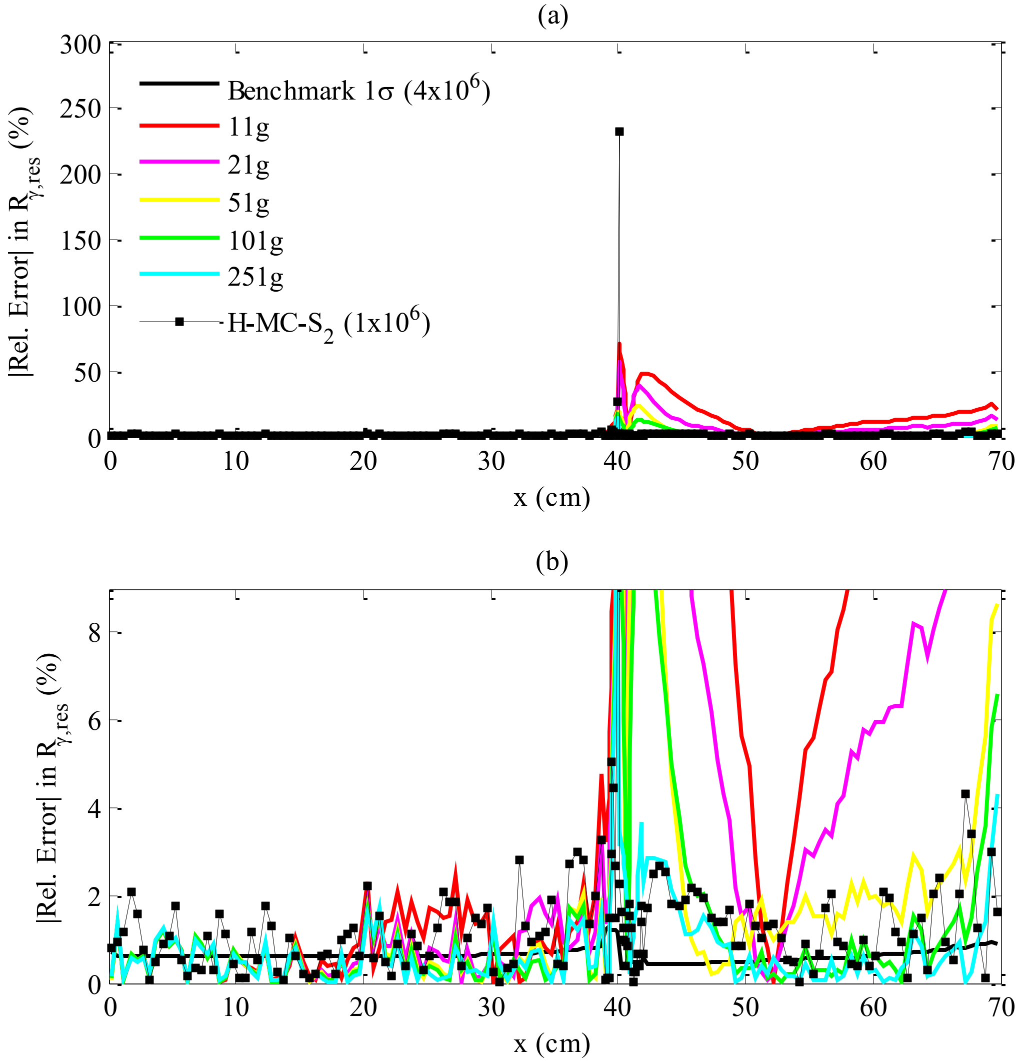

Figure 2.11 (a) Relative errors in resonance capture rate and (b) zoomed in for detail.

The resonance capture rate results are similar to the scalar flux results. The H-MC-S_2 method performs well throughout the entire problem, except for a single point at the interface. This error is due to spatial truncation, not transport effects; we discuss this shortly. For the rest of the range, the H-MC-S_2 relative error is much less than the corresponding error in the discrete ordinates solutions, but is slightly increased compared to the scalar flux computation. This is expected because the success of the H-MC-S_2 method depends on the correlation of the quantities in the nonlinear functionals. This is further explained in Chapter 4, but for now we simply state that the integrals in the nonlinear functional ratios are less correlated for the resonance capture rate problem than for the scalar flux problem, and this decrease in correlation causes increased variance.

The MGS_{16} calculations again show significant errors in the region near the core-reflector interface. These errors are well above benchmark uncertainty, particularly in the reflector region and near the vacuum boundary. The MGS_{16} method becomes more accurate as the number of groups G increases, as expected. However, significant transport effects are still apparent even in the $G = 251$ solution. In addition, the MGS_{16} method has significant spatial truncation error at the interface (like H-MC-S_2).

Returning to the large error in the H-MC-S_2 and MGS_{16} methods at the interface, we recall that both of these methods have spatial truncation error. At the core-reflector interface, the capture cross section is spatially discontinuous, due to the material heterogeneity. Therefore, the resonance capture rate is discontinuous at the interface and changes steeply near the interface. We see from Figure 2.11 that even when a fine grid (0.1 cm) is used, significant spatial truncation errors appear near the interface in both the H-MC-S_2 and MGSN solutions. Further refining the grid would yield more accurate results for the H-MC-S_2 method, but not necessarily for the MGS_{16} solution because the latter is dominated by transport effects, not spatial truncation error. Refining the grid does not suppress transport effects unless more accurate multigroup cross sections are generated for each spatial cell.

While refinement of the spatial grid is an obvious way to reduce spatial truncation error for H-MC-S_2, we now discuss a more effective technique.

2.7.6 Continuous Function Technique

The *continuous function*, or CF, technique can be used to decrease the spatial truncation error in the H-MC-S_2 method. The key idea is that during the deterministic sweep step, spatial truncation error propagates through the system. This propagation can be avoided by constructing the solution from spatially continuous functions.

We demonstrate this technique for the computation of the resonance capture response rate as in the previous section. The response function for this computation is spatially discontinuous because of the material heterogeneity:

$$r(x,E)=\begin{cases}\Sigma_{\gamma,res}^{core}(E) & 0<x<40\\ \Sigma_{\gamma,res}^{ref}(E) & 40<x<70.\end{cases} \tag{2.39}$$

The use of this spatially discontinuous response function resulted in significant spatial truncation error near the core-reflector interface (x=40 cm). Instead, we use the spatially continuous response functions

$$r_1(x,E)=\Sigma_{\gamma,res}^{core}(E) \quad 0<x<70 \tag{2.40}$$

$$r_2(x,E)=\Sigma_{\gamma,res}^{refl}(E) \quad 0<x<70 \tag{2.41}$$

to obtain two solutions $R_1(x)$ and $R_2(x)$ over $0<x<70$. Discarding the parts of the solutions that are not physical, the final solution is the piecewise function

$$R_{CF}(x)=\begin{cases}R_1(x) & 0<x<40\\ R_2(x) & 40<x<70\end{cases} \tag{2.42}$$

The CF technique requires the solution of multiple deterministic low-order problems with different sets of functionals, but the required functionals are all obtained from a single Monte Carlo run. Since the low-order problems are inexpensive, solving several of them (rather than one) adds little overhead and significantly reduces the spatial truncation error.

The CF technique proved to be much more efficient than simply refining the spatial grid. Figure 2.12 and Figure 2.13 show that the H-MC-S_2 solution improved significantly when the continuous function technique was used.

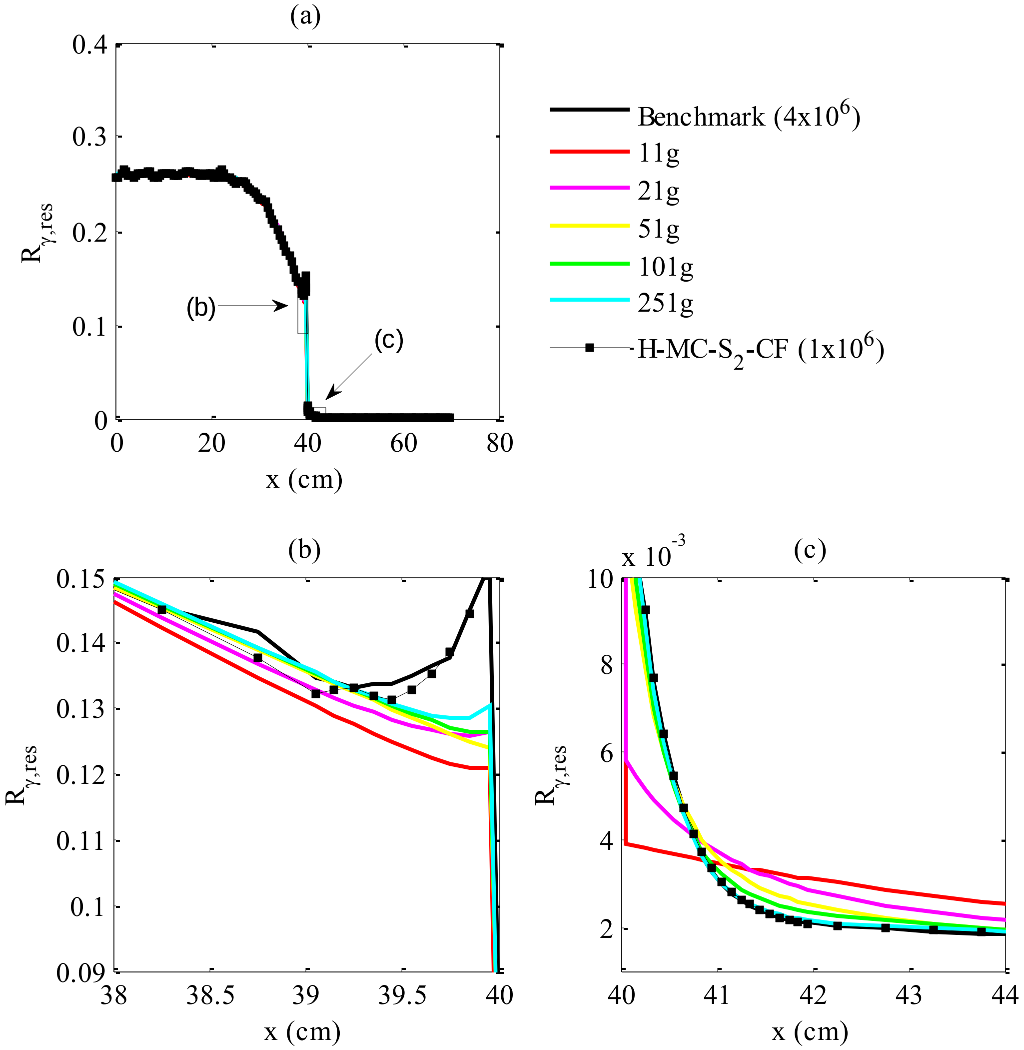

Figure 2.12 Resonance group capture rates for (a) slab, and (b)-(c) interface region using continuous function method to suppress spatial truncation error.

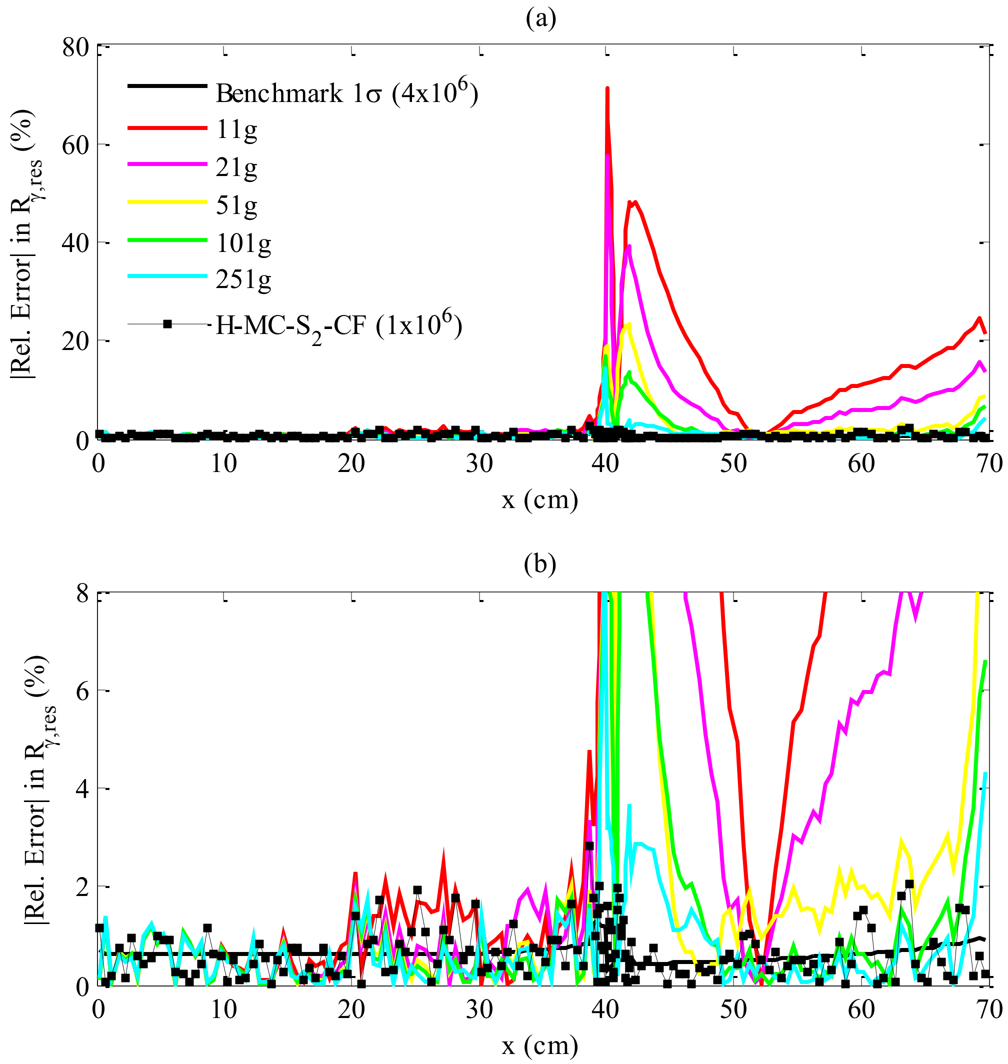

Figure 2.13 (a) Relative errors in resonance capture rate for H-MC-S_2 with continuous function technique and (b) zoomed in for detail.

The continuous function technique can be used with any grid size but is most effective when used in tandem with fine spatial grids. The following figures compare the H-MC-S_2 method with and without the continuous function technique on a coarse grid and a fine grid near the interface.

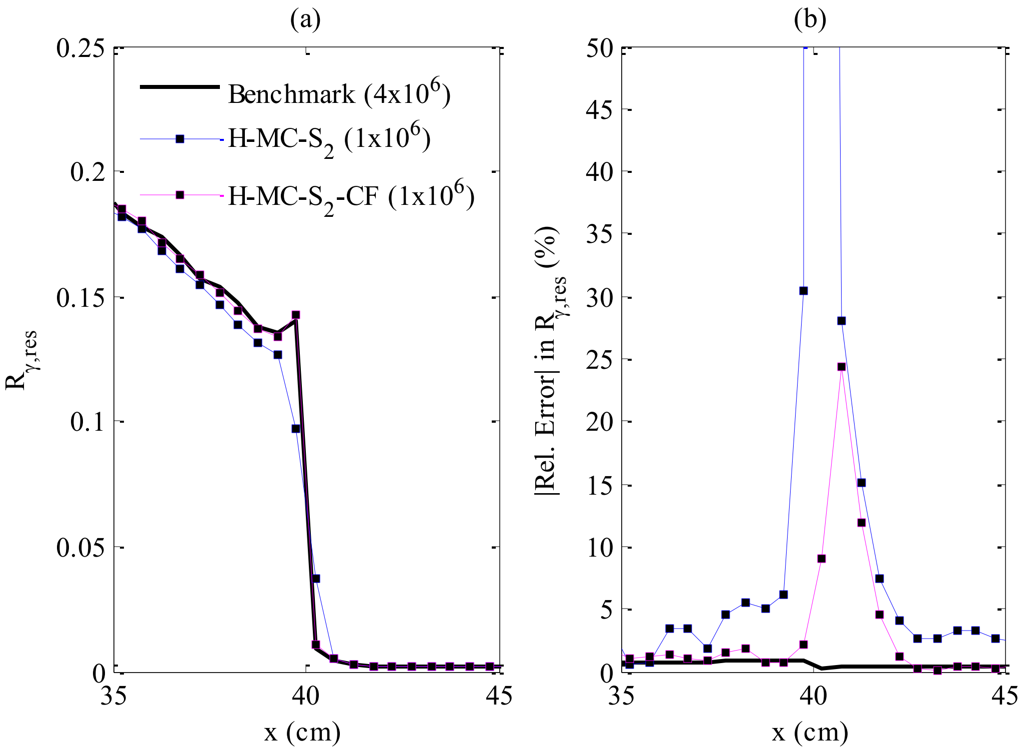

Figure 2.14 Effect of CF near interface on coarse grid.

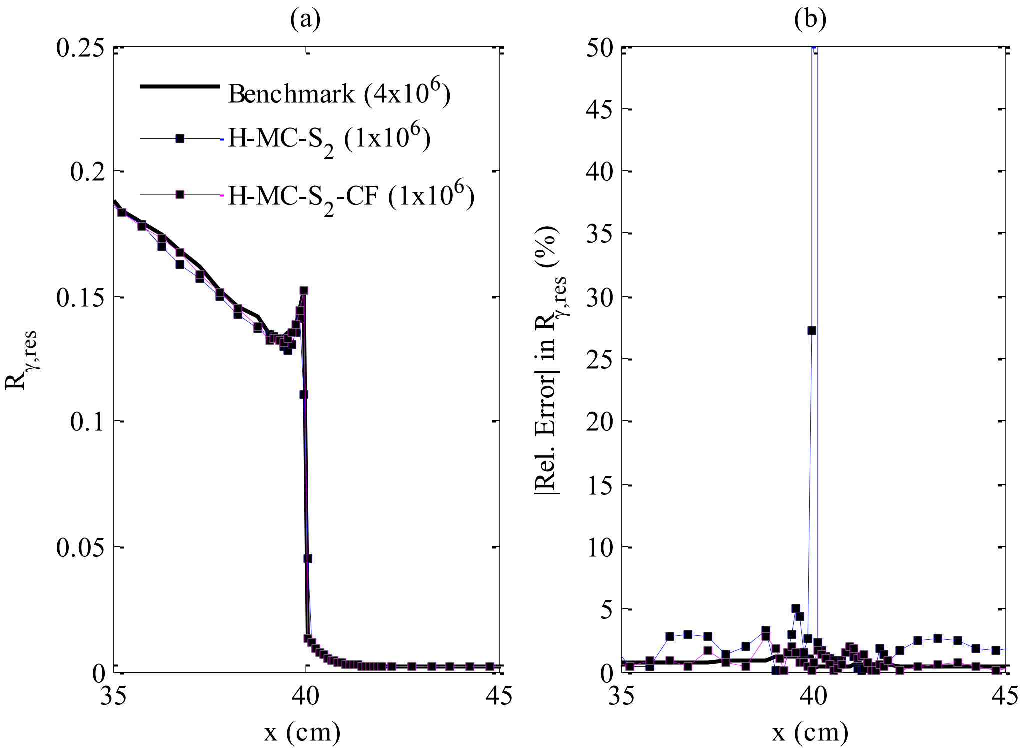

Figure 2.15 Effect of CF near interface on fine grid.

Method (10^6 particles)	Grid	Max. Rel. Error
H-MC-S_2	Coarse	293%
H-MC-S_2	Fine	233%
H-MC-S_2-CF	Coarse	24%
H-MC-S_2-CF	Fine	3%

Table 2.5 Summary of spatial truncation error suppression techniques for resonance capture rate calculation.

The use of the continuous function technique with a fine spatial grid suppressed the truncation error to within stochastic uncertainties. Therefore, the H-MC-S_2 method is capable of handling discontinuous and rapidly changing solutions when used with the continuous function technique and a sufficiently fine grid.

2.8 Conclusions

We have developed a hybrid method for accurately and efficiently solving difficult transport problems. The method consists of collapsing the transport equation in angle, energy, and space with only a small spatial truncation error. It should be noted that although the numerical results here were generated using the diamond difference spatial discretization scheme, the H-MC-S_2 method does not require the use of this specific approximation. The collapsing process produces nonlinear functionals that can be accurately computed by Monte Carlo. These functionals are similar to one-group flux-weighted cross sections and flux-weighted angular quadrature. The H-MC-S_2 low-order equations have a similar form to one-group S_2 equations, but are more accurate because the nonlinear functionals account for the energy and angular dependence of the full transport solution.

For a core-reflector test problem containing significant transport effects, the H-MC-S_2 results agreed with the benchmark Monte Carlo solution, and had less variance than computation time-equivalent Monte Carlo solutions. The reduced variance translates into a 50% savings in computing time in the H-MC-S_2 method. In addition, the H-MC-S_2 method was more accurate than conventional multigroup discrete ordinates methods.

The hybrid method can handle problems with discontinuous and rapidly varying solutions by refining the spatial grid and using the continuous function technique described. In addition, the H-MC-S_2 method eliminates possible sources of error such as improper choice of energy group boundaries and insufficient number of discrete ordinates directions. Finally, because the hybrid method has no approximation in angle, it may be advantageous for solving problems where discrete ordinates calculations exhibit undesirable ray effects. This could be tested in the future by implementing the method in 2-D geometry. We have demonstrated the success of this method on a meaningful fixed source problem. H-MC-S_2 could easily be extended to eigenvalue problems as well.

In the next chapter, we modify the H-MC-S_2 method in order to eliminate the spatial truncation error.

2.9 References

[1] E.R. Wolters, E.W. Larsen, and W.R. Martin, "A Hybrid Monte Carlo-S_2 Method for Preserving Neutron Transport Effects", *Proc. M&C 2009 – International Conference on Mathematics, Reactor Physics, and Computational Methods,* Saratoga Springs, NY, May 3-7, 2009, American Nuclear Society (2009) (CD-ROM).

[2] L. Roberts and D.Y. Anistratov, "Nonlinear Weighted Flux Methods for Particle Transport Problems," *Transp. Theory Stat. Phys.*, **36**, 7, 589-608 (2007).

[3] Monte Carlo Team, "MCNP – A General Monte Carlo N-Particle Transport Code, Version 5," *LA-UR-03-1987,* Los Alamos National Laboratory (2003).

[4] G. Aliberti, G. Palmiotti, M. Salvatores, J.F. Lebrat, J. Tommasi, and R. Jacqmin, "Methodologies for Treatment of Spectral Effects at Core-Reflector Interfaces in Fast Neutron Systems," *Proc. 2004 International Conference on the Physics of Reactors,* April 25-29, 2004, Chicago, Illinois, American Nuclear Society (2004).

[5] J.F. Lebrat, R. Jacqmin, F. Gabrielli, M. Carta, V. Peluso, G. Buzzi, G. Bianchini, A. D'Angelo, G. Aliberti, and G. Palmiotti, "Fast Reactor Core-Reflector Interface Effects Revisited," *Proc. 2002 International Conference on the Physics of Reactors,* October 7-10, 2002, Seoul, Korea, American Nuclear Society (2002).

[6] Evaluated Nuclear Data File Database, National Nuclear Data Center, Brookhaven National Laboratory. Retrieved December 12, 2008, from http://www.nndc.bnl.gov/exfor/endf00.jsp

Chapter 3

The Hybrid Monte Carlo – S_2X Method

3.1 Introduction

In this chapter, we develop the Hybrid Monte Carlo-S_2 Method with No Spatial Truncation Error (H-MC-S_2X). This method is closely related to the H-MC-S_2 method developed in Chapter 2. That method effectively solved difficult neutron transport problems but had spatial truncation error. The H-MC-S_2X method was developed to satisfy the following properties:

1. (1) The method should incorporate computationally inexpensive low-order equations similar to coarse-group deterministic methods.
2. (2) The method should eliminate discretization errors in energy, angle, and space.
3. (3) When tested on problems with transport effects, the method should be more accurate and less expensive than conventional deterministic methods that use the multigroup approximation.

The H-MC-S_2X method does not use the multigroup approximation or multigroup cross sections. Instead, physically meaningful "nonlinear functionals" are introduced [1][2], which are simply the ratio of two correlated physical quantities, similar to a multigroup cross section. The nonlinear functionals preserve the exact physics of the problem in the low-order equations and can be estimated with only small statistical error using Monte Carlo. In this chapter, we demonstrate that the H-MC-S_2X method produces solutions with no energy, angular or spatial truncation error; the statistical error in the solution can be controlled by increasing the number of simulated neutron histories.

We now develop the H-MC-S_2X method and demonstrate its capabilities on a 1-D, fixed source problem with isotropic scattering. We begin the derivation with the neutron transport equation.

3.2 Transport Equation

To begin, we consider the planar geometry neutron transport equation and boundary conditions:

$$\mu \frac{\partial}{\partial x}\psi(x,\mu,E) + \Sigma_t(x,E)\psi(x,\mu,E) = \frac{1}{2}\int_0^\infty \Sigma_s(x,E')p(x,E'\to E)\phi(x,E')dE' + \frac{1}{2}Q(x,E) \tag{3.1}$$
$$0 \le x \le X, \qquad -1 \le \mu \le 1, \qquad 0 < E < \infty$$

$$\psi(0,\mu,E) = \psi(0,-\mu,E) \qquad 0 < \mu \le 1, \qquad 0 < E < \infty \tag{3.2}$$

$$\psi(b,\mu,E) = 0 \qquad -1 \le \mu < 0, \qquad 0 < E < \infty \tag{3.3}$$

The following assumptions have been made: (a) no fission, (b) no inelastic scattering, (c) no upscattering, and (d) P_0 elastic scattering (isotropic). These assumptions have been made only for simplicity. Any changes in these assumptions can be incorporated with only slight modifications to the derivation of the method. The probability density function $p(E' \to E)$ is defined in Eq. (2.4).

3.3 Derivation of the H-MC-S_2X Method

The goal of this method, as in the previously described H-MC-S_2 method, is to compute one or more response rates throughout the system. Defining an arbitrary spatial mesh where $h_j = x_{j+1/2} - x_{j-1/2}$ is the width of the j^{th} cell, the response rate averaged over cell j is

$$R_j = \frac{1}{h_j}\int_{x_{j-1/2}}^{x_{j+1/2}}\int_0^\infty\int_{-1}^{1} r(x,E)\psi(x,\mu,E)d\mu dE dx, \tag{3.4}$$

where the response function $r(x,E)$ is known and given. Typical response functions include $r(x,E) = \Sigma_a(x,E)$ for the spatially-averaged absorption rate, and $r(x,E) = 1$ for the energy-integrated, spatially-averaged scalar flux. As in the H-MC-S_2 method, the response functions must be chosen *a priori*, but an arbitrary number of them may be chosen simultaneously. In the following derivation, we have chosen a single response function $r(x,E)$.

3.3.1 Special Notation

The H-MC-S$_2$X method incorporates quantities that have been integrated over *subsets* of the $-1 \le \mu \le 1$ angular range. The superscripts $\left(^{+}\right)$ and $\left(^{-}\right)$ denote angular integration over the sub-ranges $0 < \mu \le 1$ and $-1 \le \mu < 0$, respectively. Quantities integrated over $-1 \le \mu \le 1$ can be written as the sum of integrals over the two sub-ranges. For example, the scalar flux can be written $\phi(x,E) = \psi^{+}(x,E) + \psi^{-}(x,E)$. The response rate can be written $R_j = R_j^{+} + R_j^{-}$, where

$$R_j^{\pm} = \pm \frac{1}{h_j} \int_{x_{j-1/2}}^{x_{j+1/2}} \int_0^{\infty} \int_0^{\pm 1} r(x,E)\psi(x,\mu,E)\, d\mu\, dE\, dx\,. \tag{3.5}$$

3.3.2 Procedure

In the H-MC-S$_2$X method, we formulate equations for the response rates $R_j^{\pm}$ directly by performing straightforward manipulations of the transport equation. As in Chapter 2, we introduce no approximations in energy, angle, or space, and avoid the generation of multigroup cross sections.

In the derivation of H-MC-S$_2$ in Chapter 2, we applied the operators $H_j^{\pm} = \int_0^X \int_0^{\infty} \int_0^{\pm 1} \chi_j(x)\left(\cdot\right) d\mu\, dE\, dx$ to the transport equation, where $\chi_j(x)$ is a histogram function. Spatial approximations were eventually required to close the resulting system of equations. We now avoid spatial approximations by applying a different operator to the transport equation.

First, we introduce an arbitrary spatial grid, $x_{1/2} < \cdots < x_{J-1/2} < x_{J+1/2}$, and define the $J+1$ tent functions, $f_{j+\frac{1}{2}}(x)$, $0 \le j \le J$, that live on the grid. For interior cells $1 \le j \le J-1$, the tent functions are defined:

$$f_{j+\frac{1}{2}}(x)=\begin{cases}\dfrac{x-x_{j-1/2}}{h_j}, & x_{j-1/2}<x<x_{j+1/2}\\[2ex] \dfrac{x_{j+3/2}-x}{h_{j+1}}, & x_{j+1/2}<x<x_{j+3/2}\\[2ex] 0, & otherwise.\end{cases} \tag{3.6}$$

The tent functions living on the boundary cells ($j=0$ and $j=J$) are truncated outside the system boundaries:

$$f_{\frac{1}{2}}(x)=\begin{cases}\dfrac{x-x_{3/2}}{h_1}, & x_{1/2}<x<x_{3/2}\\ 0, & otherwise,\end{cases} \tag{3.7}$$

$$f_{J+\frac{1}{2}}(x)=\begin{cases}\dfrac{x_{J-1/2}-x}{h_J}, & x_{J-1/2}<x<x_{J+1/2}\\ 0, & otherwise.\end{cases} \tag{3.8}$$

The j^{th} tent function is depicted with its neighboring tent functions in Figure 3.1.

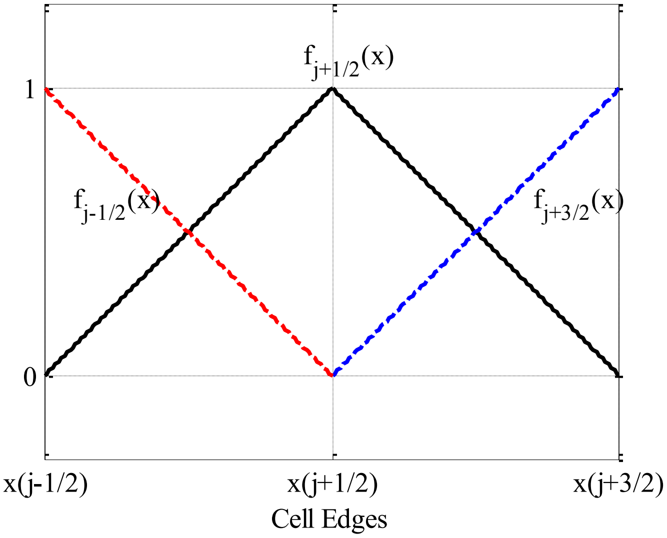

Figure 3.1 The j^{th} tent function and its neighbors.

Next, we apply the operators

$$T^{+}_{j+\frac{1}{2}} = \int_0^X \int_0^\infty \int_0^1 f_{j+\frac{1}{2}}(x)\left(\cdot\right) d\mu \, dE \, dx \tag{3.9}$$

$$T^{-}_{j+\frac{1}{2}} = \int_0^X \int_0^\infty \int_{-1}^0 f_{j+\frac{1}{2}}(x)\left(\cdot\right) d\mu \, dE \, dx \tag{3.10}$$

to the transport equation. These operators perform a weighted spatial integral over spatial cells j and $j+1$, and integrate over all energy and over a specified angular sub-range. Application of $T^{+}_{j+\frac{1}{2}}$ and $T^{-}_{j+\frac{1}{2}}$ to the transport equation yields two modified cell balance equations. Cell balance is held over two adjacent cells and over angular sub-ranges, rather than over all angles. The result of applying $T^{\pm}_{j+\frac{1}{2}}$ to the transport equation and using $\int_0^\infty p(x, E' \to E) dE = 1$ is:

$$\begin{aligned}
&\pm \int_0^X \int_0^\infty \int_0^{\pm 1} f_{j+\frac{1}{2}}(x) \mu \frac{\partial}{\partial x} \psi(x, \mu, E) d\mu \, dE \, dx \\
&\pm \int_0^X \int_0^\infty \int_0^{\pm 1} f_{j+\frac{1}{2}}(x) \Sigma_t(x, E) \psi(x, \mu, E) d\mu \, dE \, dx \\
&\qquad = \pm \frac{1}{2} \int_0^X \int_0^{\pm 1} f_{j+\frac{1}{2}}(x) \int_0^\infty \Sigma_s(x, E') \phi(x, E') dE' d\mu \, dx \\
&\qquad\quad \pm \frac{1}{2} \int_0^X \int_0^\infty \int_0^{\pm 1} f_{j+\frac{1}{2}}(x) Q(x, E) d\mu \, dE \, dx \, .
\end{aligned} \tag{3.11}$$

3.3.3 Result of the Operator on the Leakage Term

The leakage term can be evaluated without approximation. First, we define the partial currents

$$J^{\pm}(x) = \int_0^\infty \int_0^{\pm 1} \mu \psi(x, \mu, E) \, d\mu \, dE \tag{3.12}$$

[Note: This definition is equivalent to the standard (strictly non-negative) partial current $J^{+}(x) = \int_0^\infty \int_0^1 \mu \psi(x, \mu, E) \, d\mu \, dE$ and $J^{-}(x) = \int_0^\infty \int_{-1}^0 |\mu| \psi(x, \mu, E) \, d\mu \, dE$.] Using this notation, the leakage term in Eq. (3.11) can be written:

$$\pm\int_0^X\int_0^\infty\int_0^{\pm 1} f_{j+\frac{1}{2}}(x)\mu\frac{\partial}{\partial x}\psi(x,\mu,E)\,d\mu\,dE\,dx=\pm\int_0^X f_{j+\frac{1}{2}}(x)\frac{\partial}{\partial x}J^{\pm}(x)\,dx. \tag{3.13}$$

Before proceeding, we recall the special properties of the tent functions on cell boundaries:

$$f_{j+\frac{1}{2}}(x)=\begin{cases}0, & x=x_{j-1/2}\text{ or }x=x_{j+3/2}\\ 1, & x=x_{j+1/2}.\end{cases} \tag{3.14}$$

In addition, the derivative of each tent function is constant in a cell and equal to:

$$\frac{\partial}{\partial x}f_{j+\frac{1}{2}}(x)=\begin{cases}\dfrac{1}{h_j}, & x_{j-1/2}\le x\le x_{j+1/2}\\ -\dfrac{1}{h_{j+1}}, & x_{j+1/2}\le x\le x_{j+3/2}\end{cases} \tag{3.15}$$

These properties enable simplification of the leakage term without introduction of spatial approximations.

3.3.3.1 Interior cells $j=1,\dots J-1$

The interior tent functions $f_{j+\frac{1}{2}}(x)$ are non-zero in spatial cells j and $j+1$. The spatial integral in Eq. (3.13) therefore reduces to integrals over cells j and $j+1$:

$$\pm\int_0^X f_{j+\frac{1}{2}}(x)\frac{\partial}{\partial x}J^{\pm}(x)\,dx=\pm\int_j f_{j+\frac{1}{2}}(x)\frac{\partial}{\partial x}J^{\pm}(x)\,dx\pm\int_{j+1} f_{j+\frac{1}{2}}(x)\frac{\partial}{\partial x}J^{\pm}(x)\,dx \tag{3.16}$$

Each spatial integral on the right hand side of Eq. (3.16) is integrated by parts using the properties of the tent functions:

$$\begin{aligned}\int\limits_{j} f_{j+\frac{1}{2}}(x)\frac{\partial}{\partial x}J^{\pm}(x)\,dx &= \int\limits_{j}\frac{\partial}{\partial x}\Big[f_{j+\frac{1}{2}}(x)J^{\pm}(x)\Big]dx - \int\limits_{j}\frac{\partial f_{j+\frac{1}{2}}(x)}{\partial x}J^{\pm}(x)\,dx\\ &= f_{j+\frac{1}{2}}(x)J^{\pm}(x)\Big|_{x_{j-1/2}}^{x_{j+1/2}} - \int\limits_{j}\frac{1}{h_j}J^{\pm}(x)\,dx\\ &= 1\cdot J^{\pm}(x_{j+1/2}) - 0\cdot J^{\pm}(x_{j-1/2}) - \frac{1}{h_j}\int\limits_{j}J^{\pm}(x)\,dx\\ &= J^{\pm}_{j+1/2} - \frac{1}{h_j}\int\limits_{j}J^{\pm}(x)\,dx\end{aligned} \tag{3.17}$$

$$\begin{aligned}\int\limits_{j+1} f_{j+\frac{1}{2}}(x)\frac{\partial}{\partial x}J^{\pm}(x)\,dx &= \int\limits_{j+1}\frac{\partial}{\partial x}\Big[f_{j+\frac{1}{2}}(x)J^{\pm}(x)\Big]dx + \int\limits_{j+1}\frac{\partial f_{j+\frac{1}{2}}(x)}{\partial x}J^{\pm}(x)\,dx\\ &= f_{j+\frac{1}{2}}(x)J^{\pm}(x)\Big|_{x_{j+1/2}}^{x_{j+3/2}} - \int\limits_{j+1} -\frac{1}{h_{j+1}}J^{\pm}(x)\,dx\\ &= 0\cdot J^{\pm}(x_{j+3/2}) - 1\cdot J^{\pm}(x_{j+1/2}) + \frac{1}{h_{j+1}}\int\limits_{j+1}J^{\pm}(x)\,dx\\ &= -J^{\pm}_{j+1/2} + \frac{1}{h_{j+1}}\int\limits_{j+1}J^{\pm}(x)\,dx\end{aligned} \tag{3.18}$$

The partial currents $J^{\pm}_{j+1/2}$ in Eqs. (3.17) and (3.18) cancel, and Eq. (3.16) becomes

$$\pm\int_0^X f_{j+\frac{1}{2}}(x)\frac{\partial}{\partial x}J^{\pm}(x)\,dx = \pm\left(\frac{1}{h_{j+1}}\int\limits_{j+1}J^{\pm}(x)\,dx - \frac{1}{h_j}\int\limits_{j}J^{\pm}(x)\,dx\right). \tag{3.19}$$

The cancellation of the partial current term $J^{\pm}_{j+1/2}$ in this expression is physically consistent; cell balance is held over cells j and $j+1$, so the partial currents between these cells cancel each other.

3.3.3.2 Boundary cells $j=0$ and $j=J$

The boundary tent functions $f_{1/2}(x)$ and $f_{J+1/2}(x)$ are defined over single cells only. The spatial integral in Eq. (3.13) reduces to an integral over cell 1 and cell $J+1$, respectively.

$$\begin{aligned}\int_0^X f_{\frac{1}{2}}(x)\frac{\partial}{\partial x}J^{\pm}(x)\,dx &= \int_{x_{1/2}}^{x_{3/2}} f_{\frac{1}{2}}(x)\frac{\partial}{\partial x}J^{\pm}(x)\,dx \\ &= \int_{x_{1/2}}^{x_{3/2}} \frac{\partial}{\partial x}\left[f_{\frac{1}{2}}(x)J^{\pm}(x)\right]dx - \int_{x_{1/2}}^{x_{3/2}} \frac{\partial f_{\frac{1}{2}}(x)}{\partial x}J^{\pm}(x)\,dx \\ &= f_{\frac{1}{2}}(x)J^{\pm}(x)\Big|_{x_{1/2}}^{x_{3/2}} - \int_{x_{1/2}}^{x_{3/2}} -\frac{1}{\Delta x_1}J^{\pm}(x)\,dx \\ &= 0\cdot J^{\pm}(x_{3/2}) - 1\cdot J^{\pm}(x_{1/2}) + \frac{1}{\Delta x_1}\int_{x_{1/2}}^{x_{3/2}} J^{\pm}(x)\,dx \\ &= -J^{\pm}(0) + \frac{1}{\Delta x_1}\int_{x_{1/2}}^{x_{3/2}} J^{\pm}(x)\,dx \end{aligned} \tag{3.20}$$

$$\begin{aligned}\int_0^X f_{J+\frac{1}{2}}(x)\frac{\partial}{\partial x}J^{\pm}(x)\,dx &= \int_{x_{J-1/2}}^{x_{J+1/2}} f_{J+\frac{1}{2}}(x)\frac{\partial}{\partial x}J^{\pm}(x)\,dx \\ &= \int_{x_{J-1/2}}^{x_{J+1/2}} \frac{\partial}{\partial x}\left[f_{J+\frac{1}{2}}(x)J^{\pm}(x)\right]dx - \int_{x_{J-1/2}}^{x_{J+1/2}} \frac{\partial f_{J+\frac{1}{2}}(x)}{\partial x}J^{\pm}(x)\,dx \\ &= f_{J+\frac{1}{2}}(x)J^{\pm}(x)\Big|_{x_{J-1/2}}^{x_{J+1/2}} - \int_{x_{J-1/2}}^{x_{J+1/2}} \frac{1}{h_J}J^{\pm}(x)\,dx \\ &= 1\cdot J^{\pm}(x_{J+1/2}) - 0\cdot J^{\pm}(x_{J-1/2}) - \frac{1}{h_J}\int_{x_{J-1/2}}^{x_{J+1/2}} J^{\pm}(x)\,dx \\ &= J^{\pm}(X) - \frac{1}{h_J}\int_{x_{J-1/2}}^{x_{J+1/2}} J^{\pm}(x)\,dx \end{aligned} \tag{3.21}$$

In summary, the result of the $T_{j+1/2}^{\pm}$ operators on the leakage term is:

$$T_{j+1/2}^{\pm}\left(\mu\frac{\partial}{\partial x}\psi(x,\mu,E)\right) = \begin{cases} \pm\left(\dfrac{1}{h_1}\displaystyle\int_{x_{1/2}}^{x_{3/2}} J^{\pm}(x)\,dx - J^{\pm}(0)\right), & j=0 \\ \pm\left(\dfrac{1}{h_{j+1}}\displaystyle\int_{j+1} J^{\pm}(x)\,dx - \dfrac{1}{h_j}\int_{j} J^{\pm}(x)\,dx\right), & 1\le j\le J-1 \\ \pm\left(J^{\pm}(X) - \dfrac{1}{h_J}\displaystyle\int_{x_{J-1/2}}^{x_{J+1/2}} J^{\pm}(x)\,dx\right), & j=J. \end{cases} \tag{3.22}$$

We note that Eq. (3.22) is exact. The incoming partial currents at the system boundaries appearing in this expression are known from the boundary conditions. The outgoing partial currents are considered to be additional unknowns.

3.3.4 Result of the Operator on the Transport Equation

We now use Eq. (3.22) to write the transport equation after application of operators $T^{\pm}_{j+1/2}$. Using Eq. (3.12) and introducing the notation

$$\left\langle (\cdot) \right\rangle^{\pm}_{j} \equiv \pm \int_{x_{j-1/2}}^{x_{j+1/2}} \int_{0}^{\infty} \int_{0}^{\pm 1} (\cdot)\, d\mu\, dE\, dx\,, \tag{3.23}$$

the transport equation after operating by $T^{\pm}_{1/2}$ is:

$$\begin{aligned} &\frac{1}{h_1} \left\langle \mu\psi \right\rangle^{\pm}_{1} \mp J^{\pm}(0) + \left\langle f_{\frac{1}{2}} \Sigma_t \psi \right\rangle^{\pm}_{1} \\ &\qquad = \frac{1}{2} \left\langle f_{\frac{1}{2}} \Sigma_s \psi \right\rangle^{+}_{1} + \frac{1}{2} \left\langle f_{\frac{1}{2}} \Sigma_s \psi \right\rangle^{-}_{1} + \frac{1}{2} \int_{x_{1/2}}^{x_{3/2}} \int_{0}^{\infty} f_{\frac{1}{2}}(x) Q(x,E)\, dE\, dx \end{aligned} \tag{3.24}$$

The transport equation after operating by $T^{\pm}_{j+1/2}, 1 \le j \le J-1$ is:

$$\begin{aligned} &\frac{1}{h_{j+1}} \left\langle \mu\psi \right\rangle^{\pm}_{j+1} - \frac{1}{h_j} \left\langle \mu\psi \right\rangle^{\pm}_{j} + \left\langle f_{j+\frac{1}{2}} \Sigma_t \psi \right\rangle^{\pm}_{j} + \left\langle f_{j+\frac{1}{2}} \Sigma_t \psi \right\rangle^{\pm}_{j+1} \\ &\qquad = \frac{1}{2} \left(\left\langle f_{j+\frac{1}{2}} \Sigma_s \psi \right\rangle^{+}_{j} + \left\langle f_{j+\frac{1}{2}} \Sigma_s \psi \right\rangle^{+}_{j+1} + \left\langle f_{j+\frac{1}{2}} \Sigma_s \psi \right\rangle^{-}_{j} + \left\langle f_{j+\frac{1}{2}} \Sigma_s \psi \right\rangle^{-}_{j+1} \right) \\ &\qquad + \frac{1}{2} \int_{x_{j-1/2}}^{x_{j+3/2}} \int_{0}^{\infty} f_{j+\frac{1}{2}}(x) Q(x,E)\, dE\, dx. \end{aligned} \tag{3.25}$$

The transport equation after operating by $T^{\pm}_{J+1/2}$ is:

$$\begin{aligned} &\pm J^{\pm}(X) - \frac{1}{h_J} \left\langle \mu\psi \right\rangle^{\pm}_{J} + \left\langle f_{J+\frac{1}{2}} \Sigma_t \psi \right\rangle^{\pm}_{J} \\ &\qquad = \frac{1}{2} \left(\left\langle f_{J+\frac{1}{2}} \Sigma_s \psi \right\rangle^{+}_{J} + \left\langle f_{J+\frac{1}{2}} \Sigma_s \psi \right\rangle^{-}_{J} \right) + \frac{1}{2} \int_{x_{J-1/2}}^{x_{J+1/2}} \int_{0}^{\infty} f_{J+\frac{1}{2}}(x) Q(x,E)\, dE\, dx. \end{aligned} \tag{3.26}$$

Next, we manipulate Eqs. (3.24)-(3.26) to derive equations for the desired response rates in Eq. (2.7). It is helpful to note that $R^{\pm}_{j} \equiv \frac{1}{h_j} \left\langle r\psi \right\rangle^{\pm}_{j}$.

3.3.5 H-MC-S$_2$X Equations and Functional Definitions

We introduce the unknown response rates into Eqs. (3.24)-(3.26) by multiplying and dividing each flux-containing term by an "appropriate" unknown. The "appropriate" unknown for each term is the one whose integral over space, energy and angle match the limits of integration of the original term. Performing this procedure on Eq. (3.25), we obtain:

$$\begin{aligned}
&\frac{1}{h_{j+1}}\frac{\langle\mu\psi\rangle^{\pm}_{j+1}}{R^{\pm}_{j+1}}R^{\pm}_{j+1} - \frac{1}{h_j}\frac{\langle\mu\psi\rangle^{\pm}_{j}}{R^{\pm}_{j}}R^{\pm}_{j} + \frac{\left\langle f_{j+\frac{1}{2}}\Sigma_t\psi\right\rangle^{\pm}_{j}}{R^{\pm}_{j}}R^{\pm}_{j} + \frac{\left\langle f_{j+\frac{1}{2}}\Sigma_t\psi\right\rangle^{\pm}_{j+1}}{R^{\pm}_{j+1}}R^{\pm}_{j+1} \\
&\quad = \frac{1}{2}\left(\frac{\left\langle f_{j+\frac{1}{2}}\Sigma_s\psi\right\rangle^{+}_{j}}{R^{+}_{j}}R^{+}_{j} + \frac{\left\langle f_{j+\frac{1}{2}}\Sigma_s\psi\right\rangle^{+}_{j+1}}{R^{+}_{j+1}}R^{+}_{j+1} + \frac{\left\langle f_{j+\frac{1}{2}}\Sigma_s\psi\right\rangle^{-}_{j}}{R^{-}_{j}}R^{-}_{j} + \frac{\left\langle f_{j+\frac{1}{2}}\Sigma_s\psi\right\rangle^{-}_{j+1}}{R^{-}_{j+1}}R^{-}_{j+1} \right) \\
&\quad + \frac{1}{2}\int_{x_{j-1/2}}^{x_{j+3/2}}\int_0^{\infty} f_{j+\frac{1}{2}}(x)Q(x,E)dEdx.
\end{aligned} \tag{3.27}$$

The procedure used to obtain Eq. (3.27) from Eq. (3.25) introduces no error: it simply multiplies each term by unity. We have shown Eq. (3.27) for clarity, but a more useful form of this equation is:

$$\begin{aligned}
&\left[\frac{\langle\mu\psi\rangle^{\pm}_{j+1}}{\langle r\psi\rangle^{\pm}_{j+1}}\right]R^{\pm}_{j+1} - \left[\frac{\langle\mu\psi\rangle^{\pm}_{j}}{\langle r\psi\rangle^{\pm}_{j}}\right]R^{\pm}_{j} + h_j\left[\frac{\left\langle f_{j+\frac{1}{2}}\Sigma_t\psi\right\rangle^{\pm}_{j}}{\langle r\psi\rangle^{\pm}_{j}}\right]R^{\pm}_{j} + h_{j+1}\left[\frac{\left\langle f_{j+\frac{1}{2}}\Sigma_t\psi\right\rangle^{\pm}_{j+1}}{\langle r\psi\rangle^{\pm}_{j+1}}\right]R^{\pm}_{j+1} \\
&\qquad = \frac{h_j}{2}\left[\frac{\left\langle f_{j+\frac{1}{2}}\Sigma_s\psi\right\rangle^{+}_{j}}{\langle r\psi\rangle^{+}_{j}}\right]R^{+}_{j} + \frac{h_{j+1}}{2}\left[\frac{\left\langle f_{j+\frac{1}{2}}\Sigma_s\psi\right\rangle^{+}_{j+1}}{\langle r\psi\rangle^{+}_{j+1}}\right]R^{+}_{j+1} \\
&\qquad + \frac{h_j}{2}\left[\frac{\left\langle f_{j+\frac{1}{2}}\Sigma_s\psi\right\rangle^{-}_{j}}{\langle r\psi\rangle^{-}_{j}}\right]R^{-}_{j} + \left[\frac{h_{j+1}}{2}\frac{\left\langle f_{j+\frac{1}{2}}\Sigma_s\psi\right\rangle^{-}_{j+1}}{\langle r\psi\rangle^{-}_{j+1}}\right]R^{-}_{j+1} \\
&\qquad + \frac{1}{2}\int_{x_{j-1/2}}^{x_{j+3/2}}\int_0^{\infty} f_{j+\frac{1}{2}}(x)Q(x,E)dEdx
\end{aligned} \tag{3.28}$$

Performing this procedure on Eqs. (3.24) and (3.26), we also obtain Eqs. (3.29) and (3.30):

$$\begin{aligned}&\left[\frac{\langle\mu\psi\rangle_1^{\pm}}{\langle r\psi\rangle_1^{\pm}}\right]R_1^{\pm}\mp J^{\pm}(0)+h_1\left[\frac{\left\langle f_{\frac{1}{2}}\Sigma_t\psi\right\rangle_1^{\pm}}{\langle r\psi\rangle_1^{\pm}}\right]R_1^{\pm}\\&=\frac{h_1}{2}\left(\left[\frac{\left\langle f_{\frac{1}{2}}\Sigma_s\psi\right\rangle_1^{+}}{\langle r\psi\rangle_1^{+}}\right]R_1^{+}+\left[\frac{\left\langle f_{\frac{1}{2}}\Sigma_s\psi\right\rangle_1^{-}}{\langle r\psi\rangle_1^{-}}\right]R_1^{-}\right)+\frac{1}{2}\int_{x_{1/2}}^{x_{3/2}}\int_0^{\infty}f_{\frac{1}{2}}(x)Q(x,E)dEdx,\end{aligned}\tag{3.29}$$

$$\begin{aligned}&\pm J^{\pm}(X)-\left[\frac{\langle\mu\psi\rangle_J^{\pm}}{\langle r\psi\rangle_J^{\pm}}\right]R_J^{\pm}+h_J\left[\frac{\left\langle f_{J+\frac{1}{2}}\Sigma_t\psi\right\rangle_J^{\pm}}{\langle r\psi\rangle_J^{\pm}}\right]R_J^{\pm}\\&=\frac{h_J}{2}\left(\left[\frac{\left\langle f_{J+\frac{1}{2}}\Sigma_s\psi\right\rangle_J^{+}}{\langle r\psi\rangle_J^{+}}\right]R_J^{+}+\left[\frac{\left\langle f_{J+\frac{1}{2}}\Sigma_s\psi\right\rangle_J^{-}}{\langle r\psi\rangle_J^{-}}\right]R_J^{-}\right)+\frac{1}{2}\int_{x_{J-1/2}}^{x_{J+1/2}}\int_0^{\infty}f_{J+\frac{1}{2}}(x)Q(x,E)dEdx.\end{aligned}\tag{3.30}$$

Again, the partial currents $J^{+}(0)$ and $J^{-}(X)$ are known from the boundary conditions. The partial currents $J^{-}(0)$ and $J^{+}(X)$ can be computed with the system of equations we are in the process of deriving.

Certain ratios in Eqs. (3.28)-(3.30) have been bracketed for clarity. We now define these bracketed ratios as the special *nonlinear functionals*, which (as in Chapter 2) will be estimated by Monte Carlo:

$$\mu_j^{\pm}=\frac{\langle\mu\psi\rangle_j^{\pm}}{\langle r\psi\rangle_j^{\pm}}=\frac{\int_{x_{j-1/2}}^{x_{j+1/2}}\int_0^{\infty}\int_0^{\pm1}\mu\psi\left(x,\mu,E\right)d\mu dEdx}{\int_{x_{j-1/2}}^{x_{j+1/2}}\int_0^{\infty}\int_0^{\pm1}r\left(x,E\right)\psi\left(x,\mu,E\right)d\mu dEdx},\qquad 1\le j\le J\tag{3.31}$$

$$\Sigma^{\pm}_{i,j,k} = \frac{\left\langle f_{j+k}\Sigma_i\psi\right\rangle^{\pm}_j}{\left\langle r\psi\right\rangle^{\pm}_j} = \frac{\int_{x_{j-1/2}}^{x_{j+1/2}}\int_0^{\infty}\int_0^{\pm 1} f_{j+k}(x)\Sigma_i(x,E)\psi\left(x,\mu,E\right)d\mu dEdx}{\int_{x_{j-1/2}}^{x_{j+1/2}}\int_0^{\infty}\int_0^{\pm 1} r\left(x,E\right)\psi\left(x,\mu,E\right)d\mu dEdx}, \tag{3.32}$$
$$i = \left\{s,t\right\}, \quad 1 \le j \le J, \quad k = \left\{-\tfrac{1}{2},\tfrac{1}{2}\right\}$$

The nonlinear functionals in Eq. (3.32) are similar to multigroup cross sections; however, they incorporate the true angular flux rather than an approximate energy spectrum. Like the $\mu^{\pm}_{j+1/2}$ functionals in Chapter 2, we will see an analogy between the functionals in Eq. (3.31) and the discrete angles μ_n used in discrete ordinates methods.

Using Eqs. (3.31), (3.32) and

$$Q_{j,k} = \int_{x_{j-1/2}}^{x_{j+1/2}}\int_0^{\infty} f_{j+k}(x)Q(x,E)dEdx, \;\; 1 \le j \le J, \;\; k = \left\{-\tfrac{1}{2},\tfrac{1}{2}\right\}, \tag{3.33}$$

Eqs. (3.28)-(3.30) can be written as the discrete ordinates-like equations:

$$\left(\mu^{\pm}_{j+1}R^{\pm}_{j+1} - \mu^{\pm}_j R^{\pm}_j\right) + \left(h_j\Sigma^{\pm}_{t,j,\frac{1}{2}}R^{\pm}_j + h_{j+1}\Sigma^{\pm}_{t,j+1,-\frac{1}{2}}R^{\pm}_{j+1}\right) = \left(S_{j,\frac{1}{2}} + S_{j+1,-\frac{1}{2}}\right) \tag{3.34}$$
$$1 \le j \le J-1$$

$$\mu^{\pm}_1 R^{\pm}_1 \mp J^{\pm}(0) + h_1\Sigma^{\pm}_{t,1,-\frac{1}{2}}R^{\pm}_1 = S_{1,-\frac{1}{2}} \tag{3.35}$$

$$\pm J^{\pm}(X) - \mu^{\pm}_J R^{\pm}_J + h_J\Sigma^{\pm}_{t,J,\frac{1}{2}}R^{\pm}_J = S_{J,\frac{1}{2}} \tag{3.36}$$

Like the H-MC-S$_2$ equations in Chapter 2, these equations have a one-group discrete ordinates-like structure and are easily solved with a transport sweep and source iteration. The right hand side denotes the source to be iterated upon numerically:

$$S_{j,k} = \frac{1}{2}\left(h_j\Sigma^{+}_{s,j,k}R^{+}_j + h_j\Sigma^{-}_{s,j,k}R^{-}_j + Q_{j,k}\right), \;\; 1 \le j \le J, \;\; k = \left\{-\tfrac{1}{2},\tfrac{1}{2}\right\}. \tag{3.37}$$

Assuming that the functionals are known, Eqs. (3.34)-(3.36) are a system of $2J+2$ equations for $2J$ $R_j^{\pm}$ unknowns and 4 $J^{\pm}$ partial currents. The additional two equations required are derived now from the boundary conditions.

3.3.6 Boundary Conditions

Here we demonstrate how to transform the transport boundary conditions into equations for the partial currents on the boundary.

3.3.6.1 Left boundary

We apply $\int_0^{\infty}\int_0^1 \mu(\cdot)\, d\mu\, dE$ to the reflecting boundary condition in Eq. (3.2) to obtain an expression for the partial currents at the left boundary:

$$\int_0^{\infty}\int_0^1 \mu\psi(0,\mu,E)\, d\mu\, dE\, dx = -\int_0^{\infty}\int_{-1}^0 \mu\psi(0,\mu,E)\, d\mu\, dE\, dx\,, \tag{3.38}$$

or equivalently,

$$J^{+}(0) = J^{-}(0). \tag{3.39}$$

This is the extra equation needed for the left boundary.

3.3.6.2 Right boundary

We apply $-\int_0^{\infty}\int_{-1}^0 \mu(\cdot)\, d\mu\, dE$ to the non-reflecting boundary condition in Eq. (3.3) to obtain an expression for the partial current at the right boundary:

$$-\int_0^{\infty}\int_{-1}^0 \mu\psi(X,\mu,E)\, d\mu dE = -\int_0^{\infty}\int_{-1}^0 \mu\psi^{R}(\mu,E)\, d\mu dE\,, \tag{3.40}$$

or equivalently,

$$J^{-}(X) = -\int_0^{\infty}\int_{-1}^0 \mu\psi^{R}(\mu,E)\, d\mu dE. \tag{3.41}$$

This is the additional equation needed for the partial current at the right boundary.

Eqs. (3.34)-(3.36) along with (3.39) and (3.41) are the $2J+4$ equations needed for the $2J+4$ unknowns $R_j^{\pm}$, $J^{\pm}(0)$ and $J^{\pm}(X)$. These equations resemble the H-MC-S_2 equations (Chapter 2) but have no spatial, energy, or angular truncation errors. In addition, these equations have almost identical structure to the one-group S_2 discrete ordinates equations, where the multigroup cross sections and discrete angles have been replaced by nonlinear functionals. The nonlinear functionals are exact in theory, but they are dependent on the unknown angular flux and must be estimated before Eqs. (3.34)-(3.36) can be solved. We choose to estimate these functionals using Monte Carlo to avoid the introduction of any truncation errors in the estimation of the functionals.

3.4 Monte Carlo Computation of the Functionals

To solve the H-MC-S_2X equations, we must first estimate the functionals in Eqs. (3.31)-(3.32). The nonlinear functionals contain integrals that are easily computed with a Monte Carlo simulation. Monte Carlo estimates integrals using “tallies”; a neutron history contributes information to a tally when its phase space matches the tally phase space. To estimate the nonlinear functionals in Eqs. (3.31)-(3.32), we simulate the exact physics and geometry of the problem in Monte Carlo and tally the appropriate integrals over many neutron histories. Each nonlinear functional is estimated at the end of the simulation by taking ratios of the appropriate tallies. Modified path length estimator tallies are used to estimate the following integrals:

(1) $$\int_{x_{j-1/2}}^{x_{j+1/2}}\int_0^{\infty}\int_0^{\pm 1} f_{j+k}(x)\Sigma_t(x,E)\psi\left(x,\mu,E\right)d\mu dEdx$$

(2) $$\int_{x_{j-1/2}}^{x_{j+1/2}}\int_0^{\infty}\int_0^{\pm 1} f_{j+k}(x)\Sigma_s(x,E)\psi\left(x,\mu,E\right)d\mu dEdx$$

(3) $$\int_{x_{j-1/2}}^{x_{j+1/2}}\int_0^{\infty}\int_0^{\pm 1} \mu\psi\left(x,\mu,E\right)d\mu dEdx$$

(4) $$\int_{x_{j-1/2}}^{x_{j+1/2}}\int_0^{\infty}\int_0^{\pm 1} r(x,E)\psi(x,\mu,E)d\mu dEdx$$

Once these integrals are estimated in Monte Carlo, the nonlinear functionals are estimated by taking ratios of the integrals.

3.4.1 Why Not Standard Monte Carlo?

As previously discussed in Chapter 2, standard Monte Carlo calculations compute scalar fluxes and response rates directly. We are proposing the computation of *ratios* of these quantities called nonlinear functionals. One may question the strategy of using Monte Carlo to estimate nonlinear functionals instead of estimating desired response rates directly. We hypothesized in Chapter 2 that Monte Carlo estimates of nonlinear functionals are much accurate and have less variance than direct Monte Carlo estimates of the desired response rates. This hypothesis is justified with the theory of correlated random variables and numerical results in Chapter 4.

3.5 Global Particle Balance

We show here that H-MC-S_2X preserves global particle balance, a desirable property for transport methods. To preserve global particle balance, the solution of the method must satisfy the neutron balance equation formulated over the entire system:

$$J(X) - J(0) + \int_0^X \int_0^\infty \int_{-1}^1 \Sigma_a \psi \, d\mu \, dE \, dx = \int_0^X \int_0^\infty \int_{-1}^1 Q \, d\mu \, dE \, dx. \qquad (3.42)$$

The absorption term in the neutron balance equation can be computed with H-MC-S_2X by setting $r(x,E) = \Sigma_a(x,E)$:

$$\int_0^X \int_0^\infty \int_{-1}^1 \Sigma_a(x,E) \psi(x,\mu,E) \, d\mu \, dE \, dx = \sum_{\forall j} h_j \left(R_j^+ + R_j^- \right). \qquad (3.43)$$

We now show that the H-MC-S_2X solutions $R_j^\pm$ satisfy the balance equation

$$J(X) - J(0) + \sum_{\forall j} h_j \left(R_j^+ + R_j^- \right) = \int_0^X \int_0^\infty \int_{-1}^1 Q \, d\mu \, dE \, dx \qquad (3.44)$$

3.5.1 System of Equations and Definitions

The nonlinear functionals were defined in Eqs. (3.31)-(3.32). In addition, the source notation was defined in Eqs. (3.33)-(3.37). Along with these definitions, the H-MC-S_2X equations are

$$\begin{gathered}\mu^+_{j+1}R^+_{j+1}-\mu^+_jR^+_j+h_j\Sigma^+_{t,j,\frac{1}{2}}R^+_j+h_{j+1}\Sigma^+_{t,j+1,-\frac{1}{2}}R^+_{j+1}=S_{j,\frac{1}{2}}+S_{j+1,-\frac{1}{2}}\\ 1\le j\le J-1\end{gathered} \tag{3.45}$$

$$\begin{gathered}\mu^-_{j+1}R^-_{j+1}-\mu^-_jR^-_j+h_j\Sigma^-_{t,j,\frac{1}{2}}R^-_j+h_{j+1}\Sigma^-_{t,j+1,-\frac{1}{2}}R^-_{j+1}=S_{j,\frac{1}{2}}+S_{j+1,-\frac{1}{2}}\\ 1\le j\le J-1\end{gathered} \tag{3.46}$$

$$\mu^+_1R^+_1-J^+(0)+h_1\Sigma^+_{t,1,-1/2}R^+_1=S_{1,-\frac{1}{2}}, \tag{3.47}$$

$$\mu^-_1R^-_1+J^-(0)+h_1\Sigma^-_{t,1,-1/2}R^-_1=S_{1,-\frac{1}{2}}, \tag{3.48}$$

$$J^+(X)-\mu^+_JR^+_J+h_J\Sigma^+_{t,J,1/2}R^+_J=S_{J,\frac{1}{2}}, \tag{3.49}$$

$$-J^-(X)-\mu^-_JR^-_J+h_J\Sigma^-_{t,J,1/2}R^-_J=S_{J,\frac{1}{2}}. \tag{3.50}$$

3.5.2 Proof of Particle Balance

We consider the j^{th} spatial cell in the system $\left(1\le j\le J-1\right)$, and add together the positive and negative equations for this cell, Eqs. (3.45) and (3.46). Combining like terms and using $\Sigma^{\pm}_{t,j,k}=\Sigma^{\pm}_{s,j,k}+\Sigma^{\pm}_{a,j,k}$, we obtain:

$$\begin{aligned}&\left(-\mu^+_j+h_j\Sigma^+_{a,j,\frac{1}{2}}\right)R^+_j+\left(\mu^+_{j+1}+h_{j+1}\Sigma^+_{a,j+1,-\frac{1}{2}}\right)R^+_{j+1}\\ &+\left(-\mu^-_j+h_j\Sigma^-_{a,j,\frac{1}{2}}\right)R^-_j+\left(\mu^-_{j+1}+h_{j+1}\Sigma^-_{a,j+1,-\frac{1}{2}}\right)R^-_{j+1}\\ &\qquad\qquad\qquad\qquad=Q_{j,\frac{1}{2}}+Q_{j+1,-\frac{1}{2}}.\end{aligned} \tag{3.51}$$

We now add Eqs. (3.45) and (3.46) for the j^{th} and $\left(j+1\right)^{th}$ cells. Cancellation of the $\mu^{\pm}_{j+1}$ leakage terms occurs:

$$\begin{aligned}
&\left(-\mu_j^{+}+h_j\Sigma^{+}_{a,j,\frac{1}{2}}\right)R_j^{+}+\left(-\mu_j^{-}+h_j\Sigma^{-}_{a,j,\frac{1}{2}}\right)R_j^{-}\\
&+h_{j+1}\left(\Sigma^{+}_{a,j+1,-\frac{1}{2}}+\Sigma^{+}_{a,j+1,\frac{1}{2}}\right)R^{+}_{j+1}+h_{j+1}\left(\Sigma^{-}_{a,j+1,-\frac{1}{2}}+\Sigma^{-}_{a,j+1,\frac{1}{2}}\right)R^{-}_{j+1}\\
&+\left(\mu^{+}_{j+2}+h_{j+2}\Sigma^{+}_{a,j+2,-\frac{1}{2}}\right)R^{+}_{j+2}+\left(\mu^{-}_{j+2}+h_{j+2}\Sigma^{-}_{a,j+2,-\frac{1}{2}}\right)R^{-}_{j+2}\\
&\qquad\qquad\qquad\qquad=Q_{j,\frac{1}{2}}+Q_{j+1,-\frac{1}{2}}+Q_{j+1,\frac{1}{2}}+Q_{j+2,-\frac{1}{2}}.
\end{aligned}\tag{3.52}$$

The expression $\Sigma^{\pm}_{a,j+1,-\frac{1}{2}}+\Sigma^{\pm}_{a,j+1,\frac{1}{2}}$ can be simplified:

$$\begin{aligned}
\Sigma^{\pm}_{a,j,\frac{1}{2}}+\Sigma^{\pm}_{a,j,-\frac{1}{2}}&=\frac{\int_{x_{j-1/2}}^{x_{j+1/2}}\int_0^{\infty}\int_0^{\pm1}\left(f_{j+1/2}(x)+f_{j-1/2}(x)\right)\Sigma_a(x,E)\psi\,d\mu\,dE\,dx}{\int_{x_{j-1/2}}^{x_{j+1/2}}\int_0^{\infty}\int_0^{\pm1}r(x,E)\psi\,d\mu\,dE\,dx}\\
&=\frac{\int_{x_{j-1/2}}^{x_{j+1/2}}\int_0^{\infty}\int_0^{\pm1}\Sigma_a(x,E)\psi\,d\mu\,dE\,dx}{\int_{x_{j-1/2}}^{x_{j+1/2}}\int_0^{\infty}\int_0^{\pm1}r(x,E)\psi\,d\mu\,dE\,dx}\\
&\equiv1,
\end{aligned}\tag{3.53}$$

because $r\left(x,E\right)=\Sigma_a\left(x,E\right)$. Also, $Q_{j,\frac{1}{2}}+Q_{j,-\frac{1}{2}}=\int_{x_{j-1/2}}^{x_{j+1/2}}\int_0^{\infty}Q(x,E)dEdx\equiv Q_j$. Making these simplifications to Eq. (3.52) yields:

$$\begin{aligned}
&\left(-\mu_j^{+}+h_j\Sigma^{+}_{a,j,\frac{1}{2}}\right)R_j^{+}+\left(-\mu_j^{-}+h_j\Sigma^{-}_{a,j,\frac{1}{2}}\right)R_j^{-}+h_{j+1}\left(R^{+}_{j+1}+R^{-}_{j+1}\right)\\
&+\left(\mu^{+}_{j+2}+h_{j+2}\Sigma^{+}_{a,j+2,-\frac{1}{2}}\right)R^{+}_{j+2}+\left(\mu^{-}_{j+2}+h_{j+2}\Sigma^{-}_{a,j+2,-\frac{1}{2}}\right)R^{-}_{j+2}\\
&\qquad\qquad\qquad\qquad=Q_{j,\frac{1}{2}}+Q_{j+1}+Q_{j+2,-\frac{1}{2}}.
\end{aligned}\tag{3.54}$$

The sum of Eqs. (3.45) and (3.46) over $1\le j\le J-1$ is:

$$\begin{aligned}
&\left(-\mu_1^{+}+h_1\Sigma^{+}_{a,1,\frac{1}{2}}\right)R_1^{+}+\left(-\mu_1^{-}+h_1\Sigma^{-}_{a,1,\frac{1}{2}}\right)R_1^{-}+\sum_{j=2}^{J-1}h_j\left(R_j^{+}+R_j^{-}\right)\\
&+\left(\mu_J^{+}+h_J\Sigma^{+}_{a,J,-\frac{1}{2}}\right)R_J^{+}+\left(\mu_J^{-}+h_J\Sigma^{-}_{a,J,-\frac{1}{2}}\right)R_J^{-}\\
&\qquad\qquad\qquad\qquad=Q_{1,\frac{1}{2}}+\sum_{j=2}^{J-1}Q_j+Q_{J,-\frac{1}{2}}.
\end{aligned}\tag{3.55}$$

The sum of Eqs. (3.47)-(3.50) is:

$$\begin{aligned}J^+(X)-J^-(X)+J^-(0)-J^+(0)+\left(\mu_1^+ + h_1\Sigma^+_{a,1,-\frac{1}{2}}\right)R_1^+ + \left(\mu_1^- + h_1\Sigma^-_{a,1,-\frac{1}{2}}\right)R_1^-\\ +\left(-\mu_J^+ + h_J\Sigma^+_{a,J,\frac{1}{2}}\right)R_J^+ + \left(-\mu_J^- + h_J\Sigma^-_{a,J,\frac{1}{2}}\right)R_J^- \\ = Q_{J,\frac{1}{2}} + Q_{1,-\frac{1}{2}}.\end{aligned} \tag{3.56}$$

Finally, the sum of Eq. (3.55) and (3.56) is:

$$J(X)-J(0)+\sum_{j=1}^{J} h_j\left(R_j^+ + R_j^-\right)=\sum_{j=1}^{J} Q_j, \tag{3.57}$$

where we have used the conventional definition of net current: $J(x)=J^+(x)-J^-(x)$. This is the global balance equation, and therefore, H-MC-S_2X satisfies global particle balance.

3.6 Numerical Results

3.6.1 Core-Reflector Problem

We consider the Core-Reflector Problem depicted in Figure 3.2. This problem exhibits severe transport effects at the core-reflector boundary. An in-depth description of this test problem and a discussion on transport effects are given in Chapter 2.

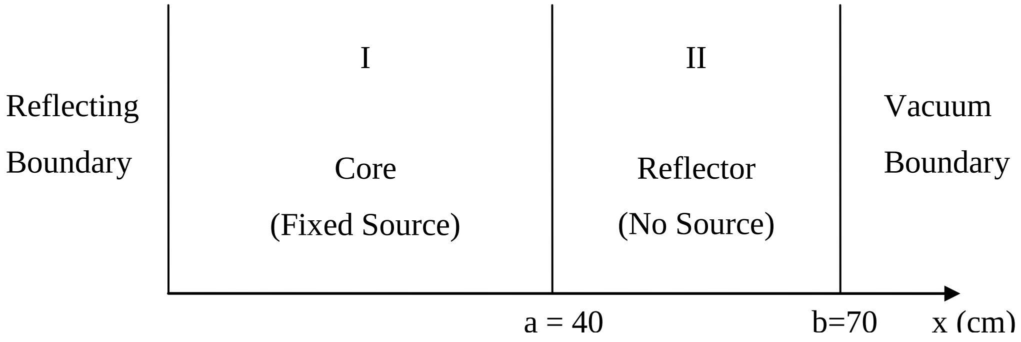

Figure 3.2 Geometry of Core-Reflector Problem.

In the following sections, we use the Core-Reflector Problem to compare the statistical properties of the H-MC-S_2X method to that of Monte Carlo, and the accuracy of H-MC-S_2X with that of conventional deterministic methods, namely multigroup discrete ordinates. We compute the energy-integrated scalar flux, the resonance-group scalar flux, and the resonance-group capture rate using Monte Carlo, H-MC-S_2X, and MGS_{16} with varied energy group structure (G=11, 21, 51, 101, and 251).

3.6.2 Comparison with Standard Monte Carlo

The variance of a standard Monte Carlo solution can be directly computed during a single simulation; the variance of the H-MC-S_2X solution may only be estimated over many simulations due to complexities in calculating the covariance of the functionals and propagating the error algebraically. To compare the statistical properties of standard Monte Carlo with that of H-MC-S_2X, twenty five independent estimates of the scalar flux were obtained with each method (a different random number seed was used for each estimate). The numerical properties of the Monte Carlo simulations are presented in Table 2.2.

# of Independent Simulations (K)	Histories per Simulation (N)	Grid Size [cm]
25	50,000	0.5

Table 3.1 Monte Carlo numerical properties for variance estimation of test problem.

The *sample pdf variance* [see Chapter 2] was computed for each cell-averaged scalar flux value ϕ_j for each method. The sum of relative sample pdf variances and the average computational time (sec) were used to compute the figure of merit, *FOM* (defined in Chapter 2).

Method	SRV	*T*	FOM
Monte Carlo	2.10e-02	262	0.182
H-MC-S_2X	1.10e-02	312	0.291

Table 3.2 Figure of merit comparison for calculation of test problem scalar flux.

The *fractional computing time,* $f^{(m)} = \frac{FOM^{(MC)}}{FOM^{(m)}}$ (introduced in Chapter 2) is the fraction of time required by method m to achieve a given error obtained by standard Monte Carlo. For this problem, $f^{(\text{H-MC-S}_2\text{X})} = 0.63,$ meaning that the H-MC-S_2X method requires 63% of the standard Monte Carlo computing time to achieve a given error.

However, as discussed in Chapter 2, optimal implementation of tallies (not performed in our research codes) could reduce this fraction to 0.52. In this case, the H-MC-S_2X method would require 52% of the Monte Carlo computing time to achieve a given error. These results also imply that the H-MC-S_2X solution is 52% of the variance of the standard Monte Carlo solution for fixed computational cost. As in Chapter 2, this numerical result is consistent with the hypothesis that the estimation of nonlinear functionals in Monte Carlo is more efficient than the estimation of traditional linear quantities.

3.6.3 Comparison with Standard Deterministic Methods

We now compare the accuracies of H-MC-S_2X and multigroup discrete ordinates (MGS_N). We calculate the scalar flux and capture rate for the test problem. The numerical parameters of each method are summarized in Table 2.4. (The number of histories differs for the scalar flux and capture rate because the capture rate required more particles for an accurate result.)

Method	**Grid Spacing [cm]**	**# of Histories**	**Energy Groups, Quadrature Order**
Benchmark Monte Carlo	0.5	2×10^6 (scalar flux) 4×10^6 (capture rate)	Continuous energy, Continuous angle
H-MC-S_2X	0.5	5×10^5 (scalar flux) 1×10^6 (capture rate)	Continuous energy, Continuous angle (“Exact” collapse to G=1, S_2)
MGS_N	0.5	-	G=11, 21, 51, 101, 251, S_{16}

Table 3.3 Numerical properties for Core-Reflector Problem.

Details on the generation of multigroup cross section for this problem are given in Chapter 2.

3.6.4 *Computation of Scalar Flux*

The scalar flux for the test problem was computed on a uniform 0.5 cm grid using MGS$_{16}$ ($G = 11, 21, 51, 101, 251$) and H-MC-S$_2$X (5x10^5 particles). The scalar flux results for both methods are compared to a benchmark Monte Carlo calculation (2x10^6 particles) in Figure 3.3.

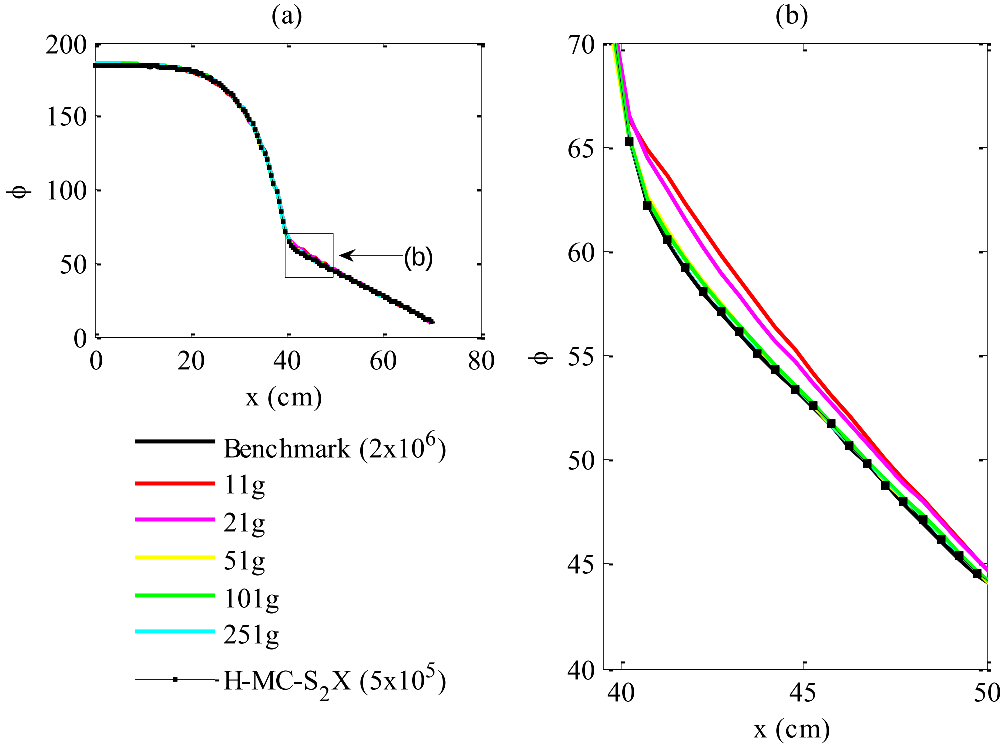

Figure 3.3 Scalar flux for (a) slab and (b) interface region.

Figure 3.3(a) shows the solution over the whole slab, and Figure 3.3(b) is a blowup of the solution close to the interface ($x = 40$ cm). Major differences are observed between the multigroup discrete ordinates solution and the benchmark Monte Carlo solution for the region just inside the reflector ($40 \text{ cm} < x < 50 \text{ cm}$). In Figure 3.4, the magnitude of error in each calculation relative to the benchmark is plotted, along with the uncertainty in the benchmark calculation, 'Benchmark 1 σ'. Only errors greater than the benchmark uncertainty are considered significant.

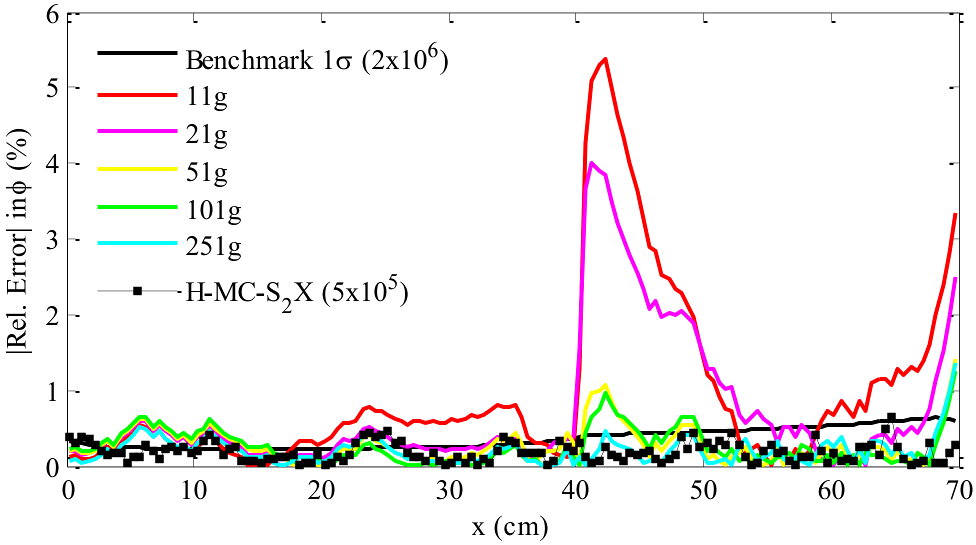

Figure 3.4 Relative errors in scalar flux.

Examining Figure 3.3 and Figure 3.4, we see that the H-MC-S$_2$X method performed well in all parts of the problem. The relative error for the H-MC-S$_2$X method is within benchmark uncertainty for almost every data point. This is remarkable, considering that H-MC-S$_2$X used only 25% as many histories as the benchmark Monte Carlo solution. Clearly, increasing the number of particles would further improve the hybrid result, but an excellent result is obtained nonetheless with less computational time than the benchmark solution.

In contrast to H-MC-S$_2$X, the MGS$_{16}$ methods performed poorly near material interfaces for this test problem. While the MGS$_{16}$ results approached the benchmark solution as the group structure was refined, a minimum of 251 groups was needed to achieve the same accuracy as the one-group S$_2$–like hybrid method. This result confirms our belief that the multigroup approximation is the origin of most of the error.

Since the spectral effects occur mostly in the *resonance group* (630.957 eV to 10 keV), a calculation was performed to compute the resonance-group scalar flux. The resonance-group scalar flux is compared with the benchmark Monte Carlo solution in Figure 3.5 and Figure 3.6. The MGS$_{16}$ errors were more severe for the resonance-group flux than for the total-energy integrated flux, but the H-MC-S_2X errors were not significantly increased.

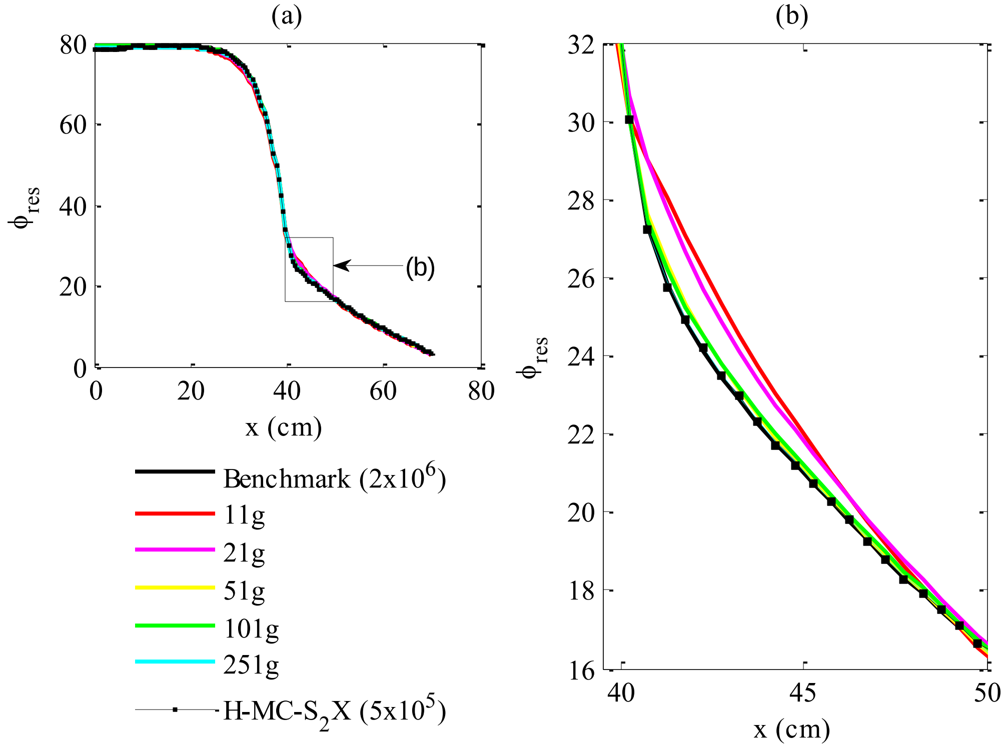

Figure 3.5 Resonance group flux for (a) slab, and (b) interface region.

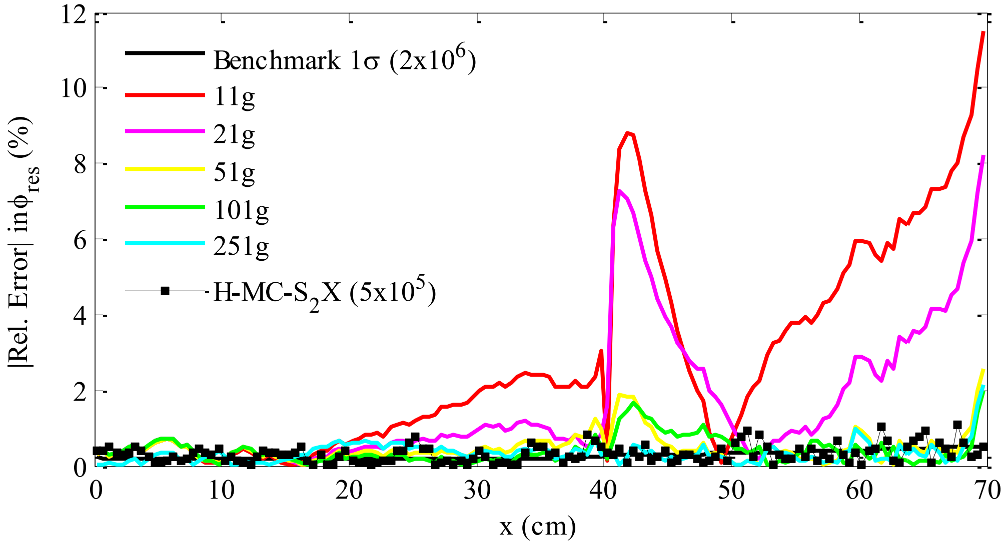

Figure 3.6 Relative errors in resonance group flux.

Figure 3.5 and Figure 3.6 indicate that even for a simple scalar flux calculation, a 251 group structure is required to reduce the MGS_{16} error near material interfaces to acceptable levels. This is an important result: the one-group H-MC-S_2X method performs at the same level as the 251 group structure by incorporating directional, angular, and spatial information. It should be noted that both 51g and 101g calculations perform reasonably well but still exhibit systematic errors at the interface and vacuum boundary, with errors up to 2%.

3.6.5 Computation of Resonance Group Capture Rate

The H-MC-S_2X resonance group capture rate is compared with the benchmark Monte Carlo solution and deterministic MGS_{16} calculations in Figure 3.7 and Figure 3.8.

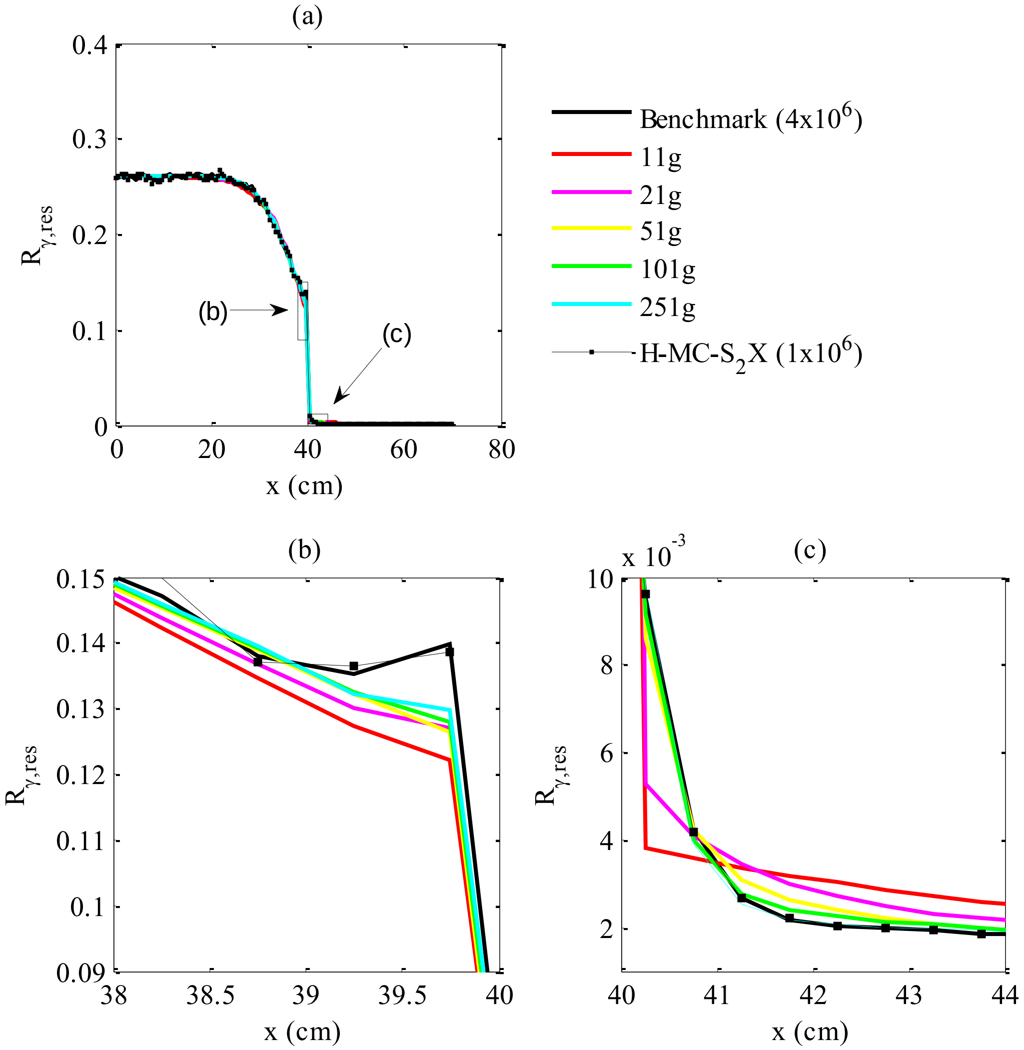

Figure 3.7 Resonance group capture rate for (a) slab, and (b)-(c) interface region.

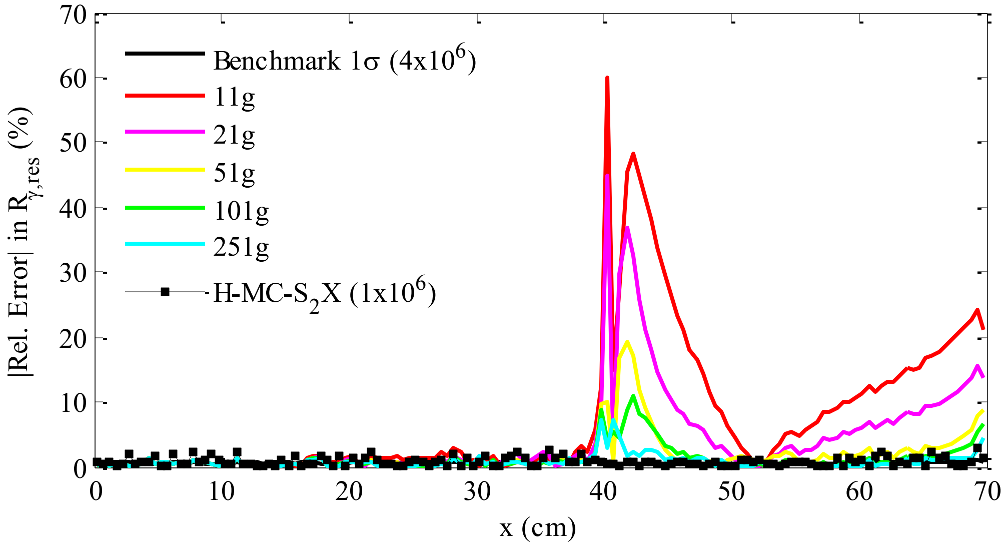

Figure 3.8 Errors in resonance group capture rate.

The MGS$_{16}$ calculations had significant errors in the region near the core-reflector interface and vacuum boundary. The MGS$_{16}$ method clearly becomes more accurate as the number of groups increases. However, significant transport effects are still apparent in the finest group ($G = 251$) solution. The H-MC-S$_2$X method exhibited no transport effect errors and had uniform statistical error throughout the problem.

The large spatial gradient in the resonance capture rate near the core-reflector interface is problematic for MGS$_N$ due to spatial truncation error. While the MGS$_N$ results could be improved by refining the spatial grid, the optimum refinement is not known *a priori*. In contrast, H-MC-S$_2$X has no spatial truncation error and handles this gradient easily. Therefore, H-MC-S$_2$X offers a significant advantage over conventional deterministic methods because it works on coarse spatial grids.

3.7 Conclusions

We have developed a hybrid method called H-MC-S$_2$X for accurately and efficiently solving difficult transport problems. The method consists of collapsing the transport equation in angle, energy, and space with no truncation errors. The collapsing process produces nonlinear functionals that can be accurately computed by Monte Carlo. These functionals are similar to one-group flux-weighted cross sections and quadrature angles, and the low-order equations are similar to the one-group S$_2$ equations.

For a test problem containing significant transport effects, the H-MC-S_2X results agreed with the benchmark Monte Carlo solution. The H-MC-S_2X solution had one half the variance of a history-equivalent Monte Carlo solution. This translates into a time savings of approximately 50% when the extra H-MC-S_2X tallies are optimally implemented. In addition, the H-MC-S_2X method was more accurate than conventional multigroup discrete ordinates methods.

In contrast to the H-MC-S_2 method developed in Chapter 2, the H-MC-S_2X method has no spatial truncation error, and the method can handle problems with discontinuous and rapidly varying solutions on *any* spatial grid. For many practical problems, material interfaces are surrounded by boundary layers where the transport solution has strong spatial gradients. A method with spatial truncation error (e.g., H-MC-S_2) requires refinement of the spatial grid in the boundary layers to obtain an accurate solution. However, a method with no spatial truncation error (e.g., H-MC-S_2X) eliminates the need to refine the spatial grid within boundary layers. Therefore, H-MC-S_2X has an important advantage over H-MC-S_2 because it has no spatial truncation error. In Chapter 2, the continuous function technique was required with a 0.1 cm spatial grid to reduce the H-MC-S_2 spatial truncation error (in the resonance capture rate) to acceptable levels. In contrast, the H-MC-S_2X used a spatial grid of 0.5 cm and had comparable errors. The size of the H-MC-S_2X grid is dictated by the desired spatial detail, not by consideration of spatial truncation errors.

Other than spatial grid considerations, the H-MC-S_2X method also eliminates sources of error due to improper choice of energy group boundaries or insufficient number of discrete ordinates directions. Finally, because the method has no approximation in angle, it may be advantageous for solving problems where discrete ordinates calculations exhibit undesirable ray effects. This could be tested in the future by implementing the method in 2-D geometry. We have demonstrated the success of this method on a meaningful fixed source problem. H-MC-S_2X could easily be extended to eigenvalue problems as well.

In the next chapter, we discuss the statistical properties of H-MC-S_2X and how this method fares against standard Monte Carlo for more problems. We seek to demonstrate why methods utilizing nonlinear functionals (such as H-MC-S_2 and H-MC-S_2X) have less variance than standard Monte Carlo calculations.

3.8 References

[1] E.R. Wolters, E.W. Larsen, and W.R. Martin, “A Hybrid Monte Carlo-S2 Method with No Spatial Truncation Error”, Trans. Am. Nucl. Soc., **101**, 714-716 (2009).

[2] E.R. Wolters, E.W. Larsen, and W.R. Martin, “A Hybrid Monte Carlo-S2 Method with No Spatial Truncation Error”, *Proc. 2010 Am. Nucl. Soc. Student Conference*, Ann Arbor, MI, April 8-10, 2010, CD-ROM, American Nuclear Society (2010).

[3] G. Aliberti, G. Palmiotti, M. Salvatores, J.F. Lebrat, J. Tommasi, and R. Jacqmin, “Methodologies for Treatment of Spectral Effects at Core-Reflector Interfaces in Fast Neutron Systems,” *Proc. 2004 International Conference on the Physics of Reactors*, April 25-29, 2004, Chicago, Illinois, CD-ROM, American Nuclear Society (2004).

[4] J.F. Lebrat, R. Jacqmin, F. Gabrielli, M. Carta, V. Peluso, G. Buzzi, G. Bianchini, A. D’Angelo, G. Aliberti, and G. Palmiotti, “Fast Reactor Core-Reflector Interface Effects Revisited,” *Proc. 2002 International Conference on the Physics of Reactors*, October 7-10, 2002, Seoul, Korea, CD-ROM, American Nuclear Society (2002).

Chapter 4

Statistical Properties of the H-MC-S_2X Method

4.1 Introduction

The H-MC-S_2 and H-MC-S_2X methods developed in Chapters 2 and 3 utilize special nonlinear functionals rather than multigroup cross sections and discrete ordinates. We hypothesized that stochastic estimates of these nonlinear functionals, defined as ratios of linear functionals, are more accurate, and have less variance, than stochastic estimates of the numerator and denominator, provided the same neutron histories are used to evaluate the functionals in the numerator and denominator. In this chapter, we present theory and numerical results to support this hypothesis. In addition, we show that the accuracy and variance of the H-MC-S_2X method depends on the following:

(1) Number of simulated particle histories,
(2) Correlation of the random variables in the functional definitions,
(3) Sensitivity of the low-order deterministic equations to statistical fluctuations in the functionals.

Item (1) can be controlled by running more histories. Item (2) is problem-dependent because the functionals depend on the angular flux and material cross sections. Item (3) is difficult to analyze theoretically. However, we present numerical results indicating that the H-MC-S_2X solutions typically have less variance than the corresponding history-equivalent standard Monte Carlo solution.

We begin by using the theory of random variables to discuss the advantages of using Monte Carlo to compute nonlinear functionals rather than standard linear quantities. We then present numerical results confirming that the stochastically-computed nonlinear functionals have less variance than standard linear quantities. Last, we test the sensitivity of the H-MC-S$_2$X low-order equations to statistical variations in the nonlinear functionals.

4.2 Stochastic Computation of Random Variables

The Boltzmann equation describes the mean behavior of a large number of stochastically moving neutrons. Standard Monte Carlo methods solve the transport equation by simulating individual neutrons and tallying information, i.e., the scalar flux and response rates, over many neutron histories. The scalar flux and response rates are *random variables* whose mean and variance are computed during the simulation. The mean can be computed exactly only in the limit of an infinite number of neutron histories. In practice, a finite number of histories are used, and the uncertainty in the mean (standard deviation) is reported to reflect the confidence in this solution. The variance (standard deviation squared) is governed by both the probability density function of the quantity and the number of histories simulated.

4.2.1 Theory

Let us consider the H-MC-S$_2$X method formulated for the response rate $R_j^{\pm} = \pm\frac{1}{h_j}\int_{x_{j-1/2}}^{x_{j+1/2}}\int_0^{\infty}\int_0^{\pm 1} r(x,E)\psi(x,\mu,E)\,d\mu\,dE\,dx$. The H-MC-S$_2$X equations for interior cells $1 \le j \le J-1$ are:

$$\begin{aligned}&\left(\mu_{j+1}^{\pm}R_{j+1}^{\pm} - \mu_j^{\pm}R_j^{\pm}\right) + \left(h_j\Sigma_{t,j,\frac{1}{2}}^{\pm}R_j^{\pm} + h_{j+1}\Sigma_{t,j+1,-\frac{1}{2}}^{\pm}R_{j+1}^{\pm}\right)\\ &= \frac{1}{2}\left(h_j\Sigma_{s,j,\frac{1}{2}}^{+}R_j^{+} + h_j\Sigma_{s,j,\frac{1}{2}}^{-}R_j^{-} + Q_{j,\frac{1}{2}}\right) + \frac{1}{2}\left(h_{j+1}\Sigma_{s,j+1,-\frac{1}{2}}^{+}R_{j+1}^{+} + h_{j+1}\Sigma_{s,j+1,-\frac{1}{2}}^{-}R_{j+1}^{-} + Q_{j+1,-\frac{1}{2}}\right).\end{aligned} \tag{4.1}$$

The nonlinear functionals $\mu_j^{\pm}$, $\Sigma_{s,j,\pm\frac{1}{2}}^{\pm}$, and $\Sigma_{t,j,\pm\frac{1}{2}}^{\pm}$ are defined as ratios of standard Monte Carlo tallies. In this case, each nonlinear functional can be written as $F = \frac{X}{Y}$, where F is the nonlinear functional, X is the numerator of the functional, and Y is the denominator of the functional. For example, if $F = \mu_j^{+}$, then

$X = \frac{1}{h_j}\int_{x_{j-1/2}}^{x_{j+1/2}}\int_0^{\infty}\int_0^{1}\mu\psi\left(x,\mu,E\right)d\mu dE dx,$ and $Y = \frac{1}{h_j}\int_{x_{j-1/2}}^{x_{j+1/2}}\int_0^{\infty}\int_0^{1} r\left(x,E\right)\psi\left(x,\mu,E\right)d\mu dE dx.$

(In all functional definitions, the denominator Y is the standard Monte Carlo estimate of the desired response rate.) We now derive (approximately) the *pdf mean* and *pdf variance* of F. We use the notation $\left[\cdot\right]$ to express the expected value (mean) of the quantity inside the brackets. A random variable can be expressed as the sum of its mean and some statistical error:

$$X = \left[X\right] + \sigma_X, \text{ where } \left[\sigma_X\right] = 0, \tag{4.2}$$

$$Y = \left[Y\right] + \sigma_Y, \text{ where } \left[\sigma_Y\right] = 0. \tag{4.3}$$

The variance of X and Y are:

$$\begin{aligned} \operatorname{Var}(X) &= \left[\left(X - [X]\right)^2\right] = \left[X^2\right] - \left[X\right]^2 \\ &= \left[\sigma_X^2\right], \end{aligned} \tag{4.4}$$

$$\begin{aligned} \operatorname{Var}(Y) &= \left[\left(Y - [Y]\right)^2\right] = \left[Y^2\right] - \left[Y\right]^2 \\ &= \left[\sigma_Y^2\right]. \end{aligned} \tag{4.5}$$

The mean of F is estimated by neglecting terms order σ^3 and higher:

$$\begin{aligned} \left[F\right] &= \left[\frac{X}{Y}\right] = \left[\frac{\left[X\right] + \sigma_X}{\left[Y\right] + \sigma_Y}\right] \\ &= \frac{1}{[Y]}\left[\left(\left[X\right] + \sigma_X\right)\left(1 - \frac{\sigma_Y}{[Y]} + \frac{\sigma_Y^2}{[Y]^2} - \cdots\right)\right] \\ &\approx \frac{[X]}{[Y]} + \frac{[X]}{[Y]^3}\left[\sigma_Y^2\right] - \frac{1}{[Y]^2}\left[\sigma_X \sigma_Y\right]. \end{aligned} \tag{4.6}$$

Following a similar procedure to obtain the mean of F^2 and using $\operatorname{Var}(F) = \left[\left(F - [F]\right)^2\right]$, the variance of F can be approximated to second order by:

$$\begin{aligned}\mathrm{Var}(F) &\approx \frac{1}{[Y]^2}\left(\left[\sigma_X^2\right]-2\frac{[X]}{[Y]}\left[\sigma_X\sigma_Y\right]+\frac{[X]^2}{[Y]^2}\left[\sigma_Y^2\right]\right) \\ &\equiv \left[\sigma_F^2\right].\end{aligned} \tag{4.7}$$

We now wish to compare the relative variance in the functional to the relative variance in the denominator of the functional. (The denominator of the functional is the quantity we are trying to compute. We hypothesized that the relative variance in the functional should be *less* than the relative variance in the denominator because of correlation between the numerator and denominator.)

$$\begin{aligned}\mathrm{Relvar}(F) &= \frac{\left[\sigma_F^2\right]}{[F]^2} \\ &\approx \frac{\left[\sigma_X^2\right]}{[X]^2}-2\frac{\left[\sigma_X\sigma_Y\right]}{[X][Y]}+\frac{\left[\sigma_Y^2\right]}{[Y]^2} \\ &= \mathrm{Relvar}(X)-2\mathrm{Relcovar}(X,Y)+\mathrm{Relvar}(Y).\end{aligned} \tag{4.8}$$

Here we have introduced the notation for the relative covariance of two random variables:

$$\mathrm{Relcovar}(X,Y)=\frac{\left[\sigma_X\sigma_Y\right]}{[X][Y]}. \tag{4.9}$$

The covariance of two variables is a measure of how much they *covary*, or vary together. If X and Y are independent, $\left[\sigma_X\sigma_Y\right]=\mathrm{Cov}(X,Y)=0.$ Also, $\mathrm{Cov}(X,X)=\mathrm{Var}(X).$ The covariance is bounded by $0\le\left|\mathrm{Cov}(X,Y)\right|\le\sqrt{\mathrm{Var}(X)\mathrm{Var}(Y)}$. We write

$$\Lambda=\frac{\mathrm{Relvar}(F)}{\mathrm{Relvar}(Y)}, \tag{4.10}$$

where $\Lambda\ge 0$ because relative variances are non-negative. From Eq. (4.8), Λ can be written:

$$\Lambda = 1 + \frac{1}{\left[\sigma_Y^2\right]} \frac{[Y]^2}{[X]^2} \left(\left[\sigma_X^2\right] - 2\frac{[X]}{[Y]} \left[\sigma_X \sigma_Y\right] \right). \tag{4.11}$$

The condition $\Lambda < 1$ implies that the relative variance of the functional is less than the relative variance of the denominator. This condition holds when:

$$2\frac{[X]}{[Y]} \left[\sigma_X \sigma_Y\right] > \left[\sigma_X^2\right]. \tag{4.12}$$

If Eq. (4.12) is satisfied, the relative variance of the nonlinear functional $\frac{X}{Y}$ is less than the relative variance of Y. The term $\left[\sigma_X \sigma_Y\right]$ is the covariance of X and Y. Since the covariance $\left[\sigma_X \sigma_Y\right]$ increases as the amount of correlation increases, this condition is more likely to be satisfied for choices of X and Y that are highly correlated.

We emphasize that the *only* source of statistical error in X and Y is the statistical estimation of the function $\psi(x,\mu,E)$ in the integrals of these random variables. The random variables can be written as a deterministic operator on ψ:

$$X = \mathrm{M}_X \psi. \tag{4.13}$$

For example, $\mathrm{M}_X = \frac{1}{h_j}\int_{x_{j-1/2}}^{x_{j+1/2}}\int_0^\infty\int_0^1 \mu(\cdot)\, d\mu dE dx$ for the choice of

$X = \frac{1}{h_j}\int_{x_{j-1/2}}^{x_{j+1/2}}\int_0^\infty\int_0^1 \mu\psi(x,\mu,E)\, d\mu dE dx.$ Also, $\psi = [\psi] + \sigma_\psi$, so the statistical error in X can be related to the statistical error in ψ:

$$\begin{aligned} \sigma_X &= X - [X] = \mathrm{M}_X\left(\psi - [\psi]\right) \\ &= \mathrm{M}_X \sigma_\psi. \end{aligned} \tag{4.14}$$

Likewise, $\sigma_Y = \mathrm{M}_Y \sigma_\psi$.

Since the operators M_X and M_Y are deterministic, σ_X and σ_Y are correlated *only* if the same estimate of ψ (with error σ_ψ) are used to evaluate both random variables. If the function $\psi(x,\mu,E)$ is estimated using *identical* histories for X and Y, then the statistical errors $\sigma_X = \mathrm{M}_X\sigma_\psi$ and $\sigma_Y = \mathrm{M}_Y\sigma_\psi$ are correlated. In this case, the covariance $\left[\sigma_X\sigma_Y\right]$ is non-zero, allowing for the possibility of $\Lambda < 1$. The covariance $\left[\sigma_X\sigma_Y\right]$ is maximized when $\mathrm{M}_X = \mathrm{M}_Y$: in this case, $\sigma_X = \sigma_Y$ and $\left[\sigma_X\sigma_Y\right] = \sigma_X^2 = \sigma_Y^2$, (the maximum value of the covariance). We thus make the case for trying to choose operators M_X and M_Y that are as similar as possible, and for using identical particle histories to evaluate $\psi(x,\mu,E)$ in X and Y.

If *independent* estimates of $\psi(x,\mu,E)$ are used to evaluate X and Y, then the statistical errors $\sigma_X = \mathrm{M}_X\sigma_\psi^{(1)}$ and $\sigma_Y = \mathrm{M}_Y\sigma_\psi^{(2)}$ are independent, and the covariance $\left[\sigma_X\sigma_Y\right]$ is zero. In this case, Eq. (4.12) is not satisfied.

4.2.2 Intuition

We have provided a theoretical justification for computing nonlinear functionals rather than standard linear quantities. We have also demonstrated that identical particle histories must be used to evaluate the numerator and denominator of the functional, and that the numerator and denominator operators on the angular flux should be chosen to be as similar as possible.

It is difficult to theoretically predict whether Eq. (4.12) will be satisfied. However, the degree of correlation in the numerator and denominator can be qualitatively predicted by examining the operators appearing in the numerator and denominator. We emphasize that the correlation between the numerator and denominator is maximized when the numerator and denominator functions are identical. The correlation is reduced as the similarity between the operators decreases. For example, if the numerator operator utilizes a resonance cross section, and the denominator operator produces the scalar flux, the correlation is reduced between numerator and denominator due to the fine energy detail in the numerator operator. Consequently, Eq. (4.12) is less likely to be satisfied for this example than if the numerator operator were to utilize a cross section without resonances.

In the remainder of this chapter, we numerically estimate the pdf variance of the H-MC-S$_2$X functionals and compare these variances with the pdf variances in the numerator and denominator. We also compare the pdf variances of the H-MC-S$_2$X and Monte Carlo solutions. For the remainder of this chapter, we use the term “variance” to imply “pdf variance”.

4.3 Estimation of Variance

The variance of a random variable x can be estimated over K simulations using

$$S_j^{\,2} = \frac{K}{K-1}\left(\widehat{x_j^2} - \hat{x}_j^2 \right), \tag{4.15}$$

where $\hat{x}_j = \frac{1}{K}\sum_{k=1}^{K} x_j^{(k)}$ is the average value of x in the j^{th} cell over K simulations, and $\widehat{x_j^2} = \frac{1}{K}\sum_{k=1}^{K} (x_j^{(k)})^2$ is the average value of x^2 in the j^{th} cell over K simulations.

In this chapter, we compute the variance in Eq. (4.15) for the following random variables: the H-MC-S$_2$X functional numerators (“Num”), the H-MC-S$_2$X functional denominators (“Denom”), the H-MC-S$_2$X functionals (“Fcnl”), and the H-MC-S$_2$X solution. We emphasize that the functional numerators and denominators are *standard Monte Carlo tallies.*

We show that the variance in the nonlinear functionals is less than the variances of the functional numerators and denominators. Also, the variance in the H-MC-S$_2$X solution is less than the variance in the standard Monte Carlo estimate of the solution. In other words, the *distributions* of H-MC-S$_2$X functional and solution estimates (over multiple simulations) are more tightly clustered around the true mean than standard Monte Carlo estimates of the solution.

The standard Monte Carlo and H-MC-S$_2$X calculations in this chapter use identical particle histories, i.e., they are *history-equivalent*. (Consequently, the numerator and denominator of each functional are estimated using identical histories.) We emphasize again that the *denominator* of any H-MC-S_2X nonlinear functional in cell j is *the standard Monte Carlo estimate of the solution*.

4.4 Variance of the Nonlinear Functionals

4.4.1 Core-Reflector Test Problem #1

Twenty-five statistically independent Monte Carlo simulations with 50,000 histories were performed to compute the scalar flux in the core-reflector problem described in Chapter 2. In this chapter, we call this “Core-Reflector Problem #1”. (Later, a second Core-Reflector problem will be discussed.)

Number of Independent Simulations (K)	Number of Histories per Simulation (N)	Spatial Grid [cm]
25	50,000	0.5

Table 4.1 Monte Carlo numerical properties for Core-Reflector Problem variance studies.

Since the H-MC-S_2X method was formulated to solve for the scalar flux, we use the notation ϕ instead of R to refer to the H-MC-S_2X solution and standard Monte Carlo tally for this quantity.

Before examining the variance of the H-MC-S2X nonlinear functionals, we consider their average values, plotted in Figure 4.1. The $\mu_j^{\pm}$ functionals have no discontinuities and approach the value ± 0.5 in the limit of an isotropic angular flux. Deviations from this value arise when the flux is anisotropic. In contrast, the $\Sigma^{\pm}_{t,j,\pm\frac{1}{2}}$ and $\Sigma^{\pm}_{s,j,\pm\frac{1}{2}}$ functionals are discontinuous at the material boundary $(x = 40)$. They are sensitive to the energy-dependence of the flux, as is indicated by the gradual change in value just inside the reflector and near the vacuum boundary. Differences can also be observed between the left- and right-angularly integrated functionals near the material interfaces. These differences show the importance of including the energy *and* angle dependence of the flux when weighting cross sections in multigroup calculations.

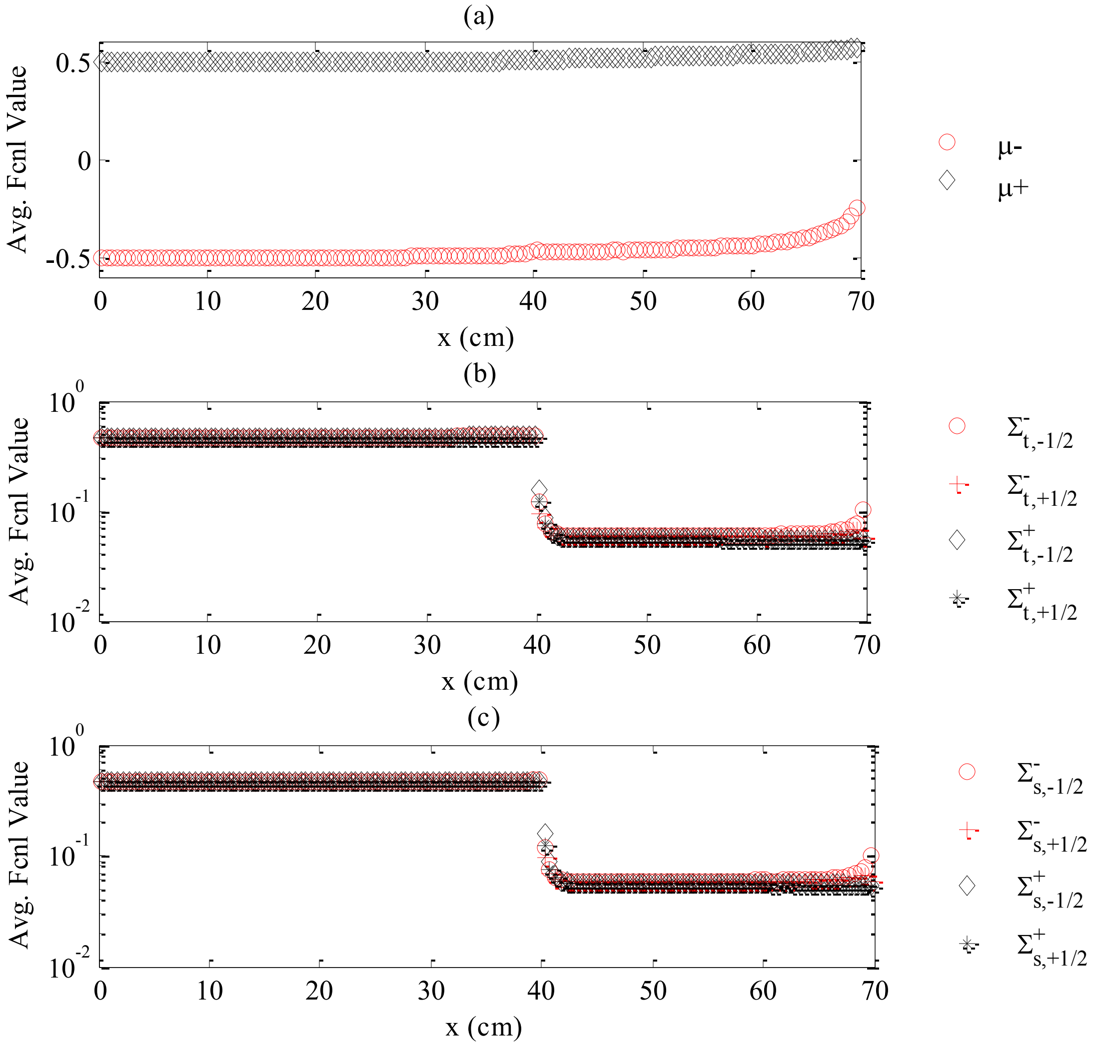

Figure 4.1 Average values of functionals over 25 independent simulations for Core-Reflector Problem #1.

We now examine the variance of the $\mu_j^{\pm}$ functionals. These functional are defined:

$$\mu_j^{\pm} = \frac{\frac{1}{h_j}\int_{x_{j-1/2}}^{x_{j+1/2}}\int_0^{\infty}\int_0^{\pm 1}\mu\psi\left(x,\mu,E\right)d\mu dEdx}{\frac{1}{h_j}\int_{x_{j-1/2}}^{x_{j+1/2}}\int_0^{\infty}\int_0^{\pm 1}\psi\left(x,\mu,E\right)d\mu dEdx}, \qquad (4.16)$$

$$1 \le j \le J.$$

Figure 4.2 plots the relative variance in this functional, labeled “Fcnl”, and the relative variance of the numerator and denominator, labeled “Num” and “Denom”, respectively. Again, the *denominator* of each functional is the Monte Carlo estimate of the solution. We plot the ratio of *the relative variance in the denominator* to *the relative variance in the functional* (referred to as the “D/F Relative Variance Ratio”) to demonstrate that the standard Monte Carlo solution has greater relative variance than the functional.

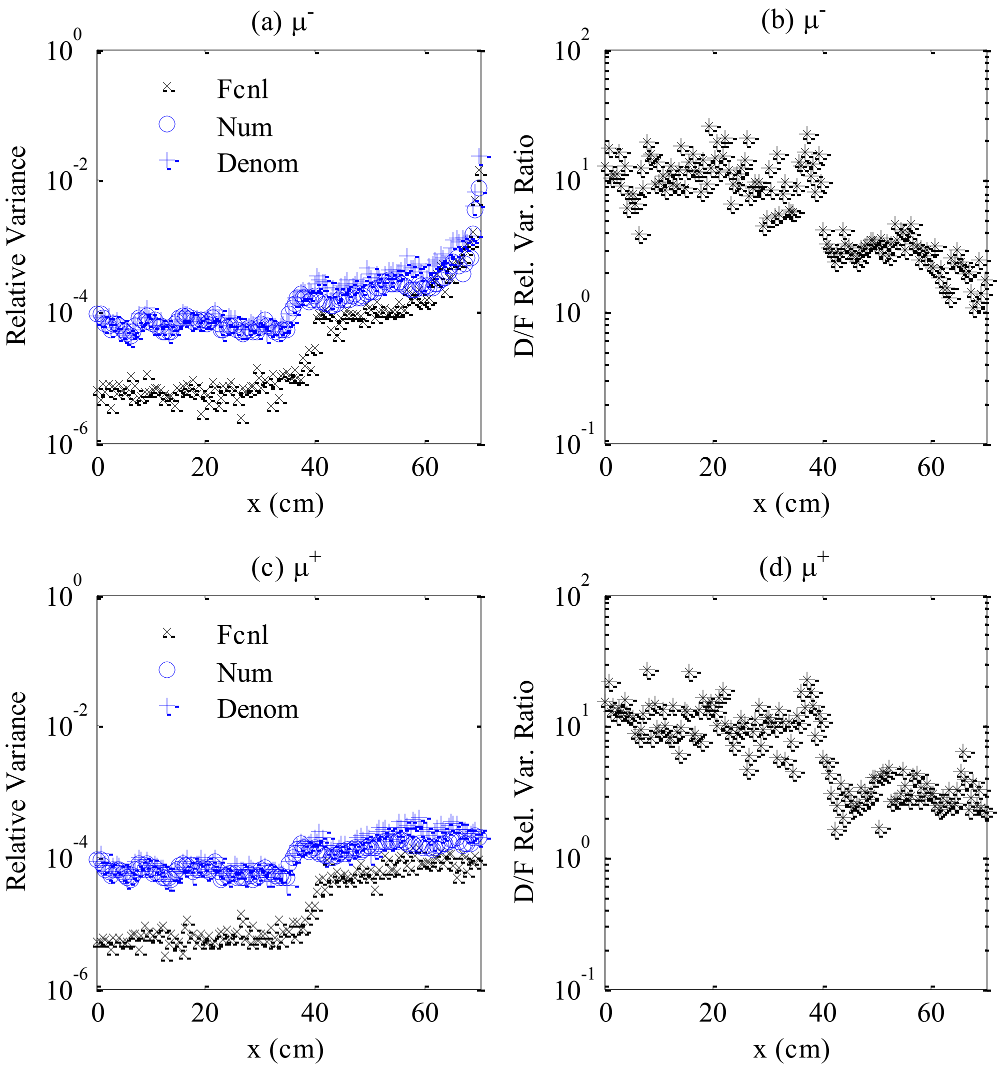

Figure 4.2. Relative variance of $\mu^{+/-}$ functionals and associated MC tallies.

In Figure 4.2(a) and (c), the relative variance of the functional is smaller than the relative variance of the standard Monte Carlo estimate of the solution for all spatial locations. The variance of the $\mu_j^{\pm}$ functional increases towards the vacuum boundary where the problem may not be sufficiently sampled, particularly in the incoming direction. This behavior could be mitigated by running more particles, or by utilizing variance reduction techniques. The D/F ratios for the μ_j^{+} and μ_j^{-} functionals indicate that the relative variance of the Monte Carlo solution is typically 10 times the relative variance of the functional in the core, but significantly less in the reflector. While the *average functional value* does not exhibit strong spatial dependence for this problem, the *variance* does, due to differences in correlation of the current and scalar flux in the core and the reflector.

The variances of the cross section functionals, $\Sigma^{\pm}_{t,j,\pm\frac{1}{2}}$ and $\Sigma^{\pm}_{s,j,\pm\frac{1}{2}}$, are plotted in Figure 4.3 through 4.6. These functionals are defined:

$$\Sigma^{\pm}_{i,j,k} = \frac{\dfrac{1}{h_j}\displaystyle\int_{x_{j-1/2}}^{x_{j+1/2}}\int_0^{\infty}\int_0^{\pm 1} f_{j+k}(x)\Sigma_i(x,E)\psi\left(x,\mu,E\right)d\mu dEdx}{\dfrac{1}{h_j}\displaystyle\int_{x_{j-1/2}}^{x_{j+1/2}}\int_0^{\infty}\int_0^{\pm 1}\psi\left(x,\mu,E\right)d\mu dEdx}, \qquad (4.17)$$
$$i=\left\{s,t\right\},\quad 1\le j\le J,\quad k=\left\{-\tfrac{1}{2},\tfrac{1}{2}\right\}.$$

The subscript $k=\pm\frac{1}{2}$ refers to the spatial tent function $f_{j\pm\frac{1}{2}}(x)$ in the numerator. Since the spatial cells are small, the tent function subscript does not significantly affect the functional values or variances.

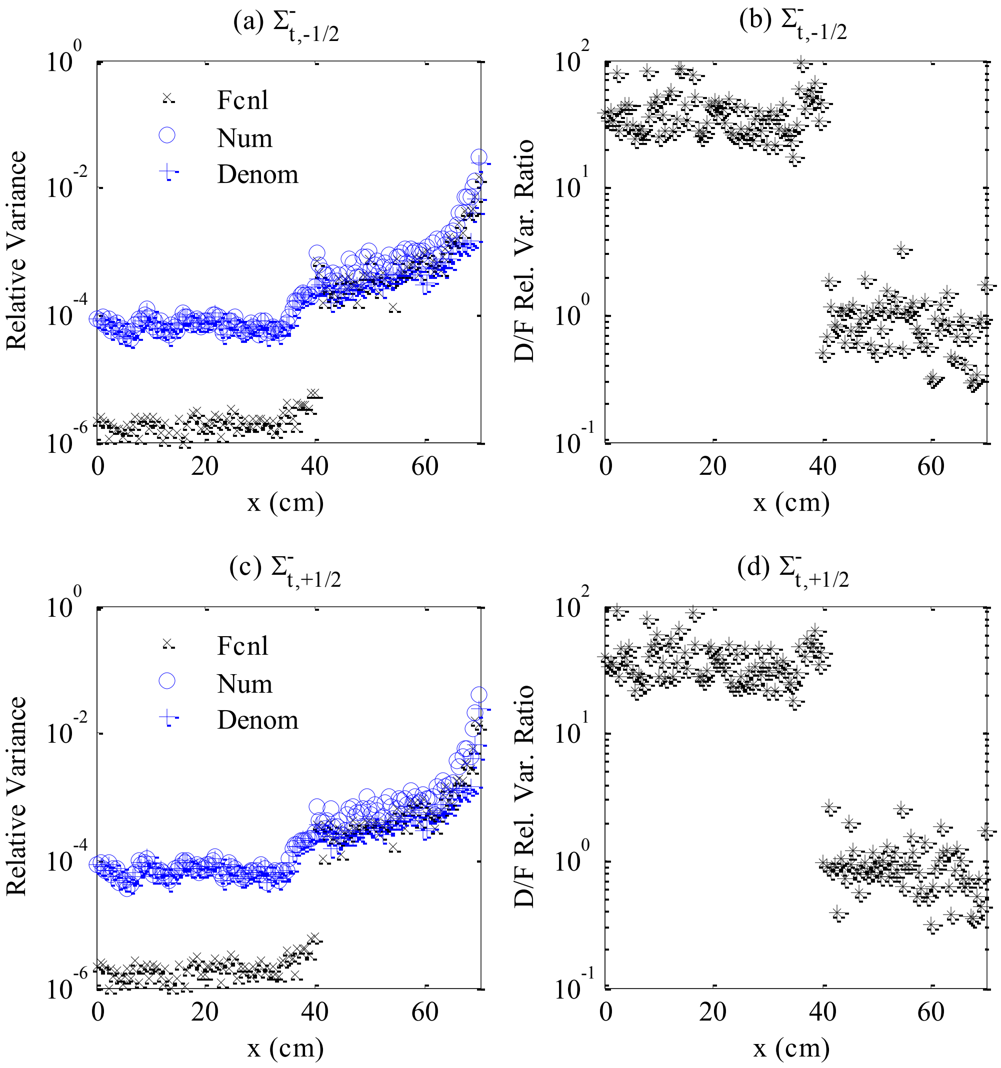

Figure 4.3 Relative variance of Σ_t^{-} functionals and associated MC tallies.

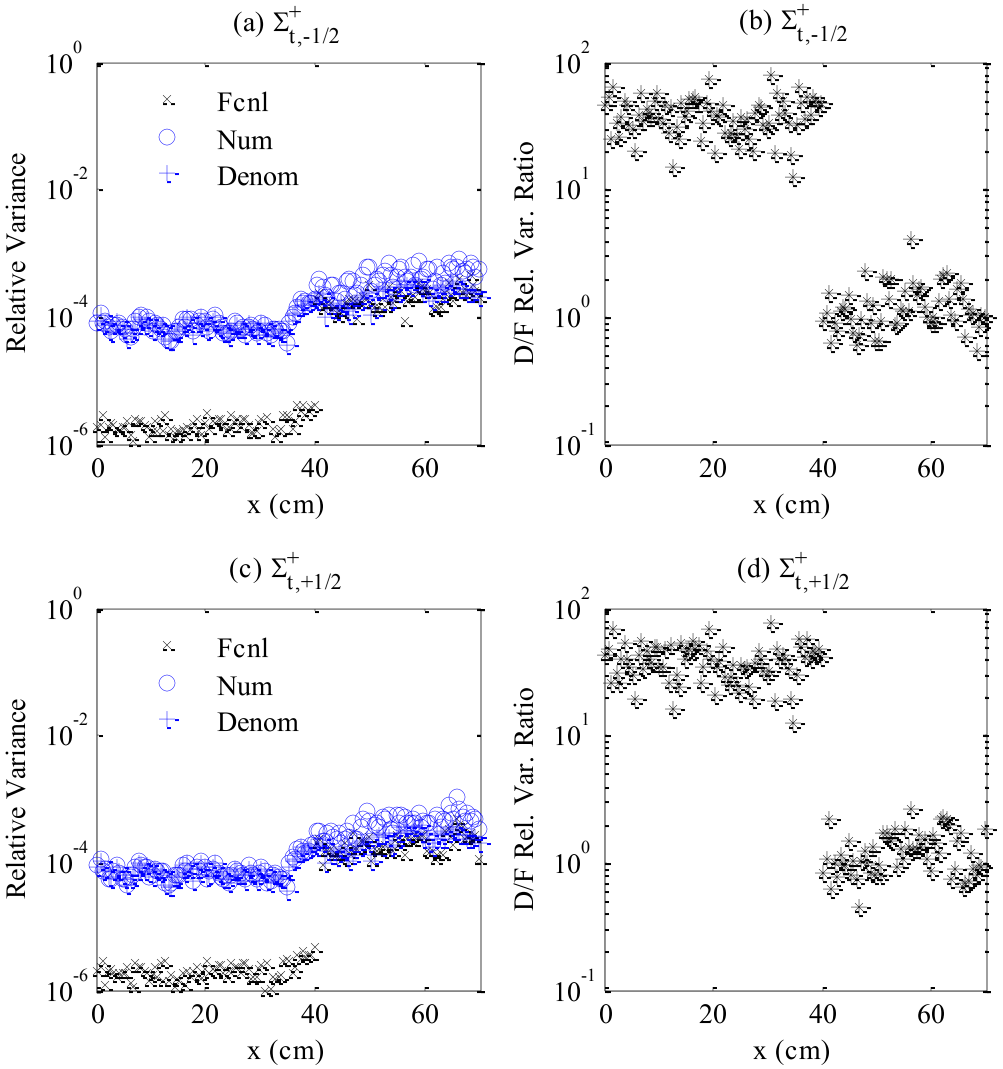

Figure 4.4 Relative variance of Σ_t^+ functionals and associated MC tallies.

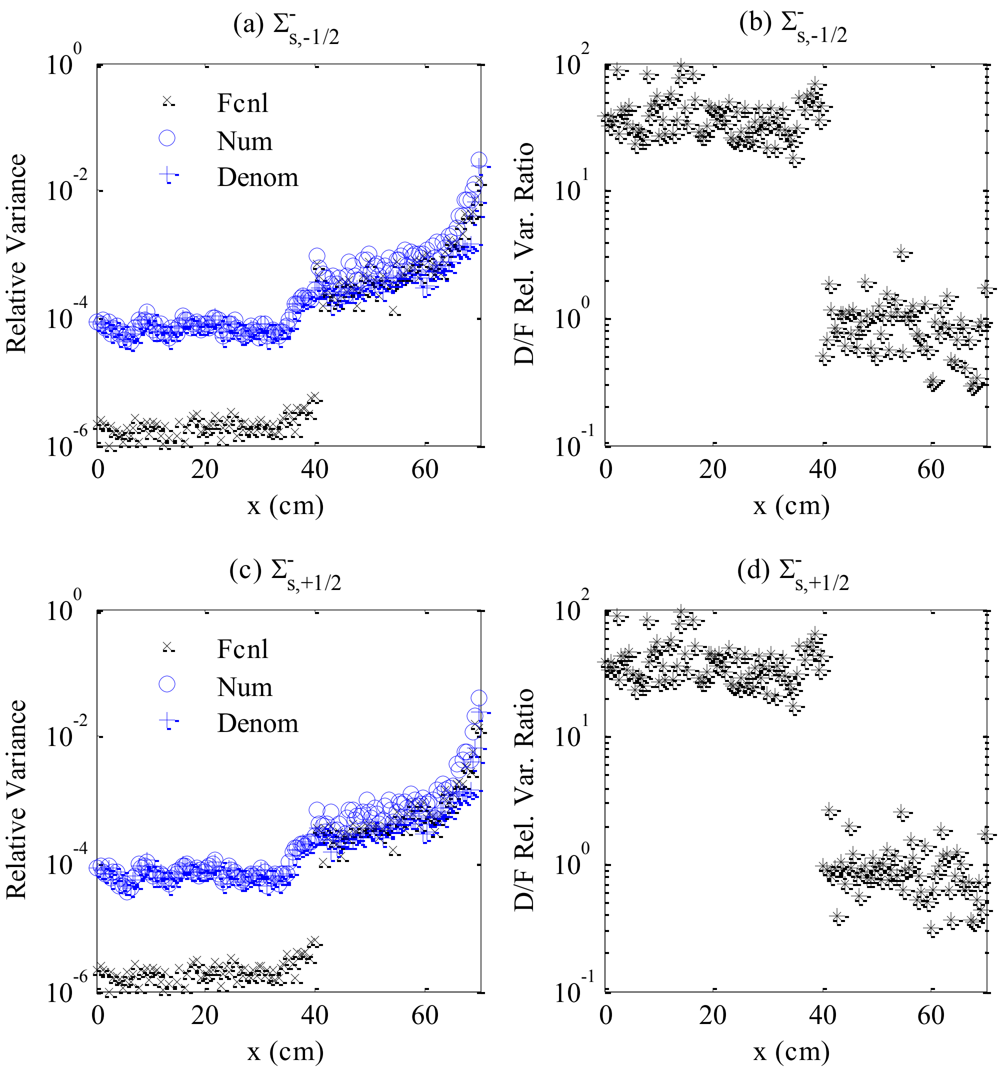

Figure 4.5 Relative variance of Σ_s^- functionals and associated MC tallies.

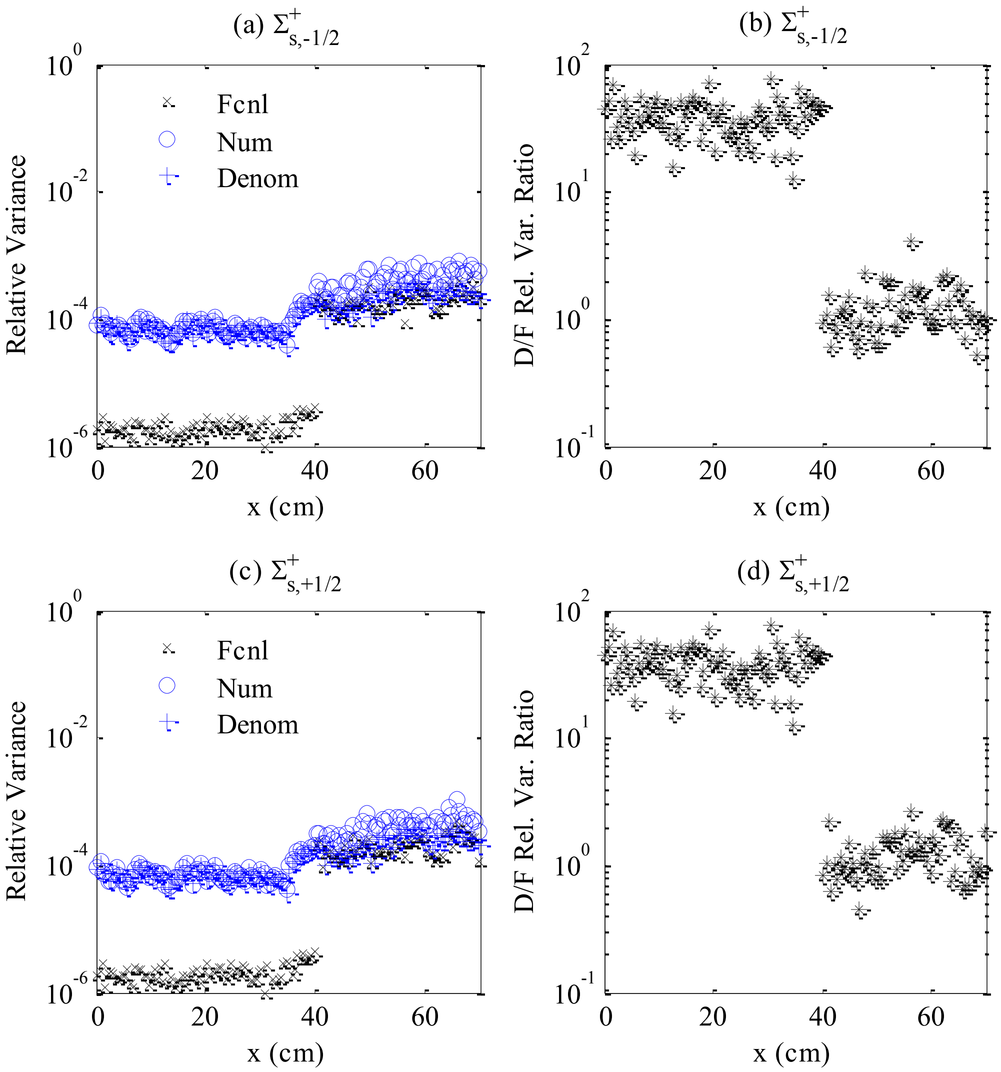

Figure 4.6 Relative variance of Σ_s^+ functionals and associated MC tallies.

The D/F ratio is approximately 80 to 100 in the core region, meaning that the Monte Carlo solution has 80 to 100 times more variance than the nonlinear functionals. This indicates that the numerators and denominators of the functionals in the core region are very highly correlated. In the reflector region, the ratio drops to unity or less than unity.

The reflector scattering cross section has a strong resonance over a wide energy range (1.9 to 3.9 keV). In the reflector, the functional denominators (scalar flux-like quantities) are not well-correlated to the numerators due to the fine energy detail in this scattering resonance. The reflector functionals therefore have higher variance than functionals in the core. A modified test problem in the next section supports this explanation.

The D/F ratios of each functional are plotted on the same scale in Figure 4.7 for Core-Reflector Problem #1.

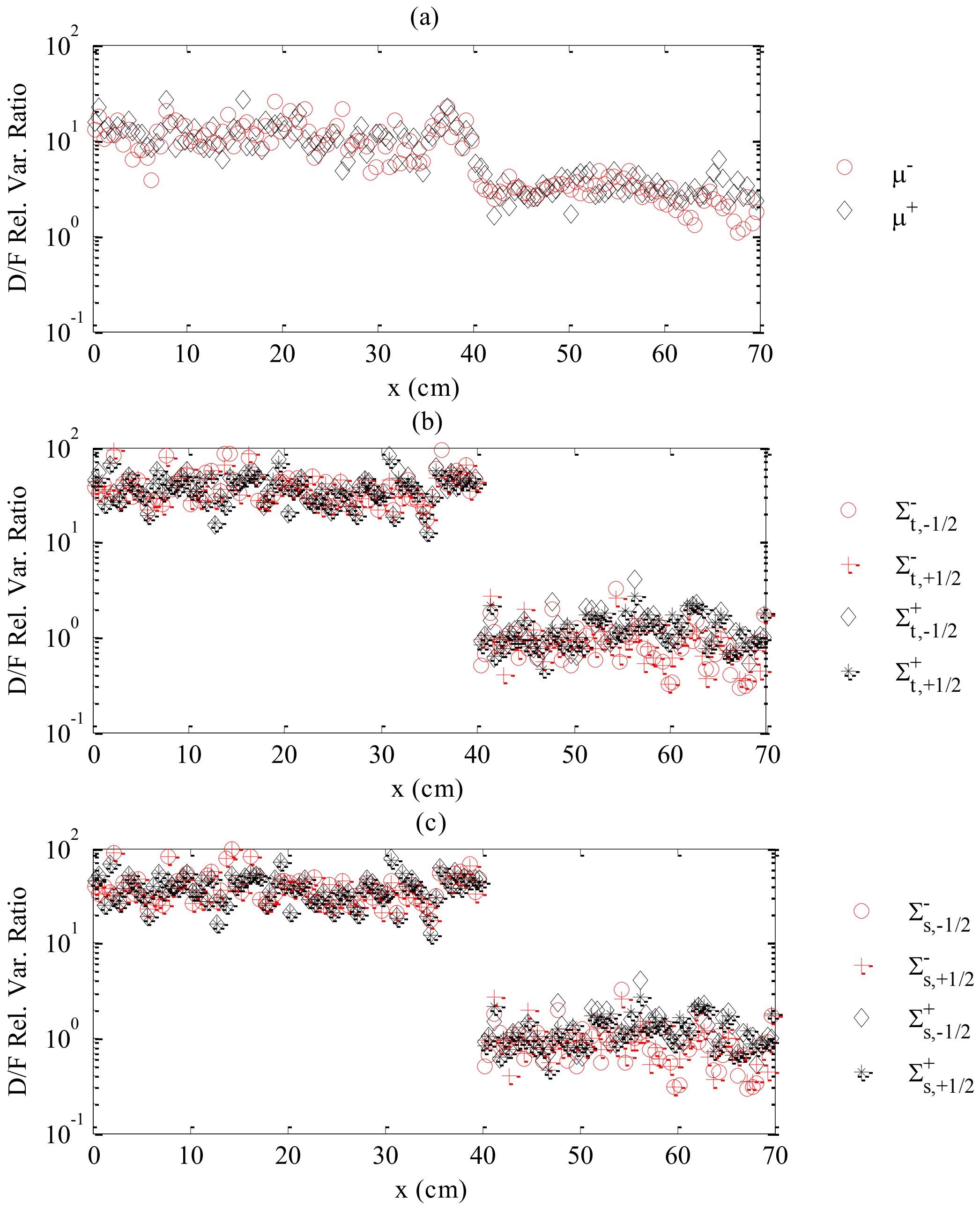

Figure 4.7 Summary of functional variances for Core-Reflector Problem #1.

Figure 4.7 shows that the variance of the standard Monte Carlo solution is generally larger than the variance of the nonlinear functionals. However, the factor of improvement is spatially-dependent and different for each functional. In particular, the existence of strong energy resonances introduces significant variance into the functionals.

4.4.2 Core-Reflector Problem #2

To confirm that the increased functional variances in the reflector are due to resonances in the reflector cross sections, the variance tests were repeated on a modified test problem, Core-Reflector Problem #2. The geometry and material parameters are identical to that of Problem #1, except the *reflector* scattering and absorption resonances have been removed to suppress the cross sections to standard linear or $\frac{1}{v}$ behavior, respectively. The scattering cross sections for Problems #1 and #2 are plotted in Figure 4.8. (In the reflector, scattering dominates, and the absorption cross sections are small in magnitude. We consider only the scattering cross section here.)

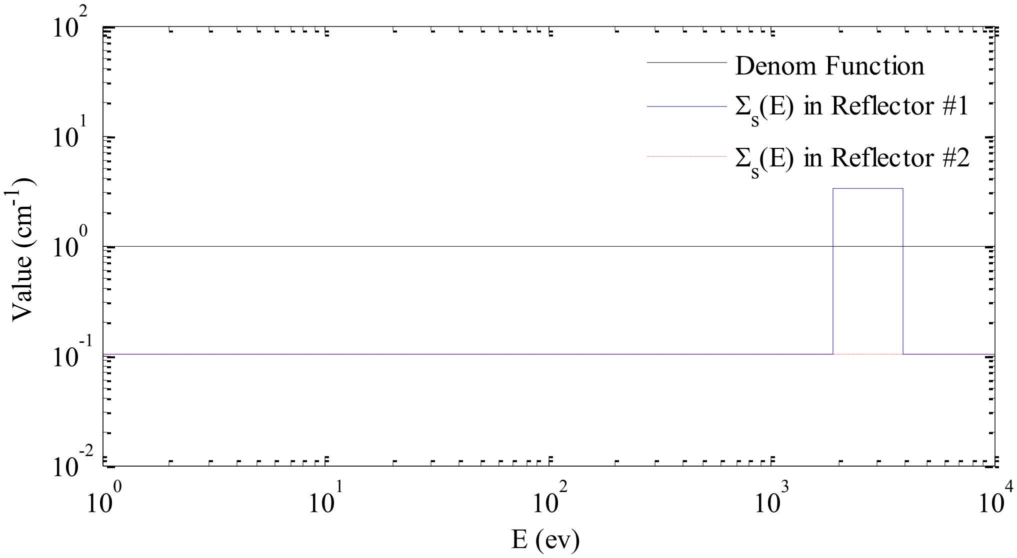

Figure 4.8 Scattering cross sections for Problems #1 and #2.

We now compare the $\Sigma^{\pm}_{s,j,k}$ functional definition for Core-Reflector Problem #1 and #2. The numerator is $\frac{1}{h_j}\int_{x_{j-1/2}}^{x_{j+1/2}}\int_0^{\infty}\int_0^{\pm 1} f_{j+k}(x)\Sigma_s(x,E)\psi\left(x,\mu,E\right)d\mu dEdx,$ where $\Sigma_s(x,E)$ is highly peaked in Problem #1 and constant in Problem #2. The denominator is $\frac{1}{h_j}\int_{x_{j-1/2}}^{x_{j+1/2}}\int_0^{\infty}\int_0^{\pm 1} r(x,E)\psi\left(x,\mu,E\right)d\mu dEdx,$ where the constant function $r(x,E)=1$ was chosen to obtain the scalar flux. Since the numerator function $\Sigma_s(x,E)$ and denominator function $r(x,E)$ for Problem #2 both behave like a constant, the numerator and denominator for Problem #2 are well-correlated. In contrast, the resonance in $\Sigma_s(E)$ for Problem #1 creates detail in energy that is not similar to the denominator function (a constant). We therefore predict that the numerator and denominator integrals for Problem #2 will be better correlated than the numerator and denominator integrals for Problem #1. Consequently, the Problem #2 reflector functionals should have lower variance than the Problem #1 reflector functionals. Figure 4.9 confirms that the reflector functional variances are much lower for Problem #2 than for Problem #1. Therefore, the reflector resonances in Problem #1 caused the high variance behavior observed in Figures 4.3 through 4.6.

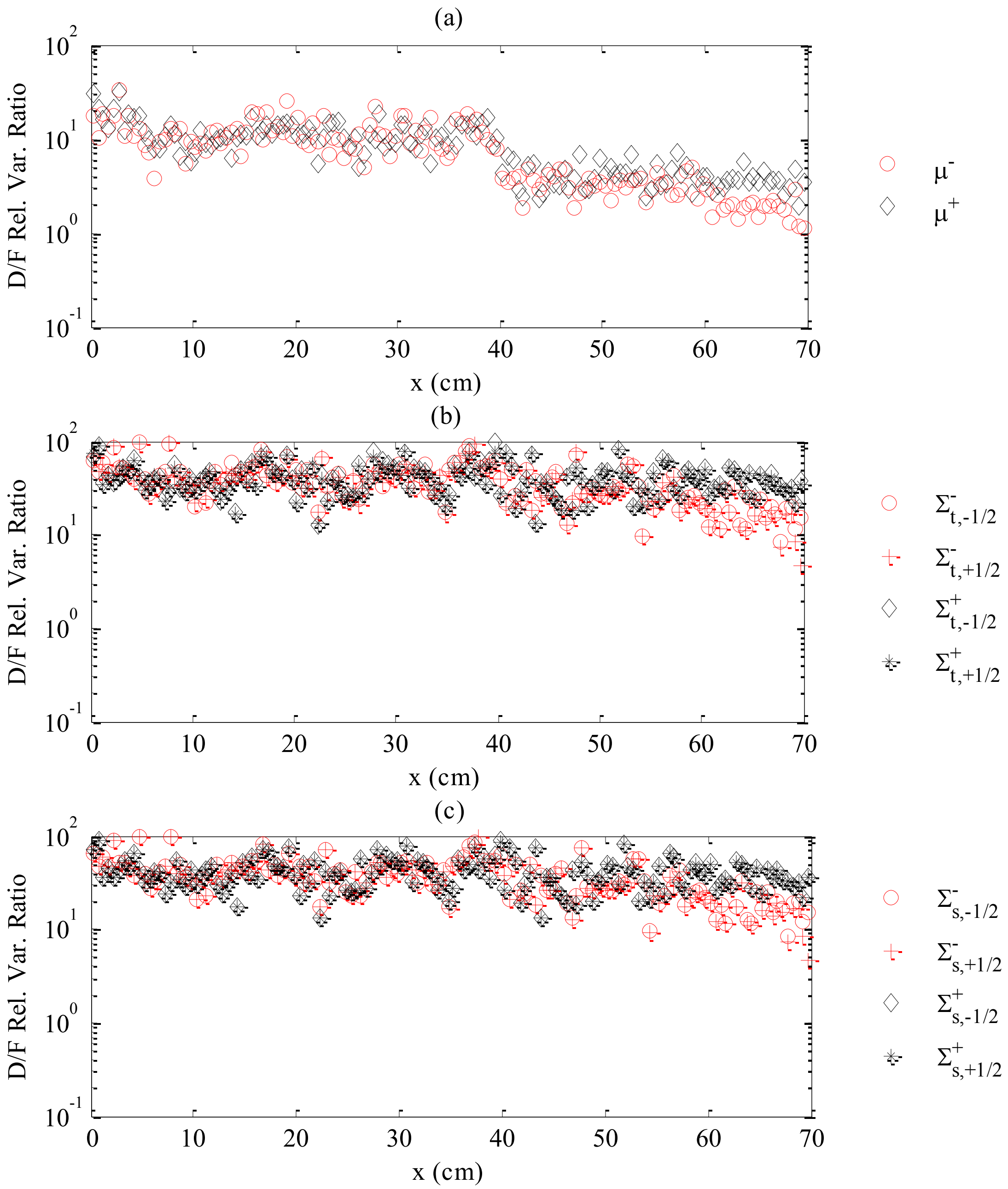

Figure 4.9 Summary of functional variance for Core-Reflector Problem #2.

4.4.3 Conclusions Regarding Functional Variance

We have shown that the H-MC-S_2X nonlinear functionals can be estimated with less variance than direct Monte Carlo estimate of the scalar flux (for equivalent computational time). However, the observed variance "reduction" is depends on several factors. The $\mu_j^{\pm}$ functionals appear inherently more "noisy" than the cross section functionals – they have between 10% to 50% as much variance as the Monte Carlo solution for both Core-Reflector Problems. The cross section functionals are estimated with 1% of the Monte Carlo variance when resonances are not present, but up to 100% (or more) of the Monte Carlo variance when resonances are present. Overall, the variance of the nonlinear functionals in almost always less than or equal to the variance of the standard Monte Carlo solution, and the variances are smaller when there are no resonance cross sections. These numerical results support our hypothesis that nonlinear functionals can be estimated more accurately, and with less variance, than direct Monte Carlo estimates of the solution.

The variances of the functionals are problem-dependent (and space-dependent, within a problem), and it is unclear how the low-order equations will propagate the observed statistical errors into the final solution. The next section, we discuss the sensitivity of the low-order equations to statistical errors in the functionals by comparing the variance of the final H-MC-S_2X solution to standard Monte Carlo.

4.5 Sensitivity of the H-MC-S_2X Equations to Functional Statistical Errors

4.5.1 Core-Reflector Problem #1

The relative variances of the H-MC-S_2X and standard Monte Carlo estimates of the scalar flux for Core-Reflector Problem #1 are plotted in the following figures.

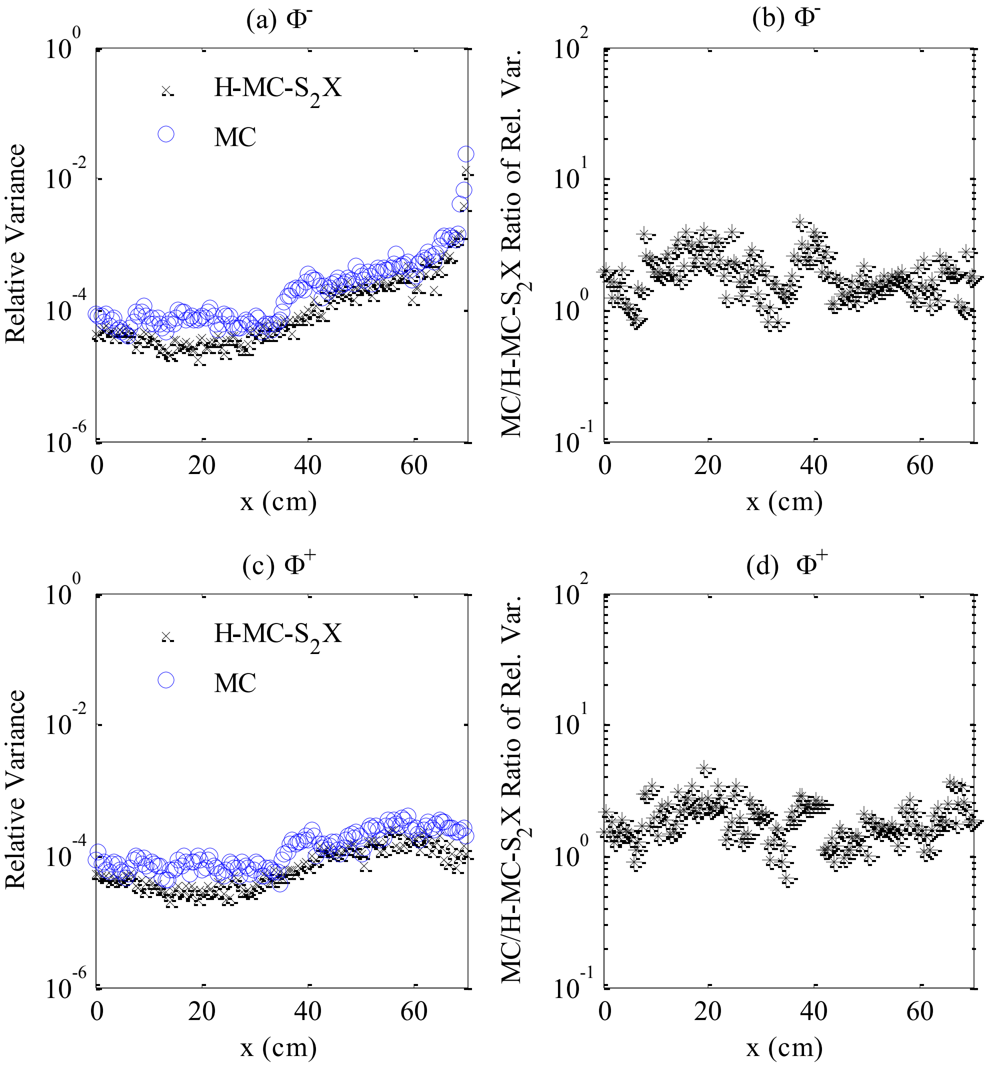

Figure 4.10 Relative variance of the left and right angularly-integrated the scalar flux for Core-Reflector Problem #1.

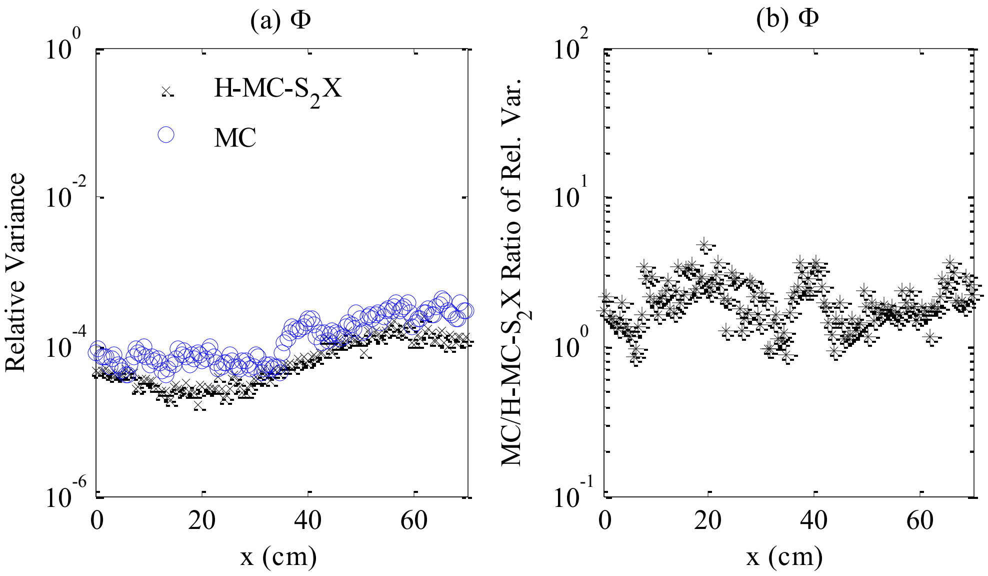

Figure 4.11 Relative variance of the solution scalar flux for Core Reflector Problem #1.

The relative variance of the H-MC-S_2X scalar flux was generally about 30-50% that of the Monte Carlo scalar flux. This ratio indicates that the H-MC-S_2X result *does* have lower variance than standard Monte Carlo. This factor of improvement is reasonable considering the high variance functionals in the reflector region. In order to see whether these high variance functionals are a significant source of error in the final solution, we examine the solution for Core-Reflector Problem #2 to see whether H-MC-S_2X performs significantly better when the cross section functionals have less statistical noise.

4.5.2 Core-Reflector Problem #2

The relative variances of the H-MC-S_2X and standard Monte Carlo estimates of the scalar flux for Core-Reflector Problem #2 are plotted in Figure 4.12.

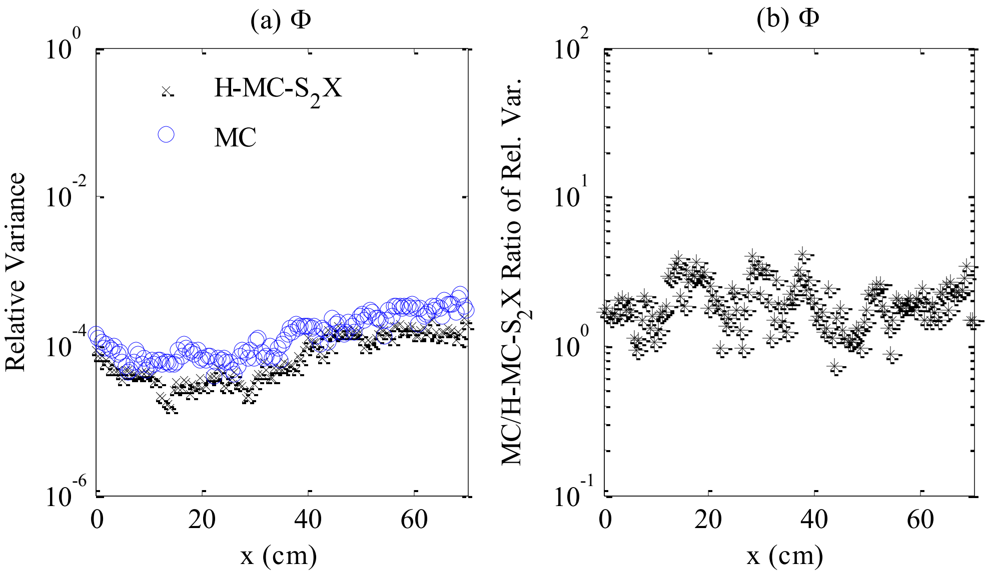

Figure 4.12 Relative variance of the solution scalar flux for Core Reflector Problem #2.

Comparing Figure 4.11 and Figure 4.12, we see that the variance in the H-MC-S_2X solution again has variance between 30-50% that of standard Monte Carlo, despite the improvement in the estimation of the cross section functionals in Problem #2. This result implies that the large statistical errors in the reflector cross section functionals are not the primary source of error in the calculation. We perform a more detailed analysis in the following section.

4.5.3 Functional Variance vs. Solution Variance

So far, we have plotted the *spatial distribution* of variance of the H-MC-S_2X functionals, H-MC-S_2X scalar flux, and Monte Carlo scalar flux for the two Core-Reflector Problems. For each quantity (i.e., Monte Carlo scalar flux, etc.), we now sum the relative variances over all spatial cells to obtain a single value (*the sum of relative variance, or SRV*). The SRV of each functional is intended to represent the overall variance of this functional across all spatial regions. Since all spatial points contribute equally to the sum, high-variance cross section functionals in any particular spatial region significantly increase the SRV. For example, in Problem #1, the cross sections functionals have low variance in the core, but high variance in the reflector. The SRVs of the cross section functionals are therefore much higher in Problem #1 than in Problem #2.

These "sum of relative variance" quantities are not very meaningful by themselves, but we can use them to compare two quantities. The *fractional computing time* of method *m*,

$$f^{(m)} \approx \frac{\text{SRV}^{(m)}}{\text{SRV}^{(MC)}}, \tag{4.18}$$

measures the fraction of computing time required to obtain a certain error compared to standard Monte Carlo.

Quantity	$f^{(\text{H-MC-S}_2\text{X})}$ **Problem #1**	$f^{(\text{H-MC-S}_2\text{X})}$ **Problem #2**
μ_j^- (MU-)	0.49	0.54
μ_j^+ (MU+)	0.25	0.21
$\Sigma^-_{t,j,-\frac{1}{2}}$ (SIGT--)	1.02	0.05
$\Sigma^-_{t,j,+\frac{1}{2}}$ (SIGT-+)	1.06	0.10
$\Sigma^+_{t,j,-\frac{1}{2}}$ (SIGT+-)	0.61	0.03
$\Sigma^+_{t,j,+\frac{1}{2}}$ (SIGT++)	0.61	0.03
$\Sigma^-_{s,j,-\frac{1}{2}}$ (SIGS--)	1.02	0.05
$\Sigma^-_{s,j,+\frac{1}{2}}$ (SIGS-+)	1.06	0.10
$\Sigma^+_{s,j,-\frac{1}{2}}$ (SIGS+-)	0.61	0.03
$\Sigma^+_{s,j,+\frac{1}{2}}$ (SIGS++)	0.61	0.03

Table 4.2 Functional fractional computing times for Core Reflector Problems #1 and #2.

Quantity	$f^{(\text{H-MC-S}_2\text{X})}$ **Problem #1**	$f^{(\text{H-MC-S}_2\text{X})}$ **Problem #2**
ϕ_j^- (PHI-)	0.58	0.65
ϕ_j^+ (PHI+)	0.57	0.59
ϕ_j (PHI)	0.52	0.54

Table 4.3 Solution fractional computing times for Core Reflector Problems #1 and #2.

We make several conclusions from the fractional computing times in the previous two tables. First, the $\Sigma^{\pm}_{s,j,k}$ and $\Sigma^{\pm}_{t,j,k}$ fractional computing times were significantly lower in Problem #2 due to the removed reflector cross section resonances (previously discussed). Second, functionals averaged over *negative* directions have consistently higher variance than functionals averaged over positive directions. This is due to poor sampling of negative directions in the reflector. In Problem #1, the overall fractional computing time for the cross section functionals in negative directions was *equal or greater than* standard Monte Carlo. We conclude that the correlation in the numerator and denominator of these functionals is small, and that poor sampling in the numerator magnified statistical errors.

Finally, the $\mu^{\pm}_{j}$ functionals appear inherently noisier than the cross section functionals: they have nearly 10 times as much variance as the cross section functionals in Problem #2. It is likely that the stronger angular dependence of the flux in the reflector and poor sampling of neutrons travelling in negative directions lowered the fractional computing time for this quantity.

It is not surprising that the fractional computing time for the scalar flux solution is only 0.52 for Problem #1. [All the functional fractional computing times are close to, or higher than, this value.] However, for Problem #2, the fractional computing time is 0.54 despite the *much* lower fractional computing times for the cross section functionals. The high variance of the $\mu^{\pm}_{j}$ functionals appears to dominate the solution variance in these core-reflector problems.

4.6 Application of the Central Limit Theorem

We have shown that the relative variance of the H-MC-S$_2$X solution is comparable to the relative variance of the "highest variance" nonlinear functionals. In this section, we examine how the variance of the H-MC-S$_2$X method behaves as the number of histories changes. The H-MC-S$_2$X method is nonlinear, so it is may not necessarily behave according to the Central Limit Theorem (CLT). Given a distribution with mean α and variance σ^2, the CLT states that the sampling distribution of the mean approaches a normal distribution with mean α and variance $\frac{\sigma^2}{N}$, as N (the number histories) increases. Sets of 25 independent simulations were generated for Core-Reflector Problem #1, with different N, to see whether the variance of the H-MC-S_2X solution obeys the CLT (like standard Monte Carlo).

N	$SRV^{(MC)}$	$SRV^{(\text{H-MC-S}_2\text{X})}$	$f^{(\text{H-MC-S}_2\text{X})}$
10,000	1.15e-01	4.70e-02	0.41
50,000	2.10e-02	1.10e-02	0.52
100,000	9.70e-03	5.22e-03	0.54
200,000	5.92e-03	2.90e-03	0.49
400,000	2.96e-03	1.44e-03	0.49

Table 4.4 Sum of relative variance and fractional computing ratio as a function of number of histories.

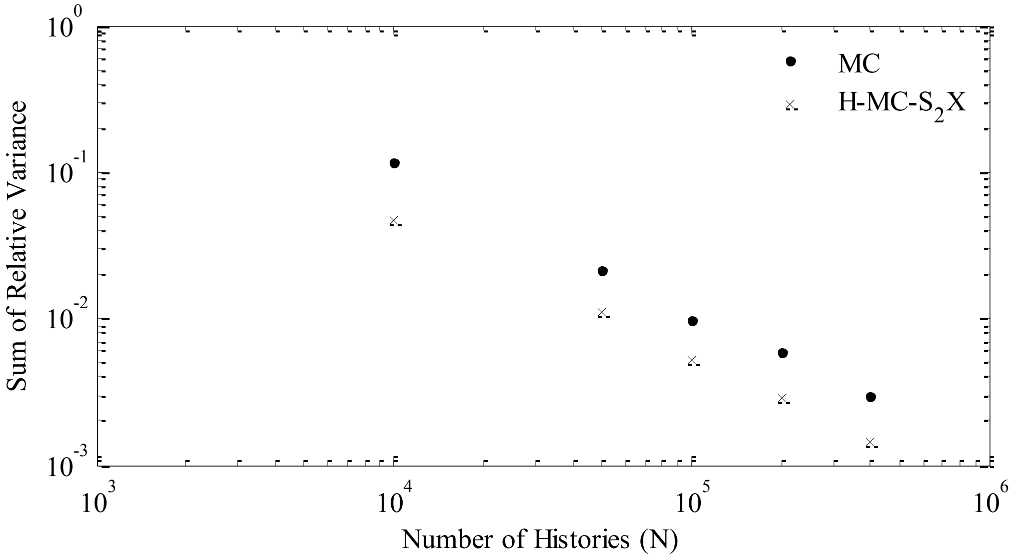

Figure 4.13 Linearity of variance with number of histories for MC and H-MC-S_2X.

Although H-MC-S_2X is a nonlinear method, its variance decreases linearly on the log-log plot in Figure 4.13. Therefore, like standard Monte Carlo, the H-MC-S_2X solution variance is inversely proportional to the number of histories and obeys the CLT.

The fractional computing time was approximately constant (0.50) for all histories, meaning that the H-MC-S_2X method requires 50% of the time used by standard Monte Carlo to achieve the same error.

4.7 Bias in the H-MC-S_2X Solution

We showed in Chapter 3 that the H-MC-S_2X solution is accurate when the number of histories is large. We now examine the accuracy of the method when the number of particles is small: the nonlinear character of the method makes it unclear whether errors in individual simulations cancel out as the number of simulations becomes large. We averaged 100 independent simulations of Core-Reflector Problem #1 for N=100 and N=1,000 histories.

When the number of histories was extremely low (N=100), there were no particle tracks in several tallies, and the nonlinear functionals could not be estimated at all. The H-MC-S_2X method could not be performed in this case. For N=1000, there were sufficient particle tracks to estimate the nonlinear functionals, and the H-MC-S_2X scalar flux was averaged over the 100 simulations and plotted in Figure 4.14.

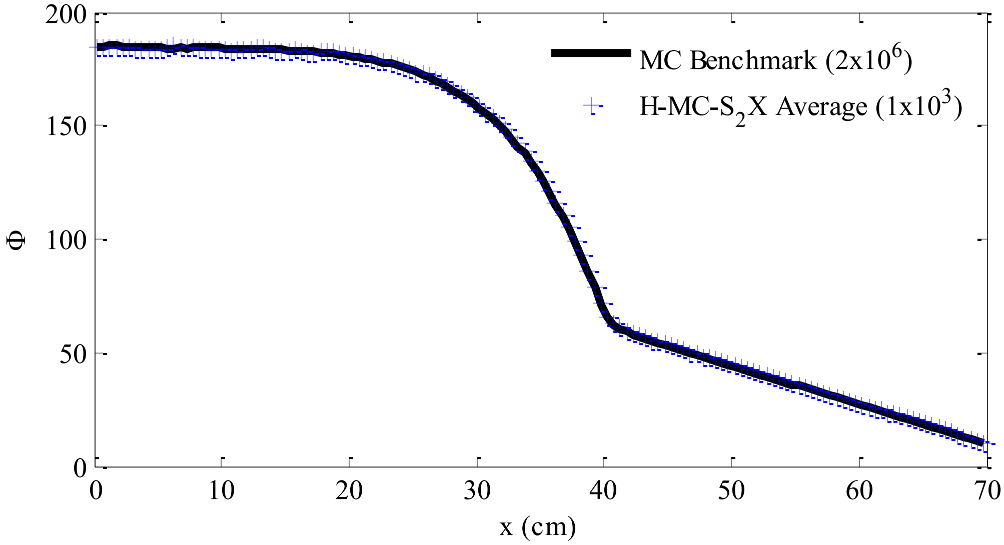

Figure 4.14 Average scalar flux over 100 H-MC-S_2X simulations with small number of histories.

The average compares well to the benchmark Monte Carlo solution. Therefore, no measurable bias was observed in the H-MC-S_2X method, even when a small number of histories is used. However, sufficiently many histories must be simulated so that the tallies in each nonlinear functional can be estimated.

4.8 Sensitivity of the H-MC-S_2X Equations to the Scattering Ratio

We now consider several monoenergetic fixed source problems. These problems are homogenous 20 cm slabs with a reflecting boundary on the left and a vacuum boundary on the right (for a total width of 40 mean free paths). The cross sections are constant in energy, and the scattering ratio, $c = \frac{\Sigma_s}{\Sigma_t}$, varies. A monoenergetic, isotropic source is *uniformly distributed* throughout the system.

Location [cm]	Σ_t [cm^{-1}]	Σ_s [cm^{-1}]
$0 < x < 20$	1.0	c

Table 4.5 Scattering ratio problem properties.

Number of Independent Simulations (K)	Number of Histories per Simulation (N)	Spatial Grid [cm]
25	N	0.5

Table 4.6 Monte Carlo numerical properties for scattering ratio problem.

The parameters c and N were varied to generate several sets of twenty-five independent simulations for the scalar flux. The sample variance of each set was computed in each spatial cell and summed over the system. The purpose of these calculations was to estimate the sensitivity of the H-MC-S_2X equations to the scattering ratio.

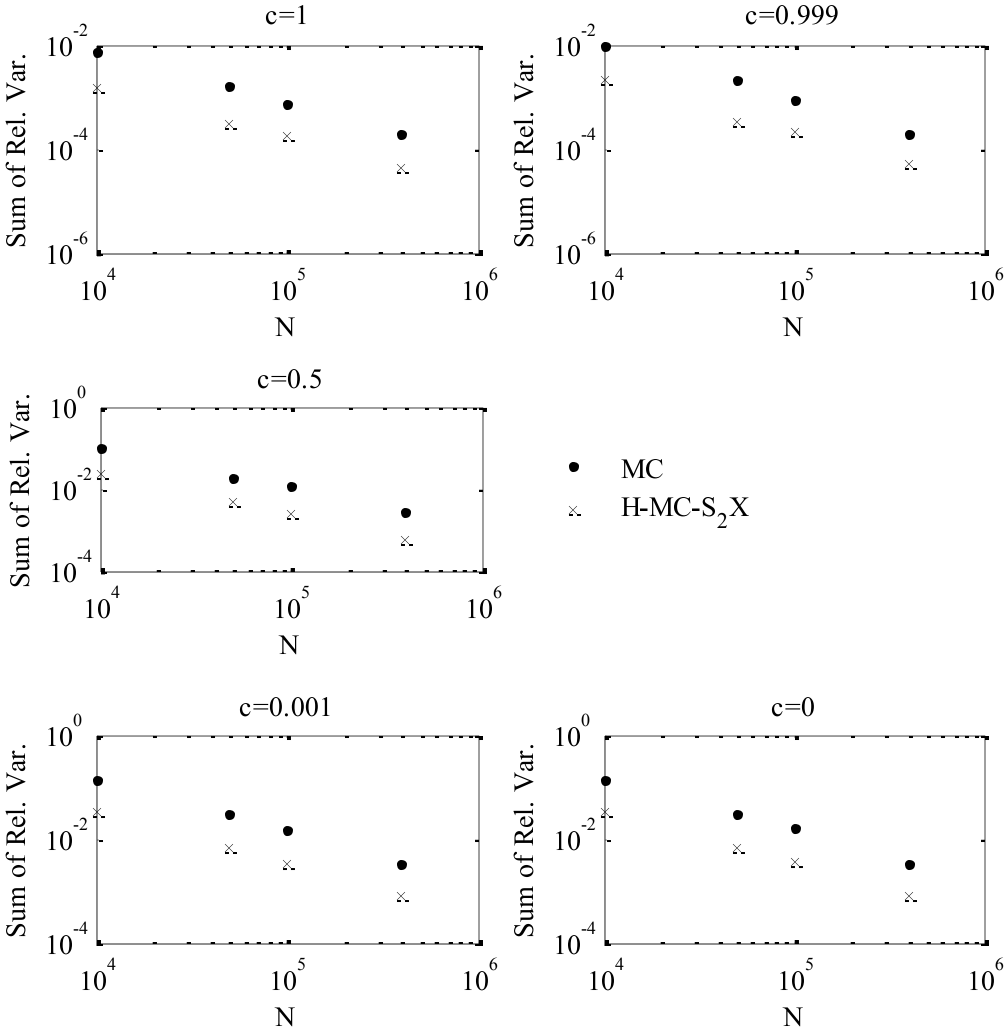

Figure 4.15. Linear relationship of variance with histories for various scattering ratios.

Scattering Ratio	$f^{(\text{H-MC-S}_2\text{X})}$
c = 0.000	0.22
c = 0.001	0.23
c = 0.500	0.22
c = 0.999	0.23
c = 1.000	0.25

Table 4.7 Fractional computing times for various scattering ratios (data taken from N=100,000).

Figure 4.15 confirms that the variance of the H-MC-S_2X solution is inversely proportional to the number of histories, like standard Monte Carlo. For all scattering ratios tested, the H-MC-S_2X solution had less variance than the standard MC solution. The fractional computing time for H-MC-S_2X compared to standard Monte Carlo was approximately 0.23 for each scattering ratio. This is a *significant* improvement over the ~0.50 fractional computing time for the core-reflector problems.

Before discussing this in more detail, we make a note regarding the low-order equations in the H-MC-S_2X method. These equations are solved using transport “sweeps” and source iterations as in conventional S_N. We observed that the number of source iterations required in the low-order H-MC-S_2X equations is strongly dependent on the scattering ratio. The average number of iterations required for high scattering ratios was approximately 9000 $\left(c=1\right)$ and 6050 $\left(c=0.999\right)$. For $c \leq 0.5$, the average number of iterations was 34 or less. These results are entirely consistent with the behavior conventional S_N methods for high scattering ratios.

We now return to our discussion of the monoenergetic fixed source problem. We examine the specific monoenergetic problem with $c=0.999$ from above, and we call this “Problem #3”. The solutions of this problem are compared with the Core-Reflector Problems in Table 4.8.

Quantity	$f^{(\text{H-MC-S}_2\text{X})}$ **Core-Reflector Problem #1**	$f^{(\text{H-MC-S}_2\text{X})}$ **Core-Reflector Problem #2**	$f^{(\text{H-MC-S}_2\text{X})}$ **Problem #3 c=0.999**
ϕ_j^- (PHI-)	0.58	0.65	0.22
ϕ_j^+ (PHI+)	0.57	0.59	0.26
ϕ_j (PHI)	0.52	0.54	0.23

Table 4.8 Solution fractional computing times for a variety of problems.

We see a *significant* improvement in the fractional computing time required for Problem #3: the core-reflector problems requires approximately 53% of Monte Carlo computing time, but Problem #3 requires only 23% of Monte Carlo computing time.

This increase in efficiency over the core-reflector problems could be due to (a) the absence of energy-dependence, (b) diffusive nature of the flux, or (c) better sampling in all phase space due to the uniform fixed source. We compare the fractional computing times for the *functionals* in Table 4.9.

Quantity	$f^{(\text{H-MC-S}_2\text{X})}$ **Core-Reflector Problem #1**	$f^{(\text{H-MC-S}_2\text{X})}$ **Core-Reflector Problem #2**	$f^{(\text{H-MC-S}_2\text{X})}$ **Problem #3 c=0.999**
μ_j^- (MU-)	0.49	0.54	0.07
μ_j^+ (MU+)	0.25	0.21	0.06
$\Sigma_{t,j,-\frac{1}{2}}^-$ (SIGT--)	1.02	0.05	0.02
$\Sigma_{t,j,+\frac{1}{2}}^-$ (SIGT-+)	1.06	0.10	0.03
$\Sigma_{t,j,-\frac{1}{2}}^+$ (SIGT+-)	0.61	0.03	0.01
$\Sigma_{t,j,+\frac{1}{2}}^+$ (SIGT++)	0.61	0.03	0.01
$\Sigma_{s,j,-\frac{1}{2}}^-$ (SIGS--)	1.02	0.05	0.02
$\Sigma_{s,j,+\frac{1}{2}}^-$ (SIGS-+)	1.06	0.10	0.03
$\Sigma_{s,j,-\frac{1}{2}}^+$ (SIGS+-)	0.61	0.03	0.01
$\Sigma_{s,j,+\frac{1}{2}}^+$ (SIGS++)	0.61	0.03	0.02

Table 4.9 Functional fractional computing times for a variety of problems.

These results suggest the following effects of energy and angular dependence on the performance of the H-MC-S_2X method. Going from “continuous energy with resonances” to “continuous energy without resonances” improves the cross section functionals by an order of magnitude. Going from “continuous energy without resonances” to “monoenergetic” problems does not improve the cross sections functionals significantly. The cross section functionals are estimated with a given error using only 1-10% of Monte Carlo computing time when no resonances are present, but the presence of resonances increases this fraction to 100%.

The angular dependence of the flux is also simpler in Problem #3. In Core-Reflector Problems #1 and #2, the flux is strongly anisotropic and not well-sampled in negative directions in the reflectors. In Problem #3, the flux is nearly isotropic and well-sampled in all directions. In Problem #3, the simpler angular dependence of the flux and better sampling improves the estimation of the $\mu_j^{\pm}$ functionals by an order of magnitude from the core-reflector problems (7% vs 54%). This improvement in efficiency occurs because the numerator and denominator of the $\mu_j^{\pm}$ functionals are more highly correlated when the flux is not strongly peaked in a particular direction, as in Problem #3. Additionally, particles are sampled sufficiently in negative directions for Problem #3 because source particles are *isotropically, uniformly distributed* throughout the system. In Problems #1 and #2, very few source particles are sampled travelling in negative direction at the outer reflector edge.

On a final note, the H-MC-S_2X functionals in Problem #3 were estimated with 1%-7% of the variance in the standard Monte Carlo solution. The H-MC-S_2X solution has 23% of the variance of the standard Monte Carlo solution. This is evidence that even small statistical errors in the functionals become magnified during solution of the low-order equations. The order of magnification appears to be problem-dependent.

4.9 Conclusions

In this chapter, we provided a theoretical justification for using Monte Carlo to estimate nonlinear functionals rather than standard linear functionals. In order for this technique to be advantageous, the nonlinear functionals should be defined so that the numerator and denominator operators are as similar as possible. Also, identical particle histories must be used to evaluate the numerator and denominator of each functional. When the numerators and denominators are defined and estimated in this way, the variance of the resulting nonlinear functional is less than the variance of the individual numerator and denominator. This theory applies to the functionals defined in the H-MC-S_2 and H-MC-S_2X method developed in Chapters 2 and 3.

The accuracy and variance of the H-MC-S_2X method depends on the number of neutron histories, correlation of random variables in the nonlinear functional definitions, and sensitivity of the low-order equations to statistical errors in the functionals. Numerical results for a variety of test problems confirmed our hypothesis that Monte Carlo estimates of nonlinear functionals are more accurate and have less variance than history-equivalent estimates of the linear quantities in the numerator and denominator of these functionals. The variance of the H-MC-S_2X solution follows the Central Limit Theorem, i.e., is inversely proportional to the number of histories. No significant dependence on the scattering ratio was observed besides the number of deterministic iterations required. Overall, the findings in this chapter can be summarized as follows:

1) The H-MC-S_2X nonlinear functionals have less variance than their corresponding numerator and denominator (standard Monte Carlo tallies).
2) The H-MC-S_2X final solution has less variance and is more accurate than the corresponding standard Monte Carlo solution, but the efficiency of the H-MC-S_2X method is problem dependent.

Our results show that the H-MC- S_2X method is always more efficient than standard Monte Carlo, but the performance is problem-dependent. The H-MC-S_2X method fractional computing time compared to standard Monte Carlo ranged from 0.20 to 0.54 for our test problems. The performance is *optimum* when particles are well-sampled in all areas of phase space, conditions are diffusive, and cross section energy dependence is simple. As these conditions are relaxed, the efficiency of the method decreases. We make the following suggestions on how the efficiency might be improved "harder" problems.

To address the issues of complex energy dependence, the H-MC-S_2X method could be modified so that the low-order equations resemble multigroup equations. Strategically partitioning energy groups over resonances would greatly increase the correlation of the functional numerator and denominators in the cross section functionals. However, this procedure would incur more computational expense: more tallies would be required in Monte Carlo, and solution of the algebraic system of multigroup-like equations would be more expensive.

A similar modification would address the issues of more complex angular dependence: the number of direction "groups" could be increased so that the low-order equations resemble higher-order S_N equations. Doing this should decrease the variance in the $\mu_j^{\pm}$ functionals, but would again increase the expense of solving the algebraic system of equations.

Finally, weight windows or other biasing techniques could be used to encourage particles to “travel” in regions of low particle density. These techniques are traditionally used to reduce the variance in regions of phase space that are not well-sampled in analog Monte Carlo.

Therefore, the H-MC-S_2X method could be modified in several ways to improve its performance in “difficult” fixed source problems. Additionally, its performance on criticality problems should be tested. However, in this thesis, we have shown that the performance of the H-MC-S_2X method is promising on a subset of test problems.

We now turn our attention towards a fundamentally different nonlinear functional method recently proposed by M.J. Lee, K. Smith, H.G. Joo and D.J. Lee: CMFD-Accelerated Monte Carlo [2]. This method has been used for the acceleration of Monte Carlo source convergence in high dominance ratio criticality problems. In subsequent chapters, we develop generalized hybrid Monte Carlo-CMFD methods using nonlinear functionals and demonstrate the efficiency of these methods on “difficult” criticality problems.

4.10 References

[1] A. Papoulis and S.U. Pillai, *Probability, Random Variables and Stochastic Processes*, McGraw-Hill, New York (2002).

[2] M.J. Lee, H.G. Joo, D. Lee, and K. Smith, “Investigation of CMFD Accelerated Monte Carlo Eigenvalue Calculation with Simplified Low Dimensional Multigroup Formulation,” *Proc. 2010 International Conference on the Physics of Reactors*, May 9-14, 2010, Pittsburgh, PA, CD-ROM, American Nuclear Society (2010).

Chapter 5

Generalized Hybrid Monte Carlo – CMFD Methods

5.1 Introduction

In the previous three chapters, we derived hybrid methods whose low-order equations resemble the discrete ordinates equations, and we showed that the nonlinear functionals in these low-order equations can be computed with Monte Carlo more accurately, and with less variance, than standard linear quantities. In this chapter, we present several techniques that utilize stochastically-computed nonlinear functionals to couple the Coarse Mesh Finite Difference (CMFD) method to Monte Carlo. These hybrid techniques use diffusion-like rather than discrete ordinates-like equations to improve the Monte Carlo solution. We begin by reviewing the conventional CMFD method and the CMFD-Accelerated Monte Carlo method. We then demonstrate that this latter method can be improved by utilizing higher order space-angle moments of the neutron transport equation. Three new techniques are presented in this chapter; numerical results comparing these techniques with standard Monte Carlo and CMFD-Accelerated Monte Carlo are presented in subsequent chapters.

5.2 The Coarse Mesh Finite Difference Method

The Coarse Mesh Finite Difference Method is a well-known iterative method proposed by K. Smith [18] for deterministically solving the Boltzmann transport equation. Here we review the use of conventional CMFD to solve a one-group, planar geometry eigenvalue problem. Scattering is assumed to be isotropic. The one-group transport equation and boundary conditions are:

$$\mu \frac{\partial}{\partial x}\psi(x,\mu)+\Sigma_t(x)\psi(x,\mu)=\frac{1}{2}\left[\Sigma_s(x)+\frac{\nu\Sigma_f(x)}{k_{eff}}\right]\int_{-1}^{1}\psi(x,\mu)d\mu', \tag{5.1}$$
$$-1\le\mu\le1,\qquad 0\le x\le X,$$

$$\psi(0,\mu)=\psi^L(\mu),\qquad 0<\mu\le1, \tag{5.2}$$

$$\psi(X,\mu)=\psi^R(\mu),\qquad -1\le\mu<0. \tag{5.3}$$

5.2.1 The Neutron Balance Equation

To derive the CMFD equations, we define the angular flux moments

$$\phi_n(x)=\int_{-1}^{1}P_n(\mu)\psi(x,\mu)d\mu,\qquad n\ge0, \tag{5.4}$$

where $P_n(\mu)$ is the n^{th} Legendre polynomial. We operate on Eq. (5.1) by $\int_{-1}^{1}(\cdot)\,d\mu$ to obtain the following identity:

$$\frac{d}{dx}\phi_1(x)+\Sigma_a(x)\phi_0(x)=\frac{\nu\Sigma_f(x)}{k_{eff}}\phi_0(x), \tag{5.5}$$

where $\Sigma_a(x)=\Sigma_t(x)-\Sigma_s(x)$. Next, we introduce a “coarse” spatial grid $0=x_{1/2}<x_{3/2}<\cdots<x_{k+1/2}<\cdots<x_{K+1/2}=X$ on the system. The k^{th} spatial cell is defined on the interval $x_{k-1/2}<x<x_{k+1/2}$, with width $h_k=x_{k+1/2}-x_{k-1/2}$. Cross sections are permitted to vary within each coarse spatial cell. We integrate Eq. (5.5) over $x_{k-1/2}<x<x_{k+1/2}$. If we define the cell-averaged scalar fluxes, flux-weighted cross sections, and cell-edge currents by

$$\phi_{0,k}=\frac{1}{h_k}\int_{x_{k-1/2}}^{x_{k+1/2}}\phi_0(x)dx, \tag{5.6}$$

$$\Sigma_{t,k} = \frac{\int_{x_{k-1/2}}^{x_{k+1/2}} \Sigma_t(x)\phi_0(x)dx}{\int_{x_{k-1/2}}^{x_{k+1/2}} \phi_0(x)dx}, \tag{5.7}$$

$$\Sigma_{a,k} = \frac{\int_{x_{k-1/2}}^{x_{k+1/2}} \Sigma_a(x)\phi_0(x)dx}{\int_{x_{k-1/2}}^{x_{k+1/2}} \phi_0(x)dx}, \tag{5.8}$$

$$\nu\Sigma_{f,k} = \frac{\int_{x_{k-1/2}}^{x_{k+1/2}} \nu\Sigma_f(x)\phi_0(x)dx}{\int_{x_{k-1/2}}^{x_{k+1/2}} \phi_0(x)dx}, \tag{5.9}$$

$$\phi_{1,k\pm1/2} = \phi_1(x_{k\pm1/2}), \tag{5.10}$$

then we obtain, for $1 \le k \le K,$ the following neutron balance equations:

$$\phi_{1,k+1/2} - \phi_{1,k-1/2} + \Sigma_{a,k}h_k\phi_{0,k} = \frac{\nu\Sigma_{f,k}h_k}{k_{eff}}\phi_{0,k}. \tag{5.11}$$

5.2.2 Transport-Corrected Fick's Law

The principle component of CMFD is the introduction of an *exact* relationship between the cell-edged currents and the cell-averaged scalar fluxes in the form of a "transport-corrected" Fick's Law:

$$\phi_{1,k+1/2} = -\tilde{D}_{k+1/2}\left(\phi_{0,k+1} - \phi_{0,k}\right) + \hat{D}_{k+1/2}\left(\phi_{0,k+1} + \phi_{0,k}\right). \tag{5.12}$$

Keeping the notation consistent with Fick's Law and diffusion theory, $\tilde{D}_{k+1/2}$ is a dimensionless quantity interpreted as the diffusion coefficient of the "staggered cell" defined between the centers of cell k and cell $k+1$, divided by the width of the staggered cell:

$$\tilde{D}_{k+1/2} = \frac{h_{k+1}+h_k}{3\left(\Sigma_{t,k+1}h_{k+1}+\Sigma_{t,k}h_k\right)} \cdot \frac{2}{h_{k+1}+h_k} = \frac{2}{3\left(\Sigma_{t,k+1}h_{k+1}+\Sigma_{t,k}h_k\right)}. \tag{5.13}$$

The parameter $\hat{D}_{k+1/2}$ is a dimensionless correction factor that accounts for the part of the transport solution that does not obey Fick's Law. For diffusive problems (where Fick's Law holds), $\hat{D}_{k+1/2}$ is small in magnitude. Eq. (5.14) defines the correction factor:

$$\hat{D}_{k+1/2} = \frac{\phi_{1,k+1/2} + \tilde{D}_{k+1/2}\left(\phi_{0,k+1} - \phi_{0,k}\right)}{\phi_{0,k+1} + \phi_{0,k}}. \tag{5.14}$$

[We note that Eq. (5.13) makes the interpretation of $\tilde{D}_{k+1/2}$ in the CMFD method consistent with the interpretation of the cell-averaged diffusion coefficient divided by cell width in Fick's Law. However, it is not necessary to define $\tilde{D}_{k+1/2}$ this way. The parameter $\tilde{D}_{k+1/2}$ is free; any definition of $\tilde{D}_{k+1/2}$ may be chosen.]

Eq. (5.12) thus relates the cell-edge currents $\phi_{1,k+1/2}$ $(1 < k < K-1)$ to the cell-average scalar fluxes $\phi_{0,k}$ and $\phi_{0,k+1}$ in Eq. (5.12). Something slightly different must be done to relate the boundary currents $\phi_{1,1/2}$ and $\phi_{1,K+1/2}$ to their neighboring cell-average scalar fluxes.

5.2.3 Boundary Conditions

To obtain a relationship between $\phi_{1,1/2}$ and $\phi_{0,1/2}$, we operate on Eq. (5.2) by $2\int_0^1 \mu(\cdot)\,d\mu$, then manipulate one side of the resulting equation to extend the integration limits:

$$\begin{aligned}2J^{+}(0) = 2\int_0^1 \mu\psi^{L}(\mu)\,d\mu = 2\int_0^1 \mu\psi(0,\mu)\,d\mu &\\ &= \int_{-1}^{1}\mu\psi(0,\mu)\,d\mu + \int_{-1}^{1}|\mu|\psi(0,\mu)\,d\mu \\ &= \int_{-1}^{1}\mu\psi(0,\mu)\,d\mu + \left[\frac{\int_{-1}^{1}|\mu|\psi(0,\mu)\,d\mu}{\frac{1}{h_1}\int_{x_{1/2}}^{x_{3/2}}\int_{-1}^{1}\psi(x,\mu)\,d\mu dx}\right]\phi_{0,1} \\ &= \phi_{1,1/2} + B_1\phi_{0,1}.\end{aligned}$$

We therefore relate $\phi_{1,1/2}$ and $\phi_{0,1}$ by

$$\phi_{1,1/2} = 2J^{+}(0) - B_1\phi_{0,1}, \tag{5.15}$$

where

$$J^{+}(0) \equiv \int_0^1 \mu\psi^{L}(\mu)\,d\mu, \tag{5.16}$$

$$B_1 \equiv \frac{\int_{-1}^{1}|\mu|\psi(0,\mu)\,d\mu}{\frac{1}{h_1}\int_{x_{1/2}}^{x_{3/2}}\int_{-1}^{1}\psi(x,\mu)\,d\mu dx}. \tag{5.17}$$

To obtain a similar relationship between $\phi_{1,K+1/2}$ and $\phi_{0,K}$, we operate on Eq. (5.3) by $2\int_{-1}^{0}\mu(\cdot)\,d\mu$, and perform a similar procedure:

$$\begin{aligned}2J^{-}(X) = 2\int_{-1}^{0} \mu\psi^{R}(\mu)\,d\mu = 2\int_{-1}^{0} \mu\psi(X,\mu)\,d\mu &\\ &= \int_{-1}^{1}\mu\psi(X,\mu)\,d\mu - \int_{-1}^{1}|\mu|\psi(X,\mu)\,d\mu \\ &= \int_{-1}^{1}\mu\psi(X,\mu)\,d\mu - \left[\frac{\int_{-1}^{1}|\mu|\psi(X,\mu)\,d\mu}{\frac{1}{h_K}\int_{x_{K-1/2}}^{x_{K+1/2}}\int_{-1}^{1}\psi(X,\mu)\,d\mu dx}\right]\phi_{0,K} \\ &= \phi_{1,K+1/2} - B_K\phi_{0,K}.\end{aligned}$$

We therefore relate $\phi_{1,K+1/2}$ and $\phi_{0,K}$ by

$$\phi_{1,K+1/2} = 2J^{-}(X) + B_K \phi_{0,K}, \tag{5.18}$$

where

$$J^{-}(X) \equiv \int_{-1}^{0} \mu \psi^{R}(\mu)\, d\mu, \tag{5.19}$$

$$B_K \equiv \frac{\int_{-1}^{1} |\mu| \psi(X,\mu)\, d\mu}{\frac{1}{h_K}\int_{x_{K-1/2}}^{x_{K+1/2}} \int_{-1}^{1} \psi(X,\mu)\, d\mu dx}. \tag{5.20}$$

5.2.4 CMFD Equations

Eqs. (5.12), (5.15), and (5.18) enable us to formally eliminate the ϕ_1 terms in Eq. (5.11) and obtain equations for the scalar fluxes $\phi_{0,k}$ in terms of the yet-unknown correction factors $\hat{D}_{k+1/2}$ and nonlinear functionals B_1 and B_K. For $2 \le k \le K-1,$ we get

$$\begin{aligned} -\tilde{D}_{k+1/2}\left(\phi_{0,k+1} - \phi_{0,k}\right) + \tilde{D}_{k-1/2}\left(\phi_{0,k} - \phi_{0,k-1}\right) + \Sigma_{a,k} h_k \phi_{0,k} \\ = \frac{\nu \Sigma_{f,k} h_k}{k_{eff}} \phi_{0,k} - \hat{D}_{k+1/2}\left(\phi_{0,k+1} + \phi_{0,k}\right) + \hat{D}_{k-1/2}\left(\phi_{0,k} + \phi_{0,k-1}\right), \end{aligned} \tag{5.21}$$

and similar equations are obtained for $k=1$ and K. These equations form a linear system of equations,

$$\mathbf{A}\phi = y, \tag{5.22}$$

where $\mathbf{A}$ is a tri-diagonal matrix:

$$\begin{bmatrix} b_1 & c_1 & 0 & \cdots & 0 \\ a_2 & b_2 & c_2 & 0 & 0 \\ 0 & \ddots & \ddots & \ddots & 0 \\ \vdots & 0 & a_{K-1} & b_{K-1} & c_{K-1} \\ 0 & \cdots & 0 & a_K & b_K \end{bmatrix} \begin{bmatrix} \phi_1 \\ \vdots \\ \phi_k \\ \vdots \\ \phi_K \end{bmatrix} = \begin{bmatrix} y_1 \\ \vdots \\ y_k \\ \vdots \\ y_K \end{bmatrix}.$$

The elements of $\mathbf{A}$ are:

$$a_k = -\tilde{D}_{k-1/2} - \hat{D}_{k-1/2}, \qquad 2 \le k \le K, \tag{5.23}$$

$$b_k = \begin{cases} B_1 + \tilde{D}_{3/2} + \hat{D}_{3/2} + \Sigma_{a,1} h_1, & k = 1 \\ \tilde{D}_{k-1/2} - \hat{D}_{k-1/2} + \tilde{D}_{k+1/2} + \hat{D}_{k+1/2} + \Sigma_{a,k} h_k, & 2 \le k \le K-1 \\ B_K + \tilde{D}_{k-1/2} - \hat{D}_{K-1/2} + \Sigma_{a,K} h_K, & k = K, \end{cases} \tag{5.24}$$

$$c_k = -\tilde{D}_{k+1/2} + \hat{D}_{k+1/2}, \qquad 1 \le k \le K-1. \tag{5.25}$$

The vector y has the following elements:

$$y_k = \begin{cases} h_1 s_1 + 2J^+(0), & k = 1 \\ h_k s_k, & 2 \le k \le K-1 \\ h_K s_K - 2J^-(X), & k = K. \end{cases} \tag{5.26}$$

For fixed source problems, this matrix equation has a unique solution for $\phi_{0,k}$ because the source vector contains the known terms:

$$s_k \equiv Q_k = \frac{1}{h_k} \int_{x_{k-1/2}}^{x_{k+1/2}} Q(x)dx. \tag{5.27}$$

For criticality problems, the matrix equation is an eigenvalue problem because the source vector contains the unknown fission source:

$$s_k \equiv \frac{\nu\Sigma_{f,k}}{k_{eff}} \phi_{0,k}. \tag{5.28}$$

The normalized eigenfunction $\phi_{0,k}$ and the eigenvalue k_{eff} are solved for by iteration.

We note that all of the preceding equations were derived without approximation from Eq. (5.1)-(5.3). Thus, if the flux-weighted quantities $\Sigma_{a,k}$, $\nu\Sigma_{f,k}$, and $\hat{D}_{k+1/2}$ and the boundary functionals B_1 and B_K are known exactly, then Eq. (5.22) exactly determines the coarse-mesh scalar fluxes $\phi_{0,k}$, and the eigenvalue k_{eff}. However, $\Sigma_{a,k}$, $\nu\Sigma_{f,k}$, and

$\hat{D}_{k+1/2}$, B_1, and B_K are not known exactly: they are typically estimated by a single high-order transport sweep of Eq. (5.1) on a *fine grid*. The fine grid transport sweep generates the fine grid scalar flux and currents $\phi_{0,j}$ and $\phi_{1,j+1/2}$, which are used to collapse the parameters in Eqs. (5.6)-(5.10), (5.13)-(5.14), and B_1 and B_K. We use the subscript j to denote quantities defined on the fine grid. The number of fine cells per coarse cell is denoted by the CMFD parameter " p ", so the k^{th} coarse cell consists of fine cells $j = p(k-1)+1$ through $j = kp$.

Once $\Sigma_{a,k}$, $\nu\Sigma_{f,k}$, $\hat{D}_{k+1/2}$, $\tilde{D}_{k+1/2}$, B_1, and B_K are estimated, Eq. (5.22) is solved efficiently for an "updated" *coarse grid* solution $\phi_{0,k}$. The updated coarse grid solution $\phi_{0,k}$ can then be used to update the old fine grid solution $\phi_{0,j}$:

$$\phi_{0,j}^{updated} = \phi_{0,k} \frac{\phi_{0,j}}{\sum_{j=p(k-1)+1}^{j=pk} \phi_{0,j}}. \tag{5.29}$$

After the updating takes place, the scattering source in the high-order transport method is updated with the new fine grid scalar flux estimate, and the process is repeated until the fine grid flux converges.

CMFD is therefore an efficient way to solve detailed transport problems on a coarse mesh without incurring any extra homogenization or spatial truncation errors. In the next section, we briefly discuss how Lee, et al., adapted the CMFD method to accelerate the Monte Carlo solution of transport problems.

5.3 CMFD-Accelerated Monte Carlo (The HCMFD-I Method)

M.J. Lee, et al., proposed *CMFD-Accelerated Monte Carlo* [2][17][4], a hybrid method that uses Monte Carlo to estimate the parameters in Eqs. (5.6)-(5.10), correction factors $\hat{D}_{k+1/2}$, and boundary functionals B_1 and B_K. In this work, we refer to CMFD-Accelerated Monte Carlo as "the HCMFD-I method", in order to emphasize the similarity between this method and the HCMFD-II, -III and -IV methods proposed later in this chapter.

In HCMFD-I, the cell-edge currents and fine grid scalar fluxes, as well as the flux-weighted cross sections in Eqs. (5.7)-(5.9) are estimated in Monte Carlo using surface crossing tallies and path length estimators. The correction factor $\hat{D}_{k+1/2}$ in Eq. (5.14) is then computed from these stochastically estimated quantities. We rename the correction factor in the HCMFD-I method $\hat{D}^{(I)}_{k+1/2}$ to distinguish it from the deterministically-estimated correction factor $\hat{D}_{k+1/2}$ in Eq. (5.14):

$$\hat{D}^{(I)}_{k+1/2} = \frac{\phi_{1,k+1/2} + \tilde{D}_{k+1/2}\left(\phi_{0,k+1} - \phi_{0,k}\right)}{\phi_{0,k+1} + \phi_{0,k}}. \tag{5.30}$$

The HCMFD-I method can now be described:

1. A standard Monte Carlo method is used to simulate the random histories of fission neutrons born from an estimated fission “bank”. Some of these histories end in fission events, producing new fission sites. When all random histories have been completed, a new fission “bank” is obtained for the next cycle.
2. While the standard Monte Carlo process generates the fission neutron histories, it also (using tracklength and surface estimators) generates estimates of the integrals and currents in Eqs. (5.6)-(5.10). After all the fission neutrons in a generation have been processed, the quantities $\Sigma_{t,k}$, $\Sigma_{a,k}$, and $\nu\Sigma_{f,k}$ [Eqs. (5.7)-(5.9)], $\tilde{D}_{k+1/2}$ [Eq. (5.13)] and $\hat{D}_{k+1/2}$ [Eq.(5.14)] are calculated.
3. Using the estimated quantities from step 2, the coarse-grid Eqs. (5.22) are solved for $\phi_{0,k}$ and k_{eff}.
4. Feedback (*optional*): The Monte Carlo fission source “bank” obtained in step 1 is modified to become consistent with the normalized fission source $\dfrac{\nu\Sigma_{f,k}\phi_{0,k}h_k}{\sum_{k'=1}^{K}\nu\Sigma_{f,k'}\phi_{0,k'}h_{k'}}$ obtained from the solution of the CMFD equations in step 3.

   This is done by randomly duplicating or deleting fission sites in each coarse cell, making the spatial distribution of the fission bank and $\nu\Sigma_{f,k}\phi_{0,k}$ consistent.)

5. Return to step 1 and repeat for as many inactive and active cycles as are deemed necessary.

The HCMFD-I method has several benefits. First, Monte Carlo does not require homogenization procedures or incur truncation errors, so the stochastically-computed $\hat{D}_{k+1/2}$ have only statistical errors. Additionally, the flux-weighted cross sections and correction factors are *nonlinear functionals* that can be computed more accurately than traditional linear quantities, as demonstrated in Chapter 4. We emphasize that the fission source does *not* need to be well-converged in order to obtain accurate quantities for the CMFD calculations. The elliptic CMFD equations propagate information quickly throughout the system, and the HCMFD-I method can accelerate Monte Carlo source convergence when feedback is used. When feedback is not used, the solution of the low-order CMFD equations is still more accurate than that of standard Monte Carlo. These features are demonstrated in Chapters 6 and 7.

5.4 Sensitivity Issues in the HCMFD-I Method

Lee, et al., demonstrated that HCMFD-I with feedback can be used to accelerate Monte Carlo source convergence in difficult eigenvalue problems. However, it was observed [4] that the method did not perform as well as the Functional Monte Carlo method [12][13][14]. Functional Monte Carlo is a different hybrid method proposed by Larsen and Yang that uses Eddington factor-type nonlinear functionals in quasi-diffusion-like equations.

We emphasize that Functional Monte Carlo, HCMFD-I, as well as the previously presented H-MC-S_2 and H-MC-S_2X methods all rely on Monte Carlo estimation of nonlinear functionals. However, the different functional definitions, and different low-order equations in each of these methods result in significant performance differences among the methods, as observed by Lee. In this section, we attempt to understand why HCMFD-I does not perform as optimally as Functional Monte Carlo.

Consider the following nonlinear functional whose numerator is the n^{th} angular moment of the angular flux:

$$F = \frac{M_n \psi}{M_0 \psi} \tag{5.31}$$

The operators $M_n = \langle (\cdot) \rangle$ have been introduced, where $\langle (\cdot) \rangle = \int_{x_{j-1/2}}^{x_{j+1/2}} \int_{E_g}^{E_{g-1}} \int_{-1}^{1} \mu^n (\cdot) \, d\mu dE dx.$ The random variable F is generated by estimating the true flux, $[\psi]$, with some statistical error in Monte Carlo:

$$\psi = [\psi] + \sigma_\psi . \tag{5.32}$$

We assume that sufficient histories are simulated so that the statistical error is small compared to the true value: $\frac{\sigma_\psi}{[\psi]} \ll 1$. The estimated functional,

$$F = [F] + \sigma_F , \tag{5.33}$$

can be written in terms of the estimated flux:

$$\begin{aligned} F &= \frac{M_n \left([\psi] + \sigma_\psi \right)}{M_0 \left([\psi] + \sigma_\psi \right)} \\ &= \frac{M_n [\psi] + M_n \sigma_\psi}{M_0 [\psi] + M_0 \sigma_\psi} \\ &= \frac{M_n [\psi] \left(1 + \dfrac{M_n \sigma_\psi}{M_n [\psi]} \right)}{M_0 [\psi] \left(1 + \dfrac{M_0 \sigma_\psi}{M_0 [\psi]} \right)} \\ &= \frac{M_n [\psi]}{M_0 [\psi]} \left(1 + \frac{M_n \sigma_\psi}{M_n [\psi]} \right) \left(1 - \frac{M_0 \sigma_\psi}{M_0 [\psi]} + \cdots \right). \end{aligned} \tag{5.34}$$

Using $[F] = \frac{M_n [\psi]}{M_0 [\psi]}$ and neglecting terms order σ_ψ^2 and higher, and the estimated functional can be written:

$$F \approx [F] + [F]\left(\frac{M_n\sigma_\psi}{M_n[\psi]} - \frac{M_0\sigma_\psi}{M_0[\psi]}\right) \tag{5.35}$$

Therefore, the relative error in the functional is approximately:

$$\frac{\sigma_F}{[F]} = \frac{M_n\sigma_\psi}{M_n[\psi]} - \frac{M_0\sigma_\psi}{M_0[\psi]}. \tag{5.36}$$

The relative error in the functional is therefore related to the relative error of the 0^{th} and n^{th} angular-spatial-energy moments of the flux. We established that $\frac{\sigma_\psi}{[\psi]} \ll 1$ when sufficient Monte Carlo histories are simulated. However, the magnitude of $\frac{M_n\sigma_\psi}{M_n[\psi]}$ has a subtle dependence on n.

For n even, $M_n[\psi]$ is strictly non-negative because the function μ^n and the angular flux are both non-negative. The term $M_n\sigma_\psi$ can be positive or negative, but is small in magnitude because σ_ψ oscillates in sign, causing partial cancellation when the function $\mu^n\sigma_\psi$ is integrated over all angles. Thus, $\left|\frac{M_n\sigma_\psi}{M_n[\psi]}\right| \ll 1$, and $\left|\frac{\sigma_F}{F}\right| \ll 1$ for n even.

For n odd, $M_n[\psi]$ resembles a current. It can be positive or negative, but its magnitude is close to zero for diffusive problems where the angular flux is mostly isotropic. Again, $M_n\sigma_\psi$ is small in magnitude, but the ratio $\frac{M_n\sigma_\psi}{M_n[\psi]}$ could be extremely large despite small $\frac{\sigma_\psi}{[\psi]}$ when n is odd. Therefore, $\frac{\sigma_F}{[F]}$ is not guaranteed to be small: the error in F can be larger than F itself when n is odd.

This shows that nonlinear functionals having odd angular moments of the flux can be sensitive to small statistical errors. Small statistical errors in the odd angular moment of the flux term do *not* imply small errors in the nonlinear functional. We see now that

HCMFD-I utilizes the odd angular moment term $\phi_{1,k+1/2}$, in the definition of the correction factor in Eq. (5.30). In contrast, Functional Monte Carlo uses only even angular moments of the flux.

There is, in fact, some flexibility in defining the correction factor in HCMFD-I. In the following sections, we reformulate the correction factor with the goal of reducing its sensitivity to statistical fluctuations.

5.5 The HCMFD-II Method

We now consider the identity obtained by applying $\int_{-1}^{1} \mu\left(\cdot\right) d\mu$ to Eq. (5.1):

$$\frac{d}{dx}\Phi_2(x) + \Sigma_t(x)\phi_1(x) = 0. \tag{5.37}$$

Here we have introduced the notation

$$\Phi_n(x) = \int_{-1}^{1} \mu^n \psi(x,\mu) d\mu, \qquad n \geq 2. \tag{5.38}$$

Integrating over $x_{k-1/2} < x < x_{k+3/2}$, we obtain

$$\Phi_{2,k+3/2} - \Phi_{2,k-1/2} + \int_{x_{k-1/2}}^{x_{k+3/2}} \Sigma_t(x)\phi_1(x)dx = 0, \tag{5.39}$$

and define:

$$\tilde{\phi}_{1,k+1/2} \equiv \frac{\int_{x_{k-1/2}}^{x_{k+3/2}} \Sigma_t(x)\phi_1(x)dx}{\int_{x_{k-1/2}}^{x_{k+3/2}} \Sigma_t(x)dx}. \tag{5.40}$$

In Eq. (5.40), we have used the notation $\tilde{\phi}_{1,k+1/2}$ to suggest that this quantity is an approximation to the cell-edged current $\phi_{1,k+1/2}$, where the current in cells k and $k+1$ have been weighted over the total cross sections in these cells. Following directly from Eqs. (5.39) and (5.40), we define:

$$F_{k+1/2}^{(II)} \equiv \tilde{\phi}_{1,k+1/2} + \frac{\left(\Phi_{2,k+3/2} - \Phi_{2,k-1/2}\right)}{\int_{x_{k-1/2}}^{x_{k+3/2}} \Sigma_t(x)dx} = 0. \tag{5.41}$$

We now proceed to subtract $F_{k+1/2}^{(II)}$ from the numerator of $\hat{D}_{k+1/2}^{(I)}$. We emphasize that the subtraction of $F_{k+1/2}^{(II)}$ from the numerator of $\hat{D}_{k+1/2}^{(I)}$ does *not* change the value of $\hat{D}_{k+1/2}^{(I)}$ if the exact transport solution is used to evaluate $F_{k+1/2}^{(II)}$, since $F_{k+1/2}^{(II)} = 0$ in this case. The rationale for this subtraction is that $F_{k+1/2}^{(II)}$ will not be exactly zero when an approximate solution to Eq. (5.1) is used to evaluate $F_{k+1/2}^{(II)}$. For cells that are not optically thick, statistical errors in the terms $\phi_{1,k+1/2}$ and $\tilde{\phi}_{1,k+1/2}$ will, to some degree, cancel. Experimentally, we have found that this subtraction reduces the variance in $\hat{D}_{k+1/2}$, and hence in the solution of the CMFD equations [Eqs. (5.22)]. Performing this subtraction, we obtain the expression for the correction factor in the HCMFD-II method:

$$\hat{D}_{k+1/2}^{(II)} = \frac{\phi_{1,k+1/2} - \tilde{\phi}_{1,k+1/2} + \tilde{D}_{k+1/2}\left(\phi_{0,k+1} - \phi_{0,k}\right) - \frac{1}{\int_{x_{k-1/2}}^{x_{k+3/2}} \Sigma_t(x)dx}\left(\Phi_{2,k+3/2} - \Phi_{2,k-1/2}\right)}{\phi_{0,k+1} + \phi_{0,k}} \tag{5.42}$$

Again, the expressions for $\hat{D}_{k+1/2}^{(II)}$ and $\hat{D}_{k+1/2}^{(I)}$ are *equivalent* when evaluated with the exact transport solution, because of the identity in Eq. (5.41). Therefore, either $\hat{D}_{k+1/2}^{(I)}$ or $\hat{D}_{k+1/2}^{(II)}$ can be used in the CMFD method. The key idea is that these expressions are not identical when evaluated with an approximate (e.g., Monte Carlo) transport solution. Therefore, when the same Monte Carlo estimate is inserted into Eqs. (5.30) and (5.42), different $\hat{D}_{k+1/2}^{(I)}$ and $\hat{D}_{k+1/2}^{(II)}$ will result.

We now show that the dependence on the current $\phi_1(x)$ in Eq. (5.42) is greatly reduced from that of Eq. (5.30), where the numerator is directly proportional to the current. Taylor expanding $\phi_1(x)$ about the value $x_{k+1/2}$:

$$\phi_1(x) = \phi_1(x_{k+1/2}) + (x - x_{k+1/2})\phi_1'(x_{k+1/2}) + \tfrac{1}{2}(x - x_{k+1/2})^2 \phi_1''(x_{k+1/2}) + \ldots$$

and substituting this expansion into the expression $\phi_{1,k+1/2} - \tilde{\phi}_{1,k+1/2}$ yields:

$$\begin{aligned}\phi_{1,k+1/2} - \tilde{\phi}_{1,k+1/2} &= \phi_{1,k+1/2} - \frac{\int_{x_{k-1/2}}^{x_{k+3/2}} \Sigma_t(x)\left[\phi_1(x_{k+1/2}) + (x - x_{k+1/2})\phi_1'(x_{k+1/2}) + \cdots\right]dx}{\int_{x_{k-1/2}}^{x_{k+3/2}} \Sigma_t(x)dx} \\ &= -\frac{\int_{x_{k-1/2}}^{x_{k+3/2}} \Sigma_t(x)\left[(x - x_{k+1/2})\phi_1'(x_{k+1/2}) + \cdots\right]dx}{\int_{x_{k-1/2}}^{x_{k+3/2}} \Sigma_t(x)dx}.\end{aligned} \tag{5.43}$$

The term $\phi_{1,k+1/2} - \tilde{\phi}_{1,k+1/2}$ *vanishes* when the current is spatially constant, i.e. $\phi_1'(x_{k+1/2}) = 0$. In this case, statistical errors in estimation $\phi_{1,k+1/2}$ and $\tilde{\phi}_{1,k+1/2}$ exactly cancel. The cell-edged $\Phi_{2,k+1/2}$ terms in the numerator of Eq. (5.42) contribute some statistical error, but these terms are even angular moments of the angular flux, and they are computed with much less variance than the current. The expression in Eq. (5.43) is $O(h_k)$, i.e., proportional to the size of the coarse mesh. Thus, the "current" terms become small when the "coarse" grid becomes fine.

5.6 The HCMFD-III Method

We now reformulate $\hat{D}^{(I)}_{k+1/2}$ in a different way. We introduce the set of *tent functions* $f_{k+\frac{1}{2}}(x)$ defined on the coarse grid:

$$f_{k+\frac{1}{2}}(x) = \begin{cases} \frac{1}{h_k}\left(x - x_{k-1/2}\right) & x_{k-1/2} < x < x_{k+1/2} \\ \frac{1}{h_{k+1}}\left(x_{k+3/2} - x\right) & x_{k+1/2} < x < x_{k+3/2} \\ 0 & \textit{otherwise,} \end{cases} \tag{5.44}$$

where the functions $f_{\frac{1}{2}}(x)$ and $f_{K+\frac{1}{2}}(x)$ are truncated outside the system. These functions are depicted in Figure 5.1.

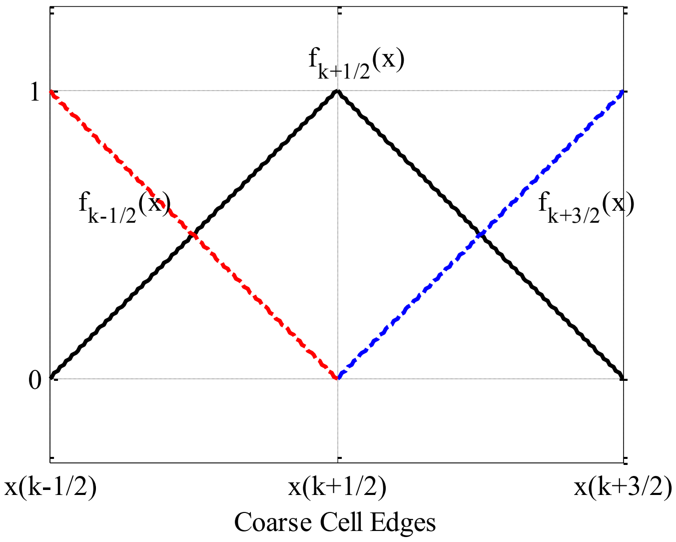

Figure 5.1 Tent function $f_{k+1/2}(x)$ and its neighbors.

We again consider the balance equation in Eq. (5.37). Multiplying Eq. (5.37) by $f_{k+\frac{1}{2}}(x)$, integrating over $x_{k-1/2} < x < x_{k+3/2}$, and then integrating by parts, we obtain:

$$f_{k+\frac{1}{2}}(x)\Phi_2(x)\Big|_{x_{k-1/2}}^{x_{k+3/2}} - \int_{x_{k-1/2}}^{x_{k+3/2}} f'_{k+\frac{1}{2}}(x)\Phi_2(x)dx + \int_{x_{k-1/2}}^{x_{k+3/2}} f_{k+\frac{1}{2}}(x)\Sigma_t(x)\phi_1(x)dx = 0.$$

Using $f_{k+1/2}(x_{k-1/2}) = f_{k+1/2}(x_{k+3/2}) = 0$ and evaluating $f'_{k+\frac{1}{2}}(x)$, the expression can be written:

$$\Phi_{2,k+1} - \Phi_{2,k} + \int_{x_{k-1/2}}^{x_{k+3/2}} f_{k+\frac{1}{2}}(x)\Sigma_t(x)\phi_1(x)dx = 0\,, \tag{5.45}$$

where

$$\Phi_{2,k} = \frac{1}{h_k}\int_{x_{k-1/2}}^{x_{k+1/2}} \Phi_2(x)dx. \tag{5.46}$$

We now define

$$\overset{\frown}{\phi}_{1,k+1/2} \equiv \frac{\int_{x_{k-1/2}}^{x_{k+3/2}} f_{k+\frac{1}{2}}(x)\Sigma_t(x)\phi_1(x)dx}{\int_{x_{k-1/2}}^{x_{k+3/2}} f_{k+\frac{1}{2}}(x)\Sigma_t(x)dx}, \tag{5.47}$$

where we have used the notation $\overset{\frown}{\phi}_{1,k+1/2}$ to suggest that this quantity is an approximation to the cell-edged current $\phi_{1,k+1/2}$. The tent function in Eq. (5.47) gives higher weight to the current closest to the cell edge, so we expect the quantity $\overset{\frown}{\phi}_{1,k+1/2}$ to be a more accurate approximation to $\phi_{1,k+1/2}$ than the quantity $\tilde{\phi}_{1,k+1/2}$. From Eqs. (5.45) and (5.47), we define:

$$F_{k+1/2}^{(III)} \equiv \overset{\frown}{\phi}_{1,k+1/2} + \frac{\Phi_{2,k+1} - \Phi_{2,k}}{\int_{x_{k-1/2}}^{x_{k+3/2}} f_{k+\frac{1}{2}}(x)\Sigma_t(x)dx} = 0. \tag{5.48}$$

We now proceed to subtract $F_{k+1/2}^{(III)}$ from the numerator of $\hat{D}_{k+1/2}^{(I)}$. As before, this procedure does *not* change the value of $\hat{D}_{k+1/2}^{(I)}$, provided the exact transport solution is used to evaluate $F_{k+1/2}^{(III)}$, since $F_{k+1/2}^{(III)} = 0$ in this case. The resulting expression is the correction factor for the HCMFD-III method:

$$\hat{D}_{k+1/2}^{(III)} = \frac{\phi_{1,k+1/2} - \overset{\frown}{\phi}_{1,k+1/2} + \tilde{D}_{k+1/2}\left(\phi_{0,k+1} - \phi_{0,k}\right) - \dfrac{\Phi_{2,k+1} - \Phi_{2,k}}{\int_{x_{k-1/2}}^{x_{k+3/2}} f_{k+\frac{1}{2}}(x)\Sigma_t(x)dx}}{\phi_{0,k+1} + \phi_{0,k}}. \tag{5.49}$$

We again show that the dependence on the current in Eq. (5.49) vanishes when the current is constant. Introducing the Taylor expansion of $\phi_1(x)$ into the expression $\phi_{1,k+1/2} - \overset{\frown}{\phi}_{1,k+1/2}$ yields:

$$\begin{aligned}\phi_{1,k+1/2} - \widehat{\phi}_{1,k+1/2} &= \phi_{1,k+1/2} - \frac{\int_{x_{k-1/2}}^{x_{k+3/2}} f_{k+\frac{1}{2}}(x)\Sigma_t(x)\left[\phi_1(x_{k+1/2}) + (x - x_{k+1/2})\phi_1'(x_{k+1/2}) + \cdots\right]dx}{\int_{x_{k-1/2}}^{x_{k+3/2}} f_{k+\frac{1}{2}}(x)\Sigma_t(x)dx} \\ &= -\frac{\int_{x_{k-1/2}}^{x_{k+3/2}} f_{k+\frac{1}{2}}(x)\Sigma_t(x)\left[(x - x_{k+1/2})\phi_1'(x_{k+1/2}) + \cdots\right]dx}{\int_{x_{k-1/2}}^{x_{k+3/2}} f_{k+\frac{1}{2}}(x)\Sigma_t(x)dx}\end{aligned} \tag{5.50}$$

The expression in Eq. (5.50) is equal to zero when the current is spatially constant, i.e., when $\psi(x,\mu) = \frac{1}{2}\phi_0(x) + \frac{3}{2}\mu\phi_1(x)$, where $\phi_1'(x_{k+1/2}) = 0$. Again, the expression is $O(h_k)$, and these current terms become smaller as the coarse mesh is refined.

5.7 The HCMFD-IV Method

The HCMFD-II and HCMFD-III methods utilize the first and second angular moments of the transport equation to derive identities that lower the statistical error in the $\hat{D}_{k+1/2}^{(I)}$ functionals. In particular, these identities eliminate dependence on the current term when the angular flux is a linear function of angle, and the current is constant. In the HCMFD-IV method, we attempt to reduce the statistical error even further by using additional transport identities to eliminate dependence on the current term when the angular flux is any linear function of angle, i.e., $\psi(x,\mu) = \frac{1}{2}\phi_0(x) + \frac{3}{2}\mu\phi_1(x)$.

We multiply the transport equation [Eq. (5.1)] by the second order Legendre polynomial, $P_2(\mu) = \frac{1}{2}\left(3\mu^2 - 1\right)$ and use the recursion relation $\mu P_2(\mu) = \frac{3}{5}P_3(\mu) + \frac{2}{5}P_1(\mu)$:

$$\begin{aligned}\left[\frac{3}{5}P_3(\mu) + \frac{2}{5}P_1(\mu)\right]\frac{d}{dx}\psi(x,\mu) + \Sigma_t(x)P_2(\mu)\psi(x,\mu)& \\ = P_2(\mu)\left[\frac{1}{2}\Sigma_s(x)\phi(x) + \frac{1}{2}\frac{\nu\Sigma_f(x)}{k_{eff}}\phi(x)\right]&.\end{aligned}$$

Now operating by $\int_{-1}^{1}(\cdot)\,d\mu$, we obtain

$$\frac{3}{5}\frac{d\phi_3}{dx}(x) + \frac{2}{5}\frac{d\phi_1}{dx}(x) + \Sigma_t(x)\phi_2(x) = 0\,,$$

or, rearranging,

$$\frac{d\phi_1}{dx}(x) = -\frac{3}{2}\frac{d\phi_3}{dx}(x) - \frac{5}{2}\Sigma_t(x)\phi_2(x).$$

Now we change the dummy variable x to x' and operate by $-\int_{x_{k+1/2}}^{x}\left(\cdot\right)dx'$ to obtain the expression

$$\phi_{1,k+1/2} - \phi_1(x) = \frac{3}{2}\left[\phi_3(x) - \phi_{3,k+1/2}\right] + \frac{5}{2}\int_{\bar{x}_{k+1/2}}^{x}\Sigma_t(x')\phi_2(x')\,dx'. \tag{5.51}$$

Eq. (5.51) is satisfied by the exact solution of the transport equation. We introduce Eq. (5.51) into the expression $\phi_{1,k+1/2} - \widehat{\phi}_{1,k+1/2}$ from the numerator of the $\hat{D}_{k+1/2}^{(III)}$ functional:

$$\begin{aligned}
\phi_{1,k+1/2} - \widehat{\phi}_{1,k+1/2} &= \frac{\int_{x_{k-1/2}}^{x_{k+3/2}} f_{k+\frac{1}{2}}(x)\Sigma_t(x)\left[\phi_{1,k+1/2} - \phi_1(x)\right]dx}{\int_{x_{k-1/2}}^{x_{k+3/2}} f_{k+\frac{1}{2}}(x)\Sigma_t(x)dx} \\
&= \frac{3}{2}\frac{\int_{x_{k-1/2}}^{x_{k+3/2}} f_{k+\frac{1}{2}}(x)\Sigma_t(x)\left[\phi_3(x) - \phi_{3,k+1/2}\right]dx}{\int_{x_{k-1/2}}^{x_{k+3/2}} f_{k+\frac{1}{2}}(x)\Sigma_t(x)dx} \\
&\quad + \frac{5}{2}\frac{\int_{x_{k-1/2}}^{x_{k+3/2}} f_{k+\frac{1}{2}}(x)\Sigma_t(x)\left[\int_{x_{k+1/2}}^{x}\Sigma_t(x')\phi_2(x')\,dx'\right]dx}{\int_{x_{k-1/2}}^{x_{k+3/2}} f_{k+\frac{1}{2}}(x)\Sigma_t(x)dx}.
\end{aligned} \tag{5.52}$$

The integral $\int_{x_{k-1/2}}^{x_{k+3/2}} f_{k+\frac{1}{2}}(x)\Sigma_t(x)\left[\int_{x_{k+1/2}}^{x}\Sigma_t(x')\phi_2(x')\,dx'\right]dx$ in Eq. (5.52) can be integrated by parts:

$$\begin{aligned}
\int_{x_{k-1/2}}^{x_{k+3/2}} f_{k+1/2}(x)\Sigma_t(x)\left[\int_{x_{k+1/2}}^{x}\Sigma_t(x')\phi_2(x')\,dx'\right]dx &= \int_{x_{k-1/2}}^{x_{k+3/2}} h'(x)\,g(x)\,dx \\
&= h(x)g(x)\Big|_{x_{k-1/2}}^{x_{k+3/2}} - \int_{x_{k-1/2}}^{x_{k+3/2}} h(x)g'(x)\,dx,
\end{aligned}$$

where $h'(x) = f_{k+1/2}(x)\Sigma_t(x)$, $h(x) = \int_{x_{k+1/2}}^{x} f_{k+1/2}(x')\Sigma_t(x')\,dx'$, $g'(x) = \Sigma_t(x)\phi_2(x)$, and $g(x) = \int_{x_{k+1/2}}^{x} \Sigma_t(x')\phi_2(x')\,dx'$. The procedure is shown here:

$$
\begin{aligned}
&\int_{x_{k-1/2}}^{x_{k+3/2}} f_{k+\frac{1}{2}}(x)\Sigma_t(x)\left[\int_{x_{k+1/2}}^{x} \Sigma_t(x')\phi_2(x')\,dx'\right]dx \\
&\qquad = \left(\int_{x_{k+1/2}}^{x} f_{k+\frac{1}{2}}(x')\Sigma_t(x')\,dx'\right)\left(\int_{x_{k+1/2}}^{x} \Sigma_t(x')\phi_2(x')\,dx'\right)\Bigg|_{x_{k-1/2}}^{x_{k+3/2}} \\
&\qquad\qquad - \int_{x_{k-1/2}}^{x_{k+3/2}} \left[\int_{x_{k+1/2}}^{x} f_{k+\frac{1}{2}}(x')\Sigma_t(x')\,dx'\right]\Sigma_t(x)\phi_2(x)dx \\
&\qquad = \left(\int_{x_{k+1/2}}^{x_{k+3/2}} f_{k+\frac{1}{2}}(x')\Sigma_t(x')\,dx'\right)\left(\int_{x_{k+1/2}}^{x_{k+3/2}} \Sigma_t(x')\phi_2(x')\,dx'\right) \\
&\qquad\qquad - \left(\int_{x_{k+1/2}}^{x_{k-1/2}} f_{k+\frac{1}{2}}(x')\Sigma_t(x')\,dx'\right)\left(\int_{x_{k+1/2}}^{x_{k-1/2}} \Sigma_t(x')\phi_2(x')\,dx'\right) \\
&\qquad\qquad - \int_{x_{k-1/2}}^{x_{k+3/2}} \left[\int_{x_{k+1/2}}^{x} f_{k+\frac{1}{2}}(x')\Sigma_t(x')\,dx'\right]\Sigma_t(x)\phi_2(x)dx.
\end{aligned}
$$

Unfortunately, the double integral $\int_{x_{k-1/2}}^{x_{k+3/2}} \left[\int_{x_{k+1/2}}^{x} f_{k+\frac{1}{2}}(x')\Sigma_t(x')\,dx'\right]\Sigma_t(x)\phi_2(x)dx$ is difficult to simplify unless each coarse cell is assumed to be homogeneous. This is not true in general, but if we make this assumption, the expression becomes:

$$
\begin{aligned}
&\int_{x_{k-1/2}}^{x_{k+3/2}} f_{k+\frac{1}{2}}(x)\bar{\Sigma}_t(x)\left[\int_{x_{k+1/2}}^{x} \Sigma_t(x')\phi_2(x')\,dx'\right]dx \\
&\qquad = \tfrac{1}{2} h_{k+1}^2 \bar{\Sigma}_{t,k+1}^2 \phi_{2,k+1} - \tfrac{1}{2} h_k^2 \bar{\Sigma}_{t,k}^2 \phi_{2,k} \\
&\qquad - \bar{\Sigma}_{t,k}^2 \int_{x_{k-1/2}}^{x_{k+1/2}} \left[\int_{x_{k+1/2}}^{x} f_{k+\frac{1}{2}}(x')\,dx'\right]\phi_2(x)dx \\
&\qquad - \bar{\Sigma}_{t,k+1}^2 \int_{x_{k+1/2}}^{x_{k+3/2}} \left[\int_{x_{k+1/2}}^{x} f_{k+\frac{1}{2}}(x')\,dx'\right]\phi_2(x)dx
\end{aligned}
\tag{5.53}
$$

where $\bar{\Sigma}_{t,k}$ is the volume-weighted (not flux-averaged) total cross section in cell k:

$$
\bar{\Sigma}_{t,k} = \frac{1}{h_k}\int_{x_{k-1/2}}^{x_{k+1/2}} \Sigma_t(x)dx \tag{5.54}
$$

The integrals in Eq. (5.53) can now be expressed analytically.

For $x_{k-1/2} \leq x \leq x_{k+1/2}$:

$$\begin{aligned}
\int_{x_{k+1/2}}^{x} f_{k+\frac{1}{2}}(x')\,dx' &= \tfrac{1}{h_k}\int_{x_{k+1/2}}^{x} \left(x' - x_{k-1/2}\right) dx' \\
&= \tfrac{1}{h_k}\int_{\bar{x}_{k+1/2}}^{x} \left[\left(x' - x_{k+1/2}\right) + h_k\right] dx' \\
&= \tfrac{1}{h_k}\left[h_k u + \tfrac{1}{2}u^2\right]\Big\|_0^{x - x_{k+1/2}} \\
&= \tfrac{1}{h_k}\left[\bar{h}_k\left(x - x_{k+1/2}\right) + \tfrac{1}{2}\left(x - x_{k+1/2}\right)^2\right] \\
&= \left(x - x_{k+1/2}\right) + \tfrac{1}{2h_k}\left(x - x_{k+1/2}\right)^2 .
\end{aligned}$$

For $x_{k+1/2} \leq x \leq x_{k+3/2}$:

$$\begin{aligned}
\int_{x_{k+1/2}}^{x} f_{k+\frac{1}{2}}(x')\,dx' &= \tfrac{1}{h_{k+1}}\int_{x_{k+1/2}}^{x} \left(x_{k+3/2} - x'\right) dx' \\
&= \tfrac{1}{h_{k+1}}\int_{x_{k+1/2}}^{x} \left[h_{k+1} - \left(x' - x_{k+1/2}\right)\right] dx' \\
&= \tfrac{1}{h_{k+1}}\left[h_{k+1} u - \tfrac{1}{2}u^2\right]\Big\|_0^{x - x_{k+1/2}} \\
&= \tfrac{1}{h_{k+1}}\left[h_{k+1}\left(x - x_{k+1/2}\right) - \tfrac{1}{2}\left(x - x_{k+1/2}\right)^2\right] \\
&= \left(x - x_{k+1/2}\right) - \tfrac{1}{2h_{k+1}}\left(x - x_{k+1/2}\right)^2 .
\end{aligned}$$

Let us define $g_{k+\frac{1}{2}}(x) \equiv \int_{x_{k+1/2}}^{x} f_{k+\frac{1}{2}}(x')\,dx'$, where:

$$g_{k+\frac{1}{2}}(x) = \begin{cases} \left(x - x_{k+1/2}\right) + \tfrac{1}{2h_k}\left(x - x_{k+1/2}\right)^2 & x_{k-1/2} \leq x \leq x_{k+1/2} \\ \left(x - x_{k+1/2}\right) - \tfrac{1}{2h_{k+1}}\left(x - x_{k+1/2}\right)^2 & x_{k+1/2} \leq x \leq x_{k+3/2} \\ 0 & \text{otherwise.} \end{cases} \tag{5.55}$$

The function $g_{k+1/2}(x)$ is graphically represented in the following figure:

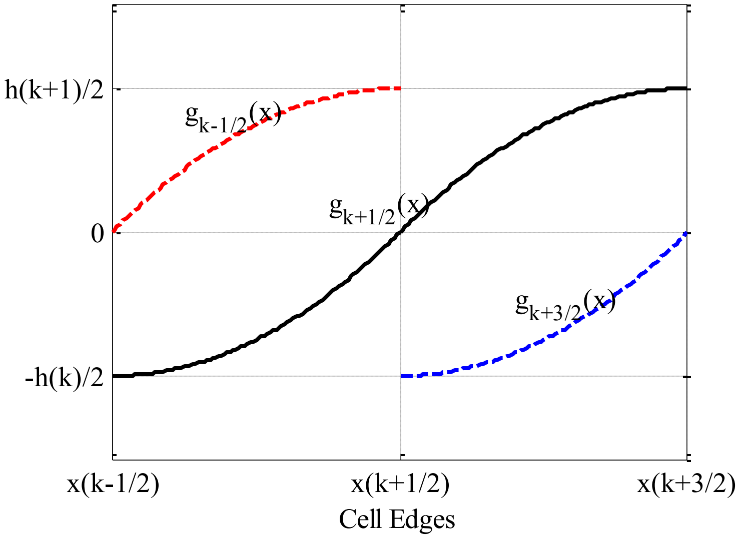

Figure 5.2 Plot of $g_{k+1/2}(x)$.

We have thus used the additional transport identity in Eq. (5.51) to express the term $\phi_{1,k+1/2} - \widehat{\phi}_{1,k+1/2}$ from the numerator of the $D_{k+1/2}^{(III)}$ functional as:

$$\begin{aligned}\phi_{1,k+1/2} - \widehat{\phi}_{1,k+1/2} = -\frac{3}{2}\phi_{3,k+1/2} + \frac{1}{\int_{x_{k-1/2}}^{x_{k+3/2}} f_{k+\frac{1}{2}}(x)\Sigma_t(x)dx}&\left\{\frac{3}{2}\int_{x_{k-1/2}}^{x_{k+3/2}} f_{k+\frac{1}{2}}(x)\Sigma_t(x)\phi_3(x)dx\right. \\ &+\frac{5}{2}\left[\tfrac{1}{2}h_{k+1}^2\overline{\Sigma}_{t,k+1}^2\phi_{2,k+1} - \tfrac{1}{2}h_k^2\overline{\Sigma}_{t,k}^2\phi_{2,k}\right. \\ &\left.\left.-\overline{\Sigma}_{t,k}^2\int_{x_{k-1/2}}^{x_{k+1/2}} g_{k+\frac{1}{2}}(x)\phi_2(x)dx - \overline{\Sigma}_{t,k+1}^2\int_{x_{k+1/2}}^{x_{k+3/2}} g_{k+\frac{1}{2}}(x)\phi_2(x)dx\right]\right\}.\end{aligned} \tag{5.56}$$

Introducing the notation:

$$\widehat{\phi}_{3,k+1/2} = \frac{\int_{x_{k-1/2}}^{x_{k+3/2}} f_{k+\frac{1}{2}}(x)\Sigma_t(x)\phi_3(x)dx}{\int_{x_{k-1/2}}^{x_{k+3/2}} f_{k+\frac{1}{2}}(x)\Sigma_t(x)dx}, \tag{5.57}$$

$$G_{k,\frac{1}{2}} = \int_{x_{k-1/2}}^{x_{k+1/2}} g_{k+\frac{1}{2}}(x)\phi_2(x)dx, \tag{5.58}$$

$$G_{k,-\frac{1}{2}} = \int_{x_{k-1/2}}^{x_{k+1/2}} g_{k-\frac{1}{2}}(x)\phi_2(x)dx, \tag{5.59}$$

the previous expression can be written:

$$\phi_{1,k+1/2} - \widehat{\phi}_{1,k+1/2} = -\frac{3}{2}\left(\phi_{3,k+1/2} - \widehat{\phi}_{3,k+1/2}\right) + \frac{\frac{5}{4}h_{k+1}^2\overline{\Sigma}_{t,k+1}^2\phi_{2,k+1} - \frac{5}{4}h_k^2\overline{\Sigma}_{t,k}^2\phi_{2,k} - \frac{5}{2}\overline{\Sigma}_{t,k}^2 G_{k,\frac{1}{2}} - \frac{5}{2}\overline{\Sigma}_{t,k+1}^2 G_{k+1,-\frac{1}{2}}}{\int_{x_{k-1/2}}^{x_{k+3/2}} f_{k+\frac{1}{2}}(x)\Sigma_t(x)dx}. \quad (5.60)$$

The correction functional for the HCMFD-IV method can thus be written *only in the case of homogeneous coarse cells* as:

$$\hat{D}_{k+1/2}^{(IV)} = \frac{-\frac{3}{2}\left(\phi_{3,k+1/2} - \widehat{\phi}_{3,k+1/2}\right) + \tilde{D}_{k+1/2}\left(\phi_{0,k+1} - \phi_{0,k}\right) + \frac{\frac{5}{4}h_{k+1}^2\overline{\Sigma}_{t,k+1}^2\phi_{2,k+1} - \frac{5}{4}h_k^2\overline{\Sigma}_{t,k}^2\phi_{2,k} - \frac{5}{2}\overline{\Sigma}_{t,k}^2 G_{k,\frac{1}{2}} - \frac{5}{2}\overline{\Sigma}_{t,k+1}^2 G_{k+1,-\frac{1}{2}} - \left(\Phi_{2,k+1} - \Phi_{2,k}\right)}{\int_{x_{k-1/2}}^{x_{k+3/2}} f_{k+\frac{1}{2}}(x)\Sigma_t(x)dx}}{\phi_{0,k+1} + \phi_{0,k}}. \quad (5.61)$$

The dependence on the current has been completely eliminated in Eq. (5.61), using transport identities to express the current in terms of higher order moments of the angular flux. However, we have now introduced another odd order moment of the angular flux, $\phi_3(x) = \int_{-1}^{1} P_3(\mu)\psi(x,\mu)d\mu = \frac{1}{2}\int_{-1}^{1}\left(5\mu^3 - 3\mu\right)\psi(x,\mu)d\mu.$ We recall that that odd order moments generally have more statistical error than even order moments. In addition, Eq. (5.61) can only be derived when the coarse cells are homogeneous, which is not true in general. This is a limitation of the HCMFD-IV method because it requires the CMFD calculations be performed on a very fine grid in highly heterogeneous problems.

5.8 Summary

In this chapter, we have proposed three hybrid Monte Carlo-CMFD methods (HCMFD-II, -III and -IV) that extend CMFD-Accelerated Monte Carlo (HCMFD-I) by using extra identities from the transport equation to reformulate the correction functionals in the CMFD equations. The reformulated functionals should exhibit cancellation of errors in the current terms. Therefore, the functionals should be less sensitive to statistical errors, and it should be possible to calculate $\hat{D}_{k+1/2}^{(II)}$, $\hat{D}_{k+1/2}^{(III)}$ and $\hat{D}_{k+1/2}^{(IV)}$ more accurately than $\hat{D}^{(I)}_{k+1/2}$ with a fixed number of Monte Carlo histories, leading to time savings in the Monte Carlo calculation step.

We compare these four methods in Chapter 6 for a simple fixed source problem in order to rank their performance. The remainder of Chapter 6 consists of numerical results for criticality calculations (without CMFD feedback). In Chapter 7, we present numerical results for criticality calculations using CMFD feedback.

5.9 References

[1] K.S. Smith, "Nodal Method Storage Reduction by Nonlinear Iteration," *Trans. Am. Nucl. Soc.*, **44**, 265-266 (1983).

[2] M.J. Lee, H.G. Joo, D. Lee, and K. Smith, "Investigation of CMFD Accelerated Monte Carlo Eigenvalue Calculation with Simplified Low Dimensional Multigroup Formulation," *Proc. 2010 International Conference on the Physics of Reactors*, May 9-14, 2010, Pittsburgh, PA, CD-ROM, American Nuclear Society (2010).

[3] M.J. Lee, H.G. Joo, D. Lee, and K. Smith, "Multigroup Monte Carlo Reactor Calculation with Coarse Mesh Finite Difference Formulation for Real Variance Reduction," *Proc. 2010 Joint International Conference on Supercomputing in Nuclear Applications and Monte Carlo,* October 17-21, 2010, Tokyo, Japan, CD-ROM, SNA+MC2010 (2010).

[4] M.J. Lee, H.G. Joo, D. Lee, and K. Smith, "Application of CMFD Acceleration to Monte Carlo Simulation for Eigenvalue Problems," Personal Communication, Saratoga Springs, NY (2009).

[5] E.W. Larsen and J. Yang, "A Functional Monte Carlo Method for k-Eigenvalue Problems," *Nucl. Sci. Eng.*, **159**, 107-126 (2008).

[6] J. Yang and E.W. Larsen, "Application of the 'Functional Monte Carlo' Method to Estimate Continuous Energy Eigenvalues and Eigenfunctions," *Proc. 2009 International Conference on Advances in Mathematics, Computational Methods, and Reactor Physics*, May 3-7, 2009, Saratoga Springs, New York, CD-ROM, American Nuclear Society (2009).

[7] J. Yang and E.W. Larsen, "Calculation of k-Eigenvalues and Multigroup Eigenfunctions Using the Hybrid 'Functional Monte Carlo' Method," *Proc. PHYSOR 2010 – Advances in Reactor Physics to Power the Nuclear Renaissance,* May 9-14, 2010, Pittsburgh, PA, CD-ROM, American Nuclear Society (2010).

[8] H.G. Joo, Personal Communication, Ann Arbor, MI (2010).

Chapter 6

Hybrid Monte Carlo – CMFD Numerical Results

6.1 Fixed Source Problem #1

The HCMFD-I, -II, -III, and -IV methods were tested on a monoenergetic fixed source problem before performing eigenvalue calculations. An isotropic source was uniformly distributed in a slab with vacuum boundaries and the following material parameters:

Location [cm]	Σ_t **[cm^{-1}]**	Σ_s **[cm^{-1}]**	Q **[cm^{-1}]**
$0 < x < 20$	1.0	0.8	1.0

Table 6.1 Material specifications for Fixed Source Problem #1.

Several independent calculations were performed with $p = 1$ (the number of fine cells per CMFD coarse cell) to estimate the variance of the solutions of each method, and how the variance depends on the number of histories.

Number of Independent Simulations (K)	**Number of Histories per Simulation (N)**	**Fine Grid [cm]**
25	N	0.5

Table 6.2 Monte Carlo numerical properties for Fixed Source Problem #1.

All methods yielded accurate solutions for this test problem, but there were differences in the variances of the solutions. Figure 6.1 plots the variance for each method as a function of number of histories in the Monte Carlo simulation.

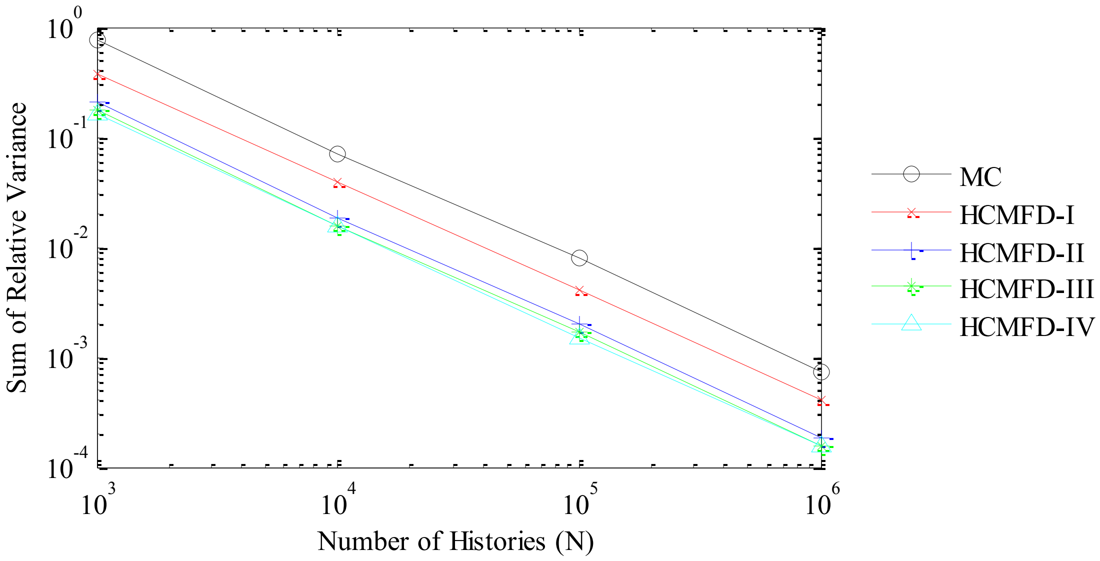

Figure 6.1 Variance of HCMFD methods and standard Monte Carlo for Fixed Source Problem #1.

The variance of each method follows a linear trend, demonstrating the applicability of the Central Limit Theorem. The reduction in variance in the HCMFD-I, -II, -III and –IV solutions implies a reduction in the number of histories (and reduction in computational expense) needed to achieve a given error. The ratio of the *sum of relative variance of the method m* to the *sum of relative variance of the Monte Carlo solution*:

$$f^{(m)} \approx \frac{\text{sum of relative variance of method m}}{\text{sum of relative variance of MC}} \tag{6.1}$$

indicates the approximate fraction of computing time required by method m to achieve a given error, compared to standard Monte Carlo. This fraction is approximately independent of the number of histories. The values fractional computing times for this test problem (with N=100,000 histories) are reported in Table 6.3.

Method	$f^{(m)}$
HCMFD-I	0.51
HCMFD-II	0.24
HCMFD-III	0.21
HCMFD-IV	0.18

Table 6.3 Fractional computing time required for the HCMFD methods to achieve the same error as a standard Monte Carlo calculation.

If a standard Monte Carlo calculation is performed to achieve a given error, the HCMFD-I, -II, -III and –IV methods achieve the same error in 51%, 24%, 21% and 18% of the computing time required by standard Monte Carlo. [We note that the H-MC-S_2X fractional computing time for this problem is 19%. Therefore, HCMFD methods –II, -III, and –IV appear to have similar efficiency to H-MC-S_2X on this specific test problem, whereas HCMFD-I appears to be much more sensitive.]

These numerical results establish a preliminary ranking of the new methods: HCMFD-IV, -III, -II and then -I performed better than standard Monte Carlo, in that order. However, since HCMFD-IV is more complex to implement, limited to homogeneous coarse cells, and fared only slightly better than HCMFD-III, we did not pursue further testing of HCMFD-IV in eigenvalue calculations.

6.2 Monte Carlo Criticality Calculations

Before presenting further numerical results, we briefly review the simulation of criticality problems in Monte Carlo. First, an initial spatial distribution of the fission source is guessed (the source is often initially assumed to be spatially flat). Then, N fission sites are stored in a "source bank" according to this distribution, representing N source particles. Each source particle is transported to generate a history that terminates in leakage, capture, or fission. When a fission event occurs, the spatial location of the event is stored (multiple times, according to the average number of neutrons released per fission event, ν) in the "fission bank". When all particles in the original source bank have been transported, the "cycle" ends.

At the end of a cycle, the eigenfunction (normalized flux distribution) and eigenvalue (number of particles in the fission bank divided by number of particles in the source bank) are estimated. Then, sites in the fission bank are randomly duplicated or killed to make the resulting number of sites in the bank approximately equal to N. This adjusted fission bank is then used as the source bank for the next cycle. This process repeats for several "inactive" cycles in order to converge the fission source. The Shannon entropy [1],

$$H_{src} = -\sum_{k=1}^{K} P_k \ln P_k \tag{6.2}$$

where $P_k = \frac{\nu\Sigma_{f,k}\phi_k h_k}{\sum_{k'=1}^{K} \nu\Sigma_{f,k'}\phi_{k'} h_{k'}} =$ the fraction of fission source neutrons in cell k, is often used to determine when the source has converged. The Shannon entropy begins at a maximum or minimum value at the beginning of the calculation, depending on the guessed source distribution. As the fission source converges, the Shannon entropy rises or falls, and eventually approaches an asymptotic limit. The fission source is assumed to be converged when the cycle-wise Shannon entropy is asymptotic. Once the fission source has converged, the "active" cycles begin. The eigenfunction and eigenvalue are averaged over only active cycles to produce the reported mean eigenfunction and eigenvalue.

A criticality calculation therefore consists of sequential "fixed source" calculations (referred to as *cycles* or *generations*), where the source for cycle i is the fission source from cycle $i-1$. Because of inter-cycle correlation, the fission source converges very slowly in problems with high dominance ratios. For large problems, i.e., light water reactor cores, Monte Carlo can be prohibitively expensive due to slow source convergence. For these problems, the fission source does not converge at all, unless the number of histories per cycle is high enough to overcome the high dominance ratio. Unfortunately, the required number of histories per cycle can be excessively high.

6.3 Hybrid Monte-Carlo CMFD Without Feedback

In the following sections, we consider a non-obtrusive implementation of the hybrid Monte Carlo-CMFD methods for criticality problems. We perform a standard Monte Carlo criticality calculation, but during each Monte Carlo cycle, the nonlinear functionals required in the CMFD equations are estimated. At the end of each cycle, the Monte Carlo eigenfunction and eigenvalue are estimated, and the functionals are used to obtain separate CMFD estimates of the eigenfunction and eigenvalue. The CMFD estimates *do not affect* the Monte Carlo simulation in any way. We refer to this technique as "Hybrid Monte Carlo-CMFD without Feedback". The purpose of this exercise is to demonstrate that the HCMFD methods implemented in this "non-obtrusive" way are more efficient than standard Monte Carlo. We compare the Monte Carlo eigenfunction and eigenvalue with the HCMFD-I, HCMFD-II and HCMFD-III eigenfunctions and eigenvalues, and we show that the HCMFD values are more accurate than the Monte Carlo values. We also show that the HCMFD methods have better source convergence and variance properties than standard Monte Carlo.

6.4 Criticality Problems #1A-#1D: Homogeneous Slabs of Varying Width

6.4.1 Problem Description

Problems #1A-#1D are homogeneous fissile slabs of width X, with vacuum boundary conditions and isotropic scattering. The material specifications are listed in Table 6.4. Various slab widths were tested $(X = 10, 40, 70, 100 \text{ cm})$ and assigned problem numbers #1A, #1B, #1C, #1D, respectively.

Location [cm]	Σ_t **[cm^{-1}]**	Σ_s **[cm^{-1}]**	Σ_f **[cm^{-1}]**	ν
$0 < x < X$	1.0	0.5	0.2	2.4

Table 6.4 Material specifications of Criticality Problem #1A-#1D.

The first two eigenvalues of each slab were estimated according to slab geometry diffusion theory [1],

$$k_n = \frac{\nu\Sigma_f}{\Sigma_a}\frac{1}{1+\frac{D}{\Sigma_a}\left(\frac{n\pi}{L^*}\right)^2}, \quad n = 0,1, \tag{6.3}$$

where $D = \frac{1}{3\Sigma_t}$ is the diffusion coefficient, and $L^* = X + 2(0.7104)\frac{1}{\Sigma_t}$ is the effective slab width. The approximate dominance ratio of each problem is presented in the following table.

Problem	**Slab Width [cm]**	k_1	k_2	$DR = \frac{k_2}{k_1}$
#1A	10	0.913899	0.798816	0.874075
#1B	40	0.956332	0.945496	0.988668
#1C	70	0.958763	0.955072	0.996150
#1D	100	0.959386	0.957550	0.998086

Table 6.5 Dominance ratio as a function of slab width.

As the slab width increases, the dominance ratio approaches unity, and more cycles are required in Monte Carlo to converge the primary eigenfunction due to noise from slowly-converging higher-order eigenfunctions. We emphasize that problems with large dominance ratios are computationally expensive in Monte Carlo because they require numerous cycles to converge the fission source due to high inter-cycle correlation. For these problems, the source might not converge unless a very large number of histories per cycle is used.

6.4.2 Numerical Parameters

The Monte Carlo numerical specifications for Problems #1A-#1D are listed in Table 6.6.

Problem	X **[cm]**	**Number of Histories/Cycle (N)**	**Inactive Cycles (NI)**	**Active Cycles (NA)**	**Fine Grid [cm]**	**CMFD Parameter** p
#1A	10	100,000	100	200	0.5	1
#1B	40	100,000	100	200	0.5	1,2,4
#1C	70	100,000	200	200	0.5	1
#1D	100	100,000	400	200	0.5	1

Table 6.6 Numerical parameters of Problem #1 for different slab widths.

In addition, benchmark solutions for each problem were generated using S_{16} discrete ordinates calculation with uniform 0.01 cm grids.

6.4.3 Numerical Results

We begin with the numerical results for Problem #1B ($X = 40$ cm and $p = 1$). The Shannon entropy behavior of standard Monte Carlo and individual hybrid CMFD methods is presented in Figure 6.2. Approximately 100 inactive cycles are required for the Monte Carlo entropy to converge. However, even after 100 cycles, the Monte Carlo entropy fluctuates around the asymptote, indicating that the source has difficulty staying converged from cycle to cycle.

In contrast, the Shannon entropies of the hybrid CMFD methods converge immediately during the first few cycles. Therefore, the CMFD eigenfunctions converge immediately, despite the fact that their input parameters come from a poorly converged Monte Carlo solution. Lee, et al., previously demonstrated the success of HCMFD-I for accelerating Monte Carlo source convergence [3][4][5], and these results confirm that work.

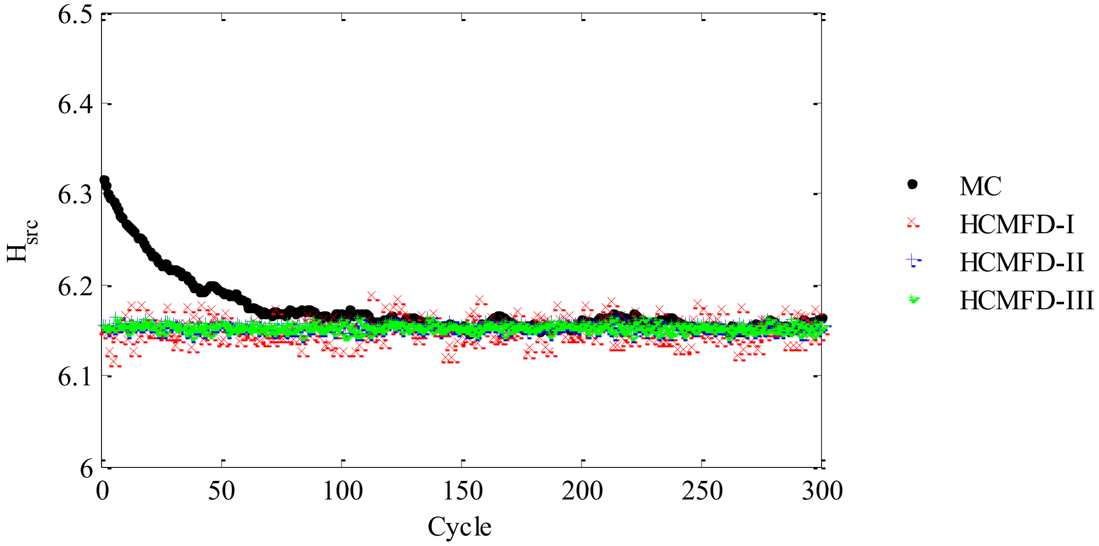

Figure 6.2 Shannon entropy behavior of 40 cm slab (Problem #1B, p=1).

The Shannon entropies of HCMFD-I, -II, and -III all converge immediately for this Problem #1B, but the degree of fluctuation about the asymptote is dramatically reduced in HCMFD-II and HCMFD-III. This is beneficial because it indicates that the variance of the eigenfunction is greatly reduced. Fewer active cycles are necessary to accurately estimate both the eigenvalue and eigenfunction in HCMFD-II and -III. The cycle-wise eigenvalues in Figure 6.3 exhibit similar behavior.

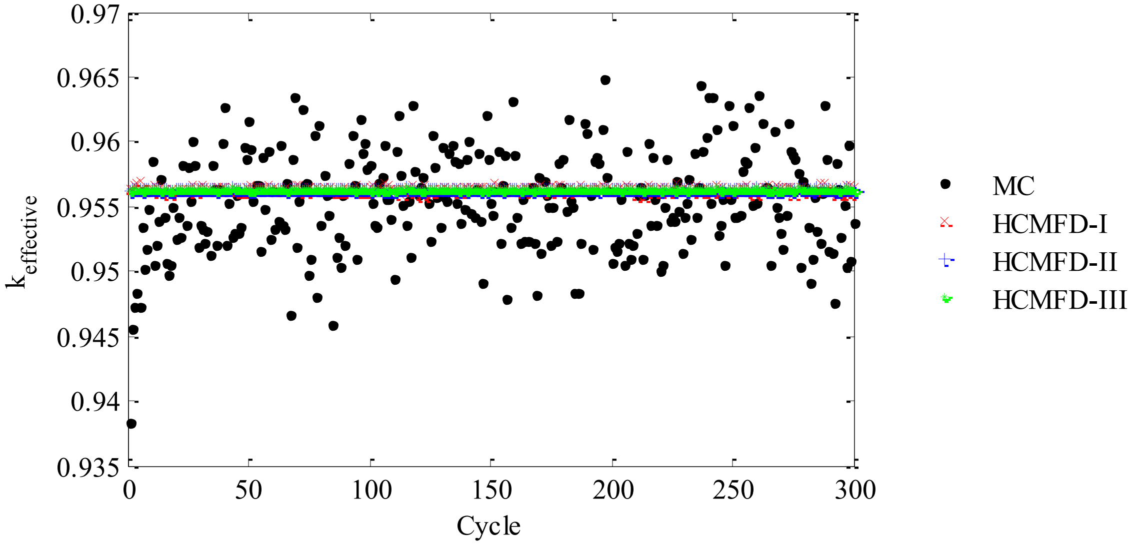

Figure 6.3 Eigenvalue behavior of 40 cm slab (Problem #1B, p=1).

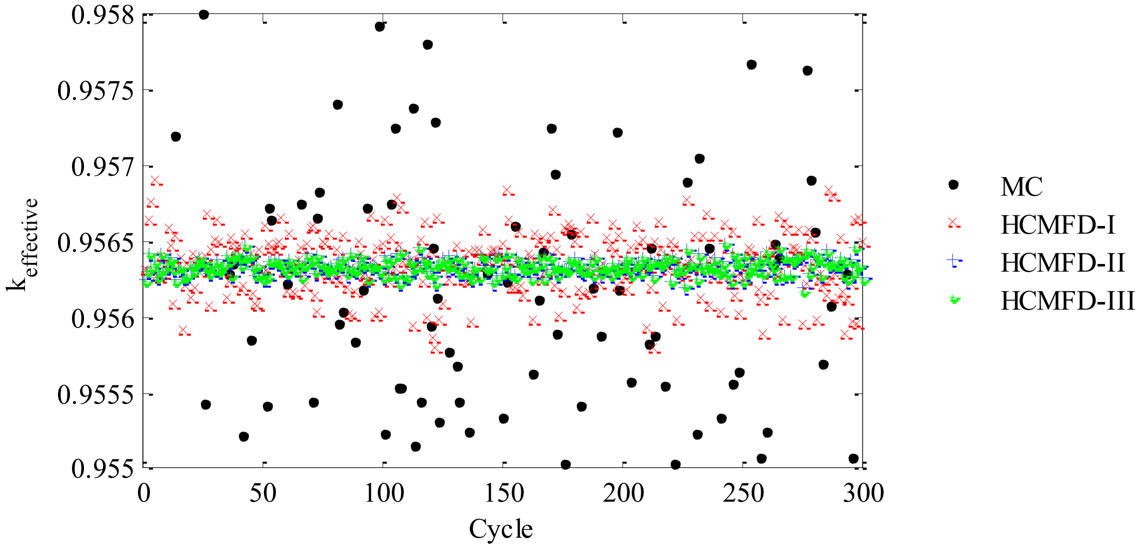

Figure 6.4 Eigenvalue behavior of 40 cm slab, magnified (Problem #1B, p=1).

Figure 6.4 is a blowup of the cycle-wise eigenvalue estimates. The cycle-wise HCMFD-II and -III k_{eff} distributions have less variance than that of HCMFD-I, and standard Monte Carlo. The differences in the HCMFD-II and HCMFD-III eigenvalue distributions are negligible for this test problem, where the coarse cells are optically thin (0.5 mfp). However, as shown in Table 6.7, HCMFD-III is slightly more accurate than HCMFD-II as the coarse cell width increases. This dependence on coarse cell size is discussed in detail in Section 6.4.4.

We now examine the mean eigenfunction (averaged over active cycles) plotted in Figure 6.5(a). The benchmark solution is labeled “SN”.

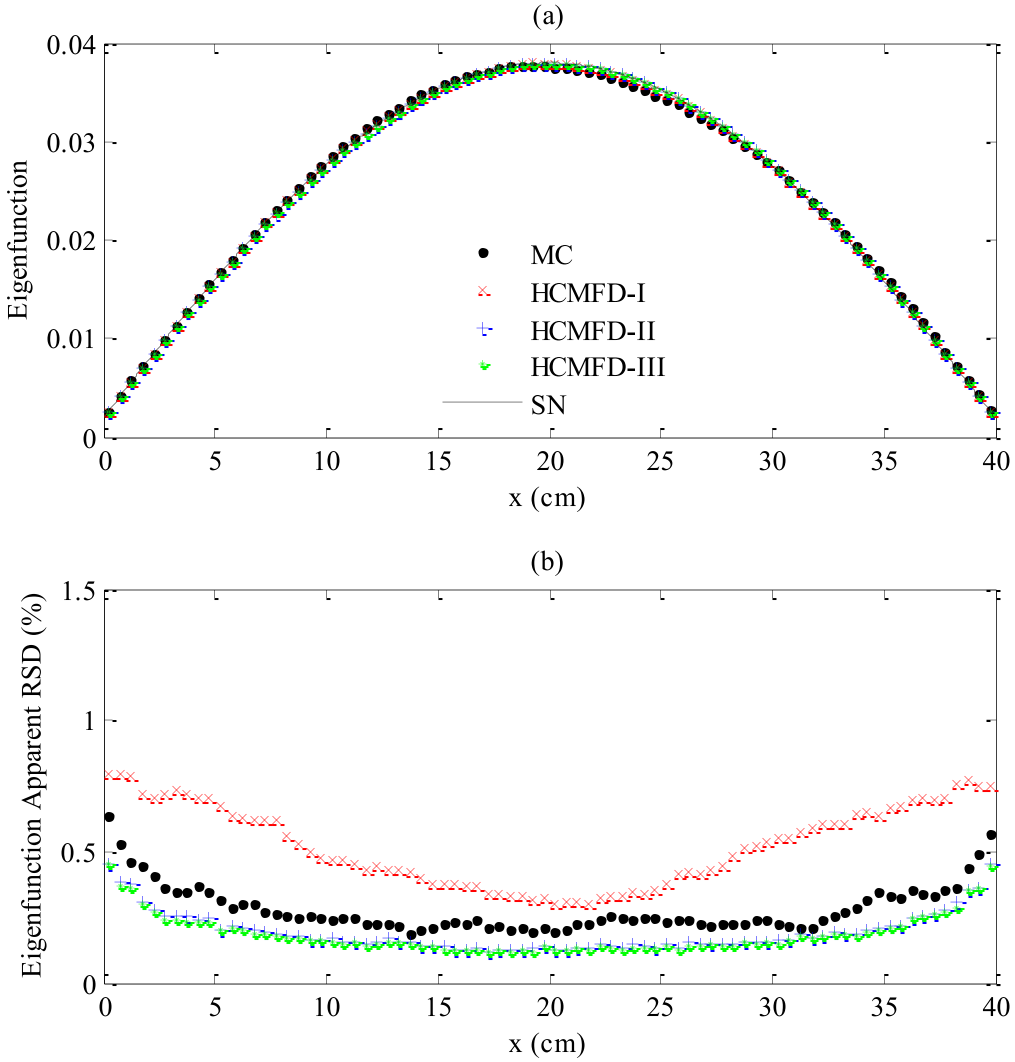

Figure 6.5 Mean eigenfunction and apparent RSD of 40 cm slab (Problem #1B, p=1).

The eigenfunctions of the hybrid CMFD methods are well-converged and have a smooth, symmetrical cosine shape. However, the standard Monte Carlo eigenfunction is slightly asymmetrical. This is consistent with the Shannon entropy plot, which indicates that the Monte Carlo source wobbles during active cycles.

Figure 6.5(b) plots the apparent relative standard deviation (RSD) of the various eigenfunctions. The *apparent standard deviation* is the observed measure of how much the eigenfunction wobbles, or varies, over active cycles. However, inter-cycle correlation often causes the apparent standard deviation to underestimate the true standard deviation. Since apparent standard deviation is typically used to indicate the confidence in the mean eigenfunction, underestimation of the true standard deviation leads the user to believe that the eigenfunction is more accurate than it is. We discuss this topic further in Section 6.4.8. For now, we emphasize that the apparent standard deviation should not be trusted, especially for problems with large dominance ratios.

6.4.4 Dependence on Coarse Mesh Size

We now increase p (the number of fine cells per coarse cell in CMFD) to assess the effect on the hybrid method results. We expect all hybrid CMFD solutions to degrade slightly compared to standard Monte Carlo, since less "work" is being done as the mesh becomes coarser. However, we anticipate that HCMFD-II and -III will be more sensitive to the mesh size than HCMFD-I.

We recall that HCMFD-II and -III attempt to cancel statistical error in the cell-edged current term $\phi_{1,k+1/2}$ of $\hat{D}^{(I)}_{k+1/2}$ by making use of the following cell-averaged currents, respectively:

$$\tilde{\phi}_{1,k+1/2} \equiv \frac{\int_{x_{k-1/2}}^{x_{k+3/2}} \Sigma_t(x)\phi_1(x)dx}{\int_{x_{k-1/2}}^{x_{k+3/2}} \Sigma_t(x)dx}, \tag{6.4}$$

$$\widehat{\phi}_{1,k+1/2} \equiv \frac{\int_{x_{k-1/2}}^{x_{k+3/2}} f_{k+\frac{1}{2}}(x)\Sigma_t(x)\phi_1(x)dx}{\int_{x_{k-1/2}}^{x_{k+3/2}} f_{k+\frac{1}{2}}(x)\Sigma_t(x)dx}. \tag{6.5}$$

The statistical errors in Eq. (6.4) and (6.5) are both correlated to the statistical error in $\phi_{1,k+1/2}$. As the coarse cell width becomes larger, this correlation decreases, and less cancellation of statistical error occurs. Since HCMFD-I does not make use of the terms in Eqs. (6.4) and (6.5), it should be less sensitive to the size of the coarse mesh than HCMFD-II and HCMFD-III.

Comparing Figures 6.2, 6.6, and 6.7, we can see the effects of increasing p (size of the coarse mesh) on source convergence. The hybrid CMFD methods converge the fission source within a few cycles for all values of p, but the fission source has more variance for larger p. Similar behavior occurs for the cycle-wise k_{eff}.

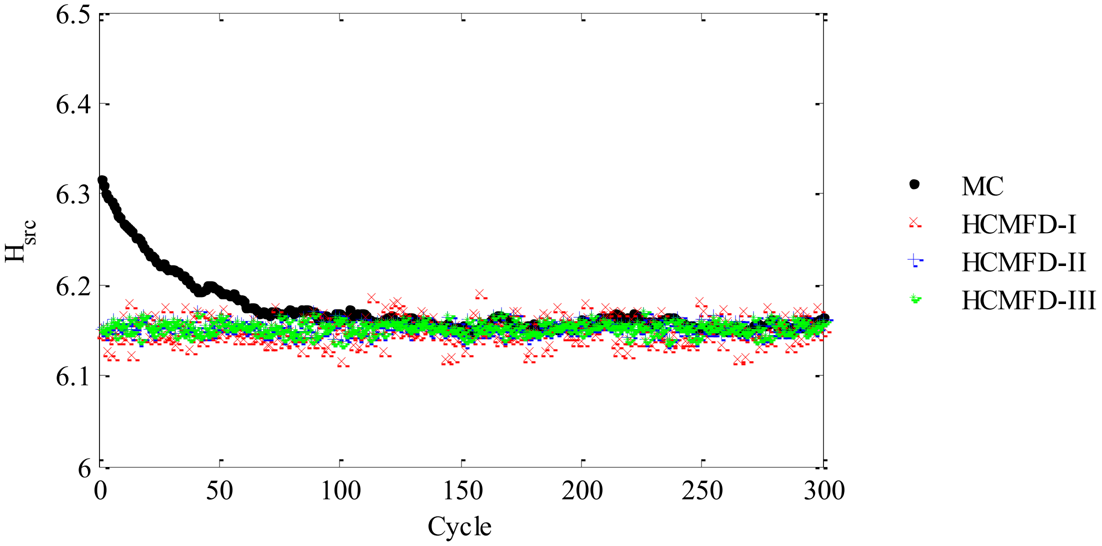

Figure 6.6 Shannon entropy behavior of 40 cm slab (Problem #1B, p=2).

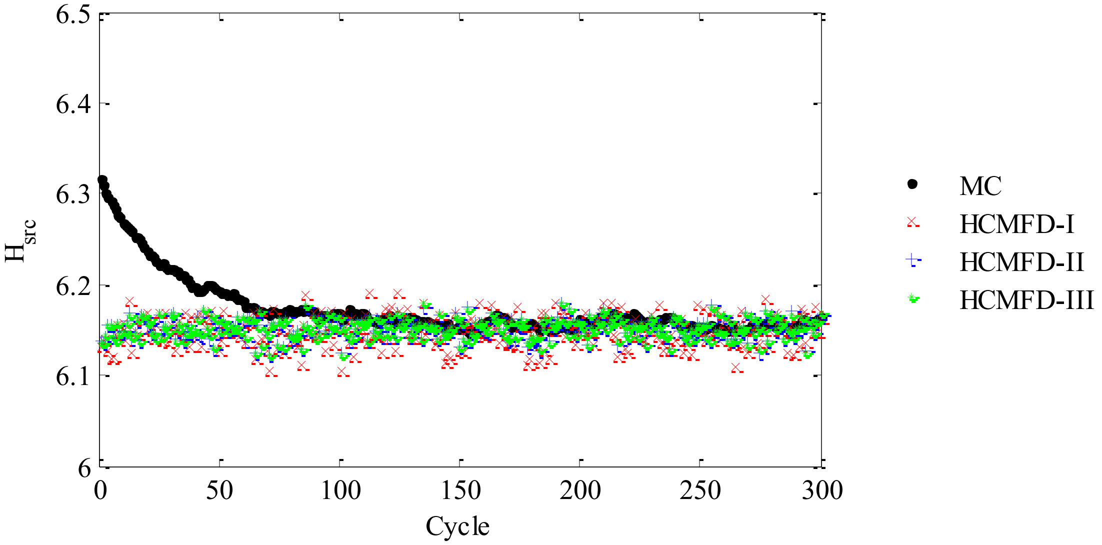

Figure 6.7 Shannon entropy behavior of 40 cm slab (Problem #1B, p=4).

The mean eigenfunction and apparent RSD for $p = 2$ and $p = 4$ are plotted in Figure 6.8 and Figure 6.9, respectively. The mean eigenfunction is *accurate* for all p, for all hybrid methods. However, as p increases, the apparent RSD increases more for HCMFD-II and -III than for HCMFD-I. Again, this is expected because of the cell-averaged approximation to the current used in HCMFD-II and -III.

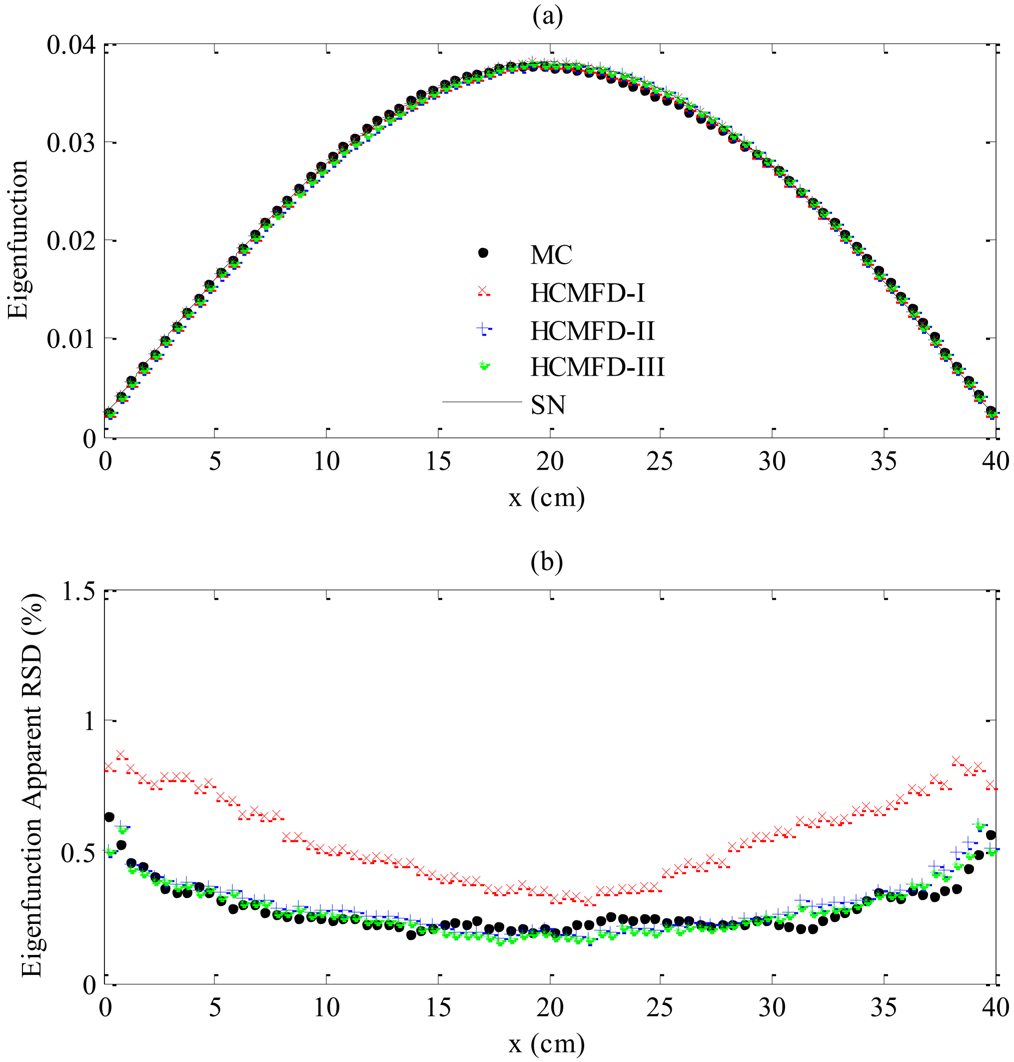

Figure 6.8 Mean eigenfunction and apparent RSD for 40 cm slab (Problem #1B, p=2).

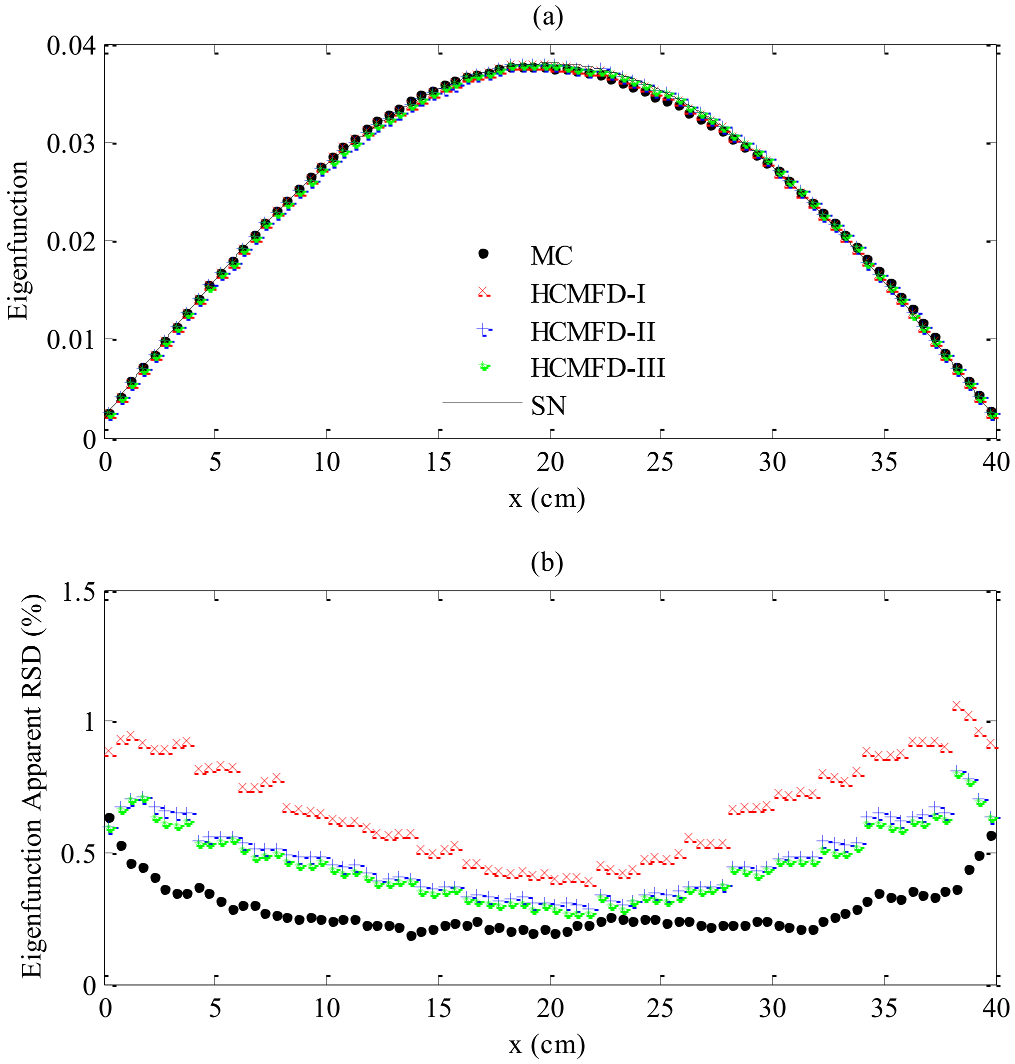

Figure 6.9 Mean eigenfunction and apparent RSD for 40 cm slab (Problem #1B, p=4).

Table 6.7 reports the mean eigenvalues and apparent standard deviations for the benchmark, standard Monte Carlo, and HCMFD-I,-II, and -III methods.

Method		Eigenvalue	Apparent S.D.
S_{16} (Benchmark)		0.956337	-
	MC	0.955782	0.000256
p=1 $\Delta = 0.5$	HCMFD-I	0.956355	0.000015
	HCMFD-II	0.956338	0.000004
	HCMFD-III	0.956338	0.000004
p=2 $\Delta = 1$	HCMFD-I	0.956356	0.000015
	HCMFD-II	0.956339	0.000006
	HCMFD-III	0.956338	0.000006
p=4 $\Delta = 2$	HCMFD-I	0.956360	0.000019
	HCMFD-II	0.956349	0.000013
	HCMFD-III	0.956347	0.000013

Table 6.7 Mean eigenvalues for Criticality Problem #1B.

As p and the optical width of the coarse cell $\Delta = \frac{h_k}{\Sigma_t}$ increase, the apparent standard deviations of $k_{eff}^{(II)}$ and $k_{eff}^{(III)}$ increase more quickly than the standard deviation of $k_{eff}^{(I)}$. Therefore, we must be conscious of the mesh size when using HCMFD-II and HCMFD-III. There is a problem-dependent maximum mesh size at which these methods cease to be advantageous compared to HCMFD-I.

6.4.5 Dependence on Dominance Ratio

We now examine the effect of the dominance ratio on the performances of the hybrid methods. We compare results for the slabs in Problems #1A, #1B , #1C, and #1D ($p = 1$in all cases). The optical width of the coarse cells is $\Delta = 0.5$ mean free paths (mfp). As the slab thickness increases, the dominance ratio increases and causes increasingly slow Monte Carlo fission source convergence. In the following figures, we examine the entropy behavior of the different methods.

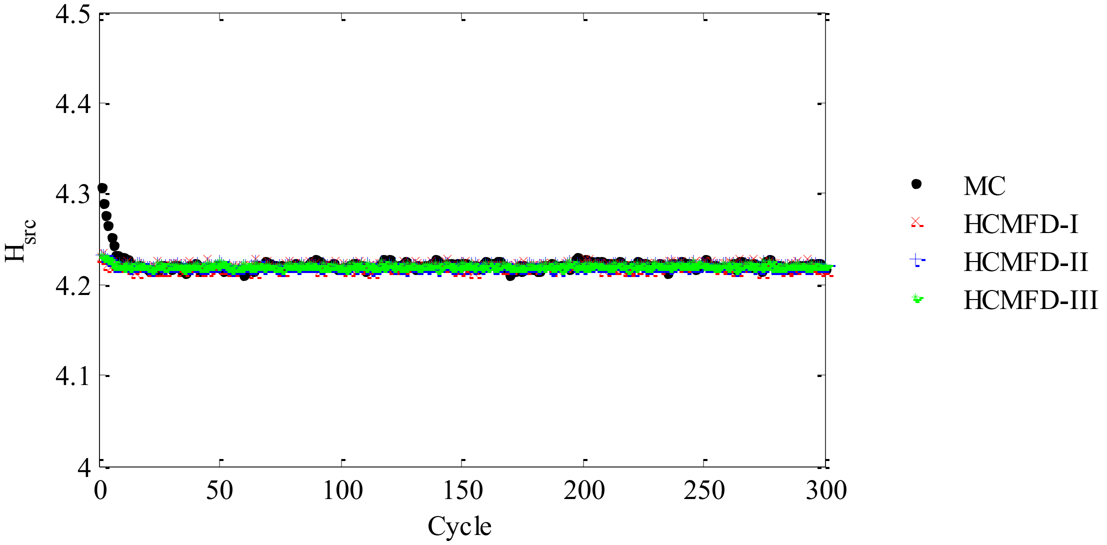

Figure 6.10 Entropy behavior for 10 cm slab (DR=0.874).

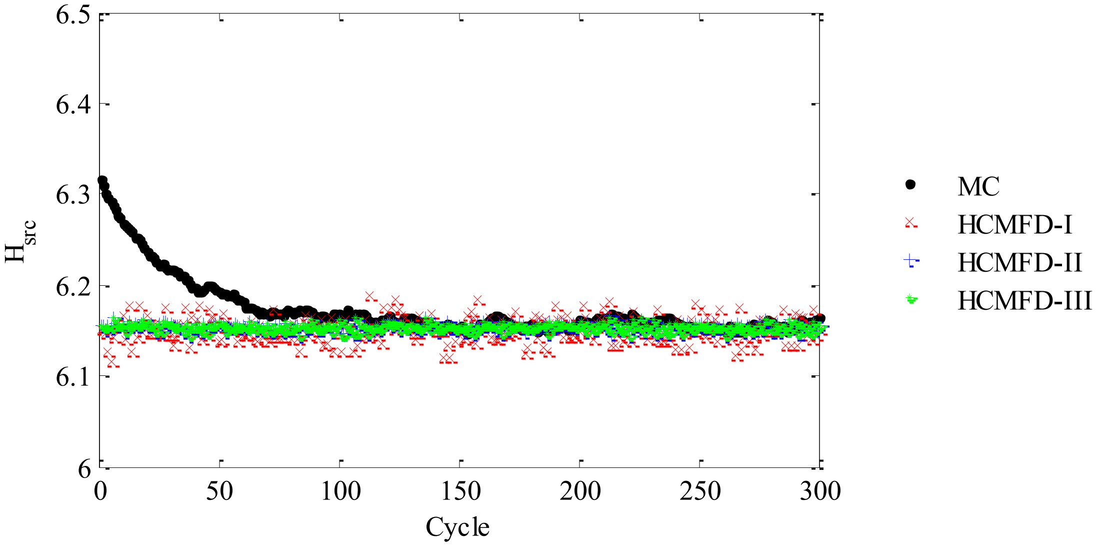

Figure 6.11. Entropy behavior for 40 cm slab (DR=0.989).

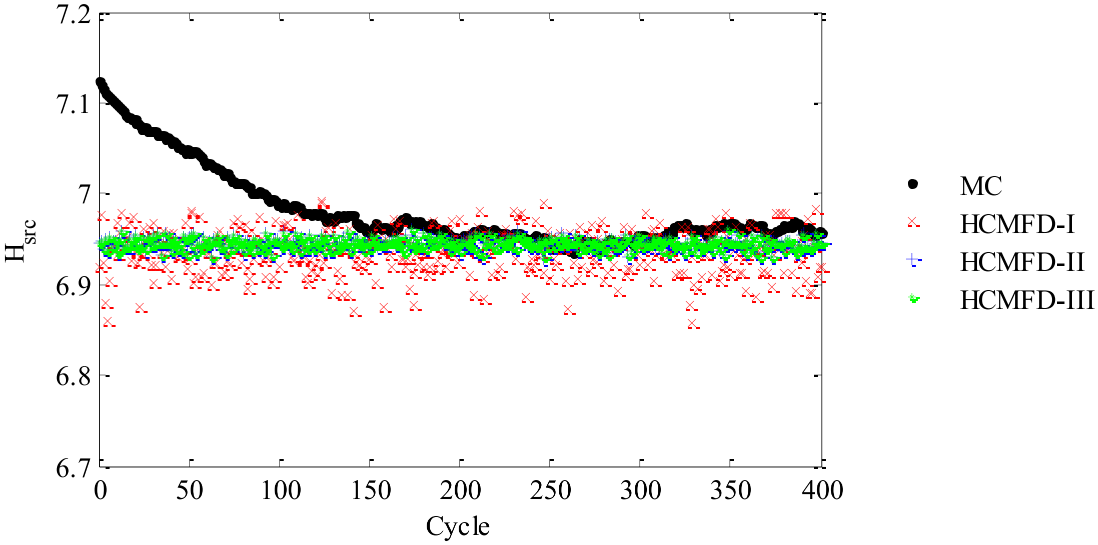

Figure 6.12 Entropy behavior for 70 cm slab (DR=0.996).

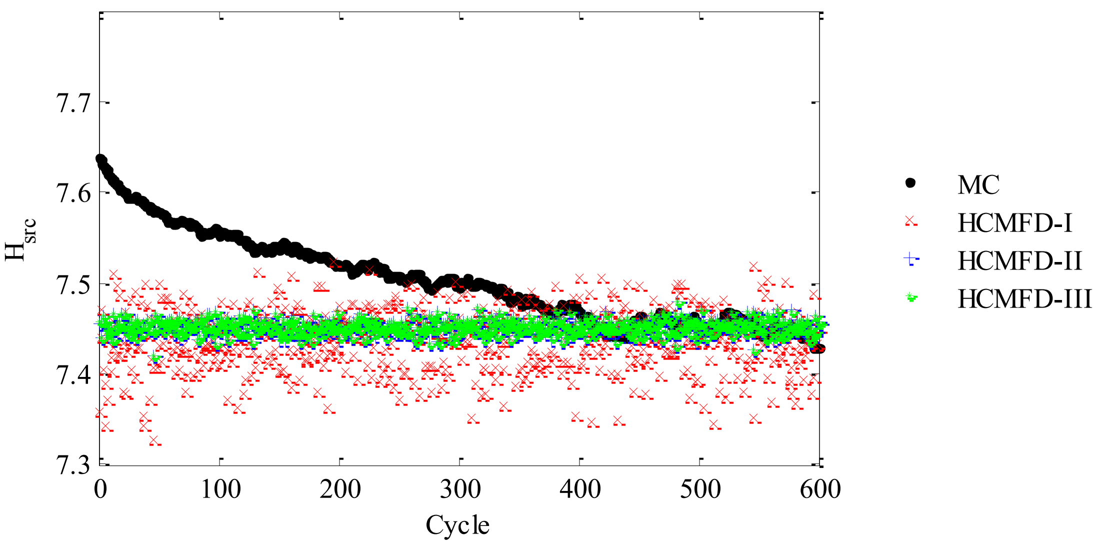

Figure 6.13 Entropy behavior for 100 cm slab (DR=0.998).

Figures 6.10-6.13 are presented with the same entropy scaling. These figures show that the Monte Carlo source convergence is extremely sensitive to the slab width (and dominance ratio). Monte Carlo required approximately 20, 100, 200, and 400 inactive cycles to converge the fission source for slab widths 10, 40, 70, and 100 cm, respectively. In contrast, HCMFD-I, -II, and -III converged the fission source within the first few inactive cycles regardless of the dominance ratio. The variance of the HCMFD-I entropy distribution increased at a faster rate than HCMFD-II and -III for high dominance ratios.

This indicates that HCMFD-I is more sensitive to the dominance ratio than HCMFD-II and -III. We now plot the mean eigenfunctions for the different slab thicknesses.

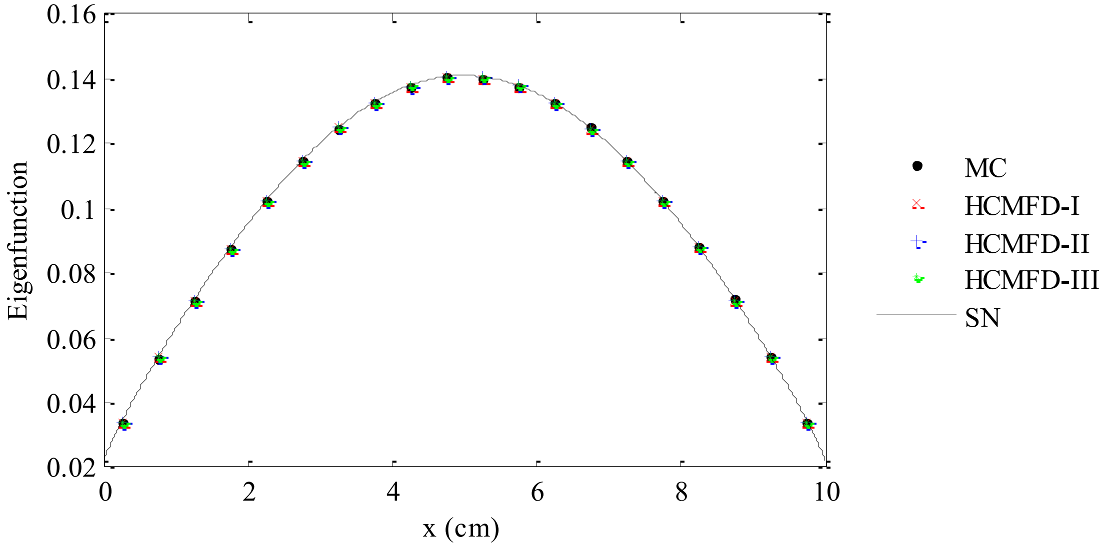

Figure 6.14 Mean eigenfunction for 10 cm slab (DR=0.874).

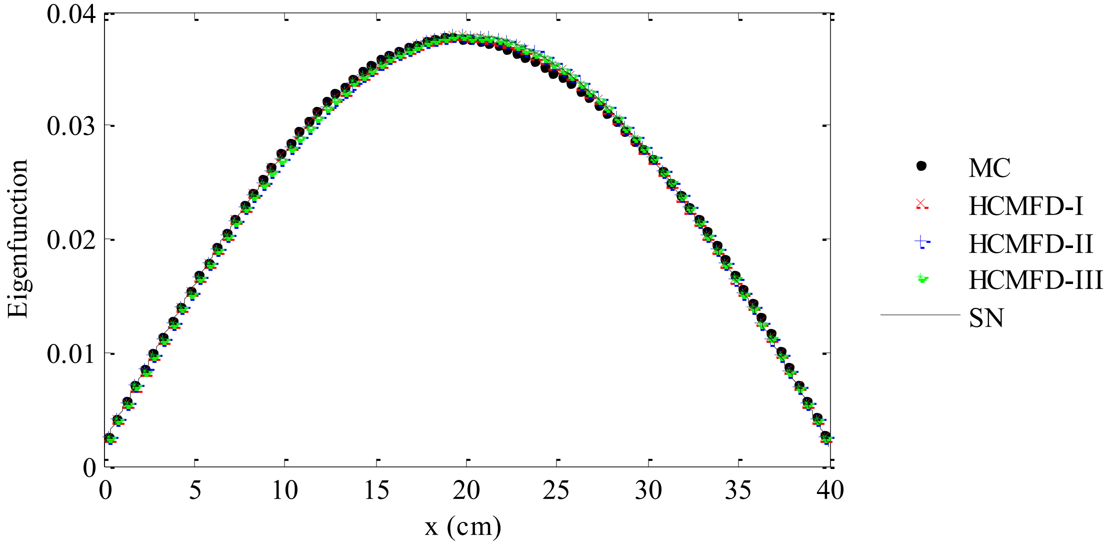

Figure 6.15 Mean eigenfunction for 40 cm slab (DR=0.989).

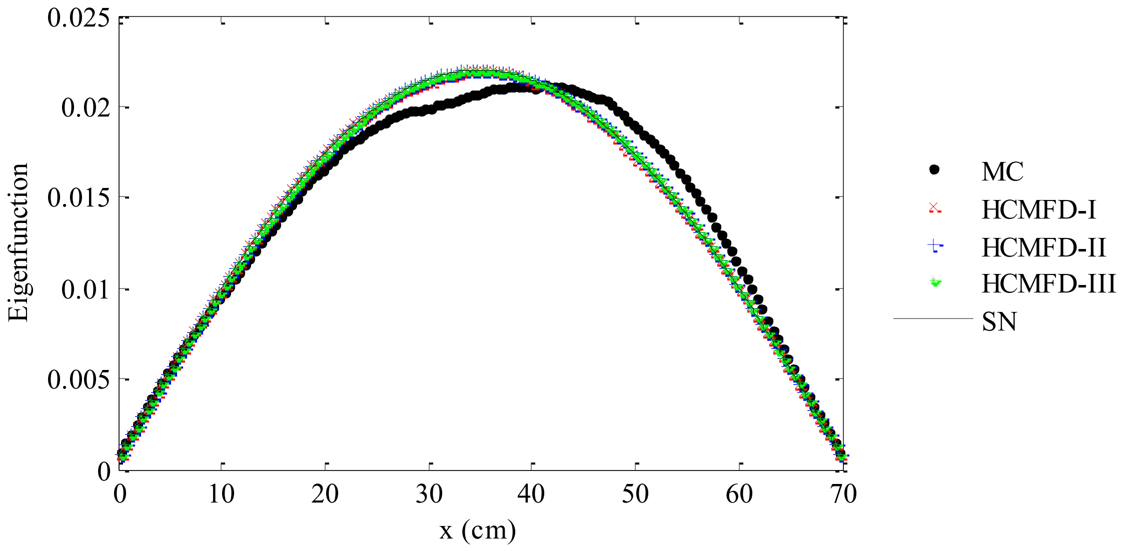

Figure 6.16 Mean eigenfunction for 70 cm slab (DR=0.996).

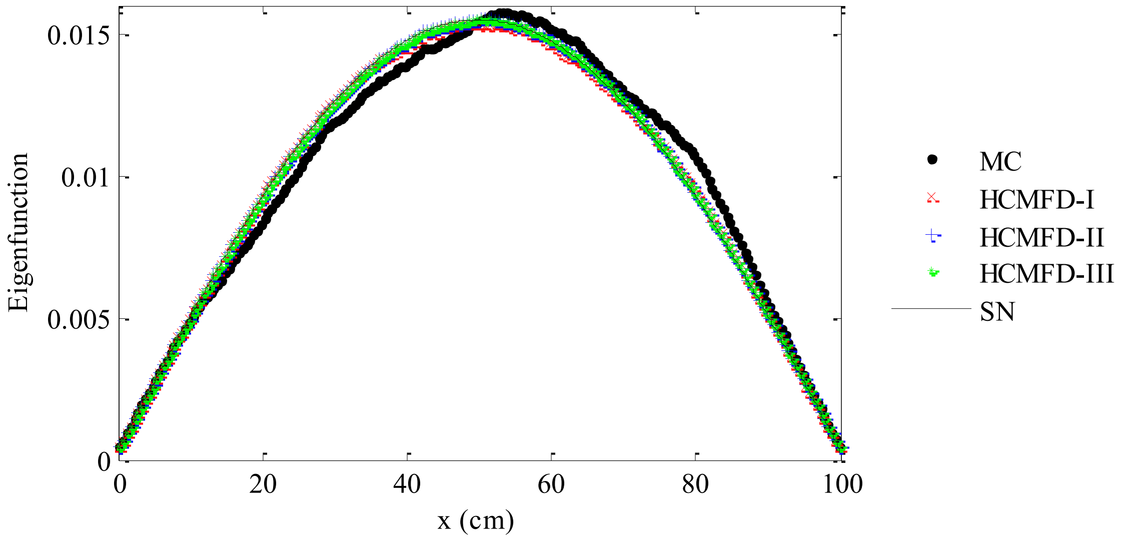

Figure 6.17 Mean eigenfunction for 100 cm slab (DR=0.998).

The Monte Carlo and hybrid method eigenfunctions are both very accurate when the dominance ratio is not close to unity. However, as the slab thickness and dominance ratio increases, Monte Carlo has difficulty keeping the source converged during active cycles, and the Monte Carlo eigenfunction is less accurate. The hybrid method eigenfunctions are more accurate than the standard Monte Carlo eigenfunction, and the HCMFD-II and -III eigenfunctions are consistently more accurate than HCMFD-I.

In the following table, we compare the benchmark S_N eigenvalues with the standard Monte Carlo, HCMFD-I, -II, and -III eigenvalues and apparent standard deviation.

Problem	Method	Eigenvalue	Apparent S.D.
#1A (X=10)	S_{16}	0.914483	-
	MC	0.914182	0.000264
	HCMFD-I	0.914498	0.000046
	HCMFD-II	0.914499	0.000017
	HCMFD-III	0.914501	0.000016
#1B (X=40)	S_{16}	0.956337	-
	MC	0.955782	0.000256
	HCMFD-I	0.956355	0.000015
	HCMFD-II	0.956338	0.000004
	HCMFD-III	0.956338	0.000004
#1C (X=70)	S_{16}	0.958764	-
	MC	0.958328	0.000290
	HCMFD-I	0.958772	0.000008
	HCMFD-II	0.958763	0.000002
	HCMFD-III	0.958763	0.000002
#1D (X=100)	S_{16}	0.959386	-
	MC	0.959164	0.000276
	HCMFD-I	0.959393	0.000006
	HCMFD-II	0.959386	0.000001
	HCMFD-III	0.059386	0.000001

Table 6.8 Eigenvalues and apparent standard deviations for Problems #1A-#1D.

The number of histories per cycle (N) and the number of active cycles (NA) were constant for each test problem. The apparent standard deviation of the standard Monte Carlo eigenvalues is approximately the same for each test problem. However, the apparent standard deviation cannot be trusted because it increasingly underestimates the true standard deviation as the dominance ratio increases. This is discussed in Section

6.4.8. The HCMFD-I, -II, and -III eigenvalues are more accurate than the standard Monte Carlo eigenvalues: their estimates are generally well within one standard deviation of the benchmark. The HCMFD-II and –III eigenvalues are more accurate than the HCMFD-I eigenvalues for all problems except #1A, which has the lowest dominance ratio. This could be due to the fact that the mesh size in Problem #1A is large compared to the overall problem, and the current gradient over adjacent cells is larger than in Problems #1B-#1D. As previously discussed, this causes larger statistical variation in the HCMFD-II and -III solutions.

6.4.6 Performance for Small Number of Histories per Cycle

When the number of histories per cycle is small, the Monte Carlo eigenfunction may be inaccurate even when numerous active cycles are performed. This effect is most pronounced in problems with high dominance ratios, and is due to inter-cycle source correlation and slow source convergence. We examine Problem #1D and show that the standard Monte Carlo eigenfunction is inaccurate unless a sufficient number of histories per cycle are used. Then, we show that the HCMFD eigenfunctions are more accurate than the Monte Carlo eigenfunction when a small number of histories is used.

Problem #1D was simulated using 500 active cycles and different numbers of histories: N=50,000, 250,000 and 1 million histories per cycle. The standard Monte Carlo results are shown in Figure 6.18. The error in the Monte Carlo eigenfunction is apparent even for the N=1,000,000 calculation, but it is worst for N=50,000. Figure 6.19 plots the HCMFD-I, -II and –III eigenfunctions for the N=50,000 Monte Carlo calculation.

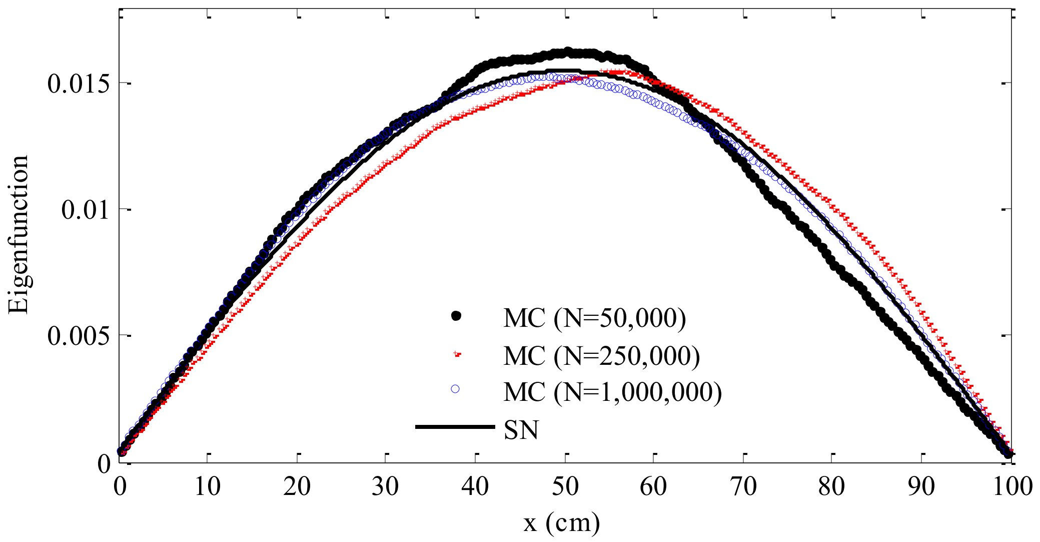

Figure 6.18 Standard Monte Carlo eigenfunctions for various number of histories per cycle.

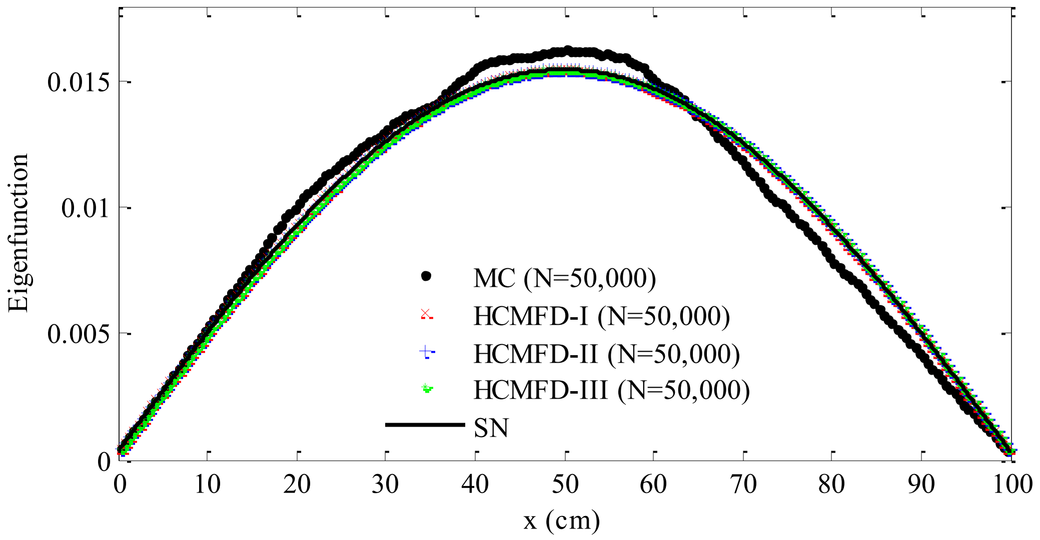

Figure 6.19 HCMFD eigenfunctions for small number of histories per cycle.

The HCMFD eigenfunctions in Figure 6.19 are very accurate, even though they were computed with a small number of histories per cycle. Therefore, when the number of histories per cycle is limited, the HCMFD eigenfunctions are much more accurate than the standard Monte Carlo calculation. [Note: For this problem, no significant error in the eigenvalue was observed, but the HCMFD eigenvalue is also more accurate than the standard Monte Carlo eigenvalue for problems. This follows logically from the reduction in eigenfunction error shown here, and the results in the previous sections.]

It is important to note that when the number of particles per cycle is too small, the correction factors $\hat{D}_{k+1/2}^{(I-III)}$ and boundary functionals B_1 and B_K cannot be estimated, and the CMFD calculations cannot be performed. For this problem, the CMFD calculations could not be performed when $N \leq 25,000$ histories per cycle.

6.4.7 Performance for Small Number of Active Cycles

In high dominance ratio criticality problems, the Monte Carlo estimates of the eigenfunction and eigenvalue must be averaged over several hundred active cycles. The Monte Carlo eigenfunction and eigenvalue estimates from a given single cycle are not very accurate, but averaging over many cycles reduces statistical errors and produces a good estimate of the true values. We now show that the HCMFD methods require fewer active cycles than standard Monte Carlo to obtain accurate estimates of the eigenfunction and eigenvalue for a high dominance ratio problem.

Problem #1D (the 100 cm slab) was simulated with 100,000 histories per cycle with 1 active cycle, and with 10 active cycles. The mean HCMFD and Monte Carlo eigenfunctions are compared in Figure 6.20. The mean eigenvalues are compared to the benchmark S_N eigenvalue, $k_{eff} = 0.959386$ in Table 6.9. The error is listed in per cent mille $(1 \text{ pcm} = 10^{-5} \frac{\Delta k}{k})$.

(a) Number of Active Cycles = 1

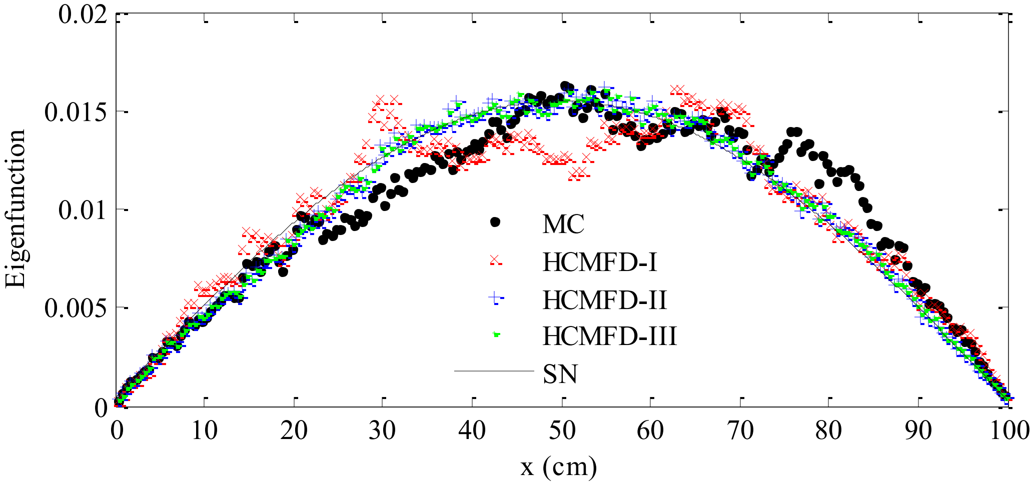

(b) Number of Active Cycles = 10

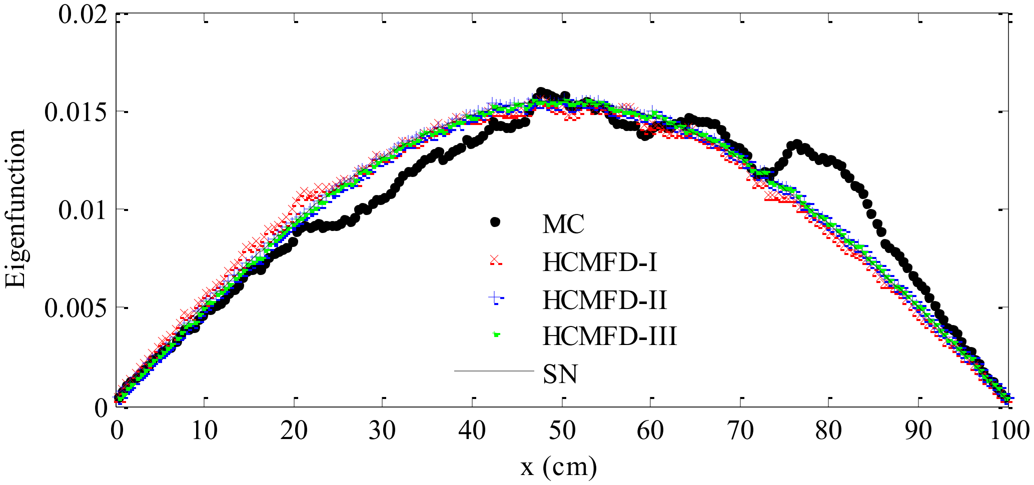

Figure 6.20 Eigenfunctions averaged over one and ten active cycles.

Method	**Eigenvalue (Error compared to S_N [pcm])**		
	NA=1	**NA=10**	**NA=200**
MC	0.961257 (195)	0.959109 (-29)	0.959164 (-23)
HCMFD-I	0.959367 (2)	0.959393 (1)	0.959393 (1)
HCMFD-II	0.959396 (1)	0.959392 (1)	0.959386 (0)
HCMFD-III	0.959397 (1)	0.959392 (1)	0.959386 (0)

Table 6.9 Eigenvalue averaged over one and ten active cycles.

The results for a single cycle are remarkable: the HCMFD eigenfunctions and eigenvalues are very close to the benchmark solution. The HCMFD-II and -III eigenfunctions are significantly more accurate than the HCMFD-I eigenfunction. The three hybrid methods are all much more accurate than the standard Monte Carlo eigenfunctions and eigenvalues.

These results show that the individual cycle estimates of the HCMFD eigenfunction and eigenvalue are very accurate. Therefore, very few active cycles are necessary to obtain accurate HCMFD solutions for high dominance ratio problems. In contrast, many active cycles are necessary to obtain accurate solutions in standard Monte Carlo.

6.4.8 Real vs. Apparent Variance

We have stated that the apparent standard deviations (square root of the apparent variance) plotted in the previous figures should not be trusted yet. To explain the difference between “real” and “apparent” variance, we consider an individual standard Monte Carlo criticality calculation with NA active cycles. This simulation generates an estimate of the mean eigenfunction in a specific spatial cell, $\hat{\phi}_{NA}$, where the mean has been obtained by averaging individual cycle estimates, ϕ_n, over active cycles. The apparent variance of the mean eigenfunction, $\sigma^2\left(\hat{\phi}_{NA}\right)$, is computed with the sample variance of the mean formula from Chapter 1:

$$\sigma^2\left(\hat{\phi}_{NA}\right)=\frac{1}{NA-1}\left[\frac{1}{NA}\sum_{n=1}^{NA}\phi_n^2-\left(\frac{1}{NA}\sum_{n=1}^{NA}\phi_n\right)^2\right]. \tag{6.6}$$

The value $\sigma^2\left(\hat{\phi}_{NA}\right)$ in Eq. (6.6) reflects the uncertainty in the mean $\hat{\phi}_{NA}$ due to fluctuations over the active cycles in an individual simulation.

If we were to repeat this simulation K independent times, we would obtain K estimates: $\hat{\phi}_{NA,k}$ and $\sigma_k^2\left(\hat{\phi}_{NA,k}\right)$. The "average apparent variance" of the $\hat{\phi}_{NA}$ samples is estimated by averaging the apparent variances:

$$\sigma_A^2=\frac{1}{K}\sum_{k=1}^{K}\sigma_k^2\left(\hat{\phi}_{NA,k}\right). \tag{6.7}$$

The "real variance" of the $\hat{\phi}_{NA}$ samples is estimated using the sample pdf variance formula:

$$\sigma_R^2=\frac{K}{K-1}\left[\frac{1}{K}\sum_{k=1}^{K}\left(\hat{\phi}_{NA,k}\right)^2-\left(\frac{1}{K}\sum_{k=1}^{K}\hat{\phi}_{NA,k}\right)^2\right]. \tag{6.8}$$

The real and apparent variances of the $\hat{\phi}_{NA}$ samples in Eqs. (6.7) and (6.8) should be *identical* when there is no correlation of the Monte Carlo eigenfunction between cycles. However, correlation does exist between cycles: the fission source from the previous cycle determines the fission source for the next cycle. In high dominance ratio problems, the correlation is very high because the eigenfunction (and therefore the fission source) changes very little within a cycle.

Due to inter-cycle correlation, the *apparent standard deviation* underestimates the *real standard deviation* in standard Monte Carlo. In this section, we show that the apparent variance of the CMFD eigenfunctions is a *much* better estimate of the real variance of these eigenfunctions than in standard Monte Carlo.

To demonstrate this, Problem #1C was simulated with 100,000 histories per cycle and 25 active cycles. The simulation was performed K=25 independent times, generating 25 independent estimates of the mean eigenfunction and apparent variance. The average *apparent variance* and *real variance* of the mean eigenfunction were calculated from Eqs. (6.7) and (6.8). The apparent and real relative standard deviations (RSD) are plotted in Figure 6.21.

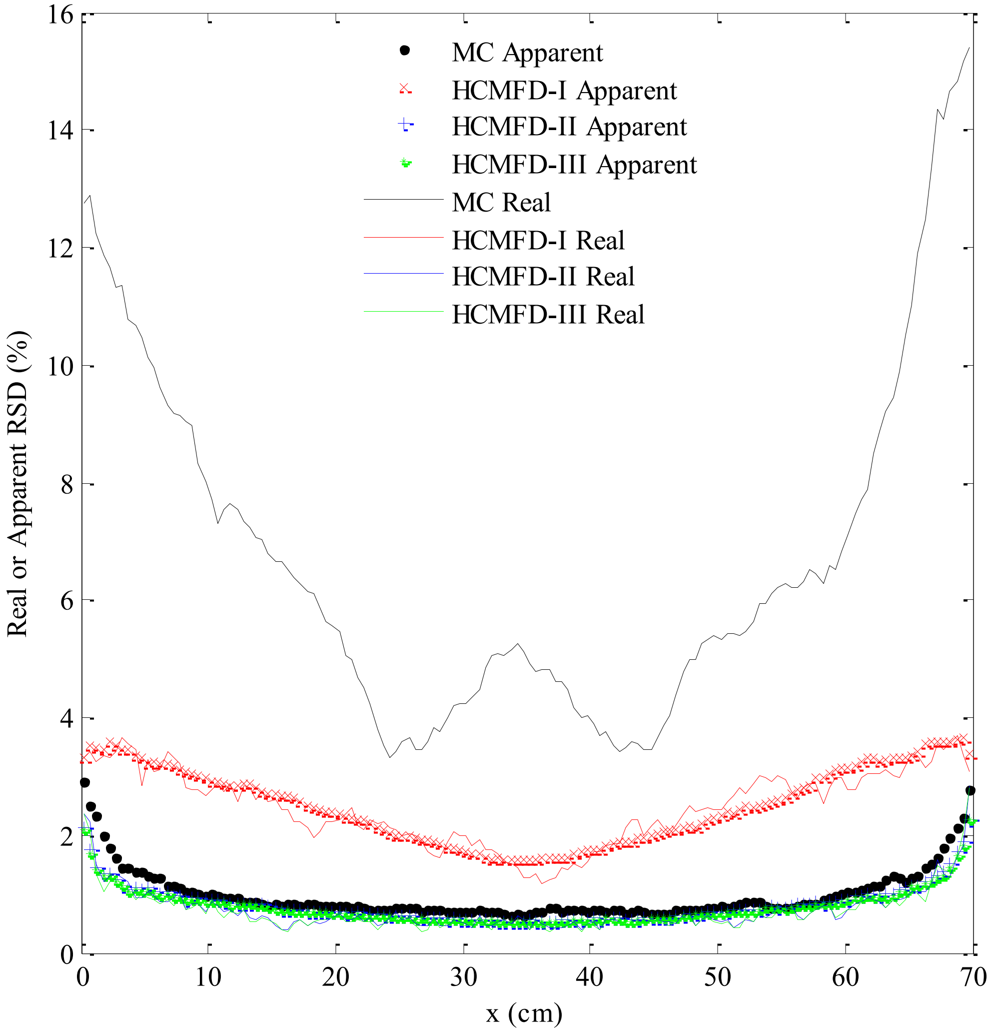

Figure 6.21 Real and apparent standard deviations of the mean eigenfunction.

We emphasize two important things about Figure 6.21. First, the real RSD of the HCMFD-II and -III eigenfunctions ranges between 1-2% for this test problem, while the real RSD of the HCMFD-I eigenfunction is about 2-4%, and the real RSD of the standard Monte Carlo eigenfunction is 4-15%. Therefore, use of the HCMFD-II and –III methods results in a significant reduction of *real* error. The HCMFD-II and –III methods achieve a given *real* error after approximately 1% of the standard Monte Carlo computing time. Therefore, the HCMFD-II and –III methods are 100 times faster than a standard Monte Carlo calculation. This computational savings refers to the number of active cycles required (or the number of histories per cycle). Additionally, fewer inactive cycles are required for convergence, which further increases the computational savings.

The second important point is that the *real* RSD of the HCMFD eigenfunctions is approximately equal to the *apparent* RSD. However, the real RSD of standard Monte Carlo is a factor of 4 to 9 greater than the apparent RSD. This can be seen by plotting the ratio of real to apparent standard deviation:

$$r_{R/A} \equiv \frac{\sigma_R}{\sigma_A} = \sqrt{\frac{\sigma_R^2}{\sigma_A^2}}. \tag{6.9}$$

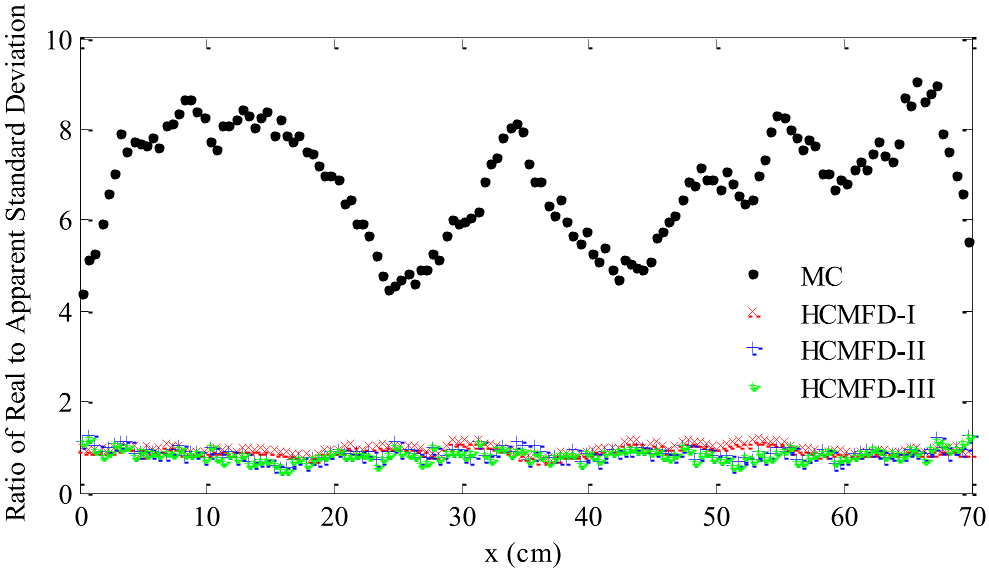

Figure 6.22 Ratio of real to apparent standard deviation.

Figure 6.22 shows that for the specified problem, the *real error* in standard Monte Carlo is 4 to 9 times greater than the apparent error. However, the real error in the HCMFD methods is approximately equal to the apparent error. Therefore, the apparent standard deviation of the HCMFD methods is a reliable estimator of the true standard deviation. However, the Monte Carlo apparent standard deviation underestimates the real standard deviation by a large factor and should not be trusted. These results confirm the relationship between real and apparent variance of the HCMFD-I method (shown by Lee, et al. [5]), and show that the same relationship holds for the HCMFD-II and -III methods.

6.5 Criticality Problem #2: Two-Fissile Region Slab

6.5.1 Problem Description

Criticality Problem #2 consists of a heterogeneous, isotropically-scattering 27 cm slab with vacuum boundaries. Two 5 cm fissile regions are separated by a 7 cm reflector and bordered by 5 cm reflectors. The material specifications are listed in Table 6.10.

Region	Location [cm]	Σ_t [cm^{-1}]	Σ_s [cm^{-1}]	Σ_f [cm^{-1}]	ν
1	$0 < x < 5$	1.0	0.856	0.0	-
2	$5 < x < 10$	1.0	0.8	0.1	2.4
3	$10 < x < 17$	1.0	0.856	0.0	-
4	$17 < x < 22$	1.0	0.8	0.1005	2.4
5	$22 < x < 27$	1.0	0.856	0.0	-

Table 6.10 Material specifications of Problem #2.

Because the fissile regions in this problem are separated, the eigenfunction is extremely sensitive to any small changes in any of the system parameters. (The eigenvalue is not as sensitive.) The slight asymmetry (0.5%) in the fission cross sections of this problem makes source convergence very difficult in both Monte Carlo and deterministic methods. The challenges in Problem #2 are characteristic of criticality problems for subcritical spent fuel storage facilities.

6.5.2 Numerical Parameters

The Monte Carlo specifications for Problem #2 are listed in Table 6.11.

Number of Histories/Cycle (N)	Inactive Cycles (NI)	Active Cycles (NA)	Fine Grid [cm]	CMFD Parameter p
200,000	500	500	0.5	1

Table 6.11 Numerical parameters of Problem #2.

A benchmark S_{32} solution was performed with a uniform 0.001 cm grid.

6.5.3 Numerical Results

The cycle-wise entropy behavior is plotted in Figure 6.23, and the cycle-wise eigenvalues for Problem #2 are plotted in Figure 6.24.

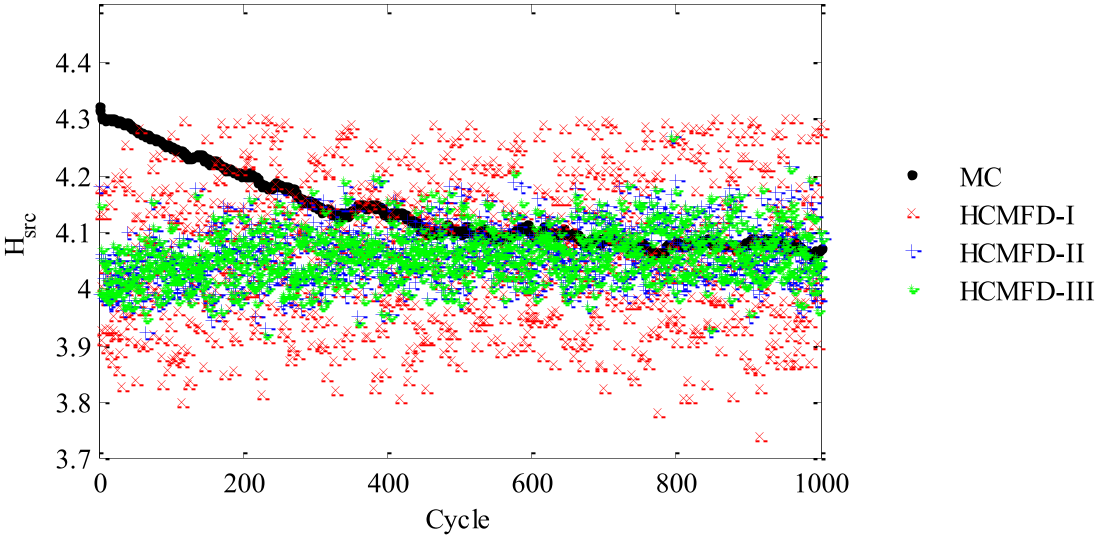

Figure 6.23 Shannon entropy behavior of Problem #2.

The HCMFD-I, -II, and –III methods converged the fission source within approximately the first twenty cycles, compared to 600 cycles in standard Monte Carlo.

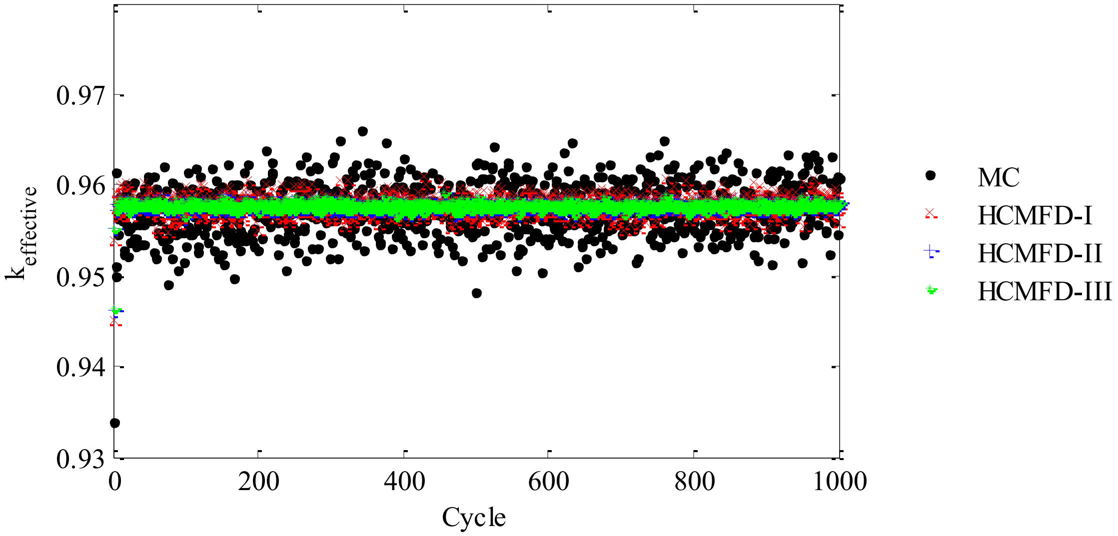

Figure 6.24 Eigenvalue behavior of Problem #2.

The mean eigenfunctions and their apparent RSD are plotted in Figure 6.25. The HCMFD-II and –III eigenfunctions were very close to the benchmark S_N solution. The HCMFD-I eigenfunction was less accurate than the standard Monte Carlo solution, shown in Figure 6.26.

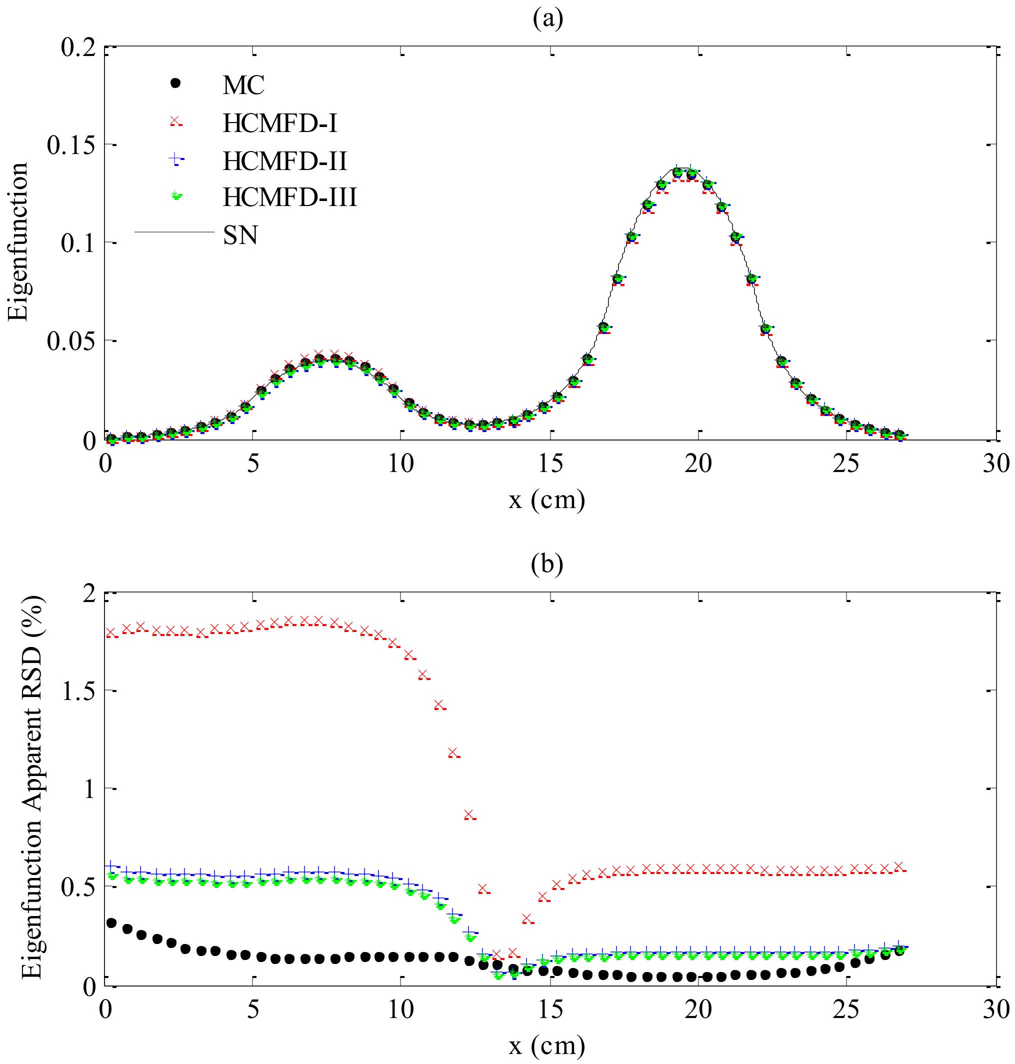

Figure 6.25 Mean eigenfunction and apparent RSD of Problem #2.

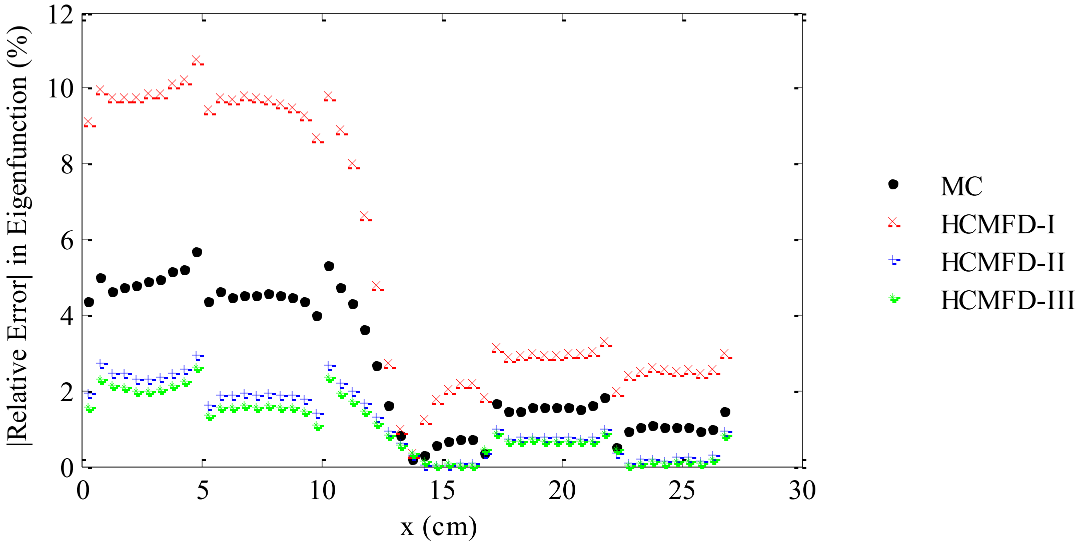

Figure 6.26 Relative error in eigenfunction compared to benchmark solution for Problem #2.

This problem was repeated with a larger number of histories per cycle (500,000), and similar results were obtained (HCMFD-II and –III were most accurate, followed by standard Monte Carlo, and then HCMFD-I). We emphasize that this problem is particularly difficult for most computational methods because small changes in the cross sections lead to large changes in the eigenfunction. Increasing the number of active cycles may improve the HCMFD-I solution, but our results suggest that the proposed HCMFD-II and HCMFD-III methods are more accurate and less sensitive to statistical errors than the HCMFD-I method. We emphasize that *identical* particle histories were used to generate the MC, HCMFD-I, HCMFD-II and HCMFD-III solutions. The eigenvalues and standard deviations are presented in Table 6.12.

Method		**Eigenvalue**	**Apparent S.D.**
S_{32} (Benchmark)		0.957779	-
MC		0.957618	0.000120
p=1	HCMFD-I	0.957897	0.000044
	HCMFD-II	0.957799	0.000016
	HCMFD-III	0.957801	0.000015

Table 6.12 Mean eigenvalues for Problem #2.

The HCMFD-II and -III eigenvalues are closer to the benchmark eigenvalue, and they have lower apparent standard deviation than the standard Monte Carlo and HCMFD-I eigenvalues. These results suggest that for extremely sensitive problems like Problem #2, the HCMFD-II and HCMFD-III methods are more accurate for calculating both the eigenfunction and eigenvalue.

6.6 Criticality Problem #3: Heterogeneous Reactor Core

Problem #3 is a 1-D, 1-G heterogeneous reactor core problem formulated by M.J. Lee and H.G. Joo of Seoul National University. The 346.8 cm core consists of 17 assemblies. Each assembly consists of 16 pin cells, and each pin cell consists of three 0.425 cm material regions. This problem illustrates that the hybrid Monte Carlo-CMFD methods are effective for more realistic geometrically-detailed problems. The core, assemblies, pin cells, and materials are defined in the following figures and tables.

R	**C**	**C**	**B**	**B**	**M**	**B**	**B**	**M**	**B**	**B**	**M**	**B**	**B**	**A**	**C**	**R**

Figure 6.27 Core configuration for Problem #3 consisting of 17 assemblies.

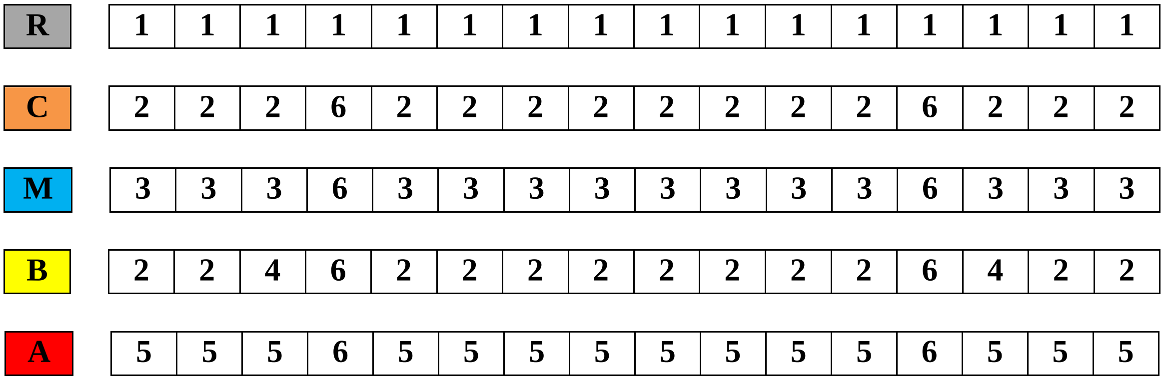

R	**1**	**1**	**1**	**1**	**1**	**1**	**1**	**1**	**1**	**1**	**1**	**1**	**1**	**1**	**1**	**1**
C	**2**	**2**	**2**	**6**	**2**	**2**	**2**	**2**	**2**	**2**	**2**	**2**	**6**	**2**	**2**	**2**
M	**3**	**3**	**3**	**6**	**3**	**3**	**3**	**3**	**3**	**3**	**3**	**3**	**6**	**3**	**3**	**3**
B	**2**	**2**	**4**	**6**	**2**	**2**	**2**	**2**	**2**	**2**	**2**	**2**	**6**	**4**	**2**	**2**
A	**5**	**5**	**5**	**6**	**5**	**5**	**5**	**5**	**5**	**5**	**5**	**5**	**6**	**5**	**5**	**5**

Figure 6.28 Assembly configurations (16 pin cells each) for Problem #3.

1	**Reflector**	**m6**	**m6**	**m6**
2	**UO$_2$ Pin A**	**m1**	**m2**	**m1**
3	**MOX Fuel**	**m1**	**m3**	**m1**
4	**GD Fuel**	**m1**	**m4**	**m1**
5	**UO$_2$ Pin B**	**m1**	**m5**	**m1**
6	**Water Hole**	**m7**	**m7**	**m7**

Figure 6.29 Pin cell configurations (three 0.425 cm material regions each) for Problem #3.

Material	**Description**	Σ_t	Σ_s	$\Sigma_a = \Sigma_\gamma + \Sigma_f$	$\nu\Sigma_f$
m1	Water adjacent to Fuel	1.74712e-01	1.73779e-01	9.33242e-04	-
m2	UO$_2$ Fuel A	3.32736e-01	2.74910e-01	5.78256e-02	7.97840e-02
m3	MOX Fuel	2.82549e-01	2.14888e-01	6.76607e-02	8.64238e-02
m4	UO$_2$ Fuel with Gd	8.58461e-02	4.32728e-02	4.25733e-02	1.85589e-03
m5	UO$_2$ Fuel B	3.33356e-01	2.75534e-01	5.78218e-02	7.96455e-02
m6	Water in Reflector	7.85602e-02	7.77942e-02	7.65957e-04	-
m7	Water in Water Hole	9.01554e-02	8.96296e-02	5.25823e-04	-

Table 6.13 Material cross sections for Problem #3.

The numerical parameters of the calculation are listed in Table 6.14. The Monte Carlo calculation was performed on a fine grid (0.425 cm) with 816 spatial cells, and the hybrid CMFD methods were performed on a coarse grid on the quarter assembly level (5.1 cm) with A benchmark S_{32} calculation was performed with a uniform 0.05375 cm grid.

Histories/Cycle	**Inactive Cycles**	**Active Cycles**	**Fine Grid [cm]**	**CMFD Parameter** p
100,000	150	100	0.425	12

Table 6.14 Numerical parameters of Problem #3.

The Shannon entropy behavior of Problem #3 is plotted in Figure 6.30. The HCMFD calculations converged the fission source within 20 cycles, and the standard Monte Carlo source required approximately 150 cycles.

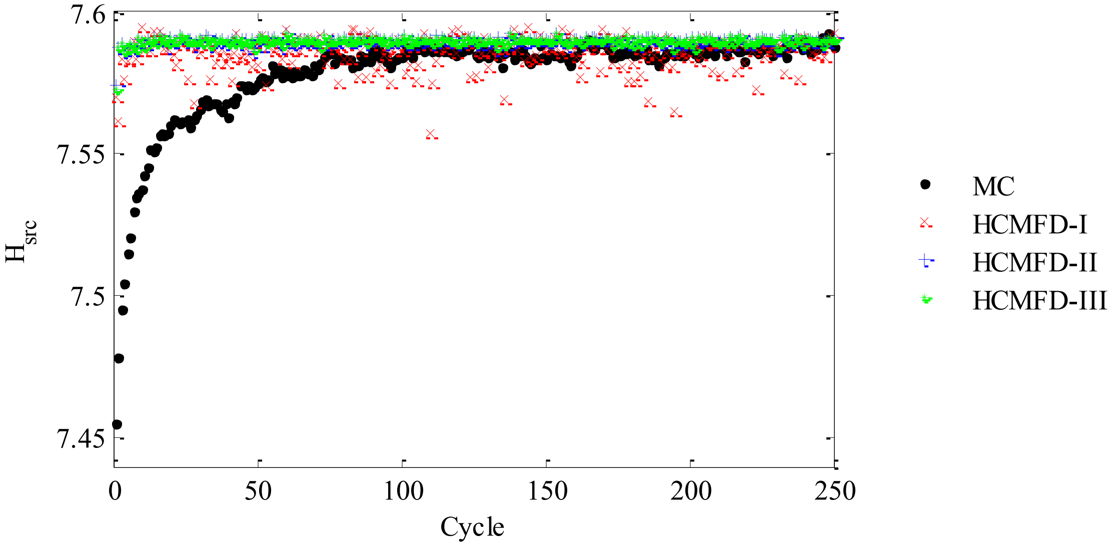

Figure 6.30 Shannon entropy behavior of Problem #3.

The cycle-wise eigenvalue estimates are plotted in Figure 6.31.

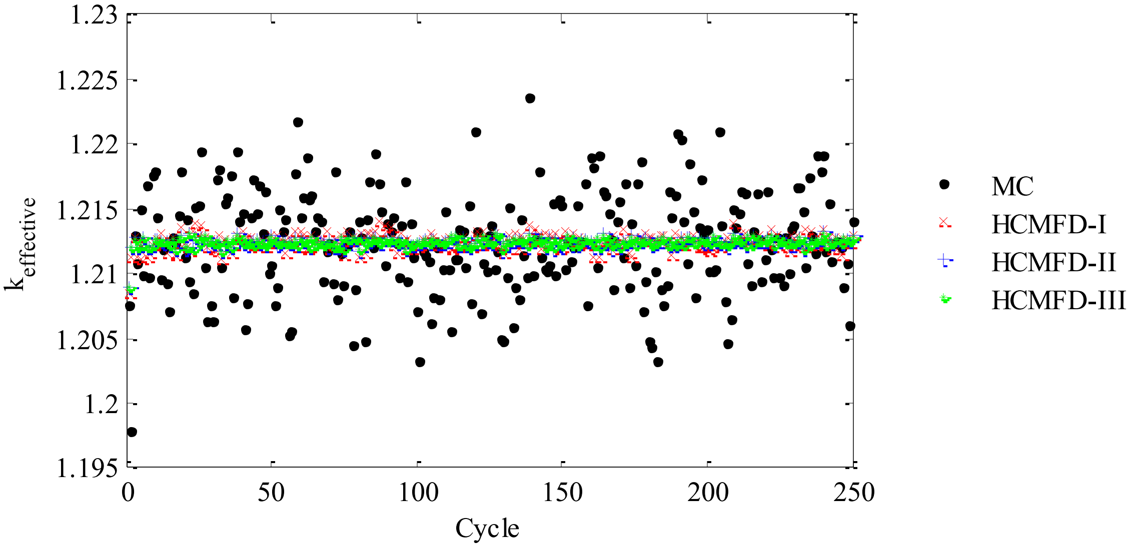

Figure 6.31 Eigenvalue behavior of Problem #3.

The mean eigenfunction and apparent RSD are plotted in Figure 6.32. In addition, the relative errors of each eigenfunction compared to the benchmark solution are plotted in Figure 6.33. The apparent standard deviations in Figure 6.32 underestimate the *true* standard deviation, but the results in Section 6.4.8 suggest that the HCMFD-I, -II, and –III methods underestimate the true variance much less than standard Monte Carlo.

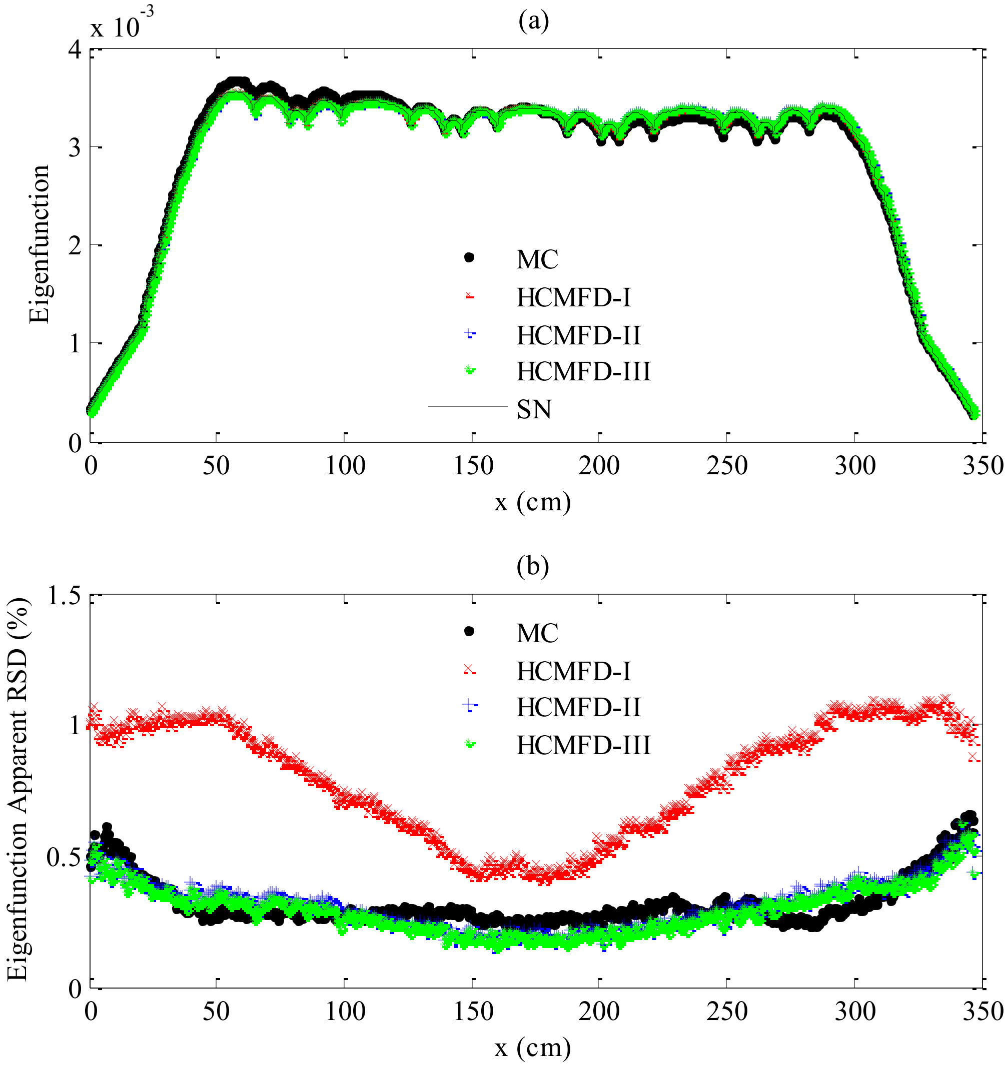

Figure 6.32 Mean eigenfunction and apparent RSD of Problem #3.

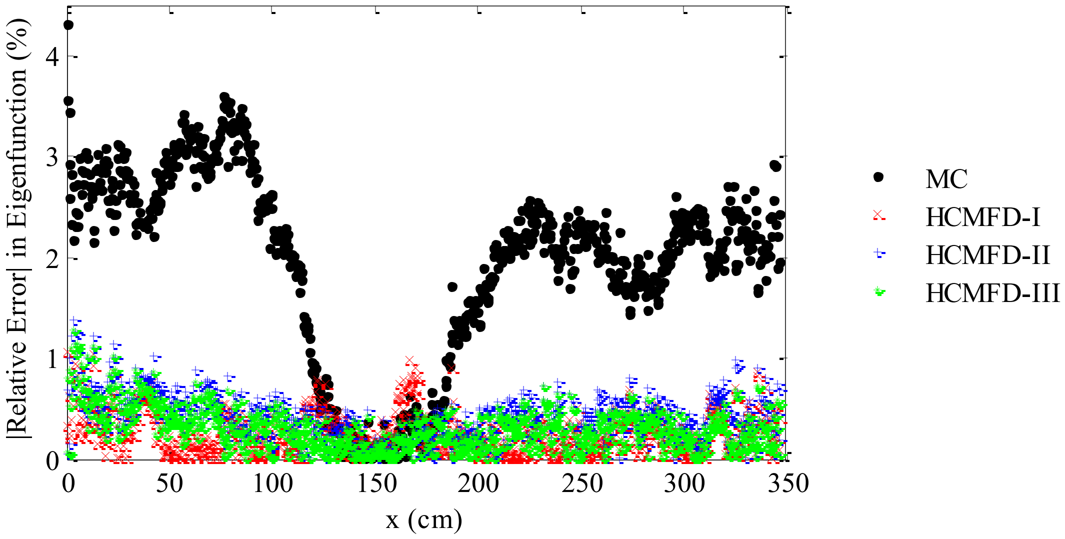

Figure 6.33 Relative error in eigenfunction compared to benchmark solution for Problem #3.

From Figure 6.33, the HCMFD-I, -II, and –III eigenfunctions have similar accuracy; they each differ about 1% from the benchmark solution. In contrast, the standard Monte Carlo eigenfunction differs up to 3.5% from the benchmark solution. While HCMFD-I, -II, and –III have similar accuracy, the apparent standard deviation of HCMFD-II and HCMFD-III is about half that of HCMFD-I.

The eigenvalue results are presented in Table 6.15. There may be a small bias in the Monte Carlo-based calculations, which could be suppressed by using more histories per cycle. However, the HCMFD-I, -II, and –III are much closer to the benchmark eigenvalue than standard Monte Carlo.

Method		Eigenvalue	S.D.
S_{16} (Benchmark)		1.212212	-
MC		1.212821	0.000386
p=12 (Quarter Assembly)	HCMFD-I	1.212504	0.000050
	HCMFD-II	1.212512	0.000027
	HCMFD-III	1.212512	0.000025

Table 6.15 Summary of eigenvalue results for Problem #3.

We emphasize that this problem was performed with a very coarse mesh (on the quarter assembly level). As previously discussed, the HCMFD-II and HCMFD-III are more sensitive to mesh size than HCMFD-I, but for this problem, HCMFD-II and HCMFD-III still yielded excellent results. If the mesh size were decreased, the HCMFD-II and HCMFD-III solutions would improve.

6.7 Summary of Numerical Results

At the beginning of this chapter, we showed that the variances of the HCMFD-I, -II, -III and -IV solutions follow the Central Limit Theorem for a fixed source problem. For this problem, HCMFD-IV had the lowest variance, followed by -III, -II, -I and then standard Monte Carlo. We did not pursue further development of HCMFD-IV due to its limitation of homogeneous coarse cells. The computational efficiency of the HCMFD-II -III and -IV methods (fractional computing times 18-24%) were comparable to the H-MC-S_2X method (19%) for a monoenergetic fixed source problem, whereas the efficiency of the HCMFD-I method was lower (51%).

We then performed several criticality test problems comparing the performance of HCMFD-I, -II, and –III with standard Monte Carlo. No feedback was performed for these simulations, meaning that the HCMFD calculations did not affect the Monte Carlo simulation in any way. The eigenvalues and eigenfunctions of the hybrid methods were more accurate, and had less variance, than those quantities computed with standard Monte Carlo. The HCMFD eigenfunctions converged within a few inactive cycles, even for problems where the dominance ratio is close to unity. In contrast, standard Monte Carlo required several hundred inactive cycles for source convergence. In addition, the HCMFD eigenfunctions are very accurate when small numbers of histories per cycle are used, and when small numbers of active cycles are used. Overall, the number of inactive cycles, number of active cycles, and number of histories can be greatly reduced when performing the HCMFD calculations, with HCMFD-II and –III being more accurate than HCMFD-I when all numerical parameters are identical. For a particular problem, we demonstrated that the HCMFD-II and –III methods require less than 1% of the standard Monte Carlo computing time to achieve equivalent real errors.

The HCMFD-II and –III methods are more sensitive to the coarse mesh size than HCMFD-I, due to the use of a cell-averaged current term in the definition of their correction functionals $\hat{D}^{(II)}_{k+1/2}$ and $\hat{D}^{(III)}_{k+1/2}$. However, when the mesh is fine, these methods outperform HCMFD-I in terms of accuracy and variance. As the mesh becomes coarser, the performances of these three methods become similar.

Finally, the *apparent standard deviation* of the HCMFD solutions is a much more accurate estimator of the *real standard deviation* than in standard Monte Carlo. In standard Monte Carlo, the true standard deviation can be up to an order of magnitude larger than the apparent standard deviation. In HCMFD, the apparent standard deviation is approximately equal to the true standard deviation. Therefore, applying the HCMFD methods to Monte Carlo reduces the *real error*, and this real error can be estimated very accurately. In Chapter 7, we repeat many of these criticality calculations with CMFD “feedback”, in which the CMFD fission source is used to update the Monte Carlo fission source.

6.8 References

[1] F.B. Brown, “Fundamentals of Monte Carlo Particle Transport,” *LA-UR-05-4983*, Los Alamos National Laboratory (2005).

[2] D.P. Griesheimer and B.R. Nease, “Spectral Analysis of Stochastic Noise in Fission Source Distributions from Monte Carlo Eigenvalue Calculations,” *Proc. of the 2010 Joint International Conference on Supercomputing in Nuclear Applications and Monte Carlo,* Oct 17-21, 2010, Tokyo, Japan, CD-ROM, SNA+MC2010 (2010).

[3] M.J. Lee, H.G. Joo, D. Lee, and K. Smith, “Application of CMFD Acceleration to Monte Carlo Simulation for Eigenvalue Problems,” Personal Communication, Saratoga Springs, NY (2009).

[4] M.J. Lee, H.G. Joo, D. Lee, and K. Smith, “Investigation of CMFD Accelerated Monte Carlo Eigenvalue Calculation with Simplified Low Dimensional Multigroup Formulation,” *Proc. of the 2010 International Conference on the Physics of Reactors,* May 9-14, 2010, Pittsburgh, PA, CD-ROM, American Nuclear Society (2010).

[5] M.J. Lee, H.G. Joo, D. Lee, and K. Smith, “Multigroup Monte Carlo Reactor Calculation with Coarse Mesh Finite Difference Formulation for Real Variance Reduction,” *Proc. of the 2010 Joint International Conference on Supercomputing in Nuclear Applications and Monte Carlo*, Oct 17-21, 2010, Tokyo, Japan, CD-ROM, SNA+MC2010 (2010).

Chapter 7

Hybrid Monte Carlo – CMFD Numerical Results with Feedback

7.1 Hybrid Monte Carlo – CMFD with Feedback

In Chapter 6, we compared the HCMFD-I, -II and -III methods with standard Monte Carlo for various criticality problems. The results in Chapter 6 were generated using the procedure referred to as *Hybrid Monte Carlo-CMFD without Feedback.* In this technique, the nonlinear HCMFD functionals are estimated during each cycle and an HCMFD calculation is performed at the end of the cycle. The HCMFD eigenfunction and eigenvalue do not perturb the Monte Carlo calculation in any way. We showed that the HCMFD-I, -II, and -III eigenfunctions and eigenvalues converge more rapidly than the standard Monte Carlo fission source. In addition, the HCMFD eigenfunctions and eigenvalues were more accurate and had less variance than the standard Monte Carlo solution.

In this chapter, we perform criticality problems using *Hybrid Monte Carlo-CMFD with Feedback*. In this procedure, one method is chosen to perform the feedback: HCMFD-I, HCMFD-II, or HCMFD-III. During the i^{th} Monte Carlo cycle, estimates of the Monte Carlo eigenvalue, Monte Carlo eigenfunction, and HCMFD nonlinear functionals are generated. At the end of the cycle, an HCMFD calculation is performed to generate estimates of the HCMFD eigenvalue and HCMFD eigenfunction. If feedback is not applied, the procedure returns to the next Monte Carlo cycle. When feedback is applied, the HCMFD fission source is used to *modify the Monte Carlo fission bank* to match the HCMFD source distribution. The modified Monte Carlo fission bank is then used as the source for cycle $i+1$.

We now describe the details of the fission bank modification. The fission source in HCMFD is converted to a probability density function over coarse cells $1 \le k \le K$:

$$P_k = \frac{\nu\Sigma_{f,k}\phi_k h_k}{\sum_{k'=1}^{K}\nu\Sigma_{f,k'}\phi_{k'}h_{k'}}. \tag{7.1}$$

The HCMFD probability density function in Eq. (7.1) is then multiplied by the target number of histories per cycle, N, to determine the desired number of fission sites in cell k:

$$N_k = NP_k. \tag{7.2}$$

The unmodified number of Monte Carlo fission sites in cell k, M_k, is then compared with N_k. If $\frac{M_k}{N_k} > 1$, then each site in cell k is killed with probability $p_k^{kill} = 1 - \frac{N_k}{M_k}$. If $\frac{M_k}{N_k} < 1$, then each site in cell k is copied $f = floor\left(\frac{N_k}{M_k}\right)$ times with probability $p_k^{copy} = ceil\left(\frac{N_k}{M_k}\right) - \frac{N_k}{M_k}$, and is copied $f+1$ times with probability $1 - p_k^{copy}$. [The functions *floor* and *ceil* round a real number to the next lowest and next highest integer, respectively.] The result of this modification is a Monte Carlo fission bank of approximately N fission sites; these sites form a distribution that approximately matches the CMFD fission source distribution. Alternatively, the source bank could be modified using adjusted particle weights as in Lee, et al. [4][5]

The HCMFD fission source converges more quickly and is more stable than the standard Monte Carlo fission source, especially for high dominance ratios. Therefore, modifying the Monte Carlo source distribution to match the HCMFD fission source should accelerate source convergence and stabilize the Monte Carlo source. The HCMFD feedback can be turned off after any given cycle. We show, however, that the Monte Carlo source immediately destabilizes when CFMD is turned off.

In this chapter, we compare standard Monte Carlo and Monte Carlo with HCMFD-I, -II, and -III feedback for several criticality test problems. All entropy, eigenfunction, and standard deviation figures reflect the Monte Carlo source entropy and Monte Carlo eigenfunction. The entropy and eigenfunctions resulting directly from the HCMFD calculations are not reported. However, both the Monte Carlo eigenvalues and HCMFD eigenvalues are reported; we show that the HCMFD eigenvalues are more accurate.

7.2 Feedback Effect on Source Convergence

In this section, we show that performing Monte Carlo with HCMFD feedback converges and stabilizes the Monte Carlo fission source. When HCMFD feedback is turned "off", the Monte Carlo source destabilizes, so the HCMFD feedback should be kept on for all cycles. We demonstrate the effects of feedback on source convergence on Problem #1C, a homogeneous 70 cm slab with a dominance ratio of approximately 0.996. The cross sections are listed in Table 6.4.

Location [cm]	Σ_t [cm^{-1}]	Σ_s [cm^{-1}]	Σ_f [cm^{-1}]	ν
$0 < x < 70$	1.0	0.5	0.2	2.4

Table 7.1 Material specifications of Criticality Problem #1C.

The problem was simulated using no feedback ("MC"), feedback during inactive cycles ("MC-FB-x (Inactive Only)"), and feedback during all cycles ("MC-FB-x"), where "x" is the numeral I, II or III corresponding to the HCMFD-I, -II, or –III method, respectively. The numerical parameters are listed in Table 7.2.

Histories/Cycle	Inactive Cycles	Active Cycles	Fine Grid [cm]	CMFD Parameter p
100,000	200	200	0.5	1

Table 7.2 Numerical parameters of Problem #1C.

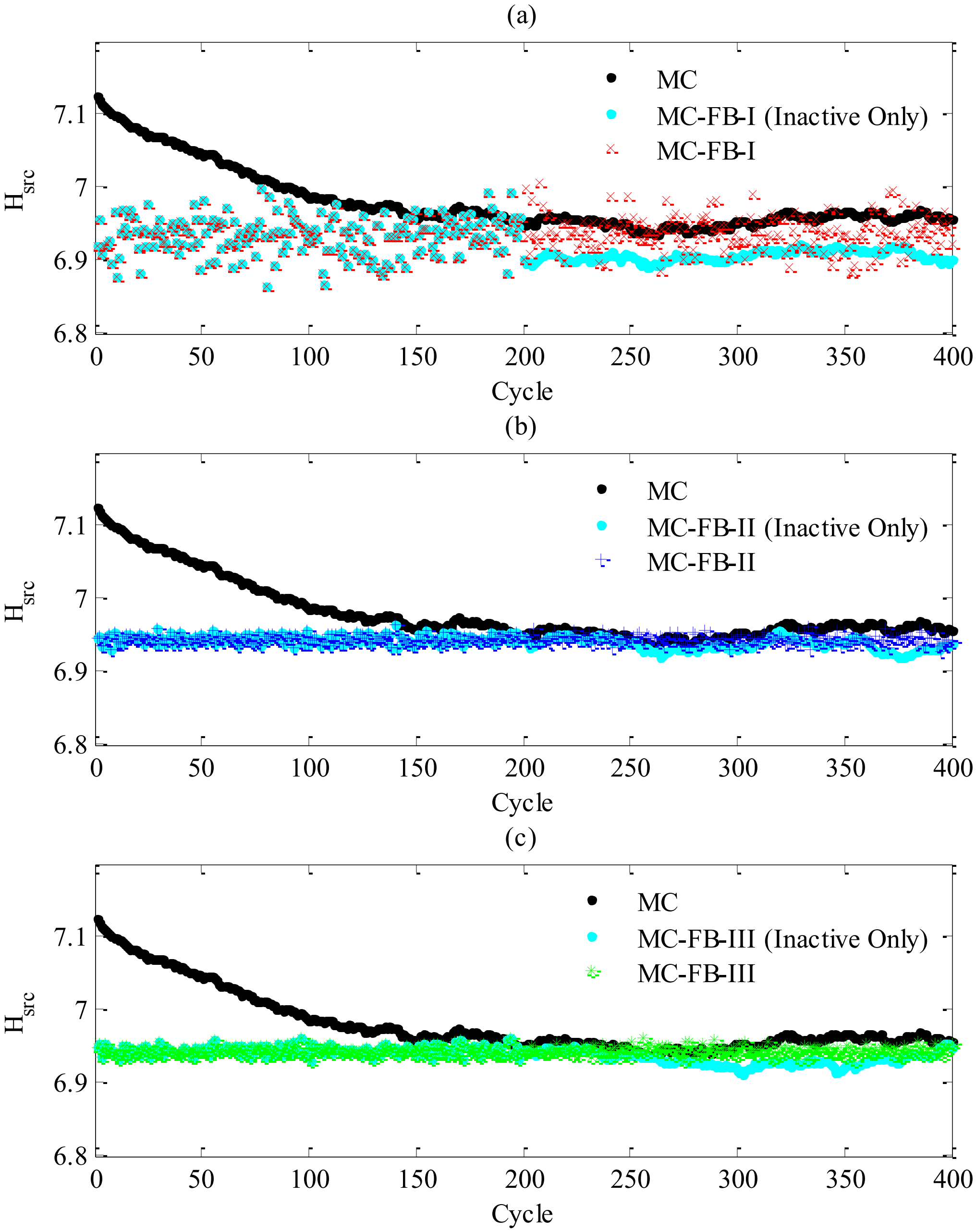

Figure 7.1 Entropy behavior of Monte Carlo with and without HCMFD feedback for Problem #1C.

Figure 7.1 shows that the standard Monte Carlo source converges around cycle 200. Applying HCMFD-I, -II, or -III feedback at the beginning of the calculation converges the fission source immediately, and keeps the source converged as long as the feedback is "on". When the feedback is turned off during active cycles, the fission source immediately destabilizes, and the Shannon entropy wobbles and diverges from the asymptote. These source convergence effects can be seen in the mean eigenfunction (averaged over active cycles) in Figure 7.2.

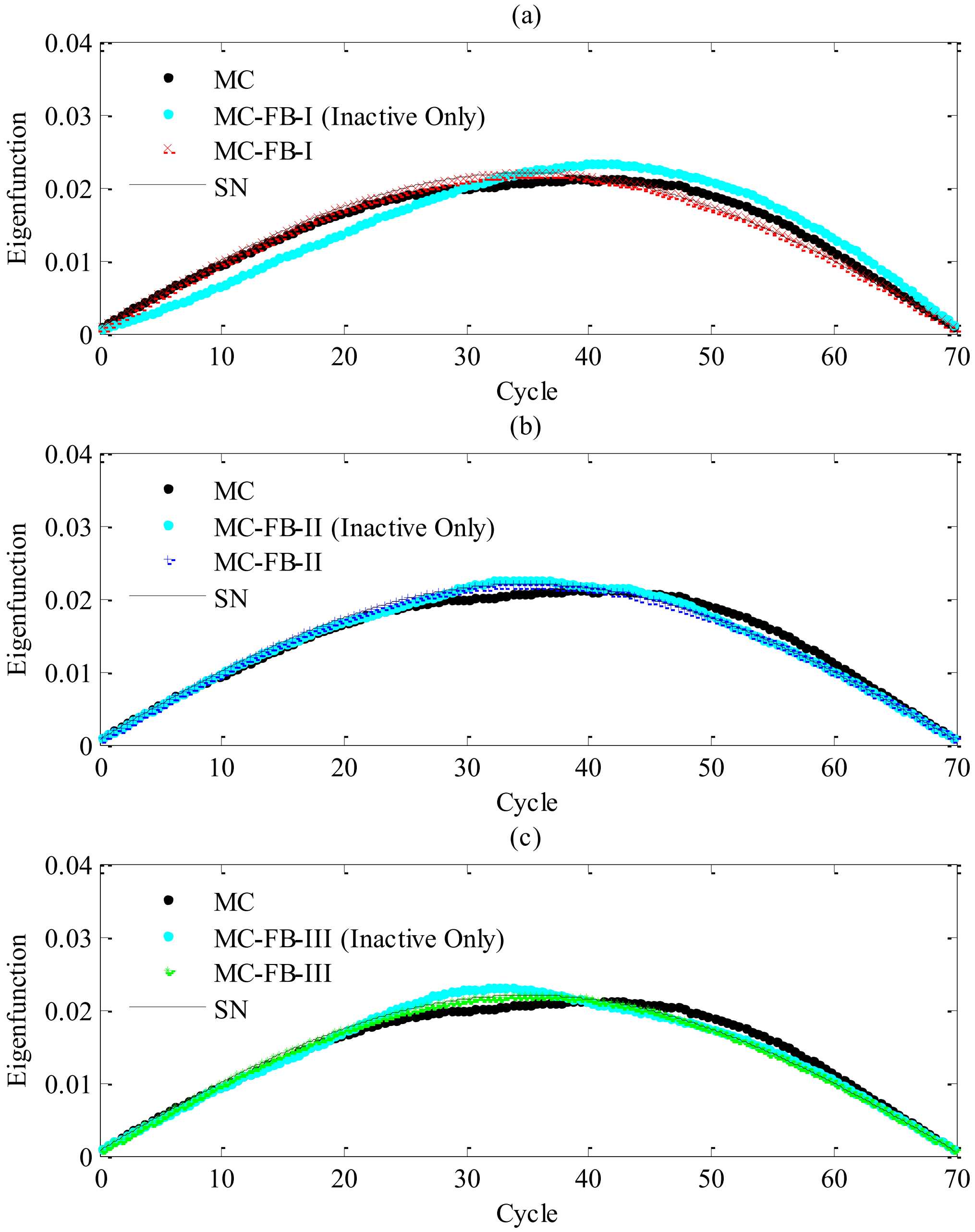

Figure 7.2 Monte Carlo eigenfunctions with and without HCMFD feedback for Problem #1C.

The mean eigenfunction is accurate when feedback is applied for all cycles. However, when feedback is turned off during active cycles (or not used at all), the eigenfunction has significant errors.

As shown in Table 7.3, applying feedback during active cycles improves the accuracy of the Monte Carlo eigenvalue slightly, but does not significantly change its (apparent) variance. This is expected because feedback is used only to stabilize the fission source at the beginning of each cycle, and the Monte Carlo eigenvalue is computed by *standard Monte Carlo transport* within the cycle. Additionally, the eigenvalue is less sensitive to statistical errors than the eigenfunction in high dominance ratio problems. The HCMFD eigenvalues (computed from the CMFD equations after each cycle) are more accurate and have much less variance than the corresponding Monte Carlo eigenvalues.

Method	**Eigenvalue**	**Apparent S.D.**	**HCMFD Eigenvalue**	**HCMFD Apparent S.D.**
SN	0.958764	-	-	-
MC	0.958328	0.000290	-	-
MC-FB-I (Inactive)	0.958468	0.000267	0.958747	0.000009
MC-FB-II (Inactive)	0.958823	0.000273	0.958766	0.000002
MC-FB-III (Inactive)	0.958184	0.000288	0.958765	0.000002
MC-FB-I	0.958991	0.000302	0.958755	0.000008
MC-FB-II	0.958322	0.000284	0.958766	0.000002
MC-FB-III	0.958747	0.000292	0.958765	0.000002

Table 7.3 Eigenvalue means and standard deviations for Monte Carlo with and without feedback.

The results of this section show that applying HCMFD feedback to Monte Carlo converges and stabilizes the Monte Carlo fission source, thereby lowering the number of inactive and active cycles required for accurate eigenfunction estimation. In addition, the eigenvalues computed in the HCMFD calculations are much more accurate, and have less variance, than the Monte Carlo eigenvalues. Therefore, we recommend that feedback be turned on for all cycles, and that the HCMFD eigenvalue be reported rather than the mean Monte Carlo eigenvalue.

7.3 Performance for Small Number of Histories per Cycle

In Chapter 6, we showed that standard Monte Carlo produces inaccurate eigenfunctions and eigenvalues when the number of histories is small. We now show that applying HCMFD feedback makes the Monte Carlo results more accurate. Problem #1D (the 100 cm slab from Chapter 6) was simulated using N=50,000 histories. Figure 6.19 plots the standard Monte Carlo eigenfunction and the eigenfunctions obtained with feedback (averaged over 500 active cycles).

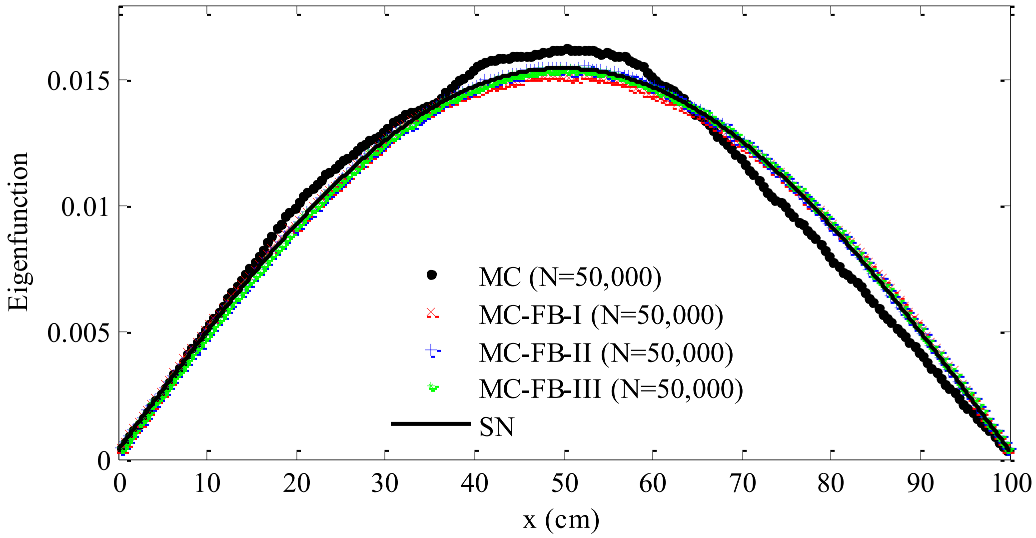

Figure 7.3 Monte Carlo eigenfunctions with and without feedback for small number of histories per cycle.

The eigenfunctions obtained using feedback in Figure 6.19 are more accurate than the standard Monte Carlo eigenfunction. [We again note that the number of histories cannot be arbitrarily low to perform Monte Carlo with feedback. All regions of the problem must be sufficiently sampled in order to estimate the required HCMFD nonlinear functionals. In contrast, standard Monte Carlo can be performed with any number of histories.]

7.4 Performance for Small Number of Active Cycles

In Chapter 6, we noted that in high dominance ratio criticality problems, the Monte Carlo estimates of the eigenfunction and eigenvalue must be averaged over several hundred active cycles in order to reduce statistical errors that are correlated from cycle to cycle. In this section, we show that applying feedback increases the accuracy of the Monte Carlo eigenfunction for individual cycles, and consequently fewer active cycles are needed. Problem #1D (100 cm slab from Chapter 6) was simulated with 100,000 histories per cycle with NA=1 and NA=10 active cycles. The mean eigenfunctions obtained with and without feedback are compared in Figure 6.20.

(a) Number of Active Cycles = 1

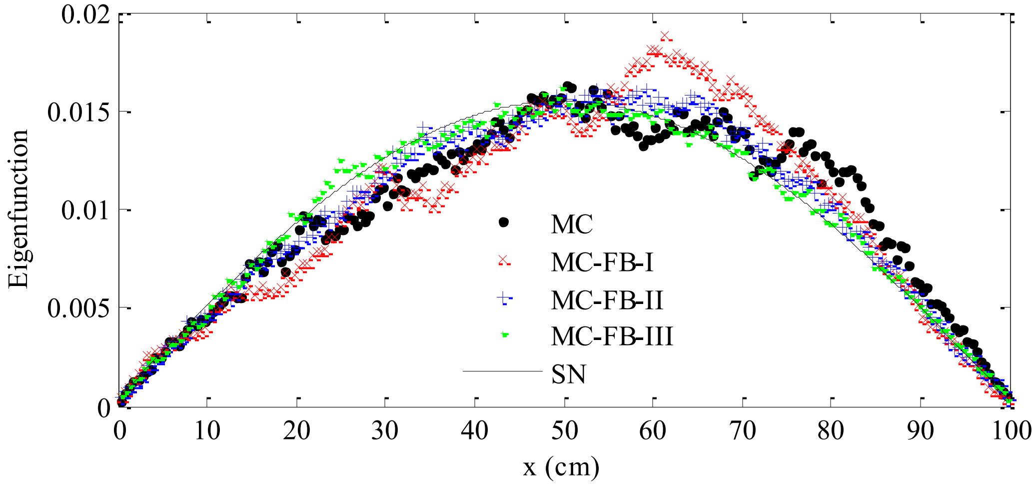

(b) Number of Active Cycles = 10

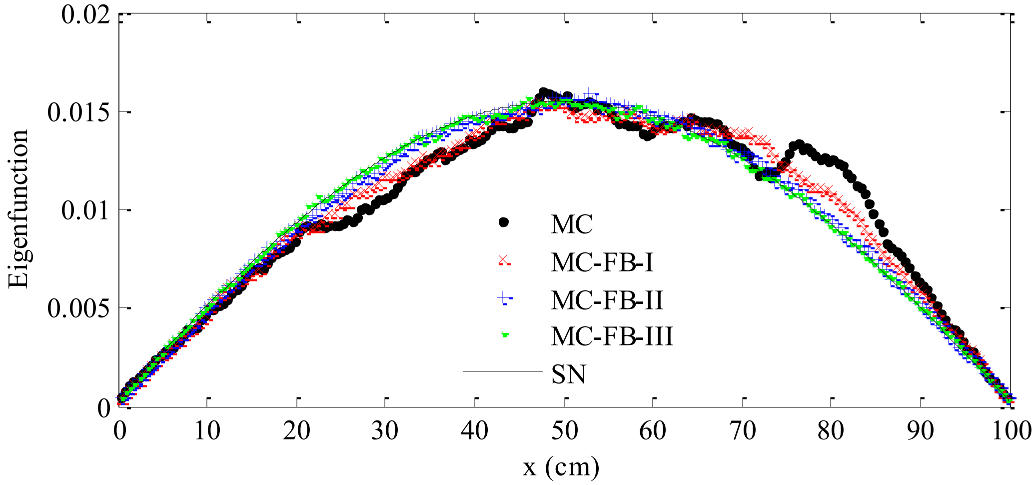

Figure 7.4 Eigenfunctions averaged over one and ten active cycles.

The mean Monte Carlo and HCMFD eigenvalues are compared to the benchmark S_N eigenvalue, $k_{eff} = 0.959386$ in Table 6.9. The error is listed in per cent mille

$(1 \text{ pcm} = 10^{-5} \frac{\Delta k}{k})$.

Method	Eigenvalue (Error in pcm)		HCMFD Eigenvalue (Error in pcm)	
	NA=1	NA=10	NA=1	NA=10
MC	0.961257 (195)	0.959109 (-29)	-	-
MC-FB-I	0.964815 (566)	0.959104 (-29)	0.959389 (0)	0.959393 (1)
MC-FB-II	0.965008 (586)	0.960491 (115)	0.959351 (-4)	0.959381 (-1)
MC-FB-III	0.961191 (188)	0.958884 (-52)	0.959410 (3)	0.959386 (0)

Table 7.4 Eigenvalues averaged over various numbers of active cycles.

The Monte Carlo eigenfunctions with HCMFD-II and HCMFD-III feedback are more accurate than the Monte Carlo eigenfunction with HCMFD-I feedback and without feedback for both NA=1 and NA=10 active cycles. For the individual cycle comparison (NA=1), the HCMFD-III feedback resulted in significantly better accuracy than the HCMFD-II feedback. When the number of active cycles increased to 10 (NA=10), the mean HCMFD-II and HCMFD-III eigenfunctions behaved similarly.

Turning on feedback did not improve the accuracy of the Monte Carlo eigenvalue. However, the HCMFD eigenvalues were much more accurate than the Monte Carlo eigenvalues in all cases (NA=1 and NA=10). In fact, for a single cycle, the HCMFD-I, -II, and –III eigenvalues had errors of only 0, 4, and 3 pcm (compared to 195 pcm in standard Monte Carlo). This is a large improvement in accuracy.

These results show that the individual cycle estimates of the Monte Carlo eigenfunction and the HCMFD eigenvalues obtained with feedback are very accurate. Therefore, fewer active cycles are necessary to obtain accurate solutions for high dominance ratio problems when feedback is used.

7.5 Real vs. Apparent Variance

As noted in Chapter 6, the Monte Carlo source converges very slowly in problems with high dominance ratios, causing the *apparent variance* of the eigenfunction to underestimate the *real variance*. We demonstrate that when the CMFD feedback is used to modify the Monte Carlo fission source, the apparent variance of the resulting Monte Carlo eigenfunction is much closer to the real variance.

To demonstrate this, Problem #1C (the 70 cm slab from Chapter 6) was simulated with N=100,000 histories per cycle and NA=25 active cycles. The simulation was performed K=25 independent times with and without feedback, generating 25 independent estimates of the mean eigenfunction and apparent variance: $\hat{\phi}_{NA,k}$ and $\sigma_k^2\left(\hat{\phi}_{NA,k}\right)$. The *average apparent variance* and *real variance* were calculated from Eqs. (6.7) and (6.8):

$$\sigma_A^2 = \frac{1}{K}\sum_{k=1}^{K}\sigma_k^2\left(\hat{\phi}_{NA,k}\right), \tag{7.3}$$

$$\sigma_R^2 = \frac{K}{K-1}\left[\frac{1}{K}\sum_{k=1}^{K}\hat{\phi}_{NA,k}^2 - \left(\frac{1}{K}\sum_{k=1}^{K}\hat{\phi}_{NA,k}\right)^2\right]. \tag{7.4}$$

The apparent and real relative standard deviations (RSD) are plotted in Figure 7.5. The *ratio of real to apparent standard deviation,* $r_{R/A} \equiv \frac{\sigma_R}{\sigma_A}$, is plotted in Figure 7.6.

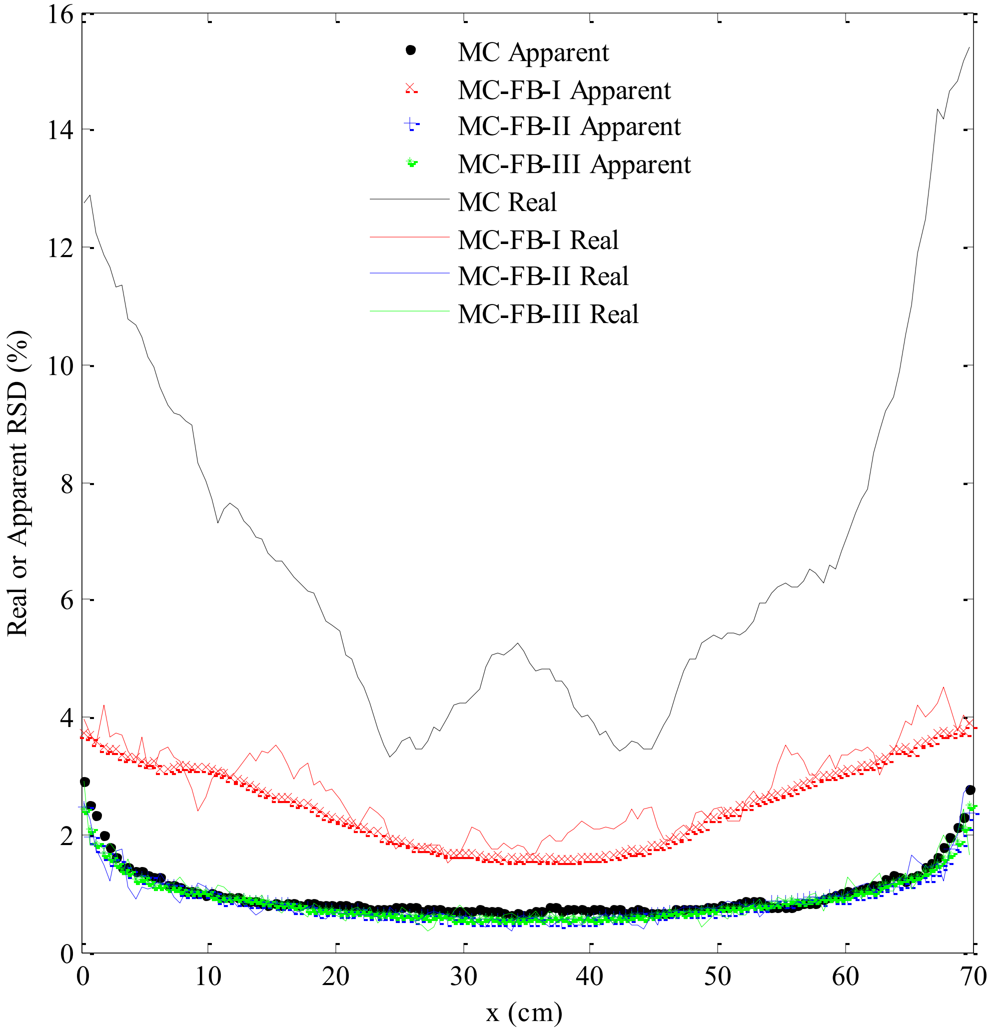

Figure 7.5 Real and apparent relative standard deviations of the mean eigenfunction when feedback is applied.

The real RSDs of the Monte Carlo eigenfunctions with HCMFD-II and -III feedback (MC-FB-II and MC-FB-III) range between 1-3% for this test problem. The real RSD of MC-FB-I is 2-4%, and the real RSD of the standard Monte Carlo eigenfunction is 4-15%. Therefore, use of HCMFD-II and –III feedback results in a significant reduction of *real* error in standard Monte Carlo. Applying HCMFD-II and –III feedback to the Monte Carlo simulation results in real variances which are 3-5% of the real standard Monte Carlo variance. Therefore, the fractional computing time of the Monte Carlo simulation with HCMFD feedback is approximately 3-5%, and the feedback calculation is 20-35 times faster than a standard Monte Carlo calculation. This *significant* computational savings refers to the savings during active cycles. The actual savings is higher when feedback is applied because fewer inactive cycles are required for source convergence.

The ratio of real to apparent standard deviation is plotted in Figure 7.6.

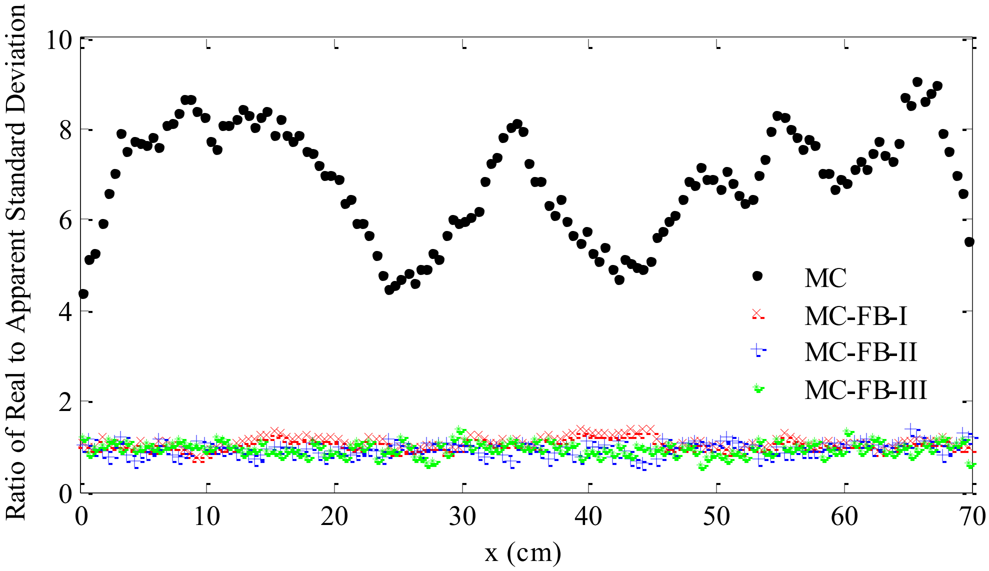

Figure 7.6 Ratio of real to apparent standard deviation when feedback is applied.

For the specified problem, the Monte Carlo apparent standard deviation underestimates the actual standard deviation by a large factor and should not be trusted. However, the real standard deviation in the HCMFD methods is *approximately equal* to the apparent standard deviation. Therefore, performing feedback is advantageous for two reasons: it reduces the real error in the Monte Carlo estimate of the eigenfunction, and this reduced real error is well-estimated by the apparent error obtained from a single calculation. This section confirms the results obtained by Lee, et al. [5] for HCMFD-I, and shows that the close relationship between real and apparent variance also holds for HCMFD-II and HCMFD-III.

7.6 Criticality Problem #2: Two-Fissile Region Slab

7.6.1 Problem Description

We again consider Criticality Problem #2 from Chapter 6, the heterogeneous, isotropically-scattering 27 cm slab with vacuum boundaries and the material parameters in Table 6.10.

Region	Location [cm]	Σ_t [cm^{-1}]	Σ_s [cm^{-1}]	Σ_f [cm^{-1}]	ν
1	$0 < x < 5$	1.0	0.856	0.0	-
2	$5 < x < 10$	1.0	0.8	0.1	2.4
3	$10 < x < 17$	1.0	0.856	0.0	-
4	$17 < x < 22$	1.0	0.8	0.1005	2.4
5	$22 < x < 27$	1.0	0.856	0.0	-

Table 7.5 Material specifications of Problem #2.

The separation of the two fissile regions causes the eigenfunction to be very sensitive to small changes in material parameters such as the 0.5% difference in fission cross sections. This problem is computationally "difficult" and is characteristic of the models required to analyze spent fuel storage. We simulate this problem in Monte Carlo with and without HCMFD-I, -II, and -III feedback.

7.6.2 Numerical Parameters

The Monte Carlo specifications for Problem #2 are listed in Table 7.6. A benchmark S_{32} solution was performed with a uniform 0.001 cm grid.

Method	**Number of Histories/Cycle (N)**	**Inactive Cycles (NI)**	**Active Cycles (NA)**	**Fine Grid [cm]**	**CMFD Parameter** *p*
MC	200,000	500	500	0.5	-
MC-FB-I, MC-FB-II, MC-FB-III	200,000	20	500	0.5	1

Table 7.6 Numerical parameters of Problem #2.

7.6.3 Numerical Results

The cycle-wise entropy behavior for Problem #2 is plotted in Figure 6.23. The feedback calculations were performed with many fewer inactive cycles due to the accelerated source convergence. Cycles 21 through 520 are active for the feedback calculations, and cycles 501 through 1000 are active for the standard Monte Carlo calculations.

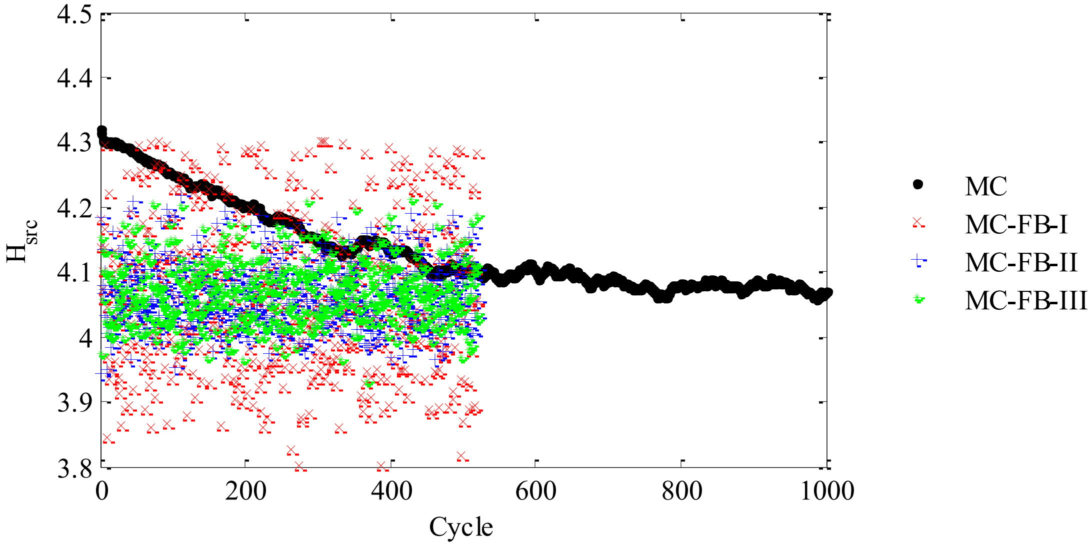

Figure 7.7 Shannon entropy behavior of Problem #2.

The Monte Carlo calculations with feedback "converged" within the first few cycles; however, their Shannon entropies have greater variance than the standard Monte

Carlo Shannon entropy. In other words, the fission source distribution fluctuates by a larger amount over cycles when HCMFD feedback is applied. This indicates that the HCMFD functionals and low-order equations are sensitive to statistical errors in this problem. However, the HCMFD-II and –III methods appear to be less sensitive than the HCMFD-I method. While the cycle-to-cycle fission source fluctuations are larger when HCMFD-II and –III feedback is applied, these statistical errors cancel, and the mean eigenfunction over active cycles is significantly more accurate. The mean eigenfunctions and their apparent RSD are plotted in Figure 6.25, and the errors compared to the benchmark solution are plotted in Figure 6.26.

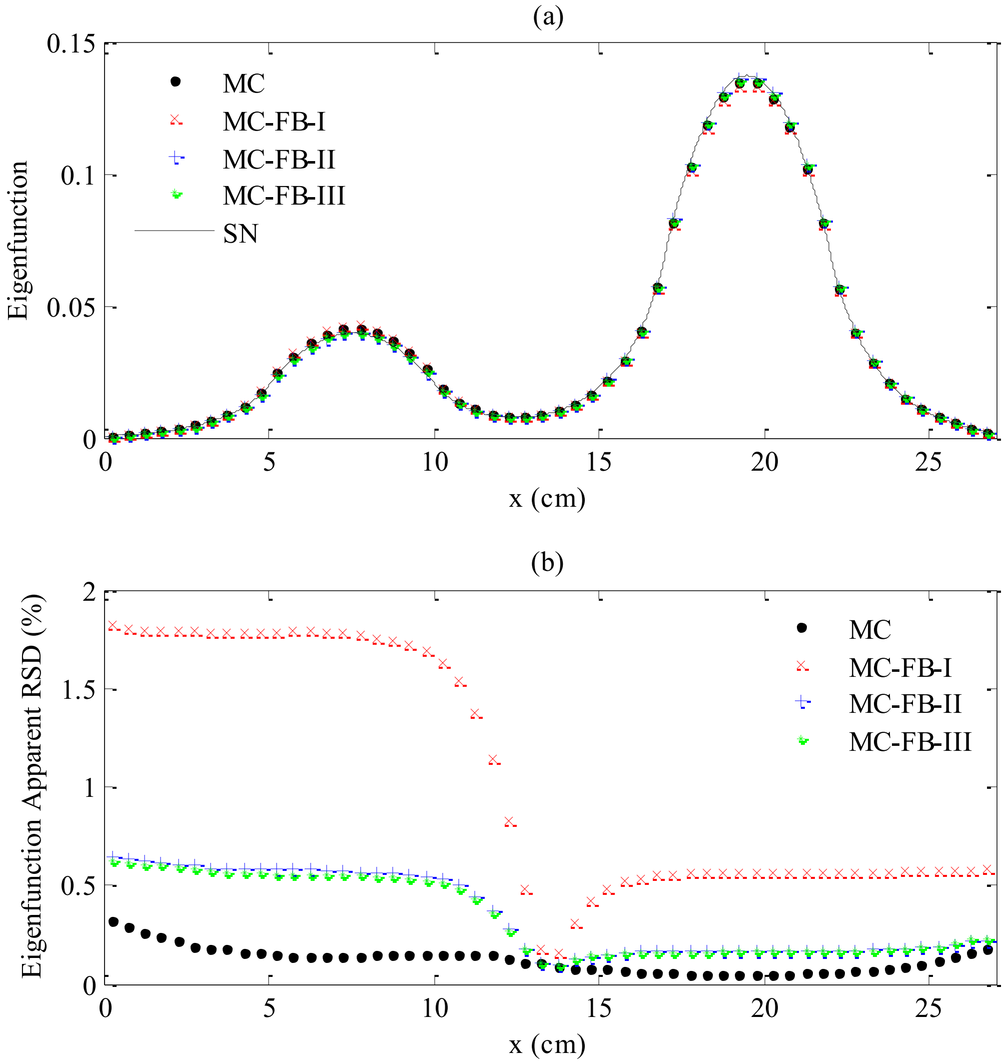

Figure 7.8 Mean eigenfunction and apparent RSD of Problem #2.

The HCMFD-II and -III eigenfunctions are accurate compared to the benchmark S_N solution (maximum relative error around 2% compared to 6% in the standard Monte Carlo solution). The HCMFD-I eigenfunction was less accurate than the standard Monte Carlo solution (maximum error around 9%). These results are consistent with results in Chapter 6, where Monte Carlo was performed without feedback and the HCMFD-I, -II, and –III eigenfunctions were compared. The errors in the HCMFD-I solution are large near the two flux peaks ($x = 7.5$ and $x = 19.5$). At these spatial locations, the net current is close to zero, and statistical errors in the $\hat{D}^{(I)}_{k+1/2}$ functionals are large because of the $\phi_{1,k+1/2}$ term. The HCMFD-II and –III functionals were specifically formulated to reduce statistical error in $\phi_{1,k+1/2}$ term, and a marked reduction in error can be seen in these methods near the same spatial locations.

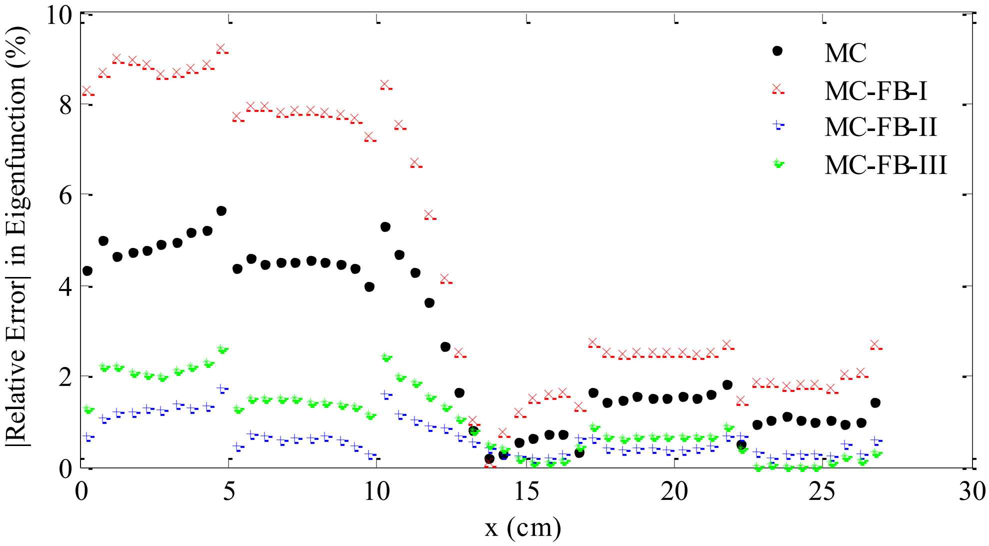

Figure 7.9 Relative error in eigenfunction compared to benchmark solution for Problem #2.

As in Chapter 6, this problem was repeated with a large number of histories per cycle (N=500,000), and again, the HCMFD-I eigenfunction was less accurate than standard Monte Carlo. We emphasize that this problem is particularly challenging, and the ability of the HCMFD-II and HCMFD-III methods to perform better than HCMFD-I indicate that they are much less sensitive to statistical errors.

The Monte Carlo eigenvalues for Problem #2 are listed in the following table, along with the corresponding HCMFD eigenvalues when feedback is present.

Method	Eigenvalue	Apparent S.D.	HCMFD Eigenvalue	HCMFD Apparent S.D.
SN	0.957779	-	-	-
MC	0.957618	0.000120	-	-
MC-FB-I	0.957282	0.000117	0.957786	0.000045
MC-FB-II	0.957722	0.000113	0.957791	0.000016
MC-FB-III	0.957662	0.000115	0.957767	0.000015

Table 7.7 Mean eigenvalues for Problem #2.

Applying method -II and -III feedback increases the accuracy of the Monte Carlo eigenvalues slightly. However, the HCMFD-II and -III eigenvalues are much more accurate, and they have low apparent standard deviation. We emphasize that when applying feedback, two eigenvalues are generated for each cycle: the Monte Carlo eigenvalue and the HCMFD eigenvalue. We recommend that the HCMFD eigenvalue be used because it is more accurate and has less variance.

7.7 Criticality Problem #3: Heterogeneous Reactor Core

7.7.1 Problem Description

Criticality Problem #3 is a 346.8 cm heterogeneous reactor core consisting of 17 assemblies and a total of 816 material regions. [A complete description of this problem is given in Chapter 6.] This problem is geometrically detailed and has a high dominance ratio due to its large size. We perform Monte Carlo with HCMFD-I, -II and -III feedback and compare the results with standard Monte Carlo to demonstrate that feedback can be used successfully on geometrically complex problems.

7.7.2 Numerical Parameters

The numerical parameters of the calculation are listed in Table 7.8. The feedback was performed on the quarter assembly level (one coarse cell consists of twelve 0.425 cm material regions). A benchmark S_{32} calculation was performed with a uniform 0.05375 cm grid.

Method	**Number of Histories/Cycle (N)**	**Inactive Cycles (NI)**	**Active Cycles (NA)**	**Fine Grid [cm]**	**CMFD Parameter** *p*
MC	100,000	150	100	0.425	-
MC-FB-I, MC-FB-II, MC-FB-III	100,000	20	100	0.425	12

Table 7.8 Numerical parameters of Problem #3.

7.7.3 Numerical Results

The feedback calculations were again performed with fewer inactive cycles than the standard Monte Carlo calculation because the fission source converges much faster when feedback is applied. Cycles 21 through 100 are active for the feedback calculations, and cycles 151 through 250 are active for the standard Monte Carlo calculations. The Shannon entropy behavior of Problem #3 is plotted in Figure 6.30.

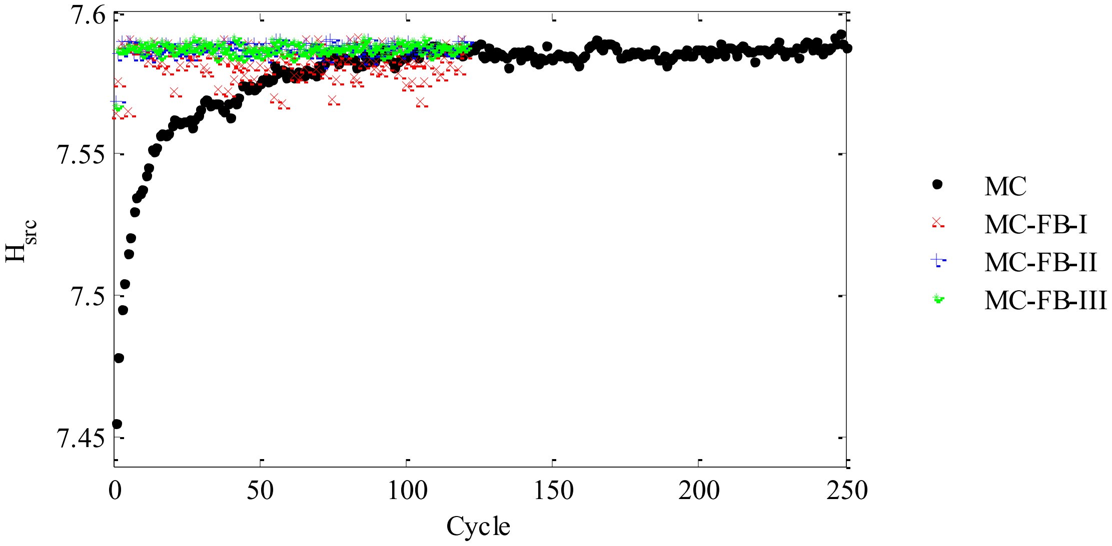

Figure 7.10 Shannon entropy behavior of Problem #3.

The mean eigenfunction and apparent RSD for Problem #3 are plotted in Figure 6.32, and the errors compared to the benchmark solution are plotted in Figure 6.33.

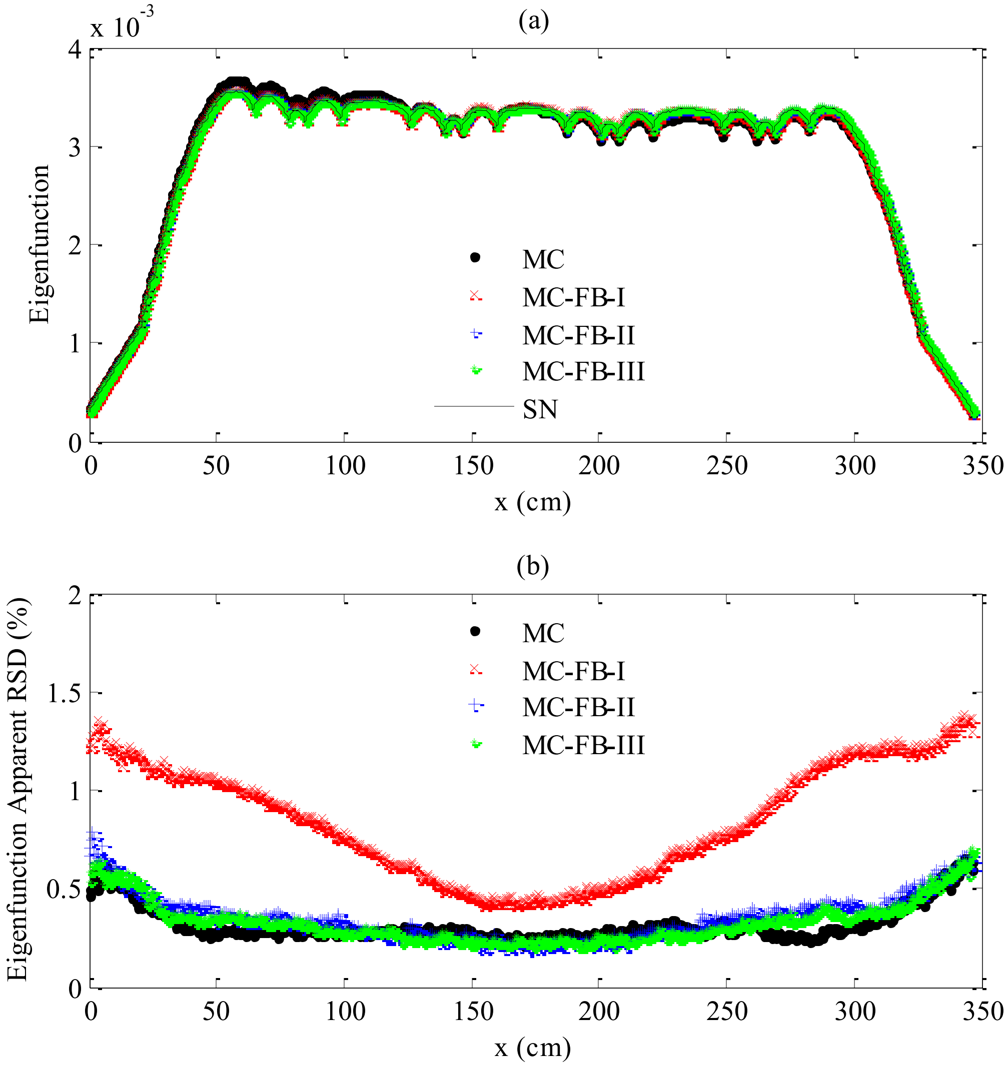

Figure 7.11 Mean eigenfunction and apparent RSD of Problem #3.

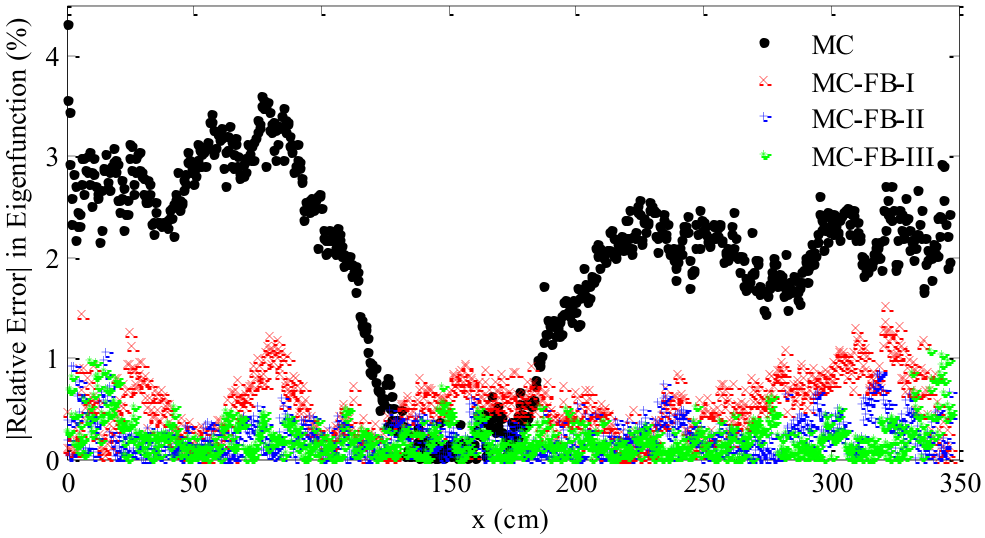

Figure 7.12 Relative error in eigenfunction compared to benchmark solution for Problem #3.

The Monte Carlo eigenfunctions with HCMFD-I, -II or –III feedback are much more accurate than the standard Monte Carlo eigenfunction. The HCMFD-II and –III feedback solutions are slightly more accurate (maximum errors around 1.1%) than the HCMFD-I feedback solution (maximum error around 1.7%). In addition, the apparent standard deviation of HCMFD-II and HCMFD-III is about half that of HCMFD-I. We showed that the HCMFD methods all underestimate the real variance by about the same factor, so the ranking (but not magnitude) of apparent standard deviations in these three methods can be trusted from Figure 6.32.

The eigenvalue results are presented in Table 6.15. There appears to be a small bias in the Monte Carlo calculations, which could be eliminated by using more histories per cycle. The Monte Carlo and HCMFD eigenvalues obtained with feedback are more accurate than the standard Monte Carlo eigenvalue.

Method	Eigenvalue	Apparent S.D.	HCMFD Eigenvalue	HCMFD Apparent S.D.
SN	1.212212	-	-	-
MC	1.212821	0.000386	-	-
MC-FB-I	1.212238	0.000353	1.212477	0.000059
MC-FB-II	1.212583	0.000351	1.212460	0.000029
MC-FB-III	1.212396	0.000399	1.212455	0.000029

Table 7.9 Summary of eigenvalue results for Problem #3.

These results indicate that performing feedback on a relatively coarse mesh (quarter assembly level) is still beneficial for stabilizing the Monte Carlo fission source and calculating more accurate eigenfunctions and eigenvalues. The time savings for this problem was significant, as the number of inactive cycles was reduced by 80%.

7.8 Summary of Numerical Results

In this chapter, we described the process of using the HCMFD fission source to stabilize the Monte Carlo fission source during a Monte Carlo criticality calculation. This "feedback" procedure accelerates fission source convergence, resulting in fewer inactive cycles required. It also stabilizes the fission source once converged, so that the source does not "wobble" in high dominance ratio problems. When feedback is turned "off", the Monte Carlo fission source destabilizes, so we recommend that feedback be kept "on" for all inactive and active cycles. It was shown that HCMFD-II and HCMFD-III stabilize the source better than HCMFD-I, but all three converge the source equally quickly.

We note that applying feedback during active cycles alters the Monte Carlo transport procedure by modifying the fission source. Therefore, the solutions obtained using feedback during active cycles are *not* "pure" Monte Carlo solutions. However, the modification is performed by using source biasing factors from an exact system of low-order equations that has no truncation error. The parameters in this system of equations are nonlinear functionals determined by the same Monte Carlo simulation. Moreover, we have presented numerical results that the solutions obtained using feedback are more accurate than standard Monte Carlo solutions because feedback “pushes” the standard Monte Carlo solution in the correct direction for difficult problems.

In addition, fewer active cycles are required when feedback is applied because each individual cycle eigenfunction estimate is more accurate (each cycle begins with a converged fission source). Finally, fewer histories per cycle are required because the nonlinear functionals in the HCMFD methods are not as sensitive to statistical errors as direct Monte Carlo estimates of the eigenfunction.

The Monte Carlo eigenfunction obtained using feedback is much more accurate than the standard Monte Carlo eigenfunction. The Monte Carlo eigenvalue obtained using feedback is also more accurate than the standard Monte Carlo eigenvalue, but the HCMFD eigenvalue calculated after each cycle is much more accurate than both of this quantities. We recommend that the HCMFD eigenvalue be reported rather than the Monte Carlo eigenvalue. For the problems considered in this work, the HCMFD-II and HCMFD-III solutions were consistently more accurate, and had less variance, than the HCMFD-I and standard Monte Carlo solutions.

It is well-known that the *apparent standard deviation* of the standard underestimates the *real standard deviation* of the standard Monte Carlo eigenfunction in high dominance ratio problems. This underestimation is due to strong inter-cycle correlation of the fission source. In high dominance ratio problems, the standard Monte Carlo eigenfunction changes very little from cycle to cycle. However, the HCMFD eigenfunctions are only weakly dependent on the standard Monte Carlo eigenfunction, and cycle-wise estimates are more randomly distributed about the true mean, and less tightly correlated. Application of feedback from HCMFD calculations therefore makes the Monte Carlo fission source less correlated to the previous cycle, and it makes the apparent standard deviation of the eigenfunction obtained with feedback approximately equal to the real standard deviation. Therefore, performing feedback is advantageous for two reasons: it reduces the real error in the Monte Carlo estimate of the eigenfunction, and the real error is well-estimated from a single calculation.

Overall, in Chapters 6 and 7, we demonstrated the efficiency of nonlinear functional hybrid Monte Carlo-CFMD techniques on monoenergetic fixed source and criticality problems. The concept of “feedback” was also explored, whereby the CMFD fission source is used to stabilize the Monte Carlo fission source. The hybrid Monte Carlo-CMFD techniques were very efficient compared to standard Monte Carlo for this subset of test problems. Work published by Lee, et al. [4][5] indicates that these types of methods can be successfully extended to include energy dependence using a multigroup formulation. Additionally, these methods can be extended to more general geometries.

7.9 References

[1] M.J. Lee, H.G. Joo, D. Lee, and K. Smith, “Investigation of CMFD Accelerated Monte Carlo Eigenvalue Calculation with Simplified Low Dimensional Multigroup Formulation,” *Proc. of the 2010 International Conference on the Physics of Reactors,* May 9-14, 2010, Pittsburgh, PA, CD-ROM, American Nuclear Society (2010).

[2] M.J. Lee, H.G. Joo, D. Lee, and K. Smith, “Multigroup Monte Carlo Reactor Calculation with Coarse Mesh Finite Difference Formulation for Real Variance Reduction,” *Proc. of the 2010 Joint International Conference on Supercomputing in Nuclear Applications and Monte Carlo*, Oct 17-21, 2010, Tokyo, Japan, CD-ROM, SNA+MC2010 (2010).

Chapter 8

Conclusions

8.1 Summary of Nonlinear Functional Technique

Several new hybrid Monte Carlo-deterministic methods (H-MC-S_2, H-MC-S_2X, HCMFD-II, HCMFD-III, and HCMFD-IV) using the nonlinear functional approach are developed in this thesis. The nonlinear functional approach consists of two fundamental steps: (1) the Monte Carlo estimation of *nonlinear functionals*, which are ratios of integrals of the particle flux, and (2) the deterministic solution of a system of low-order algebraic equations that contain these functionals as parameters. This hybrid technique is more complicated than conventional Monte Carlo, but it can offer major computational advantages, particularly for systems with high dominance ratios.

The nonlinear functionals for each hybrid method are formulated by taking space-angle-energy moments of the transport equation and performing algebraic manipulations to obtain a finite system of "low-order" algebraic equations. The stochastic nonlinear functional estimates are used in the low-order equations to solve for the particle flux. If the structure of the low-order equations is favorable, and the functionals are defined appropriately, the solution of the low-order equations will have less variance than the direct Monte Carlo estimate of the solution. Theoretical justification was given that stochastic estimates of the nonlinear functionals should have less variance than direct estimates of standard linear quantities when the same Monte Carlo histories are used to evaluate the numerator and denominator of the functional.

8.2 Summary of Proposed Methods

We have developed two fundamentally different classes of nonlinear functional methods that are computationally more efficient than standard Monte Carlo. The first class of methods (H-MC-S_2 and H-MC-S_2X) have low-order equations resembling discrete ordinates equations. These methods are developed for continuous-energy fixed source problems in 1-D planar geometry. The second class of methods (HCMFD-II, HCMFD-III, and HCMFD-IV) have low-order equations resembling diffusion equations. These methods are developed for monoenergetic fixed source and criticality problems in 1-D planar geometry. In the following sections, we summarize the formulation and performance of these hybrid methods.

8.2.1 The H-MC-S_2 Method

The H-MC-S_2 method was developed from the steady-state, planar geometry, energy-dependent, fixed source Boltzmann equation by integrating over phase space to obtain low-order equations resembling the one-group S_2 (discrete ordinates) equations. No approximations in energy or angle were introduced in this condensation process.

The H-MC-S_2 nonlinear functionals resemble flux-weighted cross sections and flux-weighted quadrature but do *not* use the multigroup approximation in energy. The H-MC-S_2 method therefore has no approximations in angle or energy, but it has small statistical and spatial truncation errors. The spatial truncation errors result from a spatial differencing approximation introduced to close the system, and a redefinition of one of the functionals to reduce its variance.

Once the nonlinear functionals are estimated in Monte Carlo, the H-MC-S_2 low-order equations are solved using a simple S_2 sweep and source iteration scheme. The H-MC-S_2 method was shown to be more accurate than standard Monte Carlo and fine-group discrete ordinates methods for a core-reflector problem with significant transport effects. The H-MC-S_2 solution also had lower variance than the history-equivalent direct Monte Carlo estimate of the solution. Therefore, the H-MC-S_2 method offers a computational advantage over standard Monte Carlo and deterministic methods for “difficult” transport problems.

8.2.2 The H-MC-S_2X Method

The H-MC-S_2X method is very similar to the H-MC-S_2 method, but the transport equation is multiplied by a spatial tent function before integration over space, energy, and angle. The tent function eliminates the need for spatial approximations; consequently, the H-MC-S_2X method has only statistical errors. The H-MC-S_2X functionals resemble flux-tent function-weighted multigroup cross sections and flux-weighted angular quadrature, and the low-order equations are again similar to the one-group S_2 equations. They can be solved efficiently with a transport sweep and source iteration.

The H-MC-S_2X method was tested on a core-reflector problem with significant transport effects. The H-MC-S_2X solution was more accurate than a 250-group discrete ordinates calculation, due to the absence of multigroup cross section errors. In addition, the H-MC-S_2X method can be used on an arbitrarily coarse spatial grid, a significant advantage in numerical neutron transport calculations. In addition to being more accurate than deterministic solutions, the H-MC-S_2X solution has less variance than history-equivalent Monte Carlo estimates of the solution, meaning that a more accurate solution can be obtained in less time.

The time savings for this method compared to standard Monte Carlo was approximately 50% for the core-reflector problem. For a much simpler monoenergetic fixed source problem, the time savings was approximately 80%. The H-MC-S_2X method is most efficient when energy-dependence is simple, flux is not highly anisotropic, and particles are well-sampled in all regions of phase space. When these conditions apply, the nonlinear functional numerators and denominators are highly correlated, and the nonlinear functionals can be computed with low variance. When these conditions are relaxed, the functional numerators and denominators become less correlated, and some loss of efficiency occurs. Possible improvements to this method are suggested in Section 8.3.

8.2.3 The HCMFD-II, HCMFD-III, and HCMFD-IV Methods

The HCMFD-II, HCMFD-III, and HCMFD-IV Methods were developed to improve the CMFD-Accelerated Monte Carlo method (referred to as HCMFD-I in this work). In CMFD-Accelerated Monte Carlo, nonlinear functionals, referred to as “CMFD correction factors”, containing the particle current are estimated in Monte Carlo and used in diffusion-like low-order equations. We provided theoretical evidence that nonlinear functionals containing odd angular moments of the flux (such as the particle current) can have large statistical errors compared to other terms. These statistical errors may cause a loss of efficiency in CMFD-Accelerated Monte Carlo.

To reduce statistical error in the current terms of the CMFD correction factors, higher-order moments of the transport equation were used to derive exact expressions relating the cell-averaged current to angular moments of the flux. These expressions were used to partially cancel the statistical error that occurs in the current term of the nonlinear functional. Doing this in three different ways resulted in nonlinear functionals with less statistical error than the original functional; the use of the different functionals define the HCMFD-II, HCMFD -III, and HCMFD-IV methods. These methods were developed for the planar geometry, monoenergetic, steady-state Boltzmann transport equation for fixed source and eigenvalue problems.

For a monoenergetic fixed source problem, the three generalized hybrid Monte Carlo-CMFD methods produced solutions that were more accurate, and had less variance, than CMFD-Accelerated Monte Carlo ("HCMFD-I") and standard Monte Carlo. HCMFD-IV was the most complicated, limited to the case of homogenous coarse cells, and performed only marginally better than HCMFD-III, so it was not tested for criticality problems. The efficiency of the HCMFD-II, -III, and –IV methods were comparable to the efficiency of the H-MC-S_2X method for monoenergetic fixed source problems (roughly 80% savings in computing time).

For criticality problems, the CMFD functionals are estimated during each cycle, and then the CMFD equations are solved for the eigenvalue and eigenfunction. The CMFD results can optionally be used to modify the Monte Carlo fission source using a process known as "feedback". Monte Carlo was performed with and without HCMFD-II and -III feedback, and numerical results showed that the new generalized methods are more effective at converging the fission source than CMFD-Accelerated Monte Carlo.

The proposed HCMFD-II and -III methods (with or without feedback) offer the following computational advantages over standard Monte Carlo and HCMFD-I in criticality problems:

(1) Fewer inactive cycles are required to converge the fission source because of accelerated source convergence.
(2) Fewer active cycles are required because of increased fission source stability.
(3) Fewer particles per cycle are required because the new nonlinear functionals are less sensitive to statistical errors.

(4) Inter-cycle correlation is reduced, and the apparent error is much closer to the true error than in standard Monte Carlo. (This property is also true in HCMFD-I).

The only apparent disadvantage of the HCMFD-II and –III methods is sensitivity to the size of the coarse mesh: the special cell-averaged current terms in the functionals become less useful as the coarse mesh becomes thicker, and performance differences between the HCMFD-I, -II, -III methods become less significant.

Overall, the proposed generalized hybrid Monte Carlo-CMFD methods offer significant computational savings in “difficult” criticality problems with high dominance ratios. For a homogenous slab with a high dominance ratio, the HCMFD-II and -III methods required 1% of the standard Monte Carlo active cycle computing time when no feedback was applied. For the same test problem, Monte Carlo with HCMFD-II or -III feedback required 3-5% of the standard Monte Carlo active cycle computing time. The total time savings is even greater because fewer inactive cycles are required to converge the fission source. We note that the efficiencies of the HCMFD methods compared to standard Monte Carlo are problem-dependent, and these new methods should be tested on different problems of varying complexity to determine the range of possible efficiencies.

Finally, the HCMFD-II and –III methods are only slightly more complex to implement than the HCMFD-I method, and they are significantly simpler to implement than Functional Monte Carlo.

8.3 Future Work

The methods in this thesis have been successfully developed and tested on a subset on neutron transport problems. We now make several suggestions about the future direction of work on these methods.

8.3.1 The H-MC-S_2X Method

The H-MC-S_2X method was developed and tested for continuous-energy fixed source problems in planar geometry. The H-MC-S_2X solutions were accurate for all test problems, but a loss of computational efficiency was observed for problems with strong energy and angle dependence. This loss of efficiency is due to reduced correlation in the nonlinear functional numerator and denominator random variables. We recommend that the H-MC-S_2X methodology be extended to utilize a multigroup-like formulation in energy. In addition, the methodology could be extended to increase the number of direction "groups". The result of these modifications would be a larger set of nonlinear functionals whose numerators and denominators are better-correlated and a larger system of low-order equations resembling multigroup discrete ordinates methods.

In addition, variance reduction techniques should be used in the Monte Carlo calculation for problems in which particles are poorly sampled in certain regions. It is unclear if the error in the core-reflector problems is due mostly to poor sampling of neutrons in the negative direction or poor correlation in the nonlinear functional numerators and denominators.

Finally, we note that the new H-MC-S_2X and HCMFD methods have similar computational efficiencies for a monoenergetic *fixed source* problem (20% of standard Monte Carlo computing time). However, the HCMFD methods have *much greater* computational efficiencies for high dominance ratio eigenvalue problems (1% of standard Monte Carlo computing time). We therefore recommend that the H-MC-S_2X method be developed and tested on high dominance ratio eigenvalue problems to see whether gains similar to the HCMFD methods can be achieved. One advantage of the H-MC-S_2X method is the absence of the high variance "total current" functional. This suggests that H-MC-S_2X may perform at the same level as the HCMFD-II and –III methods. Finally, extension to 2-D should be studied to examine whether the increased cost of the deterministic calculations is justified by the improvement in computational efficiency over standard Monte Carlo.

8.3.2 The HCMFD-II, HCMFD-III, and HCMFD-IV Methods

HCMFD-II, -III, and -IV methods were successfully demonstrated on a monoenergetic fixed source problem. While HCMFD-IV had the best performance, it is currently limited to analyzing problems in which the coarse mesh is homogeneous. If the restriction of homogeneous coarse cells could be removed, the method could be advantageous over HCMFD-II and HCMFD-III. However, the improvement in variance over these methods must be weighed against the fact that the HCMFD-IV nonlinear functional is more complicated.

The HCMFD-II and –III were extremely computationally efficient on one-group high dominance ratio criticality problems. These methods should be extended to incorporate energy dependence and anisotropic scattering. In addition, they should be derived for multi-dimensional geometries.

More studies should be done to determine when the performances of the HCMFD-II and –III methods differ: they performed very similarly for the test problems considered here. The HCMFD-III functionals are more complicated due to the introduction of the spatial tent function, so it may be best to pursue the HCMFD-II method unless practical test problems demonstrate that HCMFD-III is significantly advantageous.

8.3.3 Other Future Work

We also recommend a study on how these nonlinear functional hybrid methods amplify or reduce the bias that exists in standard Monte Carlo calculations when the number of histories per cycle is too low. (A bias is said to exist when the average of several independent simulations does not converge to the benchmark solution.) We did not perform multiple calculations to confirm whether a Monte Carlo bias exists for the "difficult" two fissile-region test problem (Criticality Problem #2 in Ch. 6), but the numerical results from a single simulation indicated that HCMFD-I amplified errors in the Monte Carlo estimate, whereas HCMFD-II and HCMFD-III reduced these errors. Independent calculations should be performed to see whether a true bias exists. The magnitude of bias in each method should then be compared, if it exists.

In addition, studies need to be done on the propagation of random error through deterministic equations. These studies would shed insight on how statistical errors in the functionals become amplified in the solution of the "low-order" equations in these hybrid methods. In addition, this would improve our understanding about the optimal structure of the low-order equations for these hybrid methods.

Finally, there are numerous choices in the implementation of these "nonlinear functional" hybrid methods. There is flexibility in how the nonlinear functionals are defined and estimated. For example, in criticality calculations, we generated new estimates of the CMFD nonlinear functionals after each Monte Carlo cycle. However, the functionals could be tallied cumulatively over all active cycles. Additionally, the hybrid methods developed in this work may be used with any Monte Carlo variance reduction technique, such as weight windows, provided the Monte Carlo simulation generates “fair” estimates of the quantities required in the nonlinear functionals. Doing this would extend the range of possible applications of these methods to include problems with areas of very low neutron density, such as radiation shielding problems.

8.4 Final Remarks

The nonlinear functional approaches proposed in this work, as well as those developed by Yang and Lee, represent a new strategy for using Monte Carlo in particle transport simulations. The development of these hybrid methods is a relatively new area of research, and we cannot yet characterize the behavior of these methods completely. We have attempted to provide both mathematical and intuitive justification for using the nonlinear functional approach. In addition, we have provided numerical results showing that the various “nonlinear functional” techniques can be used successfully on a wide array of test problems. While the new methods are only partially explored, we have shown that these techniques are promising and should be extended to more realistic problems.